Geometry and mounting optimization of lightweight gearbox components

Firas Bejar

Numéro d'ordre NNT: 2023ECDL0043 Année: 2023

THESE de DOCTORAT DE L'UNIVERSITÉ DE LYON
OPÉRÉE AU SEIN DE L'ÉCOLE CENTRALE DE LYON

ÉCOLE DOCTORALE MEGA

(Mécanique, Énergétique, Génie Civil, Acoustique)

Spécialité: MÉCANIQUE

Soutenue le 29/11/2023 par

Firas Bejar

Geometry and Mounting Optimization of Lightweight Gearbox Components

---

Devant le jury composé de:

Rapporteur:	Francesco FRANCO	-	Professeur, UNINA Frederico II
Rapporteur:	Mohamed Ali Hamdi	-	Professeur, UTC
Presidente:	Thouraya BARANGER	-	Professeur, U.Claude Bernard Lyon 1
Examinateur:	Mauro FONTANA	-	Ingénieur, Poweflex
Directeur:	Mohamed ICHCHOU	-	Professeur, LTDS, ECL
Co-directeur:	Joël PERRET-LIAUDET	-	Maître de Conférence, LTDS, ECL
Co-directeur:	Olivier BAREILLE	-	Maître de Conférence, LTDS, ECL

Acknowledgments

I would like to express my heartfelt gratitude to everyone who has supported me throughout my journey to completing this thesis project. Your encouragement, guidance, and unwavering belief in me have been instrumental in bringing this project to fruition.

First and foremost, I am deeply thankful to my dedicated supervisors, Prof. Mohamed Ichchou, Dr. Joël Perret-Liaudet, Dr. Olivier, and Dr. Mauro Fontana, for first giving me the opportunity to be part of this project but also for their invaluable mentorship and insightful feedback. Your expertise, patience, and willingness to engage in meaningful discussions have significantly shaped the direction and quality of this work. I am truly fortunate to have had the opportunity to learn from you.

I extend my sincere appreciation to my family for their unwavering love and encouragement. Your constant support, both emotionally and morally, has been my anchor during the challenging phases of this journey. To my father Noureddine, mother Serra, Brother, Wacim, Sister Sawsan, and sister-in-law, Sonia, your sacrifices and belief in my capabilities have been the driving force that kept me going despite being far from your presence.

I would like to acknowledge my team members within the LIVE-I project, who were not just colleagues but family. Our collaboration extended beyond work, creating lasting friendships that enriched our professional and personal lives.

I extend my heartfelt gratitude to the lab co-workers who were integral in fostering a friendly and inspiring environment. I also want to acknowledge those friends whom I didn't have the chance to interact with frequently over these years but whose continuous encouragement provided me with essential life balance. Your support, whether in person or from a distance, made a significant difference.

I wish to express my gratitude for the financial support extended by the Marie Skłodowska-Curie Actions to the LIVE-I project. This support has been instrumental in facilitating the effective pursuit of my research endeavors.

Last but not least, I extend my appreciation to all the supervisory board and participants of the project who generously contributed their time and insights to this study. Your willingness to participate has been crucial in shaping the empirical foundation of this work.

To everyone who played a part, whether big or small, in this journey, I offer my sincerest thanks. Your belief in me and in the importance of this project has motivated me to give my best. This accomplishment would not have been possible without you.

With heartfelt gratitude,
Firas Bejar

Résumé

Cette thèse a pour but d'établir un cadre d'optimisation visant à améliorer la légèreté des composants d'engrenage et la dynamique de la boîte de vitesses sans compromettre leurs propriétés statiques.

Notre approche comprend une méthodologie numérique complète, incluant l'évaluation de divers logiciels d'analyse de contact des engrenages. Cette analyse approfondie permet d'évaluer leur aptitude à simuler différents systèmes de transmission, y compris divers types d'engrenages, de géométries, de modèles de boîtes de vitesses, avec ou sans désalignement, et des engrenages standard ou légers. Ces analyses sont essentielles pour identifier les modèles numériques les plus adaptés à cette question complexe et évaluer l'impact des engrenages légers sur les erreurs de transmission.

Pour évaluer plus précisément les effets des composants légers des engrenages, nous construisons une boîte de vitesses simplifiée à un étage. En utilisant des analyses de convergence, nous ajustons divers paramètres d'engrènement et de réduction modale pour obtenir un modèle prêt pour l'optimisation. La réduction de poids est réalisée en deux étapes : d'abord, les épaisseurs de l'âme et de la couronne de l'engrenage sont modifiées de manière aléatoire et soumises à une analyse de contact dentaire, en prenant en compte l'absence de non-linéarités géométriques.

Notre étude explore également l'introduction de trous dans le corps de la roue, ce qui entraîne des variations dans l'excitation et nécessite une analyse de rotation complète tenant compte de l'excitation par les bandes latérales. La création d'engrenages perforées est facilitée par un générateur de corps d'engrenages aléatoires intégré à la CAO, suivi d'une analyse de sensibilité basée sur le principe de forêt aléatoire. Cette analyse évalue l'influence des paramètres de la distribution statistique du motif, principalement sur les vibrations dans le boîtier.

En utilisant les enseignements de l'analyse de sensibilité et de la génération de motifs aléatoires, nous mettons en place un processus d'optimisation par essaimage de particules à deux niveaux. La première étape optimise les épaisseurs de la jante et de l'âme, tandis que la seconde étape se concentre sur l'optimisation des trous. Ce processus est optimisé en termes de paramètres d'optimisation, ainsi que d'analyses et de mesures pour assurer la rapidité et la fiabilité des résultats.

En fonction des objectifs spécifiques, cette approche d'optimisation basée sur les données permet de réduire le poids des composants tout en améliorant les performances dynamiques de la boîte de vitesses.

Mots clés: Systèmes de transmission, conception des engrenages, analyse de sensibilité, optimisation géometrique, légéreté, vibrations.

Geometry and mounting optimization of lightweight gearbox components

Abstract: This thesis sets out to establish an efficient optimization framework, the objective of which is to enhance the lightweight properties of geared components while improving gearbox dynamics, all without significantly compromising static properties.

Our approach encompasses a comprehensive numerical methodology, which includes benchmarking various gear contact analysis software tools. This extensive benchmarking evaluates their suitability for simulating transmission systems under diverse conditions, encompassing different gear types, macro and micro geometry definitions, isolated or full gearbox models, with and without misalignment, and standard or lightweight gears. These analyses play a crucial role in identifying the most suitable numerical models for addressing this complex issue, as well as in assessing the impact of solid lightweight gears on transmission error excitation.

To provide a more precise assessment of the effects of lightweight gear components, we construct a simplified single-stage gearbox. Through convergence analyses, we vary numerous meshing and modal reduction settings to establish a higher fidelity model primed for the optimization process. The gear weight reduction is executed in two stages: initially, the gear web and rim thicknesses undergo variation in random combinations and are subjected to single-tooth contact analysis, accounting for the absence of geometrical non-linearities in the blank.

Our study delves into the introduction of holes in gear blanks, leading to fluctuations in excitation and necessitating a full-rotation analysis that factors in excitation by the sidebands. The creation of perforated blanks is facilitated through a CAD-integrated randomized gear blank generator, and a random forest-based sensitivity analysis is executed on a range of randomized samples. This analysis assesses the influence of parameters defining the statistical distribution of the pattern, primarily on the vibrations induced in the housing.

Leveraging insights gleaned from the sensitivity analysis and random pattern generation, we introduce a dual-level Particle Swarm Optimization process. The first stage optimizes rim and web thicknesses, followed by the second stage which focuses on hole optimization. This process is optimized in terms of the optimization parameters, as well as the analyses and metrics used to measure the speed and reliability of results.

Depending on the specific objectives, the implementation of this data-driven optimization scheme consistently accomplishes weight reduction in components while concurrently enhancing the dynamic performance of the gearbox.

Keywords: Transmission systems, Gear design, Sensitivity analysis, Geometry optimization, vibrations

Contents

List of Acronyms

General Introduction

Industrial and scientific context

As part of the efforts to achieve the 2030 sustainable development goals, significant attention has been given to mitigating the environmental impacts associated with the industrial era. Among the various contributors to environmental pollution, transportation is recognized as a significant factor, generating both noise and CO2 emissions. In response, several European regulations have been implemented, outlining a roadmap to progressively limit these emissions.

One notable regulation, 540/2014 of the European Parliament, plays a crucial role in enforcing limitations on acceptable noise levels generated by various vehicle categories. This regulation sets forth a paramount objective of accomplishing a gradual reduction in measured sound levels, aiming to achieve a decrease of $3-5$ dB(A) within a span of 10 years. Particularly, for vehicles possessing a power-to-mass ratio lower than $120kW/1000Kg$, precise thresholds for sound levels have been stipulated. These thresholds stand at 72 dB(A), 70 dB(A), and 78 dB(A) for the years 2016, 2022, and 2026, respectively.

Furthermore, the EU Regulation 2019/631 focuses on reducing CO_2 emissions from passenger cars, with a specific emphasis on promoting the production of lightweight vehicles. Starting from January 1, 2025, new passenger cars and light commercial vehicles must achieve a reduction of 15% in average emissions compared to the 2021 target. This requirement becomes more stringent by January 1, 2030, with a reduction target of 37.5% for passenger cars and 31% for light commercial vehicles, based on the 2021 benchmarks. Additionally, beginning in 2025, both vehicle types must comprise a 15% share of zero- and low-emission vehicles. By 2030, these shares increase to 35% for passenger cars and 30% for light commercial vehicles.

This thesis is situated within the framework of the Lightening and Innovating Transmission for Improving Vehicle Environmental Impacts (LIVE-I) project. Collaborating with various academic and industrial partners, this project aims to achieve groundbreaking advancements in lightweight transmission systems.

The LIVE-I project encompasses multiple dimensions focused on optimizing vehicle transmission systems, as illustrated in Figure 1 which are divided into distinct work packages that address passive, semi-active, and active control of the gearbox. These work packages are further allocated among three teams, each consisting of three early-stage researchers. For the purposes of this study, the primary focus lies within the passive category, specifically targeting the optimization of gearbox components from a geometrical perspective.

This thesis centers on assessing the impacts of lightweight components on gearbox excitations and dynamic responses, with the aim of formulating a robust optimization strategy applicable to commercial models. The evaluation process involves a collaborative effort between Ecole Centrale de Lyon's Laboratory of

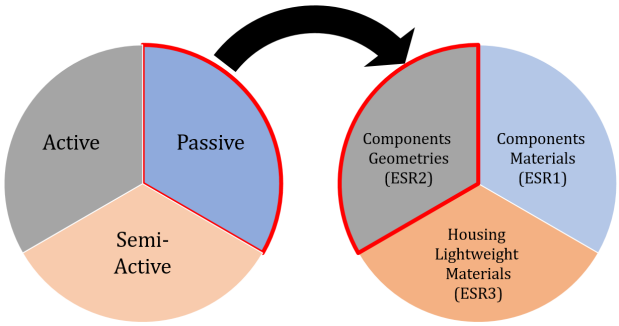

Figure 1: LIVE-I Work packages

Tribology and Dynamics of Systems (LTDS) and Powerflex IT, seeking to establish a comprehensive understanding of these effects.

Motivation of the work

The emergence of lighter car components as an environmental solution faces a gap in our understanding. Research hasn't fully explored how these changes influence a vehicle's overall behavior. Although lightweight gear designs are discussed, their selection often lacks in-depth rationale beyond adjusting mass for dynamic needs. This study is driven by the goal to fill this void, untangling the intricate interactions between lightweight gear designs and how vehicles perform.

The core purpose of this research is to establish a comprehensive guideline for optimizing car gear components. This guideline isn't confined to specific gearboxes; it's designed to be adaptable across various types. Moreover, it's not a mere theoretical construct. This framework has the potential to be applied in real-world scenarios, even commercial transmissions, bridging the gap between academic theory and practical implementation.

In recognizing the complexity of geared systems and the multitude of variables at play, it's imperative to acknowledge the limitations of this research. While our aim is to uncover crucial insights, we recognize that this study may not encompass the entirety of implications. Yet, this work is a substantial stepping stone, setting the stage for future in-depth explorations and paving the way for a meticulous approach to optimizing vehicles in the times to come.

Structure of the manuscript

The manuscript is mainly divided into five chapters. Chapter I delves into the intricate realm of gearbox noise and vibration. It begins by exploring the phenomenon of whine noise in transmission systems. The chapter then examines different aspects of gearbox dynamics, including static transmission error and mesh stiffness. Addi-

tionally, it discusses methods for dynamic modeling of gearboxes. The chapter concludes by highlighting modern advancements in approaches to reduce the weight of gears.

In Chapter 2, we embark on an in-depth benchmark study that draws comparisons between academic and commercial transmission system modeling software. Our core objective is to unravel the essential similarities and differences among these tools and their implications on the computation of static transmission error. Through a systematic exploration of diverse study cases encompassing varying levels of complexity, the chapter effectively illuminates the outcomes generated by each software and their ability to tackle the lightweight aspect of geared systems. This sheds considerable light on the substantial influence exerted by modeling methods and software selections on computation results, thus underscoring the constraints associated with adopting a fully numerical approach. Furthermore, the chapter navigates the intricate challenge of numerically simulating the multi-scale attributes inherent to transmissions, offering insights into the inherent intricacies of such simulations. In essence, this chapter lays the practical foundation for making judicious software and modeling decisions, a pivotal aspect contributing to a comprehensive transmission system analysis.

Chapter 3 seamlessly extends the exploration initiated in the preceding chapter, focusing on how variations in static transmission error resonate in the dynamic response, ultimately influencing the outcomes of optimization procedures contingent upon the employed software. This section delves deeply into the strategies employed to model gearboxes, ensuring consistency across different platforms. Moreover, it carefully identifies the main sources of result disparities. This is followed by a comprehensive convergence analysis, aimed at unraveling the interplay between model parameters and the scope of response variability. In essence, this chapter serves as a practical roadmap for cultivating a more resilient model through a solid grasp of the intricate dynamics that define transmission systems.

Chapter 4 explores how lightweight gear design affects static and dynamic gearbox conditions. The analysis investigates the influence of rim and web thicknesses on gear performance, employing both local and global sensitivity analyses. Furthermore, the study uses an Automatic Gear Blank Pattern Randomizer and sensitivity analysis to assess how varying distributions of blank holes impact gear performance, highlighting the potential for constructing lightweight gears all while maintaining and even improving their dynamic capabilities from a system point of view.

Chapter 5 takes advantage of the conclusions drawn from the analyses in Chapter 4. The objective is to develop a two-tiered optimization scheme based on Particle Swarm Optimization. This scheme aims to achieve lightweight gears while maintaining control over certain response metrics based on user preferences. In the first level, the gear's mass is adjusted by modifying rim and web thicknesses. The second level focuses on optimizing the pattern distribution to manage convergence. The algorithm was applied to a simplified single-level gearbox, with potential applicability to various dynamic models, though higher model complexity would entail greater computational demands.

Chapter 1

State of the Art

Contents

1.1 Whine noise in transmission systems

1.1.1 Introduction

Gearbox noises play a crucial role in determining the overall performance and Noise Vibration, and Harshness Noise Vibration and Harshness (NVH) characteristics of a vehicle. These noises are accompanied by vibrations that can be attributed to various internal and external factors. They can be broadly classified into two primary categories: broadband noises and tonal noises.

Broadband noises encompass a wide range of frequencies and lack a specific dominant pitch. Examples of broadband noises include grinding, knocking, or banging sounds. Grinding noises typically indicate potential issues with gear wear or misalignment, while knocking or banging noises suggest loose or worn-out components.

Conversely, tonal noises have a distinct and specific frequency or pitch. A common example is the high-pitched whine associated with rotating components

like gears. It is important to note that whine noise can occur even under perfect mounting conditions due to a gear-type excitation known as the transmission error Transmission Error (TE) which was wildly addressed in the literature [50, 38, 105, 110, 76, 100, 125, 164].

The focus of this thesis is primarily on the functioning of gears under continuous and standard operating conditions, where the whining noise is the most prominent. Therefore, this thesis places a particular emphasis on comprehending and addressing this specific noise issue.

1.1.2 Definition, Origins, and Characteristics of the Static Transmission Error

In the realm of automotive engineering, an extensive array of gears can be observed, commonly distinguished by their involute profile. This type of gear profile is formulated using a mathematically derived curve based on a rolling circle that gradually unwinds from a larger base circle as it traverses along the profile of the gear tooth. Notably, the unique shape of the involute profile allows for the smooth and efficient transmission of power between the meshing gears. This is due to the fact that the contact point moves along a designated path known as the line of contact, which results in a constant speed ratio and improved efficiency.

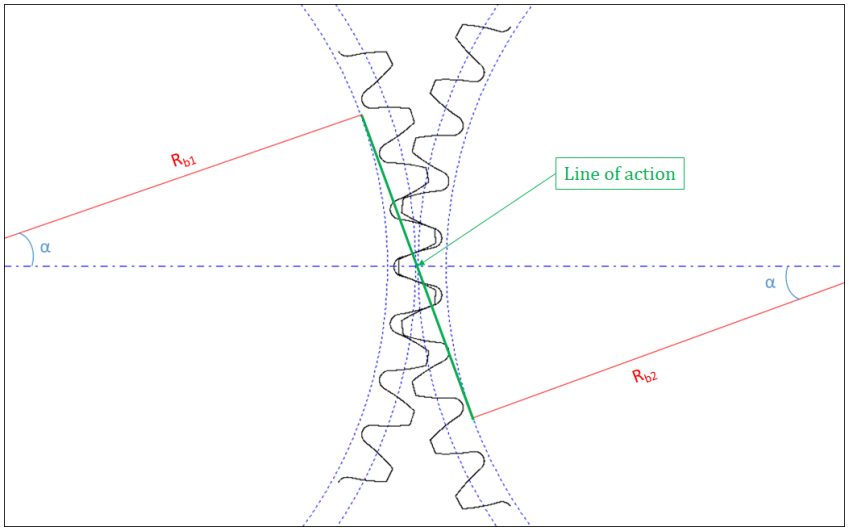

Figure 1.1: Schematic of the line of action. α represents the pressure angle of the gear pair.

When the driving gear of a gearbox system is rotated by a certain amount, it is expected that the driven gear will rotate correspondingly, occupying a position determined by the kinematic input rotation multiplied by the gear ratio. However, this ideal scenario can only be achieved if the gears are perfectly rigid. In reality, the teeth-applied loads are prone to result in a small deviation of the output angular position with respect to the position that the gears would occupy if they were under

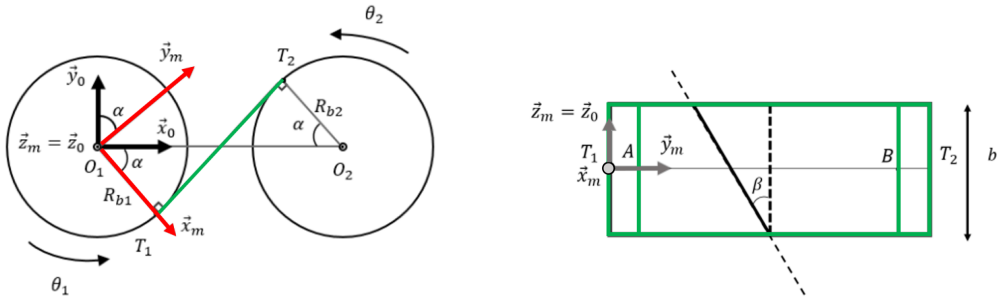

(a) (b)

Figure 1.2: Graphical representation of the line of action (a) and place of action (b).

a perfectly conjugate action. This deviation can be measured in terms of the relative difference between the kinematically-derived and real angular position of the output gear as follows:

$$\Delta\theta_2(\theta_1) = \theta_2 - \frac{Z_1}{Z_2}\theta_1 \tag{1.1}$$

where θ_1 and θ_2 are the angular positions of the meshing gears and Z_j defines the number of teeth of the j^{th} gear. The transmission error can alternatively be expressed in the form of a linear displacement along the line of action Line of action (LOA) as expressed below where R_{b_j} defines the base radius of the j^{th} wheel. This formulation describes the linear approach of the teeth for a specific angle of rotation of the driving gear.

$$STE(\theta_1) = R_{b_2}\theta_2(\theta_1) - R_{b_1}\theta_1 \tag{1.2}$$

This type of formulation is exclusively applicable to the case of isolated gears which are connected to the ground with the help of a single axial degree of freedom. In practical applications, gears are usually connected with other components of the gearbox which makes them able to displace in all 6DOFs. Therefore a geometrical column vector $\mathbf{G}$ in the reference frame $(O_1, \vec{x_0}, \vec{y_0}, \vec{z_0})$ is introduced to couple the 6DOFs of the pinion with the 6DOFs of the wheel:

$$\begin{aligned}\mathbf{G}^T = [\sin(\alpha) \quad \cos(\alpha) \quad \tan(\beta) \quad 0 \quad \frac{-R_{b1}\tan(\beta)}{\cos(\alpha)} \quad R_{b1} \\ -\sin(\alpha) \quad -\cos(\alpha) \quad -\tan(\beta) \quad 0 \quad \frac{-R_{b2}\tan(\beta)}{\cos(\alpha)} \quad R_{b2}]\end{aligned} \tag{1.3}$$

The system transmission error taking into consideration the contribution of all the components of transmission error can be expressed as:

$$\delta_s(\theta_1) = \mathbf{G}^T\mathbf{x} \tag{1.4}$$

with $\mathbf{x}$ representing all the DOFs associated with the input and output gears:

$$\mathbf{x} = [x_1, y_1, z_1, \psi_1, \phi_1, \theta_1, x_2, y_2, z_2, \psi_2, \phi_2, \theta_2] \tag{1.5}$$

This type of transmission error is addressed as "Loaded Static Transmission Error Static Transmission Error (STE)" considering that it is measured when the system is subjected to an external torque and under a relatively very low speed that will prevent any complications caused by dynamic phenomena that would alter the displacement in the line of action.

In the absence of applied torque assuming that the teeth remain in contact, the unloaded static transmission error also referred to as the kinematic transmission error [164] could result from one or a combination of the following physical origins [50, 79, 66, 169]:

- The geometric imperfections that arise due to imprecisions in both the macro and micro geometrical specifications of gears (helix angle, pitch errors, random errors...) which are a result of low quality and insufficient manufacturing tolerances.
- The assembly defects affecting the positioning of the gears relative to one another (eccentricity and parallelism).
- The voluntary microgeometrical corrections of the teeth which, despite deviating the profile from its perfectly involute nature, might have a remarkable contribution to improving the contact behavior and its resulting vibratory response. From these improvements, we can distinguish, a reduction in the friction and wear by controlling the location and intensity of the contact stresses on the tooth flanks which not only increases the transmission efficiency and load-carrying capacity but also contributes to the reduction of the emitted vibrations and noise.

The application of external torque brings some levels of deflection upon the system which contribute to the development of the static transmission error. These deflections can be classified as follows:

- The global elasto-static deformations of the teeth and the gear bodies.
- The Hertzian deformations localized within the tooth flanks.
- The system deflections that extend to include auxiliary parts of the transmission system (shafts, bearings, housing, etc.). These deflections could alter the relative positioning of the gears with respect to each other which impacts the contact region and the calculation of the STE.

The transmission error can vary depending on the rotational speed of the gears and is referred to as the Dynamic Transmission Error Dynamic Transmission Error (DTE) in this case. DTE depends on frequency-related phenomena that affect the relative positions of the gear teeth, which may include variations in meshing stiffness, gyroscopic effects, or system resonances that can significantly contribute

to the displacement along the line of action. As the rotational speed decreases, the influence of these dynamic effects decreases, causing the DTE to converge to the static transmission error.

Recent studies have increasingly emphasized the investigation of dynamic transmission error due to its strong correlation with radiated whine noise. As a result, researchers have developed several experimental methods to measure DTE, as outlined in Akerblom's study [2]. One commonly employed approach is the installation of optical encoders with appropriate resolution on the input and output shafts. These encoders convert mechanical motion into electrical signals, enabling the determination of angular displacement at their mounted positions, thereby deriving the transmission error [69, 126, 112]. Furthermore, high-precision laser vibrometers [165] and accelerometers [139, 12, 3] have been utilized as alternative methods for DTE measurement. Notably, these measurement techniques often capture velocity and acceleration data, necessitating the appropriate definition of transmission error, with the usage of $\dot{x}$ and $\ddot{x}$ denoting velocity and acceleration respectively which are more convenient for dynamic conditions.

The periodicity of the meshing process makes the transmission error periodic in nature and its value will fluctuate depending on the number of teeth in contact at a specific time frame. For every rotation of the input shaft, the associated gear meshes a number of times that is equal to the number of teeth. The product of the rotational frequency of the shaft, denoted as f_0, and the number of teeth, denoted as Z, is referred to as the fundamental meshing frequency which can be expressed as:

$$f_{GMF} = Z f_0 \tag{1.6}$$

Under standard loading conditions and without the presence of geometrical defects, the transmission error harmonic content comprises harmonics that are integer multiples of the fundamental meshing frequency. A proper spectral analysis could reveal some geometrical or mounting abnormalities that give birth to bands at specific frequency ranges. For instance, it is worth noting that the rotational speed of the shaft typically operates at a much lower frequency than the meshing frequency of the gears (i.e., several tens of hertz versus several tens of kilohertz, respectively). Under such conditions, any eccentricity effects that result in the wobbling of the gears around their geometrical center and cause pressure fluctuations are expected to have the same periodicity as the rotation of the shaft. As a result, they can create sidebands around the running speed harmonics. In a similar fashion, any defects that would influence tooth-to-tooth contact (profile defects, mesh stiffness fluctuations, parallelism...) would result in sidebands near the gear mesh frequency and its harmonics. Other defects that could influence specific sets of teeth fall in the intermediate range between the running speed and the meshing frequency.

Typically, a gear pair with a module of 2 and a tolerance class of 6 exhibits a linear transmission error (STE) of approximately $10\mu m$ along the line of action. However, achieving extremely low STE values poses challenges due to the high

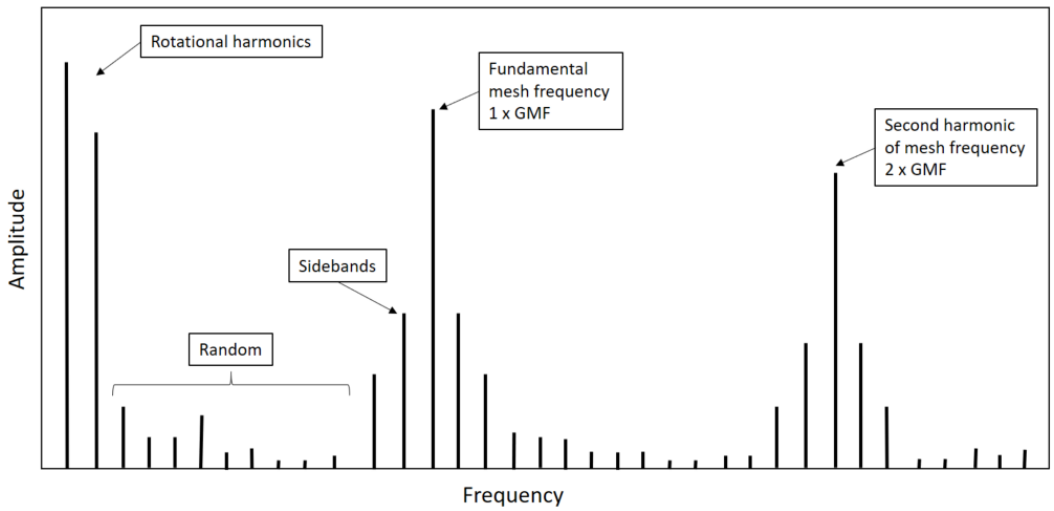

Figure 1.3: Spectral content of a transmission error response

manufacturing precision and expertise required for microgeometry modifications. To enhance the static and dynamic properties of gears, various changes have been employed on gear teeth. One of the most widely utilized profile modifications is tip relief, initially proposed by Walker [158]. Tip relief serves to prevent potential gear interference, jamming, and the formation of stress concentrations near the tooth edges, which can significantly reduce the gear's lifespan.

According to a study conducted by Harris [50], an optimized tip relief can further reduce the amplitude of transmission error, particularly within a targeted torque range. This finding has prompted numerous studies suggesting different forms of tip relief, ranging from linear [37, 140, 142, 98], parabolic [143, 91, 168], and cubic [178], to more complex types [172, 175].

The gear tooth could also be subject to a lead or profile crowning modification with the main aim of reducing the contact and root stresses enhancing the durability of the gear pair [108, 61].

Considering that the transmission error falls within the same order of magnitude as the applied microgeometry changes, geared systems have proved to be very sensitive to these changes since they are prone to primarily affect the contact patches between the mating tooth flanks, changing the pressure distribution and resulting stresses [39, 65]. This ultimately alters the general trend and peak-to-peak value of the transmission error Peak-to-Peak Transmission Error (PPTE)[149, 79, 70, 166].

Applying a microgeometry parameter change automatically results in manufacturing transmission error which excites the system even under unloaded conditions. However, carefully selecting an appropriate combination of these parameters has the potential to minimize the transmission error and enhance the vibroacoustic behavior of a gearbox within a targeted operating torque range [182]. To achieve this, various analytical methods have been employed for robust multi-objective optimization of gear microgeometry [114, 36, 78, 104]. While other studies have focused on

parametric analyses that target different types of tooth changes [154, 14, 13].

1.1.3 Mesh stiffness fluctuations

Meshing stiffness is a measure of the resistance to deformation between gears during the gear engagement process. When gears mesh, they exert pressure on each other due to applied loads, causing deformation. This deformation results in a force that opposes the relative motion of the gears and can be quantified as meshing stiffness. Accurately modeling a gearbox requires the consideration of meshing stiffness, as it represents the elastic coupling between the gears. Various factors can affect the magnitude of meshing stiffness and can be categorized as follows:

- The geometrical non-linearities dictated by an alteration of the load distribution within the contact patch due to changes in the location of the contact line across the tooth flank, and the change of the number of contacting teeth throughout the progression of the meshing cycle.

- The linear elastic deformation of the teeth due to bending, which becomes more significant as the contact line moves towards the tip of the tooth or as the load becomes distributed between a lower number of teeth.

- The non-linear Hertzian deflections resulting from the non-uniform distribution of pressure between the contacting flanks.

While spur gears have teeth that are parallel to the gear axis, leading to abrupt engagement, which in turn causes higher levels of transmission error and fluctuation in mesh stiffness, sometimes reaching up to 65% of its mean value, helical gears offer a notable contrast. The presence of a helix angle in helical gears facilitates a gradual engagement of the teeth over a larger contact area. This characteristic results in a smoother transfer of torque between gears. This gradual engagement effectively mitigates the impact of sudden changes in contact force, leading to reduced transmission error and weaker fluctuations, typically around 40% of its mean value.

The static transmission error and mesh stiffness both demonstrate periodic behavior, revealing a broad spectrum of frequencies that stimulate the system when analyzed. Moreover, the interaction between the static transmission error and mesh stiffness introduces extra harmonics into the dynamic response. Consequently, when this parametric system is subjected to harmonic excitation along with a constant static output torque, it exhibits a complex multi-frequency vibratory response.

It's important to highlight that mesh stiffness plays a crucial role in initiating two significant parametric effects within the system. First, it can induce parametric instabilities in the system's free response. Second, it contributes to the occurrence of resonances in the system's forced response. Both of these parametric phenomena lead to the amplification of vibration amplitudes. Specifically, parametric instabilities materialize when the mesh frequency (denoted as f_m) aligns with either the

sum of the natural frequencies ($f_i + f_j$) of two system modes (i and j) or their harmonics.

$$f_m = \frac{1}{n}(f_i + f_j) \qquad \text{with } n \in \mathbb{N}^* \tag{1.7}$$

Conversely, parametric resonance takes place when the natural frequency f_i aligns with the sum or difference between the excitation frequency f_m and its harmonics:

$$f_i = f \pm n f_m \qquad \text{with } n \in \mathbb{N}^* \tag{1.8}$$

The instability and resonance phenomena significantly impact system performance and lifespan, primarily due to the introduction of substantial vibrations. Therefore, precise modeling and analysis of meshing stiffness fluctuations are vital for predicting and preventing issues related to parametric excitation in gear systems.

Selecting an appropriate modeling technique is crucial and depends on the system's complexity and the desired simulation outcomes. The classification of gear systems often hinges on the chosen modeling method, which encompasses the representation of elastic coupling between gears and the consideration of non-linearities. In this context, Kahraman and Singh [67] proposed a categorization that suggests various methods can be employed, including:

- The Linear Time Invaraiant (LTI) [56, 157] consider a constant meshing stiffness taken as the mean of the time-varying stiffness and introduced as a linear spring positioned along the line of action that couples the gear pair. The model does not account for non-linearities like friction and clearance.
- The Linear Time Variant (LTV) [118] where the stiffness is introduced as a fluctuation over the meshing period as a consequence of accounting for the change in the number of teeth in mesh.
- The Non-Linear Time Invariant (NLTI) models consider a constant stiffness but might introduce some non-linearities.
- The Non-Linear Time Variant (NLTV) [115] which implements a quasi-static approach in order to solve the equations of contact at every moment of the rotation of the gears taking into consideration the induced non-linearities as well as the change in the meshing stiffness.

Considering the tight relationship between the transmission error $\delta(\theta_1)$ and the mesh stiffness $k_m(\theta_1)$, this latter can be expressed for successive angles of rotation of the input gear θ_1 as:

$$k_m(\theta_1) = \frac{\partial F}{\partial \delta(\theta_1)} \tag{1.9}$$

with F being the transmitted load to the line of action as a result of applying a torque C on the input shaft:

$$F = \frac{C}{R_b} \tag{1.10}$$

According to the provided formation, the meshing stiffness depends on several factors including the applied loads and geometrical properties of the gears. For example, gears with larger diameters or heavier loads may have higher meshing stiffness, while gears with smaller diameters or lighter loads may have lower meshing stiffness. Additionally, factors such as surface finish, lubrication, and temperature can also affect the meshing stiffness. For gears designated to automotive applications, the linear mesh stiffness is of the order of several hundreds $N/\mu m$. For a standard spur gear, Welbourn suggests a value of $14N/\mu m$ per unit of contact length expressed in mm. However, this remains a rough estimation considering that it does not depend on the loading conditions and the non-linear characteristics of the gear contact.

1.1.4 Computational Methodology for the Calculation of the Static Transmission Error

The computation of the static transmission error is well-mastered in the literature [129] and established through a Tooth-Contact-Analysis Tooth Contact Analysis (TCA) algorithm, that takes into consideration several aspects of the contact problem including the micro and macrogeometry definition of the gears, the loads, the initial gaps, and the stiffness of the components.

For each fraction of angular rotation of the input gear, the theoretical lines of contacts are determined based on the kinematics of the meshing teeth. Each line is then discretized into a number of segments and a compliance matrix $H(\theta_1)$ is built in order to relate the displacement of the contact line points to the applied force that is supposed to be constant. The matrix $H(\theta_1)$ not only accounts for the bending stiffness as established from the previously-mentioned method but also the local contact deformations based on a semi-analytical Hertzian formulation. The tooth corrections and manufacturing errors are introduced through a vector $e(\theta_1)$ that represents the gap between the mating teeth. This vector further considers any mounting defects or misalignment phenomena that result from the elasto-static deflections that could affect the gears or the gearbox overall. For each angular position θ_1 of the driving gear the contact equations can be formulated as follows:

$$\begin{cases} [H(\theta_1)].\{p(\theta_1)\} = \delta(\theta_1).\{1\} - \{e(\theta_1)\} \\ {}^T\{1\}.\{p(\theta_1)\} = F \end{cases} \tag{1.11}$$

under the constraints:

$$\begin{cases} H_{ij}p_j - \delta + e_i \geq 0 & i = 1, .., n \\ p_j \geq 0 \end{cases} \tag{1.12}$$

The system iterates over each position until the force balance between the external loads and the contact is achieved. The evaluation of the contact equations results

in the static transmission error $\delta(\theta_1)$ as well as the vector $p(\theta_1)$ that represents the load distribution along the contact lines which are assumed to remain in the plane of action for most of the TCA tools.

The complex nature of geared systems has led to the development of numerous tools to estimate static transmission errors, each with varying assumptions regarding contact handling and compliance matrix establishment. These tools will be examined in greater detail in Chapter 2.

1.2 Other Forms of Excitation

Despite transmission error being the main source of excitation causing whine noise, it's important to acknowledge the potential presence of other types of excitation that can contribute to similar noise profiles or even different types of noises. The significance of these additional sources depends on various factors such as design, mounting, and loading conditions.

1.2.1 Frictional excitation

The meshing process goes through three phases as shown in figure 1.4:

- The approach phase is where the gear teeth gradually move toward each other. During this phase, the leading edge of one tooth approaches the trailing edge of the other. The contact between the teeth starts at a point away from the pitch line, and as the gears rotate, the contact area expands along the tooth surfaces.

- The pitch point contact phase occurs right at the level of the pitch point where the gears experience a pure rolling motion.

- The recess phase is where the gear teeth gradually move away from each other. In this phase, the trailing edge of one tooth disengages from the trailing edge of the other. The contact between the teeth reduces as the gears rotate until they completely separate.

The sudden reversal of the direction, magnitude, and location of the frictional forces represents a secondary excitation source that affects the dynamic mesh forces of the gears [137] and the development of the bearing forces [53]. Frictional forces in gears generally have a lesser impact on system excitation compared to a transmission error. While they do affect the overall trend of the transmission error [42], their significance lies primarily in contributing to the higher-order harmonics [150, 151]. These harmonics are generally considered less important from a dynamic perspective. However, in high torque or low-to-medium speed applications, the influence of frictional forces becomes more pronounced [11].

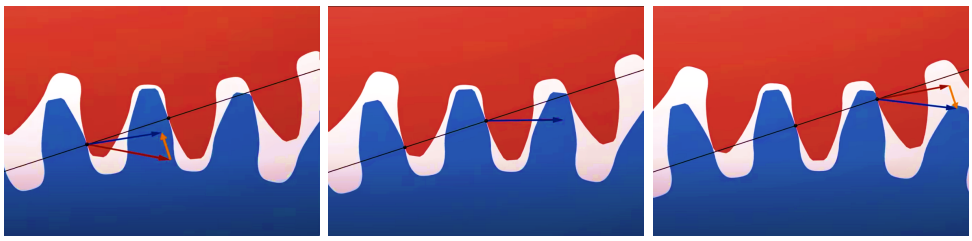

(a) Approach phase (b) Pitch point contact phase (c) Recess phase

Figure 1.4: Visualisation of the friction force vector (in orange) during the meshing process.

1.2.2 Shuttling excitation

During the meshing process, gears develop a contact force that could be decomposed to:

- The tangential force also known as the driving force or driving torque, is the force that transmits power between meshing gears and acts tangentially to the pitch circle.
- The radial force is referred to as the thrust force developing as a result of the gears' reaction to one another in the radial direction.
- The axial force acting along the gear's rotational axis is mostly present in the case of helical gears.

The interaction of radial and axial forces on gears can induce separation and twisting motions that affect the relative positioning of the gear centers. This periodic effect generates significant forces bearing forces as shown in figure 1.5 with more magnitude than those generated by the transmission error [11]. Consequently, this phenomenon leads to a substantial excitation of the housing, as observed in the study conducted by Nishino et al. [57]. Interestingly, in gearboxes with an optimized tooth geometry that minimizes transmission error, the contribution of shuttling forces to the whining noise surpasses that of transmission error [141].

The presence of mounting conditions, such as misalignment, eccentricities, runouts, and profile defects, exerts a significant influence on the magnitude of shuttling forces experienced in gear systems [141]. These mounting conditions have a direct impact on the harmonic content of the Static Transmission Error as previously mentioned.

When misalignment occurs between gear shafts, an angular offset is introduced, leading to uneven tooth engagement. Consequently, the gear teeth experience varying contact patterns, resulting in an elevation of the shuttling forces. The same holds true for eccentricities, where non-concentric gear bores or shafts cause deviations from the desired axis of rotation. These deviations disrupt the uniformity of tooth engagement along the gear mesh, generating significant axial forces that contribute to the magnitude of shuttling forces.

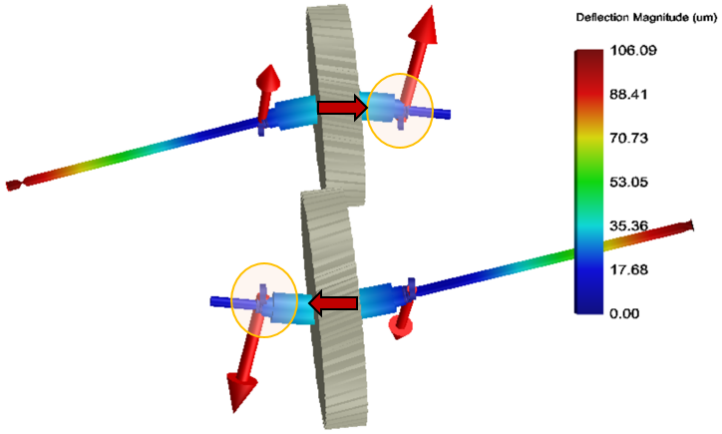

Figure 1.5: Load distribution on the bearings due to shuttling forces

Furthermore, runouts and profile defects add complexity to the gear system. Runouts, which manifest as deviations from perfect circularity, introduce periodic variations in tooth-to-tooth contact. These variations in contact give rise to fluctuations in the transmitted forces and subsequently impact the magnitude of shuttling forces experienced by the gears. Similarly, profile defects, including pitch errors, addendum errors, and dedendum errors, introduce irregularities in the tooth geometry, leading to non-uniform load distribution across the gear teeth. As a result, variations in the shuttling forces arise.

In practical scenarios, it is practically inevitable to have a combination of the aforementioned errors to some extent, which is contingent upon the component and mounting quality of the gears. Moreover, the presence of multiple components adds more intricacies and more dynamic phenomena which are beyond the scope of this research. Consequently, the actual noise frequency content of a gearbox is richer and more broadband in nature [147] as illustrated in Figure 1.6. Interpreting and identifying the distinct harmonics within this complex spectrum and establishing their relationship with the operating conditions necessitate a certain level of engineering expertise.

1.3 Dynamic Modeling of Gearboxes

In recent years, there has been significant progress in the dynamic modeling of gearboxes, driven by increasing interest in the environmental impact of transmission systems. As a result, various models with different levels of complexity have been developed.

One approach to simplify the modeling process is by assuming that reducing transmission error leads to a decrease in emitted noise. It has been observed that a reduction of $1\mu m$ in the Static transmission error corresponds to an approximate $5dB$ decrease in noise [43]. This uncoupling of excitation from dynamic effects allows

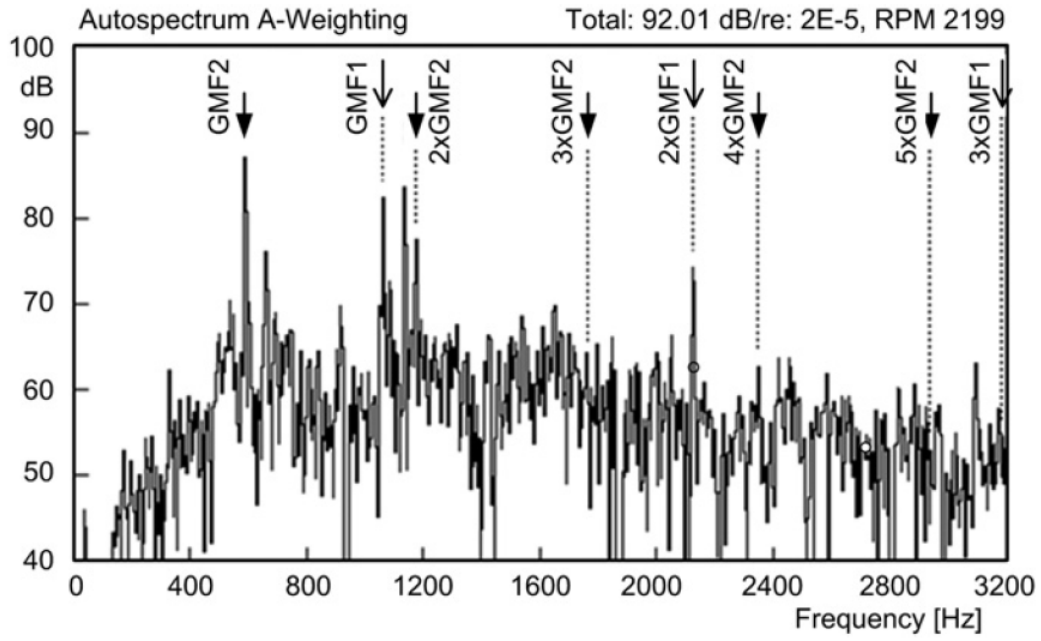

Figure 1.6: Noise frequency spectrum of a three-stage gearbox

for a simplified representation.

On the other hand, the sensitivity of dynamic models to minor changes in gearbox modeling techniques emphasizes the importance of careful consideration during model development. It is crucial to ensure that the model encompasses most of the relevant physical intricacies that contribute to the acoustic behavior of a transmission system.

Depending on the classification into LTI, LTV, NLTI, and NLTV categories, certain modeling methods are more suitable for representing specific aspects, particularly in relation to the non-linear nature of contact stiffness. Within these models, the following distinctions can be made:

- The Analytical Models: Analytical models utilize mathematical equations to describe the gear mesh behavior. While they offer insights into the system's behavior, analytical models often make simplifying assumptions to enable mathematical tractability. These assumptions may limit their accuracy and precision compared to more detailed modeling techniques.

- The Discrete Models: Discrete models, which represent gears as discrete bodies with lumped parameters, are generally less precise compared to other modeling techniques. They rely on simplified contact models and may overlook certain dynamic effects. While discrete models are computationally efficient, they provide a less detailed representation of the gear system behavior.

- The Combined Discrete and Finite Element Models: Hybrid models, which combine the advantages of both discrete and finite element methods, offer

a higher level of precision compared to discrete models. They can represent certain components using discrete models while utilizing finite element models for others. This allows for a more accurate representation of the system's behavior while balancing computational efficiency.

- The Finite Element Models: Finite element models provide a more detailed and precise representation of gear systems by discretizing gears into finite elements. They can capture complex gear geometries and consider various factors such as material properties, contact mechanics, and geometric non-linearities. Finite element models offer a higher level of accuracy and are particularly suitable for analyzing complex systems or studying localized phenomena at the cost of high computation time.

To ensure the establishment of a high-fidelity model, it is essential to consider the larger context of the problem and the interactions between the various components that affect the system at two different levels:

- The excitation: When calculating the static transmission error, distinctions may arise between examining the gears in isolation and taking into account their interactions with other components. This divergence stems from the fact that system deflection can exert an influence on the contact patches and pressure distributions along the gear flanks.

- The dynamic behavior: In isolated gear analysis, grounding boundary conditions are often assumed, neglecting the flexibility of connected parts such as the shafts and bearings. However, this assumption does not realistically reflect the system's behavior since these connected parts introduce extra degrees of flexibility that affect the modal characteristics of the system.

Taking into consideration these effects, the dynamic models can be classified according to the number of degrees of freedom they present [77] going from models of tooth compliance that consider that tooth stiffness is the only element that is able to store energy in the system to models that consider the coupling with other parts of the gearbox (Figure 1.7).

$$STE(\theta_1) = R_{b_2}\theta_2(\theta_1) - R_{b_1}\theta_1 \tag{1.13}$$

The primitive model presented by Tuplin [148] represented gears as two rigid bodies connected by a torsional spring with a constant stiffness, and gear errors represented by a wedge moving in and out between one of the masses and the stiffness spring. The low number of DOFs renders this model limited in its ability to predict any kind of bending/torsion modes within the gears themselves, and it is for these assumptions that it is more suited for stress and stiffness rather than NVH assessment. Nakada and Utagawa [30] approximated the time-varying meshing stiffness to a rectangular wave function allowing to the introduction of the torsional vibrations of the gears in the simulated model. Harris [50] also made a notable contribution to the

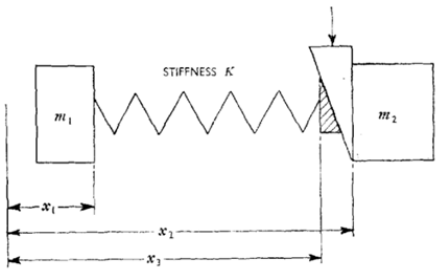

(a) Spring-mass model of Tuplin [148]

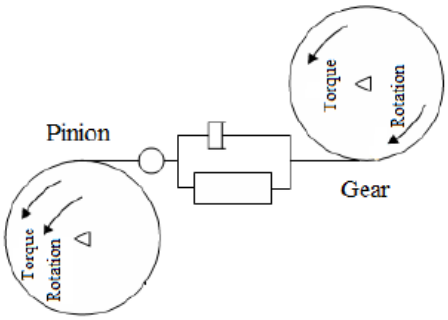

(b) SDOF non-linear model of spur gear pair [67]

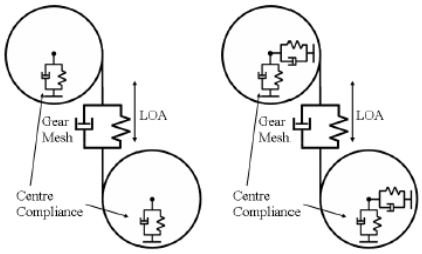

(c) Mathematical gear models with center movement [68]: (a) 4-DOF model, (b) 6-DOF model

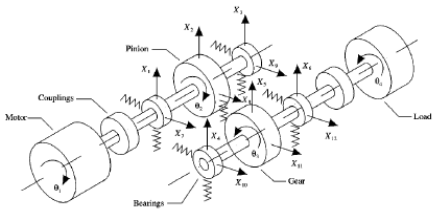

(d) 16 DOF gearbox model proposed by Howard et al. [58]

Figure 1.7: Graphical representation of the line of action (a) and place of action (b).

study of gears. He used a single-degree-of-freedom photo-elastic model to identify manufacturing errors and non-linear varying tooth stiffness as the primary sources of internal vibrations and emphasized the critical role of transmission error. His study demonstrated that at low speeds, the behavior of spur gears can be represented by a series of static transmission error curves. Gregory, et al. [37, 38] significantly contributed to gear models as we know them today. Their model treated gears as two discs with corresponding base radii, which were connected tangentially by a time-variant stiffness spring. This spring was estimated by sinusoidal approximations and accounted for the effects of the contact ratio while disregarding damping effects in the meshing region. Tordion and Geraldin [145] made a multi-degree-of-freedom model for a general rotating system with a gear mesh and reduced it to an equivalent single-degree-of-freedom torsional model having constant stiffness accompanied by a displacement excitation which was used to determine the transmission error from experimental measurements of angular vibrations. The study pinpointed the importance of considering transmission error as the main factor to determine the quality of gears. Remmers [125] integrated the transmission error as a series of harmonics using the Fourier series in a damped vibratory model with viscous damping and constant meshing stiffness. He took into consideration the effects of profile modification, rigid body approach, contact ratio, and loads. Wang's work [160] made a valuable contribution to the understanding of the impact of torsional vibrations on gear models. He used a rigid body dynamic approach to evaluate the dynamic factors analytically and showed that transmission errors can have a significant effect beyond the gear mesh itself, affecting other components of a gearbox as well. His findings emphasize the importance of accurately modeling transmission errors in gear design and analysis. Kahraman and Singh made significant contributions in the field by introducing a SDOF model [67]. This model comprised two rigid disks, representing the gears' inertial properties, which were fixed at their centers and connected by a mesh stiffness spring positioned along the Line of Action. Building upon this, they further expanded the model's capabilities by developing 4-DOF and 6-DOF versions [68] which enabled the generation of mesh forces that deviated from the LOA as well as the introduction of the concept of shaft whirl, which encompassed the simultaneous motion of both the shaft and gears within the plane of the gears. Vijayakar and Houser's work [156] introduced a semi-analytical finite element contact mechanic model, which divided the contacting bodies into two distinct regions. The regions near the contact were analyzed using Hertz contact theory, while regions far from the contact were analyzed using conventional finite element models to determine the bulk stiffness. This innovative approach reduced the need for a very thin mesh, making it computationally efficient. Wu et al. [167] developed a gear contact finite element model with a fine tooth meshing that allows a proper assessment of the meshing stiffness.

With the highlighted importance of introducing the other components of the gearbox, gear dynamics models have emerged to allow better assessment of the global dynamic behavior. These dynamic models are most useful when the torsional flexibility of the shafts and the gear webs as well as the lateral flexibility of the bearings

are sought. One of the earliest attempts to use the mesh stiffness in order to couple the torsional vibration of gear shafts started with Johnson [62] who considered a constant mean stiffness value to linearize the receptance equation solved for the natural frequencies of the coupled system. Kohler et al. [76] developed a comprehensive experimental model, which included both lateral and torsional vibrations of the carrying shafts. Through their experiments, they demonstrated that transmission error is the primary cause of steady-state vibrations in the system. Their six-degree-of-freedom model provided valuable insights into the dynamics of gear systems and helped to advance the understanding of the sources of vibration in such systems. Later, Wang and Morse [161] included a similar multi-degree of freedom spring-mass torsional model that encompassed the shaft and gear web stiffnesses along with a constant mesh stiffness. The model allowed determining the eigenmodes and eigenvalues of the system through the use of a transfer matrix method that yields the dynamic response of a gear train system. The work was then expanded by including other effects such as the tooth backlash, and linear and non-linear damping. Lida and his colleagues [60] expanded on this previous research by including the effects of imbalance and geometrical eccentricities in a six-degree-of-freedom model that coupled flexural and torsional vibrations of a geared system. Similarly, Neriya and his colleagues [107] used a different finite element method approach, modeling shafts using beam elements, and coupling them at the contact to account for tooth flexibility. They solved the equations of motion to calculate the dynamic response of the system under excitations induced by geometrical eccentricities and mounting imbalances of the gears. Both approaches provided valuable insights into the complex dynamics of geared systems and have helped to improve the accuracy of gear models. Lachet and Troeder [84] introduced the effect of backlash in the analysis of the gear trains' performance through CAD-integrated computer simulations. In their study, Howard et al. [58] presented a significant advancement in the form of a 16-DOF model that encompassed the rotational movements of the motor, load, and two gears, as well as the vertical and horizontal motions of the bearings and gears. To simplify the equations of motion, the authors assumed a gear alignment scenario, where the vertical motions were solely influenced by the normal tooth loads, while the horizontal motions were attributed to frictional forces. Mayeux, et al. [101] developed a static equilibrium-based method for the calculation of the static transmission error which included the deflections of the bearings in a coupling manner. They used it to predict the dispersion of the critical rotational speeds of the gearbox as a consequence of introducing the stiffness of the bearings in the system. Rigaud, et al. [130] introduced some coupling terms between the meshing gears which take into account their tilting motion together with the flexural deformations of the shaft and highlighted the remarkable effect on the mechanical properties of the housing at the critical speeds of the system. More on these effects can be found in a study presented by Velex and Maatar [155] which discusses in more detail the coupling between the different translational and rotational motions on a meshing level resulting from the macro and micro-geometrical deviations of the teeth. Kahraman, et al. also made a huge contribution by proposing a torsional and transverse vibration

finite element model that accounts for the bearings' flexibility in a geared system. The mesh was excited by the values of the transmission error to obtain the fluctuating mesh stiffness. Kahraman [64] developed a linear dynamic model for helical gear pairs. In this model, gears were modeled as rigid disks with symmetry conditions about their transverse plane. The model considered the flexibility of each of the shafts, as well as the flexibility of the bearings, which was assumed to be constant. Additionally, the model accounted for the dynamic coupling between different transverse, torsional, axial, and rocking motions resulting from the gear mesh. A similar approach was taken by Khang [152] where the rigid rotors were considered to be linked by a spring-damper lumped model that models the meshing stiffness along the line of action while taking into account the influences of the displacement-type transmission error excitations. The model was implemented for gear-fault detection. The third mathematical model encompasses most of the basic elements that are involved in a conventional gearbox. This makes it even more representative of the system's dynamics that the second type. In fact, studies have shown that elements such as the gearbox housing play a crucial role in the dynamic exchange between the different components. This becomes even more significant when its stiffness is reduced mostly as a result of weight reduction. Lim and Singh [90] conducted a comprehensive investigation into gearbox vibrations, taking into account the flexibility of the housing. Their approach combined a lumped parameter model with a dynamic finite element method. The study compared three different cases: a single-stage rotor with a rigid casing and flexible mounts, a spur gear drive system with a rigid casing and flexible mounts, and a high-precision spur gear drive system with a flexible casing and rigid mounts. The models utilized bearing stiffness to couple the dynamics of the shafts to the housing, ensuring a smooth transfer of motion. The gear mesh stiffness coupled the gears together. Both meshing and bearing stiffnesses were incorporated as generalized six degrees of freedom matrices, which described the forces that components could develop as a result of applied displacement to the bearing rings. Choy, et al. [22] introduced the housing's flexibility within a multi-stage transmission system as an attempt to study the influence of the vibratory motion of the housing combined with mass imbalance. The vibration analysis showcased that the influence of the additional flexibility associated with the housing becomes more significant when the compliance of the remaining components is reduced. The results showed an enriched dynamic response, highlighting the importance of considering such couplings in the modeling of gearboxes. A different analytical model built by El-Saeidy [31] in which a varying mesh stiffness was implemented for the case of a rigid housing, revealed that the tooth backlash and the bearing dead band clearances present an important influence on the vibration spectrum of the gearbox. Choy, et al. [20] later presented another combined modal synthesis finite element approach to analyze the dynamics of multi-stage gear systems with a flexible casing. The transfer matrix approach was used to evaluate the modal parameters while the finite element method was utilized to assess the dynamic modal characteristics of the geared system using the same component coupling methodology as presented by Lim and Singh [90]. The analytical model was

later compared with experiments where a good agreement was found [21]. Kato, et al. [32] evaluated the acoustic radiations radiated from a gearbox through the use of a combined finite element and boundary element method which was greatly correlated to the experimental measurements. The model included beam-element shafts, lumped models that take into account the rotating inertia of the gears which are where then integrated within the shafts, spring and damper systems for the shafts and a shell-element casing for the acoustic response simulations. The main highlight of this study was that the acoustic power is more pronounced when the system is operating at the meshing frequency compared to the other experimented frequencies. Sabot and Perret-Liaudet [131] pointed to the direct correlation of transmission error with the noise that is being generated from the gearbox and developed a numerical model where based on Rayleigh Integral Formulation to get the dynamic response of the housing through the use of finite element calculations which proved to be well-representative of the simplified experimental model that they built. In recent years, there has been a growing focus on tackling increasingly complex multi-physics problems that involve multiple types of couplings between different excitations. Ren et al. [127] incorporated housing flexibility through an impedance-based model obtained from harmonic analysis with the impedance model transformed from the lumped parameter model of the gears and shafts. Garambois et al. [34], the effect of physical coupling between the gear mesh excitation and the drag-induced fluctuating torques was investigated in the context of a vacuum pump. The results showed an enriched dynamic response, highlighting the importance of considering such couplings in the modeling of gearboxes. [96] considered a mining gearbox as a coupling between a housing and multi-stage transmission sub-systems and concluded that the cutting loads are the main reason for the system's dynamic response. Qin et al. [174, 7] conducted a study on the dynamic behavior of planetary gear systems, with a focus on electromechanical coupling. Their research aimed to provide a better understanding of how the motor affects the mechanical behavior of planetary gears. In the same context of planetary gears, Liu et al. [95, 94] investigated the dynamic characteristics of planetary gear systems during variable speed and high-speed processes emphasizing the effect of planetary centrifugal forces. Zhu et al. [185] suggested a dynamic model of a wind turbine with flexible pins and studied their effect on the dynamic response. In response to the challenge of effectively monitoring the structural health of gearboxes, various gearbox models have been developed with a specific focus on this problem. Fernandez et al. [33] proposed a model that takes into account both internal excitations caused by variable mesh stiffness and those resulting from variable bearing compliance. By incorporating these factors into the model, it is able to accurately assess the impact of mesh friction, bearing clearance, and applied torque levels on the overall performance of the gearbox. Luo et al. [97] suggested a dynamic model for gearboxes has been introduced, which takes into account the multifaceted effects of gear pitting and spalling on tooth surface characteristics. This model simultaneously considers time-varying stiffness, surface roughness, and geometric deviation, all of which are affected by the presence of defects. The model analyzes changes in the system response under

different periods of defect evolution, providing valuable insights into the behavior of gearboxes with surface defects. The model developed by Yu et al. [180] provides a good understanding of the vibration behavior of gearboxes with multiple localized defects taking into account a combination of time-varying, mesh, bearing, and lubrication-related effects.

1.4 Modern advancements in gears passive weight reduction approaches

For generations, the automotive industry has relied on transmission systems to transfer motion between different vehicle components, with little regard for their environmental impact. However, as energy, noise, and vibration standards become increasingly stringent, engineers are pressured to develop lighter, more eco-friendly transmission components that minimize fuel consumption and noise emissions. Considering that the structural weight of a vehicle contributes to around 75% of the total fuel consumption makes motivates the use of lightweight components [181]. If a vehicle's weight is reduced by 10%, it is possible to save up to $6-8\%$ of fuel consumption [177]. This poses a challenge, as achieving weight reduction while maintaining acceptable noise levels is a delicate balancing act. Often, attempts to reduce structural weight can result in amplified vibration levels, making it difficult to design parts that meet both weight and noise requirements. Nevertheless, these side effects can be mitigated through the adoption of appropriate designs that promote the development of greener aircraft and automobiles, resulting in a higher efficiency [109] and reduced energy consumption [29]. Notably, the gearbox in aircraft accounts for approximately 15% of the total mass, presenting a significant opportunity for weight reduction by as much as 50% or even more [1]. This is generally achieved by either changing the geometrical design of the components or by opting for a different material that is less dense and able to sustain the operating conditions.

1.4.1 Achieving weight reduction by changing the geometry

While microgeometry modifications have proven to significantly impact the generation of noise in a gearbox, the fractional removal of material alone falls short of achieving a noticeable reduction in gear weight. As a result, an alternative approach is often employed, wherein the material is removed from the gear web to make the web width smaller than the facewidth. A noteworthy experimental study conducted by Li et al. [86] has demonstrated the effects of this technique on the natural frequencies and bending mode shapes of gears. Furthermore, weight reduction can be achieved by introducing holes or discontinuities in the gear blanks [146, 134] (Figure 1.8). These additional measures also contribute to lowering the eigenfrequencies at the system level. However, what sets them apart from simply reducing the web width is that the introduction of holes affects the behavior of the gears throughout the rotation, as they become susceptible to a modulating mesh stiffness that cre-

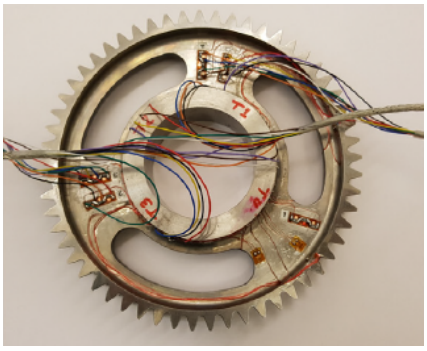

Figure 1.8: Geometrical lightweight gear: 3-slotted configurated

ates more sidebands in the frequency content. Consequently, these sidebands are more likely to effectively excite the housing modes, resulting in a modulated signal that, from a psycho-acoustic perspective, presents more nuisance compared to tonal noises. This highlights the importance of careful consideration in the design of such discontinuities. The implementation of thin-rimmed gears presents various modeling challenges, as highlighted in a study conducted by Guilbert et al. [40, 41]. In their research, they proposed a hybrid gear model that addresses these challenges by utilizing a specific interface to couple the lumped parameter model of the shaft elements with a finite element model of the thin gear. Interestingly, their findings indicated that the influence of thin-rimmed gears is more pronounced in helical gears compared to spur gears. Examining the impact of thin-rimmed gears on the evolution of static transmission error, root stresses, and dynamic factors, Yilmaz et al. [176] conducted a study focusing on symmetric and asymmetric bi-metallic gears. Their investigation shed light on the potential benefits of employing lightweight gears without compromising dynamic behavior. This important insight was later corroborated by the comprehensive research conducted by Hou et al. [55]. Hou et al. delved deeper into the consequences of rim thickness on various aspects, including transmission error, bearing forces, mesh forces, and the dynamic response of the housing. Their study revealed that the utilization of thin-rimmed gears can lead to a significant reduction of 68.5% in dynamic mesh force Dynamic Mesh Force (DMF), resulting in a remarkable 66.7% decrease in the housing response when compared to standard solid gears. The advent of advanced manufacturing techniques, such as metal additive manufacturing, has ignited the interest of researchers in exploring intricate geometries that were previously unattainable using traditional methods. In light of this, Mura et al. [106] embarked on a quest for enhanced design by employing parametric optimization to transform a wheel's structure, replacing the conventional web with an arrangement of spokes (Figure 1.9). The research encompassed multiple stages of optimization, wherein key parameters included the number of spoke pairs, number of segments, thickness, depth, and hollowness. The primary objective of the study revolved around augmenting the first natural frequency of the gears while ensuring the maintenance of acceptable levels of static and fatigue performance. In another

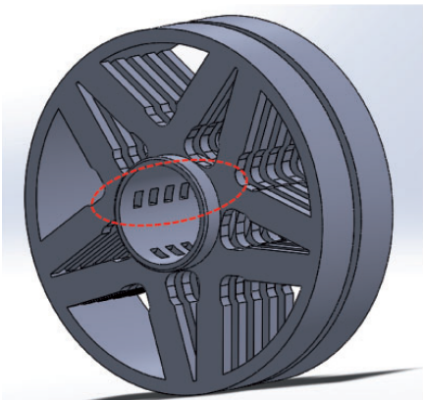

Figure 1.9: Geometrical lightweight gear: Spokes configuration

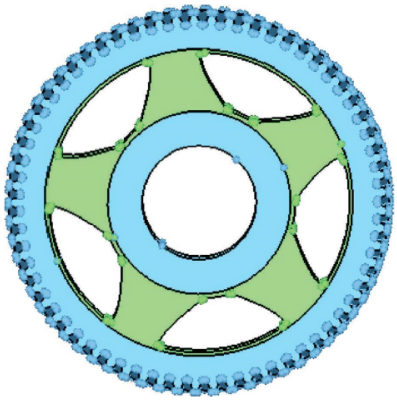

Figure 1.10: Geometrical lightweight gear: Controlled topology optimization

study, Shah et al. [133] focused on optimizing lightweight design through static topology optimization. Their objective was to maintain a safety factor greater than 1.2 while generating a symmetric pattern that ensures optimal strain distribution for the statically applied tooth loads. Similarly, Zhao et al. [184] employed a static and dynamic multi-objective controlled topology optimization approach. Their aim was to reduce gear compliance and increase low-order natural frequencies, resulting in a remarkable weight reduction of approximately 25% (Figure 1.10. Ramadani et al. [122] acknowledged a limitation in topological optimization-based methods, which typically generate a pattern that ensures an optimal solution for a specific load case. However, in the context of gears, this approach can become vulnerable to different loading scenarios due to the complex physics involved in their interactions. To address this issue, the authors proposed a modification by introducing a specific blank pattern (Figure 1.11) that is controlled by the parameters of its unit cell. Although this solution yields a sub-optimal result, it offers increased stability when subjected to changes in loading conditions. The introduction of this modified blank pattern had two significant benefits. First, it led to a noticeable reduction in

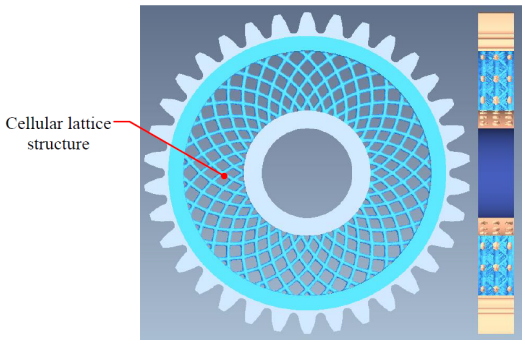

Figure 1.11: Lightweight gear: lattice configuration

sound, especially when the cavities within the gear were filled with sound-absorbing polymer materials. Second, it contributed to a weight reduction of approximately 30

1.4.2 Achieving weight reduction by changing the material

In order to address the potential side effects of geometry modification on the static and dynamic properties of the transmission system, several research studies have investigated the use of alternative materials. These studies, including those by Pogavcnik et al., Mbarek et al., and Zorko et al. [119, 102, 186], have focused on the viability of materials such as glass or carbon reinforced polymers. These materials offer advantages for low-torque applications due to their lower strength and stiffness. To overcome the low load-carrying capacities of polymer materials, other studies have explored the implementation of hybrid metal-composite structures. By incorporating Carbon Fiber Reinforced Polymers Carbon Fiber Reinforced Polymers (CFRP) as shown in figure 1.12, a portion of the metallic components can be replaced, resulting in a lighter structure with comparable mechanical properties. Additionally, CFRP exhibits improved damping and NVH characteristics. The effectiveness of this technique has been demonstrated in various applications, such as a plate-cutting machine (Kim et al. [72]), as well as automotive-related applications like hybrid and braided drive shafts (Cho et al., Lin et al. [18, 92]), a hybrid metal-composite wheel with a friction layer (Bae et al. [6]), and geared systems (Handschuh et al., Laberge et al., Karpat et al., Rezayat et al. [49, 80, 81, 71, 128]). In a similar study conducted by Handschuh et al. [48], the authors focused on investigating various combinations of hybrid and standard solid gears. Their findings indicate that a hybrid-hybrid gear pair exhibits the lowest levels of vibration, particularly at high speeds. Conversely, a hybrid-solid configuration was identified as the most noise-prone option. Incorporating hybrid gears into a system often introduces manufacturing complexities, resulting in higher costs that may not be justifiable for certain applications. However, an alternative approach using bi-metallic gears, where the composite part is replaced with a lighter metal such as aluminum, could offer a more cost-effective solution. Research conducted by Yilmaz et al. [176] re-

Figure 1.12: Material lightweight gear: CFRP configuration

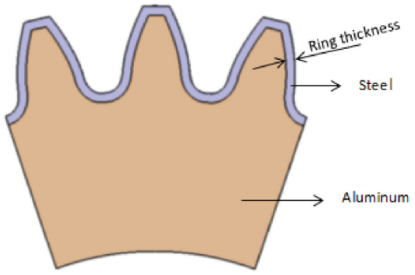

Figure 1.13: Material lightweight gear: Bi-metallic configuration

veals that employing this technique enables a significant 40% reduction in weight for the gear (Figure 1.13. Although this reduction increases stresses and single-tooth compliance, it also raises the resonance frequency due to the additional flexibility in the structure. Remarkably, these changes have minimal impact on the dynamic factor of the gear. The application of novel materials can also be used in conjunction with a unique geometry to benefit from the advantages of both techniques. Xiao et al. [170, 171] experimented with different metallic damping powders used to fill the holes in gears highlighting the important energy-dissipating role they play in attenuating the transmitted vibration and the potential applications in transmission systems (Figure 1.14).

Figure 1.14: Geometrical and Material lightweight gear: Damping powder-filled configuration

Chapter 2

Benchmarking Study of Different Gear Contact Analysis Software in Terms of the Excitation Response

Contents

2.1 Introduction

The investigation into the role of static transmission error in generating gearbox whine noise has spurred numerous studies aiming to develop accurate numerical methods for its calculation. These studies have resulted in the development of various academic and industrial gear contact analysis tools, each capable of addressing different aspects of gear contact phenomena. While having more tools provides more options, it also makes the selection process more challenging and raises questions regarding the suitability of certain software packages for specific aspects of analysis considering that most of them appear as blackboxes for the user with a little bit of information available on their working principles and formulations.

In the context of this research, the primary objective is to precisely capture the transmission error, initially focusing on standard gears, and to evaluate the implications of implementing lightweight solutions. This evaluation involves assessing the impact on the static transmission error, particularly the PPTE value and the overall trend, as well as on the system dynamics. Exhaustive research has been conducted, encompassing various scenarios such as different gear types (spur or helical), gearbox complexity (isolated or connected gears), microgeometry modifications (involute or optimized flanks), mounting defects, and geometrical cutouts for lightweight gears.

Multiple software packages, including ROMAX, MASTA, VIBRAGEAR, ANSYS, and MARC, were employed, employing different tooth and contact modeling techniques within each software package.

Furthermore, this study provides valuable insights into the physics of gear contact phenomena and the suitability of different models for addressing specific scenarios based on the gearbox model's characteristics and level of sophistication.

2.2 Overview of the different contact analysis software

Calculating the static transmission error is no easy feat, as it involves grappling with the intricate non-linearities and complexities of the meshing process, in addition to interactions within the entire gearbox. To ensure accuracy, it's crucial to use a qualified Tooth Contact Analysis tool that can account for most of these aspects. That's why contact models have been developed over the last decade, to incorporate Hertzian deflections, global deformation of the teeth, interactions with the environment, microgeometry modifications and defects, extended corner contact, and contact outside the plane of action. By considering different assumptions and modeling techniques, significant discrepancies in the derived tooth contact stiffnesses are expected which would influence the determination of the transmission error.

To address the challenges in contact stiffness modeling, various models have been developed, ranging from tooth-compliance-based models to models that consider all interactions within a gearbox [77]. Although it is crucial to consider auxiliary components in dynamic analysis, accurate numerical prediction of the static transmission error cannot be achieved if proper attention is not paid to modeling the contact be-

tween gears. However, modeling the Hertzian-level deflections of the contact region requires excessive refinement, which makes using a full finite element model computationally expensive. Therefore, most gear contact software packages nowadays use hybrid finite element contact mechanics solvers to address this issue. These solvers divide the tooth into regions that are considered to be sufficiently close to the contact where Hertzian formulations could be adopted and regions that are considered to be far enough from the contact where moderate mesh refinement could be used. This approach significantly accelerates simulations with minimum loss of precision [156, 162, 83, 134, 135].

Gear modeling poses a critical challenge in discretizing the theoretical lines of contact as the meshing progresses. One significant issue is determining how to divide these lines into smaller components to accurately estimate the stiffness of the teeth. The ISO 6336-1 model [93] has been developed to tackle this problem by dividing the lines into thin strips with constant stiffness, providing a reasonable approximation. However, this model is still outclassed by finite element non-linear models, which use the same concept but with fewer simplifications in compliance. By leveraging finite element interpolations, it is possible to achieve a smoother variable distribution of stiffness along the lines of contact. This approach results in a more precise estimation of the meshing stiffness, ultimately leading to a higher fidelity model.

Given these modeling challenges, it is critical to understand the strengths and limitations of different gear contact analysis tools. Therefore, the aim of this section is to provide a comprehensive overview of the commonalities and differences between these tools, which will be based on the following aspects:

- Establishment of the elasto-static characteristics of the gear pair represented by a compliance matrix coupling the different lines of contact.
  - Pre-analysis: The pinion-wheel compliance matrices are built before the contact analysis for each meshing step based on the kinematics of the gears and the estimation of the theoretical lines of contact.
  - Direct: The compliances are updated throughout the analysis following the progression of the contact lines across the tooth flanks.
- The bending stiffness model: Could be calculated analytically, semi-analytically, or using a full finite element formulation.
- The contact stiffness model: Could be based on the theory of Hertzian deformations or included within the FE model through an extremely refined meshing.
- Environment: This indicates which parts besides the tooth of concern are being considered in the stiffness formulation.
- microgeometry: This indicates whether the microgeometry of the tooth is directly represented as part of the mesh or introduced as gaps in the contact formulations.

Table 2.1: Summary of the characteristics of the modeling techniques associated with each software.

	Bending stiffness model	**Contact stiffness model**	**Environemnt**	**Establishmnet of the gear compliance**	**microgeometry**	**Corner contact**
VIBRAGEAR	Galerkin-Ritz plate	Hertzian deflection	Single-tooth	Pre-analysis	Indirect	Not included
ROMAX: 2D	Uncoupled springs (Weber-Banashek)	Hertzian deflection	Single-tooth Gear body (Implicit)	Pre-analysis	Indirect	Not included
ROMAX 6D	Uncoupled springs	Hertzian deflection	Single-tooth Gear body (Implicit)	Pre-analysis	Direct	Included
MASTA	3D FE model	Hertzian deflection	Adjacent teeth Gear body	Pre-analysis	Indirect	Not included
MASTA extended	3D FE model	Hertzian deflection	Adjacent teeth Gear body	Pre-analysis	Indirect	Included
GENOM: Weber	Uncoupled springs (Weber-Banashek)	Hertzian deflection	Single tooth Gear body (Implicit)	Pre-analysis	Indirect	Not included
GENOM: FE	3D FE model	Hertzian deflection	Adjacent teeth Gear body	Pre-analysis	Indirect	Not included
MARC	3D FE model	Direct	Adjacent teeth Gear body	Direct	NA (All cases are perfect involutes)	Included
ANSYS	3D FE model	Direct	Adjacent teeth Gear body	Direct	Direct	Included

- The corner contact or the extended off-line-of-action at gear tips: This feature accounts for the tooth bending under high load and means that the theoretical line of contact can extend to include the tip of the gear flank. This has the effect of increasing the contact ratio which affects the determination of tooth compliance and transmission error.

- The number of rotations per meshing period: This represents the number of small rotations to determine the transmission error.

While the modeling properties of each software can be summarized in table 2.1, we chose to categorize them based on the bending stiffness model which is one of the most important indicators of the precision and computational costs of the calculation.

2.2.1 Ritz-Galerkin-based thick plate model: TERRA of VIBRAGEAR

VIBRAGEAR was originally an academic-level gear contact solver developed in our laboratory and is now being applied for industrial applications by VIBRATEC SA and Ecole Centrale de Lyon, in the framework of the joint laboratory LADAGE. Despite the tool currently having the ability to build a finite element model of tooth compliance, the simulations done in this paper were based on a semi-analytical model [34] that couples between the Reissner-Mindlin thick plate theory and the Ritz-Galerkin approximation for the teeth deflection form. The model considers that

the tooth is a rectangular plate with a variable thickness derived from the macro-geometry parameters of the gear tooth. A Ritz-Galerkin polynomial interpolation is utilized to build a compliance matrix for each meshing period based on the macro-geometry, material properties, and loading condition of the gear pair.

The evaluation of the contact equations in Equation 1.11 taking into account the established compliance matrix, results in the static transmission error $\delta(\theta_1)$ as well as the vector $p(\theta_1)$ that represents the load distribution along the contact lines. It is essential to highlight that the tooth-bending model exclusively focuses on the tooth itself, without taking into account the impact of the gear body and the neighboring teeth on its stiffness. Essentially, the model assumes that the tooth is fixed at the base, neglecting any extra flexibility introduced by the gear body. This simplification can lead to an overestimation of the tooth's stiffness, which will be verified in the subsequent analyses. In summary, the principle of using static equilibrium to calculate transmission error, as described in this section, is applicable to all the methods analyzed. The difference between the methods lies in the tooth stiffness model used, specifically in the method used to estimate the compliance matrix $H(\theta_1)$.

2.2.2 Weber-based uncoupled spring models: Pre-analysis tooth compliance establishment

2.2.2.1 ROMAX 2D

ROMAX is a commercial-level transmission system simulation software developed by ROMAX TECHNOLOGY LTD and currently acquired by HEXAGON AB. The software is able to conduct very fast microgeometry analysis thanks to its uncoupled springs model. The estimation of the bending stiffness relies on the combination of the following effects:

- The tooth bending due to tangential forces is estimated based on Mindlin plate theory [123, 124].
- The radial deformations are based on a modified tapered Timoshenko beam element.
- The rotation and shear of the tooth root are based on empirical formulations.

On the other hand, the Hertzian contacts are accounted for through the use of the Weber-Banashek-inspired local contact model [162, 163].
In the Weber-Banashek model, tooth stiffness is determined by analyzing the deformation and stress within individual meshing teeth. These teeth are treated as rigid bodies that are connected by uncoupled springs and dampers. The stiffness of these springs and dampers depends on a range of factors including the material properties and geometry of the individual teeth, as well as the meshing parameters.

The 2D model developed by Weber-Banashek accounts for both the normal deflection within the plane of action and the misalignment about an axis normal

to this plane. However, it only considers deflections that occur in the theoretical plane of action. In other words, this model assumes that the nature of the contact will not be affected by the overall deflections of the system. Therefore, it does not account for changes in the center distance due to the potential deflection of the shafts. As a result, this model is more suitable for cases where the system deflections are minimal.

However, it is important to note that this model is unsuitable for cases where tip relief is not applied. This is because the model is unable to detect the roll in/out of the gear tip caused by the gear's tooth tip bending under contact pressure. In such scenarios, an alternative model would be required.

In summary, the Weber-Banashek model offers high computational efficiency and accurate results for systems with minimal deflections. However, it has limitations that should be taken into consideration when applying it to certain scenarios.

2.2.2.2 ROMAX 6D

As the name suggests, the 6D model captures all six degrees of freedom of the gear, enabling it to account for changes in the center distance. This is particularly important in cases with high system deflection. Additionally, unlike the 2D model, the 6D model can capture effects such as corner contact or roll in/out of the gear tip, where the contact happens before the theoretical involute-to-involute contact, especially when there is no tip relief present.

To achieve this, the 6D model is coupled with the GearBox Transmission Error (GBTE) feature in ROMAX, which enables the capture of system deflection and varying misalignment at each small rotation quasi-step.

Despite the model's additional degrees of freedom, it still assumes that the gear tooth is a rigid body attached to the gear blank and only considers deflections of the gear blank. The tooth stiffness model accounts for the linear line of action motion of the tooth, but it does not consider the rotational motion caused by tooth bending, limiting the accuracy of the contact position variation with the load.

Overall, the 6D model is more suitable for studying the system's behavior and capturing changes resulting from microgeometry modifications for one of the gears. However, the model requires a higher computation time as it relies on the establishment of 3D contact surfaces for each meshing tooth instead of the conjugate micro-geometries derived at the theoretical contact lines.

2.2.2.3 GENOM: Weber

GENOM is an industrial gear contact analysis tool developed by ALSTOM TRANSPORT SA. The Weber version of the software is similar to ROMAX 2D, as it utilizes a modified ISO standard for the Weber-based uncoupled spring model coupled with Hertzian formulations to determine tooth stiffness. However, it is important to note that some variations of the same formulation may exist.

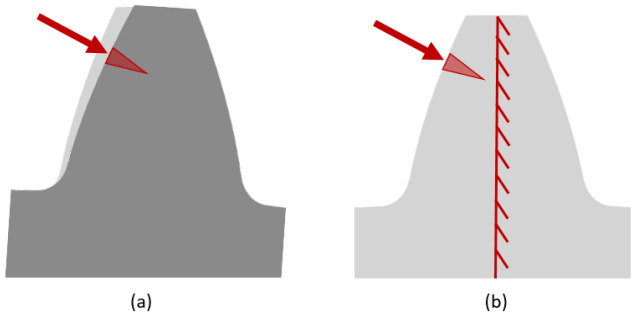

Figure 2.1: Computation steps for removing the artificial local spike from the bending stiffness. (a): Tooth bending and local spike effects, (b): Local spike effect.

2.2.3 3D FE-based models: Pre-analysis tooth compliance establishment

2.2.3.1 MASTA

MASTA is a powerful commercial gearbox analysis software developed by SMART MANUFACTURING TECHNOLOGY LTD (SMT). The tooth bending compliance is established by means of a 3D finite element model where the user is able to control different parameters including the mesh size, the number of teeth adjacent to the tooth in mesh, etc.

A kinematic analysis of the gear pair yields the theoretical lines of contact which are then discretized into a number of contact points. These points might not coincide with nodes of the flank's mesh grid. This can be handled by interpolating each contact point from the surrounding points of the mesh. The result is a compliance matrix that dictates the displacement of each contact point when a unit force is applied to it, to other points from the same contact line, or to other points from other contact lines that could belong to the same or adjacent teeth. This highlights the extent of the coupled effects involved in the estimation of the compliance matrix.

Since the bending stiffness relies on the application of a local load one at a time to one of the contact points, this has as an effect the creation of an artificial local spike that has no physical relevance. This can be removed by subtracting a grounded compliance (b) calculated by fixing the tooth at the center line from the free previously obtained bending compliance (a). The procedure is summarized in Figure 2.1.

The contact stiffness in MASTA is also constructed on the basis of Weber's approach. However, it is worth noting that several variations of this approach can be found in the literature such as the ones developed by Vedmar. [153], Steward [138], LDP [120]. With this in mind, one might speculate that some software could be reliant on exclusive locally developed variations that could include correction factors potentially serving to converge the results to tested data. This could also apply to any sort of empirical formulations hidden underneath the hood of the

graphical user interface. In other words, despite this being a comprehensive guide for the theoretical approaches of each tool, a level of variation of the same approach could be expected.
The contact analysis in MASTA is based on the same assumptions as ROMAX 2D including the constant misalignment, the constant center-to-center distance, and the small displacements remaining in the theoretical lines of contact. However, by toggling the extended tip contact feature, the estimation of the theoretical lines of contact will account for the premature contact resulting from the tooth bending which extends the conventional contact line up to the tip of the tooth flank [83].

2.2.3.2 GENOM: FE

The Finite Element version of GENOM (i.e. GENOM FE) is a software tool that can be used as an alternative to the standard MASTA model for constructing gear Finite Element models. It is fully integrated with CATIA, a popular computer-aided design software. GENOM FE allows the user to construct a gear FE model that takes into account the effect of adjacent teeth and a certain depth under the teeth root.
To determine the stiffness matrix for the gear model constructed using GENOM FE, the displacement fields are computed after grounding the bore region at the specified diameter. It is important to note that the stiffness matrix computed using GENOM FE may differ from the stiffness matrix computed using the standard MASTA model due to various factors. These factors may include differences in the extent of the geometry and boundary conditions, the material definition, the meshing parameters and element types, and the very nature of the numerical solver used to construct the stiffness matrix.

2.2.4 3D FE-based models: Direct tooth compliance establishment

The following software packages are general Finite element analysis software not exclusively designed to tackle contact analysis between gears.

2.2.5 ANSYS Mechanical developed by ANSYS, Inc.

ANSYS represents a high-end flexible multi-body dynamics (FMBD) approach. The simulation is drastically more computationally taxing compared to the others but is also considered the most accurate. Unlike the previous approaches, bending compliance is determined in real-time as part of the meshing process instead of basing it on the theoretical kinematics of gear contact. The process is also able to track the evolution of the tooth surface normal to the tooth flank in between the meshing steps which makes it more representative of the actual contact physics and goes against the assumptions that the deflections remain in the plane of action or that the contact remains exclusively inside the pre-determined theoretical contact line. Moreover, the multibody aspect allows the representation of other auxiliary parts

such as the shafts, bearings, and housing while capturing the effect of varying misalignment coming from the extra flexibility that they might confer.
The microgeometry is directly represented as part of the tooth flank geometry by using a micron-level mesh refinement sufficient enough to capture the possible Hertzian deflections. The contact is modeled using surface-to-surface contact detection which proved to be better at capturing the tooth profile change despite the computational burden. A frictionless contact algorithm based on a combination of the penalty method and Lagrange multiplier formulations was associated with the contacting elements which grant a good compromise between the accurate modeling of contact stiffness and the reduction of computation time [9].

2.2.6 MARC developed by MSC SOFTWARE CORPORATION and acquired by HEXAGON AB

Similarly to ANSYS, the finite element MARC model represents another direct way to compute tooth compliance but offers the following important limitations:

- The model is only conceived for an isolated gear pair where gears are only allowed an axial rotation around their centers which implies a fixed center-to-center distance regardless of the load intensity.
- The model presents a relatively coarser mesh refinement in comparison to ANSYS due to memory constraints imposed by the computational logistics. This suggests that the Hertzian deflections might be less precisely captured.
- The model is made to only treat perfect involute gears considering that the microgeometry defects are neither represented as part of the tooth flank profile nor introduced in the form of geometrical gaps in the contact equations.

Not having to include profile modifications streamlines the transition from the surface-to-surface contact method as used in ANSYS to a node-to-segment contact in MARC that is known to work better for simpler geometries and at a much lower computation cost.

2.3 Comparative study of the static transmission error for a case of spur gears

2.3.1 Case of a perfect involute profile

Despite the absence of perfectly-involute gear pairs in practical applications we decided to treat this case as an academic starting point before adding more modeling complexities to be able to track the potentially resulting discrepancies. The spur gear pair has its characteristics summarized in table 2.2.

It is noteworthy that in some of the software, it is imperative to represent the gears as part of a gearbox assembly instead of an isolated representation. To imitate the pivot boundary condition in the gear centers, the gears were mounted on a

Table 2.2: Characteristics of the isolated perfectly involute spur gear pair.

Name	Designation	Gear 1	Gear 2	Unit
Module	m	2		mm
Number of teeth	Z	50	50	-
Pressure angle	α	20		deg
Helix angle	β	0		deg
Base diameter	d_b	46.966	46.966	mm
Profile shift coefficient	x	0	0	-
Addendum coefficient	h_α	1	1	-
Dedundum coefficient	h_f	1.25	1.25	-
Facewidth	b	20	20	mm
Center to center distance	a_f	100		mm

couple of shafts and concept bearings were mounted at the immediate vicinities from both sides of the gears to better support the shafts and prevent any sort of bending that might be responsible for affecting the results. Moreover, the bearings and shafts were assigned a very exaggerated stiffness scaling factor approximating them to rigid bodies. The analyses have shown that these measures successfully mimicked the pivot boundary condition. In other software, we had to impose a zero misalignment condition to neglect the gearbox deflection.
The model was then used to compute the transmission error as represented in A.1 which provides a broad understanding of the transmission error trends.

Upon initial observation, a significant discrepancy in PPTE values is noticeable between the different models, the highest being between ROMAX and VIBRAGEAR with almost $2\mu m$ difference which is considered high relative to the average amplitude of the peaks ($5\mu m$). Considering that a higher transmission error implies higher contact compliance, the ascending contact stiffness order can be structured as follows: GENOM FE, ROMAX 2D, GENOM Weber, ROMAX 6D, MASTA, MASTA extended, and VIBRAGEAR. Since the latter employs a clamped-tooth boundary condition that ignores the gear blank's compliance and theoretically results in higher bulk stiffness, it's unsurprising that its associated transmission error magnitude remains lower than the other models. Conversely, MASTA's FE model considers the blank and rim effects, leading to better precision. In contrast, the Weber-Banasheck model used in ROMAX doesn't explicitly account for the stiffness of the gear body and adjacent teeth in the formulation, but it provides a better approximation of the boundary conditions, explaining the significant difference with respect to a clamped-tooth model.
The GENOM Weber model presents a lower TE amplitude compared to its equivalent ROMAX 2D model, this might suggest a level of variation of the same formulation and potentially the application of correction factors to bring the numerical results closer to numerical data as suggested in similar research [99]. The same thing could be said about the FE models, namely, GENOM FE and MASTA which have even higher variation. While it was difficult to explain for sure why is this happening, several hypotheses can be suggested including a small variation in the material properties where the young modulus in the GENOM library is 5% less than the one

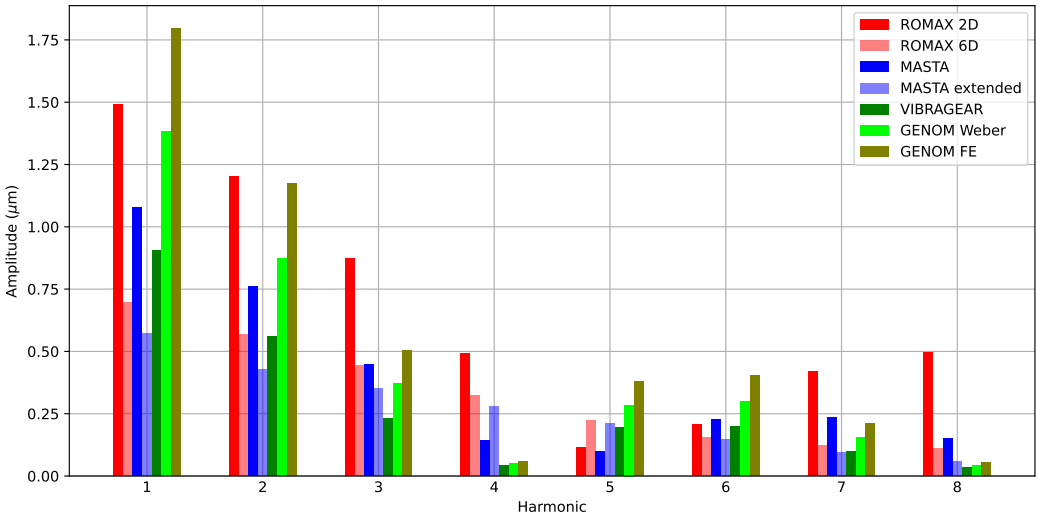

Figure 2.2: Comparison of the harmonic amplitudes of the first 8 harmonics of STE for the case of 115Nm loaded spur gears.

in MASTA. While this on its own is insufficient to explain the remarkable difference, it could be that the removal of the artificial displacement spike in GENOM is not as well handled as in MASTA. This could cause the displacement field to increase significantly and explains the higher overall compliance. Furthermore, the formulation for the Hertzian formulations could also be a source of variation. On the other hand, the classical plots transform from rectangular to triangular trends reflecting a smoother contact occurrence when the extended tip contact is activated. This accounts for the gradual and premature contact resulting from the teeth bending, bringing the ROMAX 6D and MASTA extended results much closer.
While the transition to the extended model in MASTA appears to affect only the plot's shape, the ROMAX results exhibit a remarkable decrease in amplitude. This decrease can be attributed to the 2D model's inaccuracy in ROMAX when describing a contact where no tip relief is being applied, compared to the more classical model in MASTA.
Notably, the use of different excitation signals leads to slightly different harmonic contents, resulting in varying harmonic amplitudes, as demonstrated in Figure 2.2. The similarity in the shape and magnitude of the plots explains the higher correspondence between the harmonic content associated with MASTA extended and ROMAX 6D.

The amplitude of the dynamic responses is heavily influenced by the individual harmonic amplitudes that the system is being excited by. Therefore, even if the same dynamic model is used, discrepancies in the dynamic response can be expected.
To better understand the contact handling of each tool, it's useful to examine the contact patterns on the tooth flanks. It's important to note that in this paper, only the contact charts associated with the commercial software were obtained. 2.3

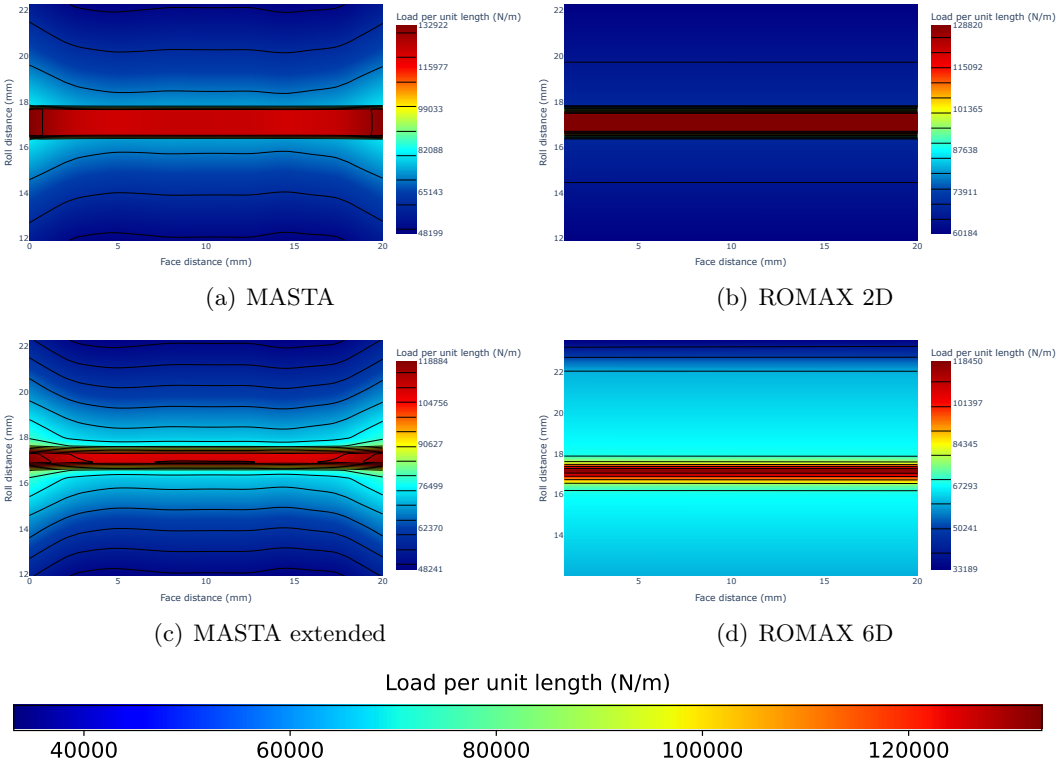

Figure 2.3: Comparison of the tooth flank contact patterns for the case of perfectly involute isolated gears using ROMAX and MASTA.

displays the contact contours indicating the force per unit length on the 2D plane of the flank for this case.

The graphs in both MASTA and ROMAX have a similar overall shape and distribution. However, the MASTA graph displays a higher maximum load and a lower minimum load than the ROMAX graph. These discrepancies can be significantly influenced by differences in the tooth stiffness models. If there is a difference in tooth compliance, it affects how the tooth is bent and locally deformed, leading to changes in the flank curvature and contact patch. This justifies why the highest pressure area in MASTA appears to be slightly wider than in the case of ROMAX. The analyses assume a nominal contact ratio of $\varepsilon_\alpha = 1.7547$ by not toggling the corner contact feature. For this specific design and throughout the meshing cycle, the gears should theoretically only have one or two teeth touching and carrying the transmission load at each time frame. This load causes the teeth to bend outward, forming a contact patch between the mating teeth. The activation of the corner contact feature accounts for additional contacts resulting from the deflection of the teeth (2.4). As a consequence, the actual contact ratio increases to involve more teeth tips in the meshing operation, sharing different percentages of the applied loads. This relieves pressure from the main contacting tooth pair, reducing the bending curvature and alleviating the stress intensity and distribution in the surface

(a) MASTA - without corner contact (b) MASTA extended - with corner contact

Figure 2.4: Visual representation of the contact handling. (a) Without corner contact; contact only occurs between teeth 2 and 3. (b) With corner contact; contact extends to teeth 1 and 4 due to bending.

of the main tooth flank. Ultimately, the resulting pattern of the extended methods will have lower overall load magnitudes and a slightly narrower area of maximum stresses.
The convex bending, which involves an outward movement of the contact patch away from the gear centerline, shifts the actual point of contact or the start of the active tooth profile (SAP) in the direction of the gear tip. The analysis of the SAP and end of active profile (EAP) shows that, in both software, the actual values of SAP and EAP are $96.953mm$ and $103.988mm$, respectively, compared to the nominal values of $96.947mm$ and $104mm$.

The load distribution on tooth flank edges in MASTA appears to be higher on both sides, in contrast to a more uniform and boundary-independent distribution observed in ROMAX. Numerical simulations using FE software also reveal increased contact pressure near the edges which suggests that the FE tooth stiffness model is more accurate for representing contact stresses.

To confirm the validity of these trends, we created a second perfectly involute spur gear pair with characteristics as outlined in Table 2.3 and benchmarked it against the finite element model in MARC, as depicted in A.2. The resulting graph supports our previous findings and demonstrates that the stiffness values calculated by the different tools maintain consistency in their order. The recently introduced MARC STE plot falls between the ROMAX and MASTA plots. Assuming that the MARC model is the most accurate, one can infer that MASTA overestimates the stiffness values while ROMAX underestimates them. Notably, the VIBRAGEAR model differs significantly from the other models, which is expected due to its underlying simplified stiffness calculation method.

Table 2.3: Characteristics of the second isolated perfectly involute spur gear pair.

Name	Designation	Gear 1	Gear 2	Unit
Module	m	1.47		mm
Number of teeth	Z	34	34	-
Pressure angle	α	20		deg
Helix angle	β	0		deg
Base diameter	d_b	46.966	46.966	mm
Profile shift coefficient	x	0	0	-
Addendum coefficient	h_α	1	1	-
Dedundum coefficient	h_f	1.25	1.25	-
Facewidth	b	1	1	mm
Center to center distance	a_f	50		mm

2.3.2 Case of an added tip relief

To improve the practicality of the gears, minor modifications were made to the same gears discussed in Table 2.2. A $5\mu m$ tip-relief modification was applied at a starting diameter of $100.52mm$. To directly compute transmission error, a flexible multibody dynamic ANSYS model was used. However, to ensure the model could operate effectively, the center-to-center distance was increased by $0.5mm$ to prevent gear jamming, which could have hindered computational convergence.
The gears were first tested under unloaded conditions with a $0.5Nm$ torque applied. The resulting plots are shown in A.3. While the different plots are close, they are not perfectly compliant which could be potentially attributed to minor kinematic errors. It's worth noting that the precision of the ANSYS model depends on mesh refinement and the number of small rotations per period, as established in [9].
Under such weak loading conditions, the extended MASTA model showed no difference compared to the standard model. This result was fairly predictable since no bending effect should have occurred. In contrast, the ROMAX 6D model shows a minor change with respect to the 2D model which might be justified by the additional DOFs taken into account.

In the second step, the gears were assessed at various torque values within the range of T = [0.5, 15, 30, 50, 80, 100, 150, 250]. The goal was to create a graphical representation of how the STE values change as the applied loads vary. The results were compared to the software's output, as shown in A.4 and A.5.

The plots provide valuable insights into the tooth stiffness models and assumptions used in the software. While the average STE values may not directly indicate the stiffness model accuracy, they suggest discrepancies among the various modeling methods, particularly for the gear blank and boundary conditions. The graph also highlights some anomalies that challenge the previous observations regarding stiffness order, which are specific to the MASTA simulations.
Surprisingly, MASTA produced the lowest PPTE value among the software compared, including VIBRAGEAR, despite being considered the software that overestimates tooth compliance the most. Additionally, the peak widths differed between the software. Upon further investigation, it was found that MASTA automatically

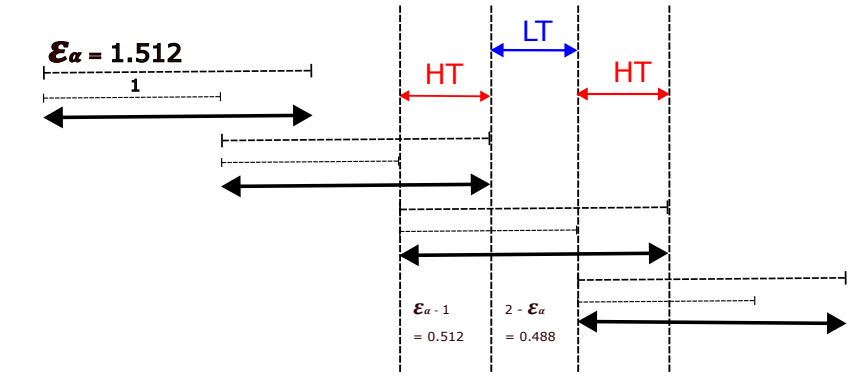

(a) ROMAX

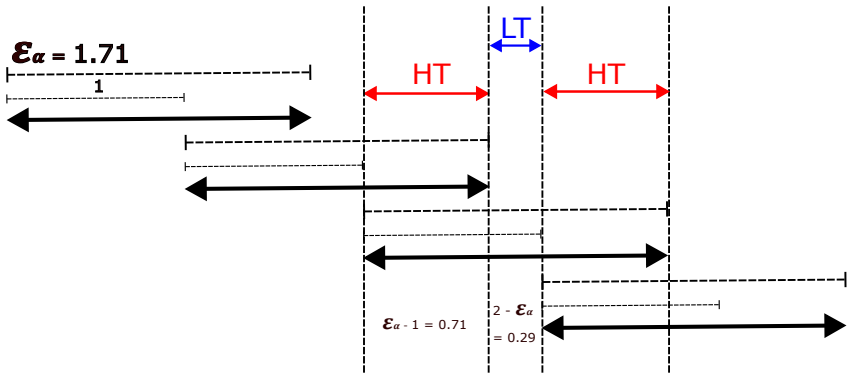

(b) MASTA

Figure 2.5: Schematic of the effect of the difference in the contact ratio on the width of the STE peak. LT and HT stand respectively for the regions of the lower and higher number of teeth in contact described by the superposition of the arrows representing the contribution of individual teeth to the meshing.

imposed a profile shift coefficient of $x = 0.1273$ as a result of a design constraint to accommodate for the increased center-to-center distance compared to the nominal model. This alteration of the tooth profile along the gear's axis affects the transverse contact ratio. As shown in Figure 2.5, the profile shift increases the contact ratio value from $\varepsilon_\alpha = 1.512$ in ROMAX to 1.71 in MASTA, leading to a decrease in the time when a lower number of teeth are in contact (LT) from 48.8% to 29% of the period duration. This decrease in LT contact time is consistent with the shape of the MASTA plots in A.4 (a) and (b).

We regard the event described herein as fortuitous, and we have included it not only to underscore the utmost precision required when defining tooth geometry but also to highlight the acute sensitivity of transmission error response to even minor deviations that may elude the user and result in misleading outputs. Such deviations can cause numerical divergences when comparing software-to-software or software-to-experiments, which is further complicated by manufacturing tolerances and errors. It is therefore very important for the numerical results to be backed up

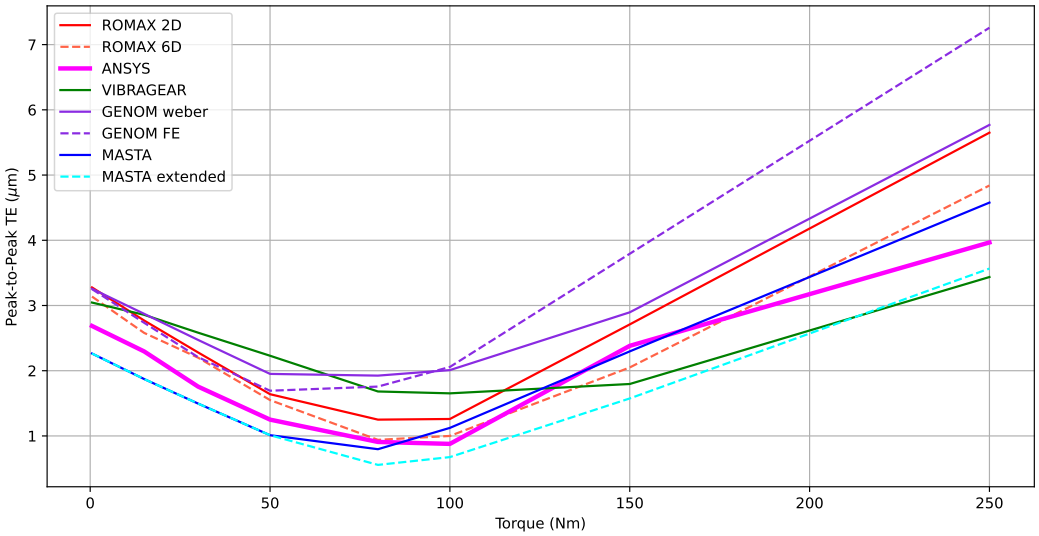

Figure 2.6: Evolution of the PPTE values with torque using different software solutions. The region of minimum STE corresponds to the optimum torque domain.

by a reliable benchmark and a good understanding of the design parameters for the analysis to be meaningful.

By adjusting the tooth thickness definition in MASTA to be coherent with the others, the plots of A.5 (i) and (j) were obtained which demonstrate a better correspondence with the remaining data, particularly in the form of a strong agreement between the extended model and the ANSYS model.

The primary aim of evaluating the displacement in the line of action versus ascending torque values is to analyze how the geometrical and loading conditions affect this displacement, which reflects the expected level of vibrations. All the plots demonstrate a consistent progression trend that aligns with Harris's results [50] regarding the effect of tip relief.

Under unloaded conditions, the STE is the result of the microgeometry deviations being the tip relief in this case. The gradual increase in torque triggers the bending and Hertzian deflections in the level of the tooth flank. These deformations grow to compensate for the microgeometry errors. This explains the lower PPTE values for the middle torque values (around $100Nm$) in A.4 and A.5. For highly loaded systems the evolution of STE will become mostly governed by the deflection of the teeth and the peaks will gain more in amplitude. By tracking this trend, we can establish the plot in Figure 2.6, which provides insights into the optimal torque that minimizes transmission error according to each software.

Overall, the plots demonstrate a similar trend. While PPTE values are similar for low torque ranges, discrepancies become more apparent as loads increase. Among the models examined, ROMAX 6D and MASTA extended produced the least error when compared to ANSYS, the examination of the optimal torque ranges showed some agreement between some of the software packages as follows:

- ROMAX 2D, ROMAX 6D, and ANSYS; T = [80, 100Nm].
- MASTA, MASTA extended, and GENOM FE; T = [50, 90Nm]. The minimum in MASTA clearly corresponds to 80Nm.
- GENOM Weber; T = [50, 80Nm].
- VIBRAGEAR; T = [80, 150Nm].

It is apparent that even when using the same modeling technique, discrepancies may arise. This is exemplified by a comparison of the Weber-based approaches, specifically ROMAX 2D and GENOM Weber. While both methods demonstrate consistency for low and high torque ranges, they diverge around the optimal range. This observation suggests that ROMAX's Weber formulation may incorporate correction factors that enhance the accuracy of its results, particularly around the optimal torque. In a similar fashion, the same thing could be said comparing GENOM FE to MASTA which is attributed once more to the small discrepancies in the definition of the material properties as well as the boundary conditions for tooth compliance.

The graph further illustrates that the ranking of stiffnesses can vary depending on the applied torque, particularly in the case of VIBRAGEAR. For torque levels above the optimal range, VIBRAGEAR demonstrated the lowest transmission error, whereas, at lower torque values, it exhibited a relatively flexible behavior, which may be attributed to a limitation of the thick plate theory formulation. However, the other trends remained consistent for the majority of the torque range. GENOM showed a high STE for the entire range, whereas MASTA and ROMAX presented discrepancies depending on the torque regimen and the nature of the analysis. At low torque levels ($< 50Nm$), the standard and extended plots of MASTA and ROMAX were nearly superimposed on each other, indicating that the load at this range should not be high enough for the teeth to bend and enter in contact prematurely. The STE in MASTA remains, overall, lower than that in ROMAX, which supports the previous findings. The Divergence between the standard and extended models begins to occur above the $50Nm$ mark, which should be the minimum torque at which the corner contact effect takes place. This increases the overall contact stiffness, which explains why the ROMAX 6D model fell close to the standard MASTA model while the extended MASTA model fell even lower below ANSYS and closer to VIBRAGEAR.

It is important to note that the high torque range examined in this study may not have any practical significance as it typically exceeds the load-carrying capacity of gears. Therefore, the results obtained from the low-to-average torque ranges are of greater interest. However, at high torques, the discrepancies with respect to the ANSYS model become more pronounced. This could be due to the increased nonlinearities of the contact and deflection behavior, which are better captured by the FMBD models. This is because the assumptions made by the TCA tools become less valid as the load increases, and the numerical models can better handle the increased complexities associated with higher loads.

In light of these findings, we have chosen a torque value of $115Nm$, which is slightly above the optimal torque, to compare the transmission error trends, as depicted in A.6.

The graph shows that each tool captures the combination of contact stiffness and tip relief effect differently, as seen from the variations in the shape and magnitude of the plots. By comparing the plots, we can conclude that ROMAX agrees most closely with the ANSYS model. However, the standard MASTA model also shows a high level of agreement, with a slightly higher PPTE than the ANSYS model. On the other hand, the extended MASTA model displays a slightly lower PPTE than the ANSYS model.

By paying close attention to the second meshing period, a minor left shift of the ROMAX 6D peak can be seen with respect to the peak in ROMAX 2D. This should account for the change in the SAP and EAP positions as a result of considering the extra degrees of freedom and the bending of the teeth. GENOM shows the highest amplitude of transmission error reaching $2.6\mu m$ which represents approximately double the reference value obtained by ANSYS.

However, the transmission behavior of some TCA tools differs from the others. For instance, GENOM Weber and VIBRAGEAR exhibit a low TE in the middle of the tooth flank, but VIBRAGEAR shows a higher average TE value. This difference in behavior is due to the fact that the applied torque of $115Nm$ is outside the optimal range for most software but falls within the optimal range for VIBRAGEAR as previously identified. This STE trend is characteristic of the optimal range which is located around $80Nm$ as observed in A.4 and A.5 for most software.

In summary, this section has demonstrated the impact of the tooth stiffness model on the evolution of the transmission error value with torque. Despite exhibiting the same trend, the software show minor discrepancies which may be attributed to the diverse modeling techniques used by different software or variations in the assumptions of the same model. The results underscore the importance of benchmarking around the same torque regimen that could differ from one tool to another given its substantial influence on the plot shape and the harmonic content of the signal. Notably, the 6D model of ROMAX, in conjunction with the MASTA models, exhibits the highest level of agreement with the ANSYS reference case.

2.3.3 Effect of flexible shafts and thin rim

The objective of this section is to further highlight the effect of the gear pair environment on the STE response. The bearings were moved to the shaft extremities and the gears from table 2.2 were mounted on two $300mm$ shafts at a $91mm$ offset in order to magnify the misalignment effects resulting from the non-uniform bending of the shafts. Moreover, the web width was reduced to $6mm$ while maintaining the standard effective face-width of $20mm$. The simulation was exclusively conducted using ROMAX and MASTA considering their ability to track the system deflection and the change in the center-to-center distance induced by the deflection of the shafts. The results are presented in Figure 2.7.

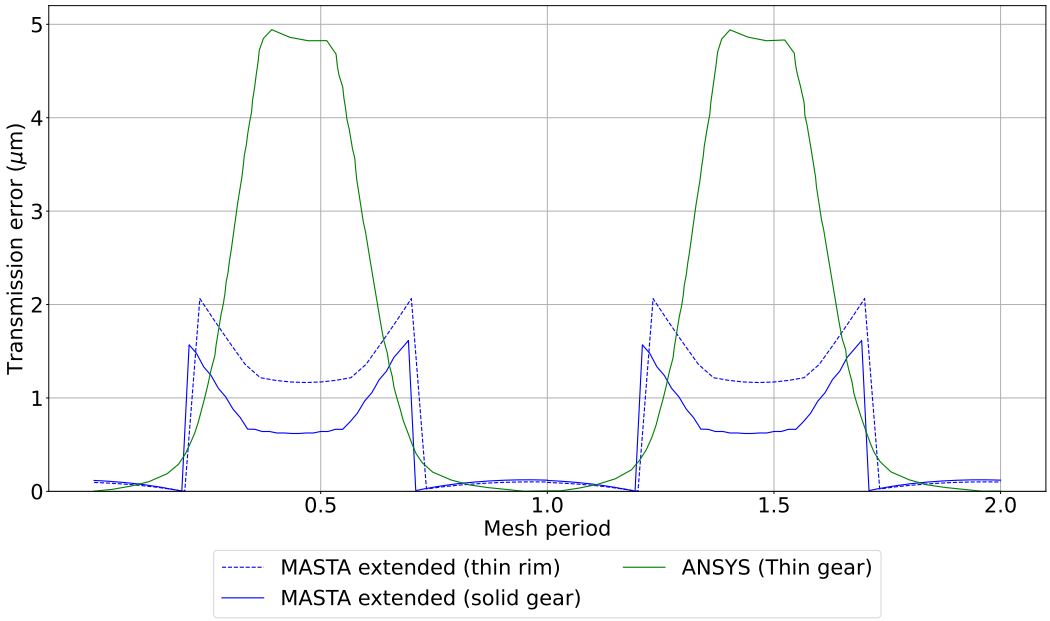

Figure 2.7: Comparison of the static transmission error, after shifting the plots such that the minimum value corresponds to zero, for the case of 115Nm loaded thin-rimmed and shaft-connected spur gears.

Given the Weber approach's limited consideration of modified gear dimensions, such as the presence of a thin rim, the ROMAX TE results were plotted based on a solid blank model. To provide a benchmark, the same scenario was replicated in MASTA, and the results exhibited a notable level of agreement between the two simulations.

Furthermore, the MASTA model displayed a perplexing reduction in TE amplitude upon implementing the thin-rimmed configuration, in contrast to the behavior observed in ANSYS. One can argue that, on one hand, increasing the gear blank's flexibility implies a decrease in bulk stiffness, resulting in a higher transmission error. However, this added flexibility simultaneously leads to the relief of the maximum flank pressure, effectively diminishing the Hertzian effect's influence on the TE.

The combined effects of these multi-scale phenomena ultimately render the computation of transmission error highly sensitive and challenging to reproduce consistently between different software platforms.

2.3.4 Effect of an imposed parallelism defect

In this section, we investigate the impact of parallelism defects on tooth stiffness models in ROMAX and MASTA, to gain a deeper understanding of their behavior. To simulate the parallelism error, a $10\mu m$ lead slope was introduced to one of the gears, as directly representing the error could prove difficult to implement. The resulting data is presented in A.7, which compares the aligned and misaligned models

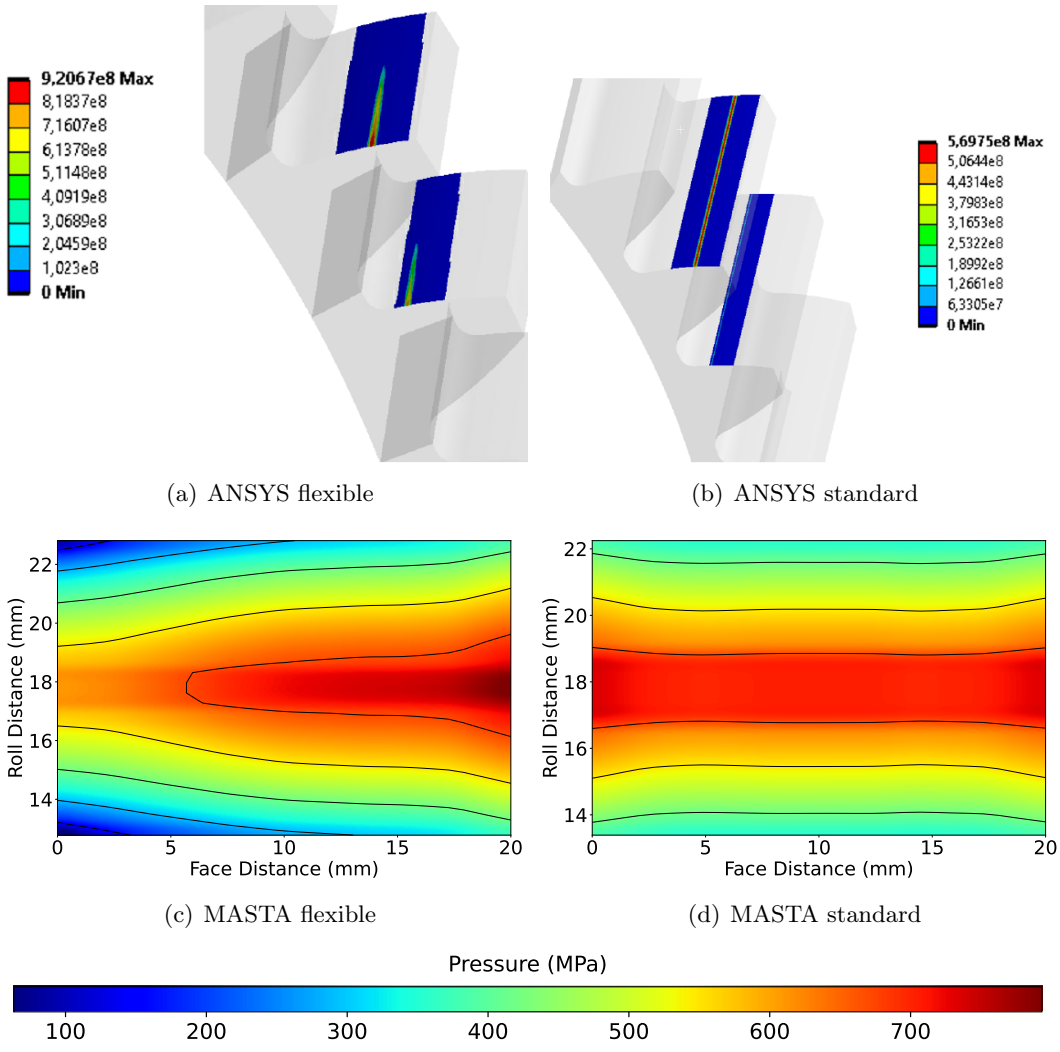

(a) ANSYS flexible

(b) ANSYS standard

(c) MASTA flexible

(d) MASTA standard

Figure 2.8: Contact pressure distribution on the mating teeth for a standard and flexible thin-rimmed gear pair in ANSYS and MASTA. The units in ANSYS are displayed in (Pa).

using both classical and extended approaches.

The comparison of the aligned cases supports the previous findings that the PPTE in MASTA is lower than in ROMAX, and the plot shape is different due to slightly varying ranges of optimal torque. However, applying a lead slope modification significantly increases the transmission error amplitude, as the loads are concentrated on the tooth flank edge, as shown in A.8. The transition to the extended models alters the shape of the peak to account for the corner contact. The sharper peak in ROMAX is attributed to minor angular misalignment.

The primary objective of this study was to create a scenario where the contact between the gear teeth is limited to a specific portion of the flank while the rest remains free of contact. This was done to illustrate a fundamental difference between a finite element model and an uncoupled strip model. In an FE model, the elements in contact are coupled to the elements in the free zone, which can affect the overall tooth stiffness and consequently the transmission error. In contrast, the Weber model does not consider the stiffness effects of the tooth flank strips outside the contact region, resulting in less smooth contact contours, particularly near the contact edge.

However, it should be noted that the software used in this study can only capture the pressure contours for the effective face-width and not for the entirety of the teeth. Additionally, creating this scenario requires either exaggerated misalignments or significant microgeometry modifications, such as a very deep crowning. As a result, this study may not be of significant practical relevance. Nonetheless, the uncoupled spring model is equally capable of accurately representing tooth stiffness in most practical applications.

2.4 Comparative study of the static transmission error for the case of helical gears

2.4.1 Case of perfectly involute helical gears

Similarly to the spur gear case, a set of perfectly involute helical gears with their characteristics summarized in table 2.4 was evaluated and the results are plotted in A.9.

The graph reinforces the previous conclusions regarding the order of magnitude for the various teeth stiffness models. The major difference lies in the extremities of the peaks where most of the plots except ROMAX exhibit what looks like the shape of "horns" manifested by a brutal increase of the transmission error amplitude from both sides of the peak. This can be better visualized by looking at the contact patches in A.10 where the pressure in ROMAX seems to be uniformly distributed within the entirety of the tooth flank. Conversely, MASTA appears to be the siege of high stress concentrations at the start and end of the active profile which is justified by the lack of profile corrections. Moving to the extended model in MASTA alleviates the edge pressure and the force per unit length in the center of the tooth

Table 2.4: Characteristics of the isolated perfectly involute helical gears.

Name	Designation	Gear 1	Gear 2	Unit
Module	m	2		mm
Number of teeth	Z	50	50	-
Pressure angle	α	20		deg
Helix angle	β	15		deg
Base diameter	d_b	96.528	96.528	mm
Profile shift coefficient	x	0	0	-
Addendum coefficient	h_α	1	1	-
Dedundum coefficient	h_f	1.25	1.25	-
Facewidth	b	20	20	mm
Center to center distance	a_f	103.528		mm

flank becomes comparable to the forces at the root and tip of the tooth. It is noteworthy that the axial forces created from the presence of a helix angle amplify the twisting effects of the gear tooth and therefore the time-evolution of the contact patch configuration which is better represented in a direct stiffness formulation as provided in MARC.

2.4.2 Case of added tip relief and crowning modifications

To investigate the impact of a $10mm$ longitudinal lead crowning, modifications were made to the previous gears. Similar to the spur gears, a tip relief modification was included, and the center-to-center distance was increased from $103.528mm$ to $104mm$ to allow the ANSYS simulation to converge. The results, shown in A.11 and A.12, demonstrate several intricacies compared to the spur gear case.

The plots of the crowning-free cases reveal significant variations in the shapes, which can be attributed to the difference in the positioning of the applied torque with respect to the optimal torque range calculated by each software. The more sophisticated ANSYS model exhibits the most significant amplitude of transmission error, which aligns with the most simplistic VIBRAGEAR model. However, this does not necessarily imply that VIBRAGEAR is the most accurate, as accuracy remains tightly case-dependent. As shown in 2.6, VIBRAGEAR showcases a superior PPTE amplitude near the optimal range compared to other alternatives, justifying the magnitude of the response, which is very comparable to ANSYS. Furthermore, the STE amplitude in ANSYS stands above the rest, which can be attributed to the better capturing of the more complicated contact forces associated with helical gears, such as the thrust forces that amplify the effects of misalignments and out-of-plane bending which contribute to the increase of the displacement response.

The shape of the trends is influenced by contact handling and the number of degrees of freedom in the model. Specifically, indirect FE models show a sharper edge near the start of the active profile than Weber models. This effect is particularly pronounced in the case of GENOME FE and to a lesser degree in MASTA. In addition, the 6D model in ROMAX has a lower amplitude than its 2D equivalent. The additional degrees of freedom likely contribute to relaxing the deflection behavior,

Table 2.5: Summary of the variation percentages of PPTE between tooth profiles with and without crowning.

Software	MASTA	MASTA extended	ROMAX 2D	ROMAX 6D	GENOM Weber	GENOM FE	ANSYS	VIBRAGEAR
PPTE (No crowning)	0.08	0.08	0.26	0.16	0.1777	0.314	0.621	0.54
PPTE (With crowning)	0.5	0.28	1.53	1.33	1.72	2.35	1.98	0.31
Variation (%)	525	250	488.46	731.25	867.92	648.40	218.84	-42.6

as evidenced by the left shift in the plot caused by the change in SAP and EAP positions. The deformation of the 6D model may confer less pressure on the flanks, resulting in a lower STE.

Moreover, the 6D model provides a higher fidelity representation of the edge contact occurring at the line that defines the start of tip relief. This is visible through the distortion of the contour lines along the pressure zone's centerline in A.13 (b), which coincides with the start of tip relief compared to the 2D model in (a). It is evident that the corner contact effect is not as significant in helical gears as it is in spur gears, given the gradual transition nature of contact in helical gears, which minimizes the stresses.

By adding a lead crown, a remarkable increase in the STE peaks is witnessed for all the tools except VIBRAGEAR which shows a transformation in the shape of the plot and the displacement between the regions of the higher and lower number of teeth in contact possibly indicating a different handling of the interaction between meshing stiffness and tip relief. The increase in the STE peaks is explained by the centralization of the loads in the tooth flank as shown in A.13 due to the presence of the crown which increases the pressure in the middle of the flank and hence the displacement along the line of action. We can also compare the development percentages as depicted in table 2.5 which showcase a very large variation between the different software. While MASTA displayed the lowest relative amplitude to ANSYS, it shows the closest variation percentage.

2.4.3 Case of a geometrically-optimized full gearbox model

Having gained a comprehensive understanding of the significant variations in results obtained from various software, we aimed to draw a comparison between them for a more complex double-stage transmission subjected to microgeometry optimization. Due to the intricacy of the model, a detailed description of the entire system was omitted, and our focus was limited to the gears of interest. The characteristics of these gears have been summarized in Table 2.6. The microgeometry alterations, intended to enhance the transmission error and gears' durability, were known in advance from a microgeometry optimization study.

Since the model is more complex, it may surpass the modeling capabilities or at least pose challenges in modeling additional aspects using some tools. Therefore, the comparison of results was only performed between ROMAX and MASTA, as

Table 2.6: Characteristics of the helical gears to be optimized.

Name	Designation	Gear 1	Gear 2	Unit
Module	m	2.101		mm
Number of teeth	Z	24	53	-
Pressure angle	α	22.5		deg
Helix angle	β	26		deg
Base diameter	d_b	50.951	112.518	mm
Profile shift coefficient	x	0	0	-
Addendum coefficient	h_α	1	1	-
Dedundum coefficient	h_f	1.25	1.25	-
Facewidth	b	20	20	mm
Center to center distance	a_f	90		mm
Involute modification				
Involute barreling	C_α	20	0	mm
Tip relief amount	$C_{\alpha a}$	25	45	μm
Tip relief starting diameter	d_s	59.24	126.11	mm
Lead modification				
Lead crown	C_β	5	0	μm
Lead slope	$C_{H\beta}$	20	0	μm

illustrated in A.14 and A.15. The plots reveal some rather interesting results. Regardless of the difference in PPTE which should be trivial at this point, both TCA tools present slightly different improvement percentages of transmission error with respect to the reference case of standard involute gears.

Table 2.7 summarizes the improvement percentages. In comparing equivalent methods, the reduction of the peak-to-peak transmission error in MASTA appears to be more significant than that in ROMAX. On the other hand, the 2D model of ROMAX produces the highest peaks compared to all the other alternatives for the non-optimized case, indicating its incapacity to properly model contact of unmodified profiles. By applying a tooth profile modification, the magnitude of the transmission error significantly decreases, and the peaks shift position, indicating that the loads have shifted from being concentrated around the edge of the flank to the center of the flank. A.16 illustrates this shift. In contrast to the optimized ROMAX case, where there is a slight difference between the 2D and 6D models, which can be attributed to the contribution of the overall system deflection, influenced by the introduction of the microgeometry errors, the MASTA model shows no difference between the standard and extended cases. To demonstrate that MASTA can equally account for the system behavior in the transmission error, we utilized the advanced system deflection (ASD) feature. This quasi-static approach considers the development of the system's deflection behavior, including the resulting misalignment, to update the contact and transmission error at each quasi-time step. The results, presented on the same plot, show a slight increase in amplitude compared to the extended cases, and the shape of the plots becomes more similar to ROMAX. This case study offers a compelling illustration of how discrepancies can magnify as the complexity of a model increases. In such scenarios, differences in the results

Table 2.7: Summary of the improvement percentages of the PPTE response as a consequence of changing the microgeometry of the gears.

Software	ROMAX 2D	ROMAX 6D	MASTA	MASTA extended	MASTA extended (asd)
Improvement (%)	58	26	70	60	45

obtained through the use of the transmission error metric can be traced to a variety of sources, such as the stiffness models used for the gears and various parts, the assumptions underlying TE calculations, and the boundary conditions set. All of these factors, among others, contribute to the superposition of errors, which can have significant implications for the accuracy and reliability of the model's outputs.

2.5 Case of lightweight gear with a circumferentially varying stiffness

The lightweight applications that tackle the optimization of components from a geometrical point of view require the removal of a fraction of the material from the parts. These geometrical alterations are very likely to reduce the overall stiffness of the components and unavoidably increase the resulting dynamic effects. In gear applications, Many studies have approached gear lightweight designs by applying holes or cavities that are equidistantly distributed within the blank. Asai et al. [4] introduced a CAE enhancement method that is able to predict the gear-related noise in the time domain through multi-body simulations based on modal synthesis methods [59, 24]. This enabled the capturing of the fluctuating blank stiffness resulting from the geometrical discontinuities and the numerical prediction the resulting vibrational response in reduced time. Benaicha et al. [8] proposed a 2D decomposition method for computing the static transmission error in the case of spur gears with holes. The method consisted of computing the static transmission error for the case of gears with rigid blanks to only account for the compliance of the teeth. The tangential loads are then extracted and applied to the FE blank to get the modulated average TE component. The resulting STE is ultimately the superposition of both displacements associated with the teeth and gear blank compliances. Although this approach makes the strict assumption of ignoring any twisting of tooth flanks in the plane of action, it showed great correlations with a flexible multi-body approach in terms of the resulting modulation sidebands for both STE and meshing stiffnesses. The method also proved to have a significant time reduction since it relies on a static Guyan condensation [47] to reduce the number of DOFs. This section is dedicated to the evaluation of the software's capability to properly capture the superposition effect coming from the presence of geometrical discontinuities in the gear blank. The comparison is exclusive to ANSYS, MARC, and MASTA considering that the modeling methods in the rest of the software were not designed or developed enough to account for the change in the stiffness.

While the direct method in ANSYS and MARC intuitively considers the change in stiffness when the gear rotates as a consequence of the direct stiffness derivation, MASTA utilizes an "Advanced Times Stepping Analysis for Modulation (ATSAM)" approach, designed to treat this problem at record speed compared to a conventional direct approach. The method consists of building a collection of linearized models built at a discrete number of large time steps corresponding to different gear mesh positions corresponding to locations above the "holes", others above the "land", and in between. The first linearized model is solved in the time domain instead of the frequency domain through modal coordinates and summation techniques. Once a sufficient amount of time has passed for the next large time step to be reached, the subsequent linearized model is employed. The model is solved in the time domain, and the initial conditions are taken from the results obtained at the final point of the previous large time step from the preceding linearized model [4]. The analysis is conducted in this manner until the designated analysis time is reached, resulting in a full time trace response.
To test the method, we conducted a preliminary study in which we designed a spur gear pair with different numbers of holes. The results of the test are presented in 2.9, which clearly shows a superposition of two signals. One signal has the same order as the number of holes in the structure, while the other has the same order as the meshing frequency. It was determined from the analysis that the presence of holes has a more significant impact on the average transmission error, as compared to the peak-to-peak transmission error (PPTE) value. This effect is likely due to the gear blank being weakened by the discontinuities, with minimal impact on the contact region.

It is important to mention that, unlike the previous analyses where the transmission error was measured as the relative displacement in the line of action which only takes the gear pair in the scope of the deflection, the current simulation treats the TE as the relative displacement between the input and the output power loads which is more representative of the general behavior of the system and the overall propagation of the excitation.

While the curve's trend aligns with the expected outcome from the simulation, the magnitude of the STE fluctuation is still unclear. In order to clarify this, we constructed and analyzed a simplified model of an identical spur gear pair, using both MASTA and ANSYS simultaneously. The characteristics of this model are outlined in Table 2.8 and are referred to as "Gear Pair 1".

The transmission error and its harmonics were plotted in A.17 which shows the tooth-level angular displacement between the input and output gears.

Upon comparing the single-tooth peaks, it becomes apparent that ANSYS exhibits a higher amplitude, consistent with previous results. Moreover, a 6^{th} order fluctuation is observed but remains very low. This is likely due to the fact that the gears have a relatively low diameter-to-width ratio, which inherently makes them stiff, even with the presence of holes. Thus, the holes in the gears do not cause a significant variation in stiffness, leading to almost no discernible sidebands next to the meshing frequency harmonics.

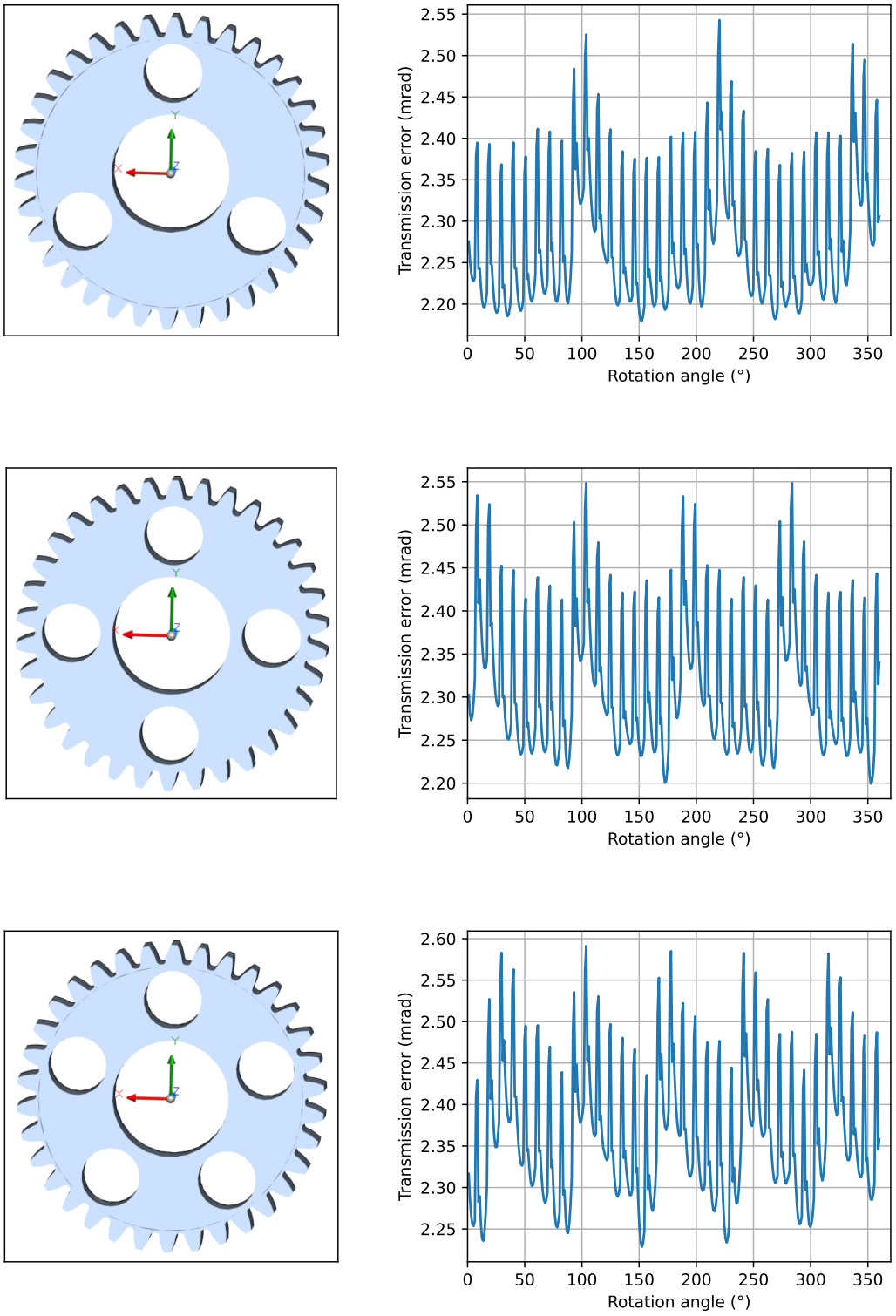

Figure 2.9: Visualization of the superposition effect for gears with 3,4 and 5 holes.

Table 2.8: Characteristics of the lightweight identical spur gear pairs.

Name	Designation	Gear pair 1	Gear pair 2	Unit
Module	m	2	1.47	mm
Number of teeth	Z	24	34	-
Pressure angle	α	20	20	deg
Helix angle	β	0	0	deg
Base diameter	d_b	45.105	46.966	mm
Profile shift coefficient	x	0	0	-
Addendum coefficient	h_α	1	1	-
Dedundum coefficient	h_f	1.25	1.25	-
Facewidth	b	20	10	mm
Center to center distance	a_f	48	49.98	mm
Blank parameters				
Bore diameter	D_{br}	6	20	mm
Number	N_h	6	8	-
Diameter	D_h	8	10	mm
Radial position	R_h	12	17	mm

To highlight the impact of incorporating holes, we developed a second gear blank with reduced facewidth and enlarged bore and hole diameters, resulting in considerably more flexible gears. A detailed account of the properties can be found in Table 2.8, specifically under the entry for "Gear pair 2". To compare the STE plot and harmonic content obtained from MASTA and MARC simulations, refer to A.18.

Upon examining the plots, it is apparent that the finite element-generated plot exhibits nearly perfect periodicity, whereas the time-stepping method-generated plot falls short in comparison. The signal averages of both signals appear to be sufficiently coherent, unlike the tooth-level peaks which are lower in MASTA, as consistent with prior findings. It is worth noting that simulations have revealed that the reduced model produces a slightly lower STE amplitude than the full DOF model. This occurs because reducing the number of DOFs causes the model to lose some of the finer displacement details, leading to a perception of increased stiffness. This effect can be mitigated by properly adjusting key reduction parameters related to the mesh density and reduction nodes. Furthermore, the observed distortions in the MASTA-calculated STE are likely due to the strict assumptions used in the calculations, which are prone to accumulating errors between time steps. Additionally, simulation parameters such as the number of condensation nodes located on the gear blank periphery and the number of time steps per rotation play a role in improving the accuracy of stiffness determination.

The differences between the two plots are easily observed through the Fast Fourier Transform (FFT) decomposition, shown in A.17(b). This decomposition highlights the most significant harmonics, including the hole order harmonic ($N_h = 8$) and the harmonic content around the first three meshing orders ($H_{Z_1} = 34$, $H_{Z_2} = 68$, $H_{Z_3} = 102$). The neater periodicity observed in the MARC plot justifies the presence of sidebands around the main meshing orders, corresponding to $H_Z \pm N_h$. This is particularly visible around the first meshing frequency, with the

presence of the 26^{th} and 42^{nd} sub-harmonics. The sidebands become less prominent in the case of MASTA due to the overall imperfect shape of the STE plot. It is important to note that the artificial sidebands appearing near the rotation frequency in MARC may be attributed to numerical errors, possibly caused by the imperfect smoothness of the STE plot.

The resulting discrepancies imply potential variation in dynamic responses due to different energy levels attributed to excitation orders. However, considering the computational time aspect and the fact that MASTA is significantly faster than MARC, one can acknowledge the ability of the time-stepping method to provide a rapid, broad assessment of the system's excitation with a reasonable degree of precision.

2.6 Conclusion

This paper investigates the capabilities of different gear contact software in evaluating the static transmission error. The paper describes the computation of tooth stiffness concepts and assumptions within the limits of the disclosable information provided by the software developers that do not cause confidentiality issues.

Several study cases were evaluated to establish clear trends in transmission error, which, while sometimes model-dependent, remain applicable for most cases. The contact stiffness values were arranged in increasing order for a low to average torque range as follows: GENOM FE, VIBRAGEAR, GENOM Weber, ROMAX 2D, ROMAX 6D, ANSYS/MARC, MASTA, and MASTA extended. The evaluation of TE values versus torque showed differences in the range of optimal torque, which explains variations in plot shape, especially when considering tooth profile modifications. The study highlights the effect of variations in models, such as the extended off-line-of-action contact at gear tips, the moment-induced misalignments in higher DOFs models, and the effect of system components on contact occurrence and transmission error calculation. The paper also showcases the limitations of the software in terms of displacement capture, gear body, and component capture, and the capture of modulation effects for lightweight applications.

When comparing identical models in different software, the study found variations that could be attributed to differences in model formulations and parameters. These discrepancies increased with the complexity of the design, limiting the reproducibility of results across software platforms. This could potentially cause minor variations in optimization results and rates of improvement. To mitigate these issues, it's important to have reference data for the design that can be used to compare and validate the results of simulations across different software. This can help ensure consistency in the results and increase confidence in the accuracy of the models.

The study provides further evidence that the uncoupled spring model can effectively address most practical cases, performing comparably to the finite element model. However, the uncoupled spring model is not as effective when dealing with thin-rimmed gears, as the blank parameters are not explicitly specified in the Weber

approach. Within the context of lightweight applications, the study found that evaluating the behavior of flexible gears yielded the greatest discrepancies between the semi-analytical and multibody models, revealing limitations in their ability to accurately capture the out-of-plane deflection behavior of the gears. Additionally, while the time-stepping approach in MASTA produced acceptable results for perforated solid blanks, deviations were observed for thin rims in the single-tooth analysis case. This calls for more extensive investigations to test a broader range of lightweight geometries, particularly in cases where the thin rim is coupled with the presence of holes.

Overall, this paper provides a comprehensive investigation of static transmission error evaluating capabilities using different gear contact software as well as a good background regarding the nature of contact physics taking place in a gear mesh. While good performance is initially observed with the TCA tools, divergences start to take place when tending to more complex and flexible models where the use FMBD model becomes more justified vis-à-vis the computation time which is several orders of magnitude above the other alternatives. Nevertheless, the results offer valuable insights into the modeling intricacies and potential pitfalls when modeling a gearbox model which can be optimized for a better outcome, ultimately paving the way for future studies and developments in the gear contact analysis field.

Chapter 3

Variability Analysis of Transmission Error Calculation and Modeling Methods: Implications for Dynamic Response of Gearboxes

Contents

3.1 Introduction

The computation of transmission errors has revealed noteworthy disparities dependent on the choice of software package and modeling methodologies.

Expanding upon the case studies presented in the preceding chapter, the objective of this chapter is to conduct a thorough examination of the impact of varying static transmission error (STE) excitations on the dynamic response of the system. Additionally, this chapter introduces an exploration of how specific meshing and modal reduction parameters influence the consistency of the response, aimed at optimizing settings to construct a higher-fidelity model that will be instrumental in the optimization process.

This chapter serves as a valuable resource for professionals engaged in gearbox analysis and design. It equips them with the requisite knowledge to make informed decisions and implement necessary precautions, ultimately facilitating the development of accurate models that faithfully capture the dynamic behavior of gearbox systems.

3.2 Overview of the Gear Whine Dynamic Model in ROMAX and MASTA

3.2.1 Description of the gearbox models

To support the simulations in this chapter, we've created a gearbox model that's been linearized under a specific load condition. This model includes all the key components responsible for transmitting vibrations in a transmission system.

We'll compare how these components are modeled in ROMAX and MASTA to understand any differences or similarities between the two software platforms. This analysis will help us gauge the reliability and correlation of the simulation results from each software package. Detailed explanations of the modeling methods for these components will follow in the next sections

3.2.2 Modeling of the shafts

In many previous transmission models, shafts were often simplified as spring elements with rotational stiffness and independent lateral stiffness, allowing only rotation around the axial axis without coupling motion in different directions. However, modeling shafts in a gearbox is more complex due to their typically non-uniform cross-sections along the length, posing challenges for providing accurate analytical solutions that capture the behavior of such intricate geometries.

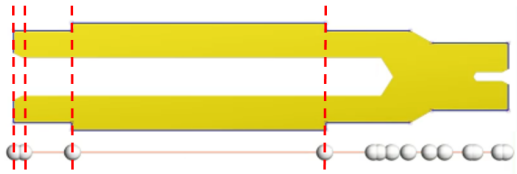

Figure 3.1: Visual representation of a non-uniform shaft and its corresponding FE Timoshenko beam model. Each element corresponds to a geometrically simple region.

To address this, Timoshenko elements within finite element analysis are better suited. In this approach, the shaft's stiffness is modeled using Przemieniecki's finite element approximation [121], which divides the shaft into uniform sections. Using beam elements for each section simplifies solving the governing equations, as illustrated in Figure 3.1. The solution for the entire shaft is obtained by combining the individual solutions of these sub-elements while adhering to equilibrium and compatibility conditions at the nodal points.

In theory, each beam element possesses a total of 12 DOFs with six DOFs representing the translational and rotational movements along the (x,y,z) axis for both of the nodes as demonstrated in figure 3.1. By aligning the xy and xz planes the element mass and stiffness matrices can be written as B.3 and B.1 respectively as established in the literature.

The resulting simplified equation of a shaft without considering the damping effect can be written as:

$$\mathbf{M}^s\ddot{\mathbf{q}}^s + \mathbf{K}^s\mathbf{q}^s = 0 \tag{3.1}$$

The shaft analysis involves nodes that are not directly associated with changes in the defined sections but instead correspond to mounting locations for connected components like gears and bearings. Moreover, the method of coupling can influence how we divide the shaft sections. In our analysis, we've assumed an integral connection, treating the shaft sections as if they extend to include the sections of the gear blanks and bearing inner races, essentially considering them as one continuous part. This assumption is valid when employing a Timoshenko representation, especially for relatively straightforward geometries.

For the single-stage transmission depicted in Figure 3.2, the numerical extents of the shaft model are highlighted in red. The shaft model encompasses the inner sections (depicted in green) and the conventional gear blank sections (shown in orange). However, it does not encompass the finite element blank section (shown in red). This omission is because the finite element blank section exhibits more complex behavior that exceeds the capabilities of a Timoshenko representation.

The accuracy of a shaft's deflection behavior is influenced by the number of beam elements used for discretization. In this study, it was observed that employing the standard discretization parameters yielded satisfactory results, and therefore, they were retained for the simulations.

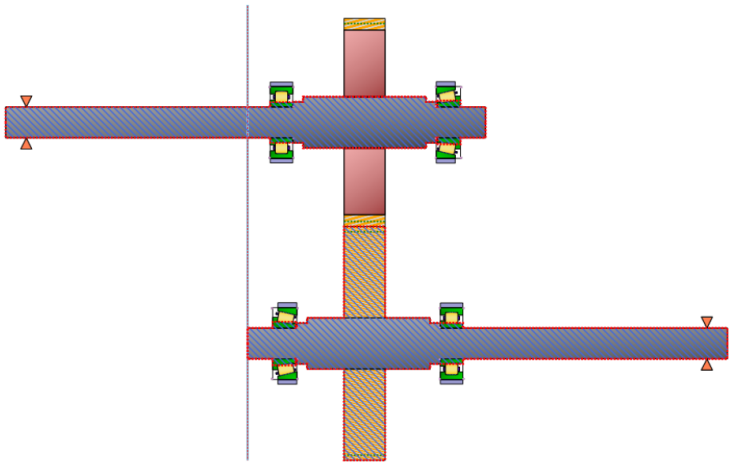

Figure 3.2: Visual representation of the numerical extents of shaft sections

Additionally, it's important to acknowledge that commercial software often includes proprietary adaptations of the standard Timoshenko beam formulation, which are regrettably not user-accessible. These adaptations are typically designed to tackle challenges like shear locking, a phenomenon that can occur in sections with low aspect ratios (Length/Diameter).

Shear locking tends to lead to an overestimation of stiffness, especially near cross-sectional discontinuities. The customized formulations within the software aim to alleviate such issues and enhance the accuracy of the results.

3.2.3 Modeling of the bearings

Bearings play a pivotal role in linking excitation sources with the dynamic response, serving as the primary components connecting these sources to the radiating surface. Therefore, achieving an accurate representation of bearing stiffness is paramount, as it can exhibit substantial non-linear characteristics. This non-linearity stems from the complex interactions of constituent elements (such as contact, friction, sliding, and collisions) within the bearing, as well as the transition of elements from an unloaded to a loaded state during rotation.

Early attempts at modeling bearings involved simplifications, like reduced degrees of freedom or idealized boundary conditions with nonlinear stiffness coefficients. However, these models, introduced by Jones, Palmgren, Gargiulo, and Harris [63, 113, 35, 51], fell short of accurately predicting the coupling between translational and rotational vibrations observed in roller bearings. Their strict assumptions failed to capture the true physical phenomena.

A breakthrough came with Lim and Singh [88, 89], who introduced a 5DOFs bearing stiffness model enabling coupling between in-plane and out-of-plane motions. They derived their models from force balance equations using a discrete summation approach, resulting in a set of algebraic nonlinear equations that could

be numerically solved for different stiffness components within the global stiffness matrix. Hernot et al. further enhanced this approach by transforming the problem from a discrete to an integral form, allowing them to calculate load summation analytically through integration [54]. Other dynamic bearing models were proposed by Gupta, and Walters [45, 46, 159], which integrated the equations of motion in different time steps for real-time simulations. These models considered additional effects like traction forces resulting from lubrication and friction. However, they lacked the inclusion of load distribution calculated iteratively from the relative positioning of the races.

In recent research, Guo and Parker introduced an innovative approach employing a hybrid finite element contact mechanics model to calculate bearing stiffness [44]. While this method offered flexibility in modeling various bearing types, it demanded careful selection of time-stepping and control parameters to ensure convergence, making it a time-intensive process. Alternatively, experimental approaches were explored for constructing bearing stiffness matrices, as evidenced in the work of Knaapen and Tiwari [75, 144].

Lim and Singh developed an accurate and efficient approach that has gained wide acceptance in rotor dynamics analysis [87]. This approach surpassed the limitations of both finite element and experimental models in terms of computational efficiency.

More recently, Zhang et al. presented a fast energy-based numerical technique that transforms the problem of determining bearing displacements into an optimization task [183]. By minimizing the system's potential energy, this technique yields displacement-type solutions, eliminating the need for ordinary integration of algebraic equations through numerical methods.

For the purpose of our analysis, we have adopted a linearized bearing stiffness. The detailed formulations can be found in [52].

In principle, the calculation of bearing stiffness is a complex process that considers several factors related to the bearing geometry, inner and outer ring deflections and tilts, and rotational speed. This static equilibrium-based stiffness determination involves an iterative approach that incorporates a Hertzian formulation. The formulation accounts for loading conditions and microgeometrical details specific to each bearing type, such as race geometries, number and size of elements, and clearances.

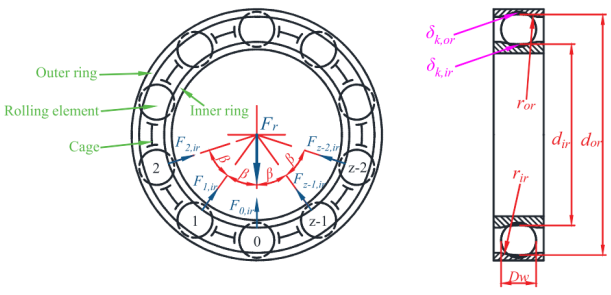

Figure 3.3: Schematic of the forces developed at the bearing elements

To calculate the stiffness of the bearing, we employ a Hertzian formulation, which is used to determine the deflection and tilt of each individual bearing element. This formulation establishes a relationship between the relative motions of the inner and outer raceways and the applied force on the bearings as shown in Figure 3.3. An iterative Newton-Raphson method is employed to adjust the deflections of the races until static equilibrium is achieved for each element, ensuring the forces are balanced.

Considering the external load vector applied to the bearing's ring $\mathbf{F} = \{F_x, F_y, F_z, M_x, M_y\}$ and the induced deflection vector of the inner ring $\delta = \{\delta_x, \delta_y, \delta_z, \theta_x, \theta_y\}$ as:

$$\boldsymbol{K_b} = \begin{pmatrix} \frac{\partial F_{rx}}{\partial \delta_{rx}} & \frac{\partial F_{rx}}{\partial \delta_{ry}} & \frac{\partial F_{rx}}{\partial \delta_z} & \frac{\partial F_{rx}}{\partial \theta_x} & \frac{\partial F_{rx}}{\partial \theta_y} \\ \frac{\partial F_{ry}}{\partial \delta_{rx}} & \frac{\partial F_{ry}}{\partial \delta_{ry}} & \frac{\partial F_{ry}}{\partial \delta_z} & \frac{\partial F_{ry}}{\partial \theta_x} & \frac{\partial F_{ry}}{\partial \theta_y} \\ \frac{\partial F_z}{\partial \delta_{rx}} & \frac{\partial F_z}{\partial \delta_{ry}} & \frac{\partial F_z}{\partial \delta_z} & \frac{\partial F_z}{\partial \theta_x} & \frac{\partial F_z}{\partial \theta_y} \\ \frac{\partial M_{\theta_x}}{\partial \delta_{rx}} & \frac{\partial M_{\theta_x}}{\partial \delta_{ry}} & \frac{\partial M_{\theta_x}}{\partial \delta_z} & \frac{\partial M_{\theta_x}}{\partial \theta_x} & \frac{\partial M_{\theta_x}}{\partial \theta_y} \\ \frac{\partial M_{\theta_y}}{\partial \delta_{rx}} & \frac{\partial M_{\theta_y}}{\partial \delta_{ry}} & \frac{\partial M_{\theta_y}}{\partial \delta_z} & \frac{\partial M_{\theta_y}}{\partial \theta_x} & \frac{\partial M_{\theta_y}}{\partial \theta_y} \end{pmatrix} \tag{3.2}$$

The linearization of the bearing stiffness is achieved by differentiating the inner race forces with respect to the radial, axial, and tilt deflections of each element. This process involves calculating the partial derivatives of the forces with respect to the displacements. These derivatives quantify the sensitivity of the forces to changes in the displacements, providing a linearized representation of the bearing stiffness.

The resulting stiffness represents the slope of the non-linear plot around the applied load of interest, as illustrated in Figure 3.4. It comprehensively captures the relationship between the applied loads and the displacements of the inner race relative to the outer race in all 6DOFs. Represented as a 5×5 matrix, it accounts for the free rotation in the axial direction and describes the stiffness characteristics of the bearing system.

$$\boldsymbol{K_b} = \begin{pmatrix} k_{xx} & k_{xy} & k_{xz} & k_{x\theta_x} & k_{x\theta_y} \\ k_{yx} & k_{yy} & k_{yz} & k_{y\theta_x} & k_{y\theta_y} \\ k_{zx} & k_{zy} & k_{zz} & k_{z\theta_x} & k_{z\theta_y} \\ k_{\theta_x x} & k_{\theta_x y} & k_{\theta_x z} & k_{\theta_x \theta_x} & k_{\theta_x \theta_y} \\ k_{\theta_y x} & k_{\theta_y y} & k_{\theta_y z} & k_{\theta_y \theta_x} & k_{\theta_y \theta_y} \end{pmatrix} \tag{3.3}$$

It is important to note that the current study does not extensively delve into the specific details of bearing stiffness effects. Instead, the focus is primarily on coupling the motion of the shafts and the housing. However, it is worth considering that incorporating a non-linear matrix, which is continuously updated throughout the quasi-static rotation of the system, would offer a more accurate representation of the dynamic response.

3.2.4 Modeling of the housing and finite elements components

While simple elements like linear springs and Timoshenko elements are commonly used to represent most elements in structural analysis, they may not adequately

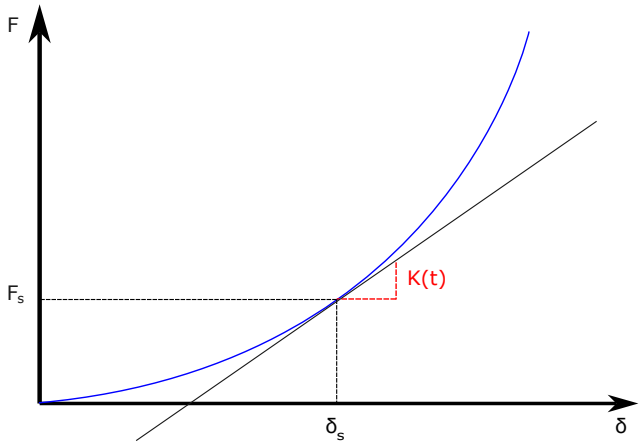

Figure 3.4: Linearization of the bearing forces around the statically applied load.

capture all degrees of freedom in certain cases. One such example is gear blanks, which extend from the shaft diameter to the base circle of the gear. Representing gear blanks using simple elements fails to accurately capture their out-of-plane motion, necessitating the use of finite element geometries that can describe various forms of deflection.

However, implementing full-scale finite element models as they are can impose significant computational burdens and slow down calculations. Modal reduction methodologies such as the Craig-Bampton Component Mode Synthesis Component Mode Synthesis (CMS) method have been developed to address this. The CMS method reduces the degrees of freedom of a large finite element model by constructing a smaller substructure model with only a few degrees of freedom while preserving the low-frequency dynamic characteristics of the original structure. It involves partitioning the finite element model into two parts: interface DOFs shared by both the substructure and the rest of the structure, and non-interface DOFs present only in the rest of the structure. The substructure is then reduced by retaining a small number of component modes, which are obtained from a modal analysis of the substructure. The reduced substructure model is therefore combined with the retained interface modes and reduced component modes to form the Craig-Bampton model that is used for the dynamic analysis. The formulation details of the method can be found in Appendix B.2.

In general, it is recommended to select the frequency range of condensation to be at least twice the operating frequency range. This ensures that modes outside the frequency range, which can potentially influence the modes within it, are appropriately accounted for. Nevertheless, for static problems or problems in which the eigenmodes have little influence on the dynamic response, it is possible to use the Guyan condensation instead to get an approximation of the structural stiffness of the reduced component.

The format of the reduced output stiffness matrix can vary depending on the software being used. In the case of MASTA software, if we consider a housing

system represented by 4 master nodes representing the inner race central nodes and accounting for 40 modes, the reduced stiffness matrix has a size of (24+40)×(24+40). This can be expressed in the following form:

$$K_h = \begin{bmatrix} K_{hh} & 0 \\ 0 & K_{mm} \end{bmatrix} \qquad K_{mm}[i,j] = 0 \quad for \quad i \neq j \tag{3.4}$$

where K_{hh} is a 24×24 submatrix representing the stiffness of the housing degrees of freedom, and K_{mm} is a 40×40 submatrix representing the stiffness coefficients of the modal degrees of freedom. The global matrix indicates that there is no coupling between the housing and modal degrees of freedom.

Figure 3.5 illustrates a graphical representation of the housing. It is important to note that for modal reduction purposes, a highly refined mesh is not necessary. Instead, a mesh that adequately captures the overall stiffness of the structure is sufficient.

In the figure, the green nodes represent the master nodes, which are superposed and coupled with the inner race bearing node using the previously derived bearing stiffness matrix. This connection is facilitated by employing kinematic rigid body elements. These elements provide a comprehensive understanding of the overall motion and position of the system while maintaining reasonable computational efficiency. This is established under the assumption that the bearings can be treated as rigid body elements, implying that there is no need to consider stresses and local deformations within the bearing cavities in which the use of distributing elements, which provides more detailed information about internal forces and deformations, becomes more justified.

The lower plate, highlighted in red, represents a grounded boundary condition in the figure. It is important to acknowledge that this configuration is relatively restrictive compared to real-world applications, where grounding is often achieved through mounting points that possess a certain level of compliance, better reflecting the behavior of actual mounting joints. However, for the purposes of this simplified mock-up and considering that precise correlations with experimental data are not the primary objective, we opted to maintain this configuration. While it may not fully capture the complexity of real mounting conditions, it provides a reasonable approximation for the analysis at hand.

3.2.5 Modeling the power loads

To replicate normal operating conditions in gearbox modeling, it is important to represent the loading conditions on the gears accurately. This involves driving the pinion with a motor at a specific rotational speed while applying an opposing torque to the output wheel using a reducer. The connection between these elements and the shaft needs to be properly represented, and one common way to assess this connection is through the use of a connecting torsional stiffness.

Torsional stiffness describes the resistance to torsional deformation at the connection point between the driving element and the shaft. By incorporating torsional

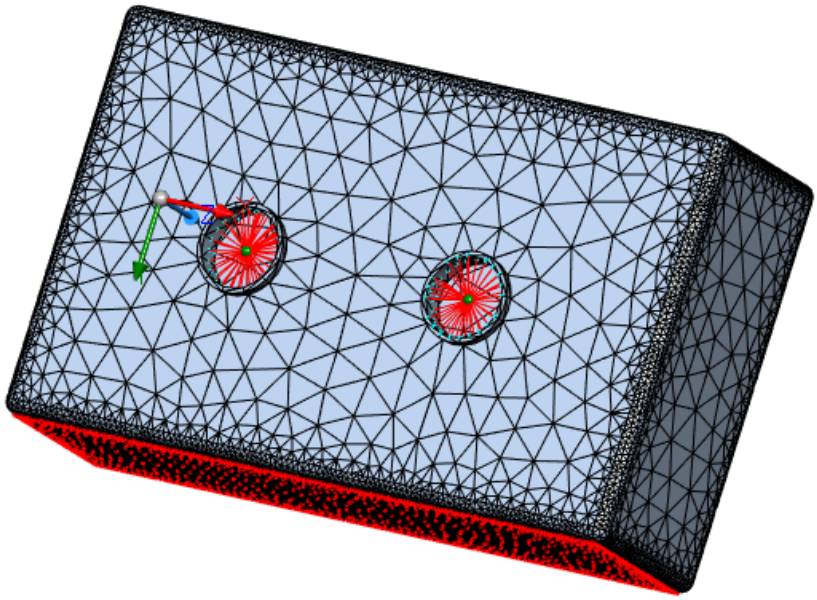

Figure 3.5: Graphical representation of the reduced housing model.

stiffness, the model can simulate the stiffness characteristics of the load and its effect on the torque transfer within the system. A higher torsional stiffness indicates a stiffer load, which can result in improved torque transfer efficiency, reduced torsional deformation, and less backlash in the load.

However, it is important to note that introducing torsional stiffness can influence the modal behavior of the system. Therefore, it is crucial to select a torsional stiffness that matches the requirements of the system to avoid any unwanted resonances.

In the context of a numerical study, where the primary focus may not be on power load stiffness, it's common to adopt a default value for torsional stiffness provided by the software. This default value, often set at $1e9N.m/rad$, is considered relatively rigid. It ensures effective load transfer, improved alignment and positioning, minimized torsional backlash, and the absence of resonance-related issues. These attributes have been validated through extensive numerical simulations.

By maintaining an appropriate level of torsional stiffness, the numerical study accurately reflects the system's behavior under typical operating conditions. This ensures efficient torque transmission, reduced deformations, and stable operation while avoiding any undesired resonance-related challenges.

3.2.6 Modeling of the meshing excitation

The interaction between gears in the gearbox is represented by the meshing stiffness, which governs the contact coupling between the gears. Detailed formulation specifics

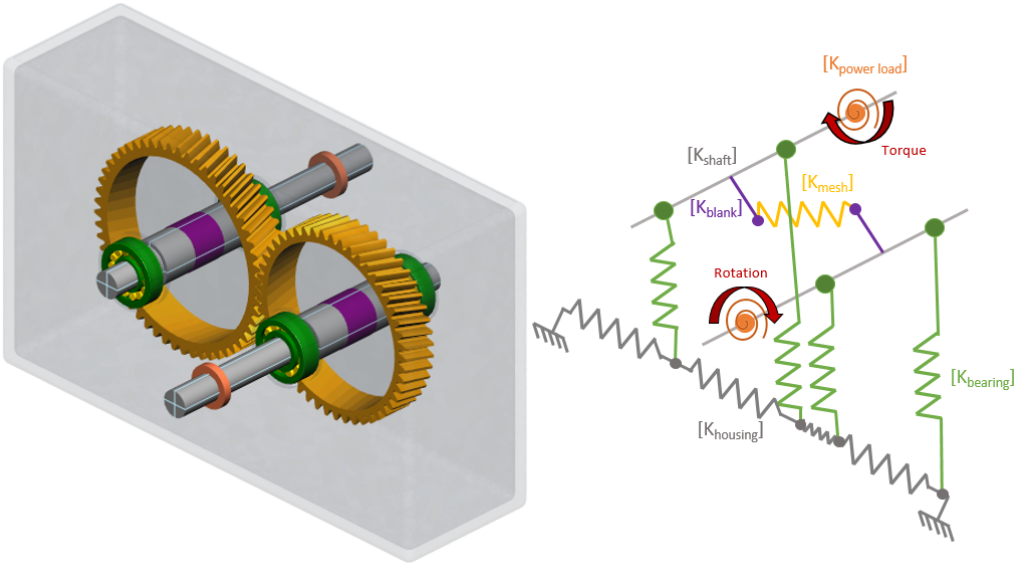

Figure 3.6: Dynamic model scheme after assembling the component stiffnesses.

of this meshing stiffness can be found in Chapter I. Depending on the type of analysis being conducted (static or quasi-static), the meshing stiffness can either be time-invariant or time-variant. Similar to the bearing, the mesh force is linearized around the applied load condition using a first-order Taylor-Young expansion as follows:

$$\mathbf{F}_L \approx \mathbf{F}_{NL}(\mathbf{x_s}) + \frac{\partial \mathbf{F}_{NL}}{\partial \mathbf{x}}(\mathbf{x}_s, t)(\mathbf{x}(t) - \mathbf{x}_s(t)) \tag{3.5}$$

where $\mathbf{x}$ contains the generalized displacement of each degree of freedom, and $\mathbf{x_s}$ verifies the static equilibrium condition:

$$\mathbf{K}\mathbf{x}_s + \mathbf{F}_{NL}(\mathbf{x}_s) = \mathbf{F}_s \tag{3.6}$$

where $F_{NL}(x_s)$ represents the non-linear mesh force that is quasi-statically-calculated for the transmitted load $\mathbf{F}_s$ in equation 1.10.

It is worth noting that the model does not take into consideration the impact of lightweight components on the frictional properties of the contact. This is due to the belief that these lightweight components have little to no influence on the frictional behavior within the contact.

3.2.7 Solving the linearized dynamic model

With the established stiffness matrices of the system components, all that is left is to assemble them through the proper connection points as shown in figure 3.6.

The linearized system equation of motion taking into account the inertial, elastic, meshing, and external forces can be written in the form:

$$\mathbf{M}\ddot{\mathbf{x}} + \mathbf{K}\mathbf{x} + \mathbf{F}_L = \mathbf{F}_s \tag{3.7}$$

where $\mathbf{M}$, and $\mathbf{K}$ are respectively the mass and stiffness matrices of the system. By introducing equations 3.12 and 3.6 into the equation of motion we obtain:

$$\mathbf{M}\ddot{\mathbf{x}} + \mathbf{K}(\mathbf{x} - \mathbf{x}_s) + \frac{\partial \mathbf{F}_{NL}}{\partial \mathbf{x}}(\mathbf{x} - \mathbf{x}_s) = 0 \tag{3.8}$$

In the context of a gearbox, the main excitation is the TCA-calculated static transmission error which is introduced as a displacement within LOA can be introduced in the global coordinates through the use of the previously defined geometrical vector $\mathbf{G}$ in Equation 1.3:

$$\delta_s(t) = \mathbf{G}^T \mathbf{x}_s(t) \tag{3.9}$$

In a similar fashion, the dynamic transmission error which represents the linear displacement in the LOA as a response to the STE excitation at different frequencies can be expressed as:

$$\delta_d(t) = \mathbf{G}^T \mathbf{x}(t) \tag{3.10}$$

The components of the developed non-linear dynamic mesh force $\mathbf{f}_{nl}$ developed along the line of action can be expressed in the global coordinates as:

$$\mathbf{F}_{NL} = \mathbf{G} f_{nl}(\mathbf{G}^T x) = \mathbf{G} f_{nl}(\delta_d) \tag{3.11}$$

The linearized mesh force in Equation 3.12 can be written with the help of Equations 3.11, 3.9, and 3.10 as:

$$\mathbf{F}_L \approx \mathbf{G} f_{nl}(\delta_s) + \mathbf{G}\mathbf{G}^T \frac{\partial f_{nl}}{\partial \delta_s}(\mathbf{x} - \mathbf{x}_s) \tag{3.12}$$

Knowing that the derivative of the transmitted mesh force f_{nl} with respect to the static transmission error δ_s represents the meshing stiffness, the gearbox equation of motion without damping becomes:

$$\mathbf{M}\ddot{\mathbf{x}} + \mathbf{K}(\mathbf{x} - \mathbf{x}_s) + [\mathbf{G}\mathbf{G}^T k_m(t)](\mathbf{x} - \mathbf{x}_s) = 0 \tag{3.13}$$

Considering that the mesh stiffness $k_m(t)$ can be decomposed into a non-zero mean component $\bar{k_m}$ and a fluctuating component $g(t)$, The equation of motion can be written as:

$$\mathbf{M}\ddot{\mathbf{x}} + \mathbf{K}(\mathbf{x} - \mathbf{x}_s) + \bar{\mathbf{K}}(\mathbf{x} - \mathbf{x}_s) + [\mathbf{G}\mathbf{G}^T g(t)](\mathbf{x} - \mathbf{x}_s) = 0 \tag{3.14}$$

with:

$$\bar{\mathbf{K}} = [\mathbf{G}\mathbf{G}^T \bar{k_m}(t)] \tag{3.15}$$

Considering the current modeling capabilities of the gear analysis software being used, it is important to note that the meshing stiffness only considers the mean component while disregarding the fluctuating component. This limitation implies that

the software may not accurately handle the phenomena of parametric resonances and instabilities, which can occur due to the time-varying nature of the stiffness.

To explore the impact of the fluctuating mesh stiffness, we conducted experiments on a single-stage gearbox design. The mesh stiffness was varied within an interval obtained from a tooth contact analysis. The observed amplitude and frequency of the dynamic response showed no significant differences when compared to using a constant stiffness. This finding suggests that it might be possible to simplify the analysis by eliminating the time-varying component and employing a constant stiffness value. By doing so, the calculations can be facilitated and computational complexity reduced.

However, it is crucial to emphasize that this simplification should be considered on a case-by-case basis. The observed results are specific to the tested single-stage gearbox design. More complex gearbox designs with increased degrees of freedom may exhibit different behaviors, and the time-varying component of the mesh stiffness could have a more pronounced effect. Therefore, caution should be exercised when generalizing these findings to other gearbox configurations.

Considering this assumption, the equation of motion becomes:

$$\mathbf{M}\ddot{\mathbf{x}} + \mathbf{K}(\mathbf{x} - \mathbf{x}_s) + \bar{\mathbf{K}}(\mathbf{x} - \mathbf{x}_s) = 0 \tag{3.16}$$

By using the modal transformation $\mathbf{x} = \mathbf{\Phi q}$ and solving the time-averaged eigenvalue problem it is possible to obtain the modal and spectral matrices Φ and Ω containing the eigenvectors (ϕ_i) and natural frequencies (ω_i) respectively. The modal extraction is achieved using the Lanczos method [82] which is memory-efficient and suitable for treating large sparse matrices.

$$|\mathbf{K} + \bar{\mathbf{K}} - w^2\mathbf{M}|\Phi = 0 \tag{3.17}$$

At this stage, a modal damping matrix $\mathbf{C}$ can be constructed from the obtained modal data such that:

$$\mathbf{C} = \mathbf{\Phi D \Phi}^T \tag{3.18}$$

Where $\mathbf{D}$ contains the damping coefficients associated with each mode of vibration.

By integrating the modal damping matrix into the equation of motion, which is mass-normalized and projected onto the modal basis, the resulting diagonal matrices yield a series of decoupled equations for each vibration mode within the modal model. Consequently, these equations can be independently solved for each mode, allowing for a simple and fast modal analysis:

$$\mathbf{I}\ddot{\mathbf{q}} + \mathbf{C}\dot{\mathbf{q}} + \mathbf{K}^{av}(\mathbf{q} - \mathbf{q}_s) = 0 \tag{3.19}$$

with: $\mathbf{I} = diag(1)$, $\mathbf{C} = diag(2\zeta_j\omega_j)$, and $\mathbf{K}^{av} = diag(\omega_j^2)$.

The matrix $\mathbf{K}^{av}$ represents the global time-averaged stiffness matrix, incorporating both the stiffness contributions from ancillary components and the time-averaged

meshing stiffness. In our simulations, a uniform modal damping of 5% was assigned to all modes within the desired operating range, utilizing a damping coefficient value of $\zeta_j = 0.05$.

It is crucial to acknowledge that while this simplified damping approach serves its purpose, it may not comprehensively capture the true damping characteristics of the system. To accurately represent the system's damping behavior, a more intricate damping model might be necessary, presenting a considerable challenge. Additionally, it would be interesting to establish the damping matrix with the help of an experimental investigation. Nevertheless, in the context of this numerical study, we have chosen to employ this approximation as a practical solution.

For clarity convenience, it is useful to express Equation 3.19 as follows:

$$\mathbf{I}\ddot{\mathbf{q}}(t) + \mathbf{C}\dot{\mathbf{q}}(t) + \mathbf{K}\mathbf{q}(t) + \bar{\mathbf{K}}\mathbf{q}(t) = \mathbf{K}^{av}\mathbf{q}_s(t) \tag{3.20}$$

Through knowledge of the ancillary stiffness $\mathbf{K}$ and average stiffness $\bar{\mathbf{K}}$ that is calculated with the help of one of the TCA tools mentioned in the previous chapter, the right-hand side of the equation representing the external forces can be calculated.

Knowing all the inertial, damping, and stiffness properties of the system, all that is left is to solve for the displacement, velocity, and acceleration quantities denoted as $\mathbf{q}(t)$, $\dot{\mathbf{q}}(t)$, $\ddot{\mathbf{q}}(t)$ respectively. However, solving this type of problem in the time domain is computationally costly as it usually requires the use of time integration methods that necessitate several iterations to give accurate results. Therefore, solving the problem in the frequency domain presents a more convenient alternative that can be achieved using a Fast Fourier Transform. Since it is not possible to numerically solve an infinite sum, it is necessary to establish the FFT decomposition in a truncated frequency range containing a specified number of harmonics N_H. The sought frequency domain solution can be written in the form:

$$\mathbf{q}(t) \approx \sum_{k=1}^{N_H} (\mathbf{a}_k \cos(k\omega t) + \mathbf{b}_k \cos(k\omega t)) \tag{3.21}$$

Applying the Fourier to all the components of the equation, the frequency domain equation of motion becomes:

$$H_j^{-1}(\omega) Q_j(\omega) = F_j(\omega) \tag{3.22}$$

with $H_j(\omega)$ representing the modal frequency response function for the j^{th} mode.

$$H_j(\omega) = \frac{1}{(\omega_j^2 - \omega^2 + 2i\zeta_j\omega_j\omega)} \tag{3.23}$$

This equation is solved for $\mathbf{Q}(\omega)$ to obtain the frequency response of the system. The obtained frequency domain solution can be reconverted to the time domain response $\mathbf{q}(t)$ using the inverse FFT. From the time domain response, the modal coordinates can be extracted for each mode of vibration, which can be accomplished using the method of Singular Value Decomposition (SVD) [74].

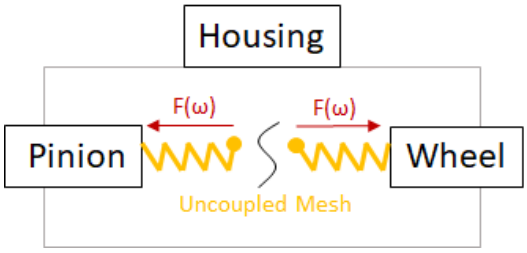

Figure 3.7: Schematic of the pinion and wheel side mesh level uncoupling.

In a geared system, the external excitation is translated into the linear compression and decompression of the meshing stiffness spring ($\bar{\mathbf{K}}$) positioned along the line of action. The frequency of this event is linearly related to the rotational speed of the gears as depicted in Equation 1.6. However, when the frequency of excitation matches the resonance frequencies of the system, an amplification of the dynamic response can be witnessed. Depending on the excited modes which can be associated with vibrations of the different components, some of these modes, are more susceptible to amplifying the displacement in the LOA and therefore cause peaks in the dynamic transmission error which could contribute to high dynamic mesh forces.

The assessment of the dynamic mesh force can be done via an uncoupled analysis [23] in which the dynamic interactions between the gears are neglected which is done by omitting the mesh stiffness as shown in Figure 3.7. The gears could still remain coupled through the housing structure. Solving the eigenvalue problem, in this case, yields the uncoupled modes.

By applying a unit force at both sides of the meshing and measuring the mesh node displacement along the line of action, the pinion and wheel side compliances can be summed up together to construct the mesh compliance $C_{mesh}(\omega)$:

$$C_{mesh}(\omega) = (C_p(\omega) + C_w(\omega)) \tag{3.24}$$

From which we can obtain the dynamic mesh stiffness $D(\omega)$:

$$D_{mesh}(\omega) = (C_{mesh}(\omega))^{-1} \tag{3.25}$$

The transmitted frequency-dependant dynamic mesh force $F_{mesh_k}(\omega)$ can be obtained for each harmonic δ_{s_k} of the static transmission error.

$$F_{mesh_k}(\omega) = D_{mesh}(\omega)\delta_{s_k} \tag{3.26}$$

The analysis of the dynamic mesh forces in a gearbox provides valuable insights into the behavior of the system's modes. To understand this, let's consider a pair of meshing gears. These compliances describe the movement of the mesh node along the line of action which can be characterized by an amplitude and a phase that vary depending on the prevailing modal behavior.

Based on these considerations, several scenarios can arise:

- Case of same phases regardless of the side compliances: In this scenario, both ends of the meshing spring, representing the contacting gear flanks, exhibit a "Precede" and "Follow" making the meshing spring appear in a synchronous motion. This prevents the tension and compression of the spring and therefore the development of significant mesh forces that would increase the vibrational levels of the gearbox.

- Case of opposite phases and different compliances: Here, the spring undergoes a compression and decompression motion. However, due to the difference in compliance between the pinion and wheel sides, one side experiences more strain than the other. As a result, the mesh force is relieved, reducing the potential for excessive forces or vibrations.

- Case of opposite phases and equal compliances: Similarly to the previous case, the spring undergoes tension and compression. The only difference is that this time, both sides will resist the motion comparably due to equal compliances leading to the development of substantial meshing forces. This condition corresponds to the occurrence of response peaks in a dynamic mesh force plot.

In the context of an uncoupled analysis, accurately capturing the modal characteristics can be challenging as it disregards the dynamic interactions between the gears. As a consequence, the damping matrix in Equation 3.18 is constructed based on the derived uncoupled modes.

To achieve enhanced dynamic accuracy, it is preferable to solve the coupled problem, which takes into account the dynamic interactions between the gears. This approach has the potential to alter the dynamics and provide a better description of the coupling between different modes. Consequently, the damping matrix derived from the coupled modes will exhibit slight differences compared to the one in the uncoupled case.

In this research, the decision was made to adopt and implement the coupled problem to obtain more precise results. This decision acknowledges the vital importance of considering the interactions between the gears in accurately characterizing the modal behavior, mode shapes, and dynamic response of the gearbox system.

3.3 Benchmarking study of the dynamic models in ROMAX and MASTA

The aim of this section is to conduct an initial evaluation of the similarity between the dynamic models represented by ROMAX and MASTA. It is important to acknowledge that both software packages are conceptually based on the same linearized dynamic model discussed earlier. However, due to the intricate details and formulations used to describe component stiffnesses, deviations can arise in the system's equation of motion.

In a comprehensive dynamic response analysis, the process typically begins with a tooth contact analysis to determine the transmission error. This information is then fed into the dynamic system. Variability in the response may stem from both the tooth contact analysis and the formulation of the dynamic system. Therefore, we propose three types of analyses for the benchmark as follows:

- Case of a calculated mesh stiffness and a unit TE excitation: This analysis decouples the dynamic model from the excitation, establishing a stable baseline for comparison. It allows us to assess the inherent differences between ROMAX and MASTA in the absence of excitation variability.
- Case of fixed meshing stiffness and calculated transmission error: Similar to the previous case, this analysis decouples the excitation from the influence of the dynamic model. Here, we focus solely on the discrepancies resulting from deviations in the LTCA calculations. Other discrepancies related to bearings, shafts, and housing are expected to be present.
- Case of calculated mesh stiffness and transmission error: This analysis provides a comprehensive view of the dynamic analysis using both software packages. It accounts for the coupled effects of the dynamic model and excitation, giving us a complete understanding of the discrepancies and similarities between ROMAX and MASTA.

3.3.1 Impact of a unit transmission error on the dynamic response of a single Stage Gearbox with a calculated mesh stiffness

For the purpose of this analysis, a simplified gearbox model was built based on the above-mentioned modeling methodologies. We have implemented the same gear pair as in table 4.1 with the 5μm tip relief. Given the academic nature of this study, the system was analyzed over a speed range of $15,000RPM$, corresponding to an operating range of $12.5kHz$, to cover differences in an extended range of frequencies, including high-frequency modes. To ensure convergence of the dynamic response and account for any modes present outside the operating range, we considered system modes up to double the frequency range of interest ($25kHz$), as only the first meshing harmonic was of interest at this stage.

The selection of the condensation frequency for the dynamic analysis of the housing depends on the specific objectives of the study. In our investigation, we aimed to understand the influence of the first three meshing harmonics. Hence, we determined the condensation frequency to cover up to three times the fundamental frequency, resulting in a value of $37.5kHz$. It is worth noting that this frequency range significantly exceeds the audible frequency range, making it practically irrelevant for acoustical assessment.

In practical terms, if we were to consider A-weighting, which takes into account the human ear's sensitivity to different frequencies, we would expect noise to peak around $2.5kHz$ and become less perceptible above $10kHz$. This observation confirms

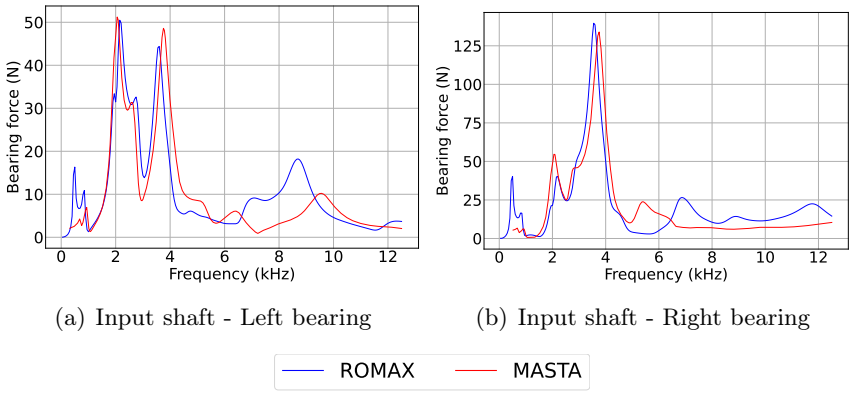

(a) Input shaft - Left bearing (b) Input shaft - Right bearing

Figure 3.8: Development of the bearing forces in ROMAX and MASTA

that the condensation within the original operating frequency range was more than sufficient for the acoustic assessment conducted in this study."

During the coupled modal analysis with a linearized reduced model, discrepancies were observed in the number of modes within the operating frequency range. ROMAX detected 95 modes, while MASTA identified only 89 modes, with an average frequency error of approximately 3.8%. These differences indicate variations in the mathematical model, as well as the number of degrees of freedom in each system, influenced by default meshing settings.

Moreover, while analyzing the bearing stiffnesses obtained from static equilibrium, we observed additional inconsistencies impacting the generation of bearing forces. Figure 3.8 illustrates this issue, with only the input shaft bearings represented due to the gearbox's symmetry. To isolate the bearing effects, we employed the ISO mesh stiffness value for both software tools during the calculation of bearing stiffness. The disparities in these calculations might arise from the complexity of the bearing contact algorithm, which remains undisclosed, as well as slight variations in the bearing microgeometry specifications, defined differently in each software library.

To further investigate and comprehend the observed discrepancies, we performed an analysis of the dynamic frequency-dependent transmission error. Our focus was particularly on examining the outcomes of excitation resulting from a unit transmission error, as illustrated in Figure 3.9. This analysis aimed to uncover the fundamental factors that contribute to the observed variations in the system's behavior.

When comparing the dynamic response trends of MASTA and ROMAX using the ISO-6336 derived stiffness, they show a minor difference that could be attributed to small errors in the calculation of the ISO mesh stiffnesses, as outlined in Table 3.1. Furthermore, it is worth considering that the overall determination of component stiffnesses could also contribute to these variances.

When the stiffness is calculated using higher accuracy contact analysis methods (i.g. the Weber and FE approaches), the disparities between MASTA and ROMAX become more apparent. Specifically, in the MASTA plot, a noticeable leftward shift of around $700Hz$ is observed due to the lower stiffness in comparison to the ISO-

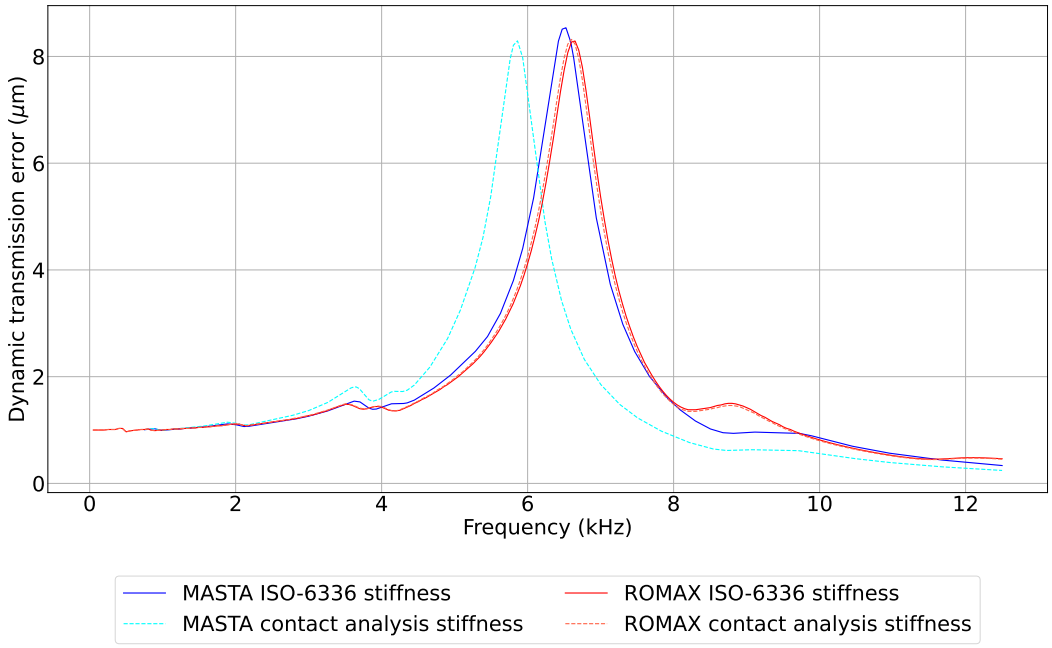

Figure 3.9: Dynamic transmission error for one unit of transmission error

calculated stiffness. Conversely, for ROMAX, the variation between both methods is slight, which justifies the alignment of the ROMAX plots.

Upon investigating the Operating Deflected Shapes Operating Deflected Shapes (ODS) at the main peak frequencies, we observed a similar deflection behavior to that shown in Figure 3.10. Additionally, an analysis of the kinetic and potential energy distribution revealed a higher concentration of energy in the shafts compared to the housing. This finding suggests that the dynamics of the shafts are the primary contributors to the displacement along the line of action at the peak frequency.

This can be further verified by examining the modal flexibility of the system which is a useful measure of the likelihood of a particular mode being excited by the transmission error at a given excitation frequency. Our analysis revealed that the 68th mode, governed by a bending behavior of the shafts, contributes the most to the ODS in ROMAX, whereas the 61th mode in MASTA was found to be the dominant contributor. This difference can be attributed to small variations in the solutions of the eigenproblem for both models, as previously noted.

In conclusion, the comparison between the ISO-6336-derived stiffness and the contact analysis stiffness reveals important insights regarding the accuracy and fidelity of the dynamic response models. While the ISO-6336-derived stiffness can provide a reasonable estimate of the dynamic response trends in tools like MASTA and ROMAX, it is recommended to use the more accurate contact analysis stiffness for a higher level of fidelity.

The variability observed in the dynamic response, particularly when different TCA methods or software are employed, underscores the sensitivity of a dynamic

	ISO-6336 stiffness	Contact Analysis stiffness
ROMAX	4.4e8 N/m	4.25e8 N/m
MASTA	4.1e8 N/m	3.2e8 N/m

Table 3.1: Summary of the calculated meshing stiffness values

model to the calculation of the meshing stiffness. The meshing stiffness plays a critical role in determining the dynamic behavior of the system, and accurately representing it is essential for obtaining reliable results.

3.3.2 Influence of the calculated transmission error on the dynamic response of a single-stage gearbox considering a fixed meshing stiffness

While the initial study provided valuable insights into evaluating the similarity of dynamic models under a unit excitation, our aim was to delve deeper into the impact of variations in transmission error calculation on dynamic response outcomes. To accomplish this objective, the FFT of the calculated STE in Figure A.6 was used to decompose the signals and construct the harmonic content associated with each software as shown in Figure 3.13. Specifically, we focused on the first three harmonics, which were used to excite the dynamic system and analyze its response.

The spectral analysis of the transmission error from different software revealed significant inconsistencies. These inconsistencies were observed in both the individual harmonic amplitudes, which were influenced by the overall amplitude of the transmission error, and the distribution of amplitudes among these harmonics which relates to the general shape of the STE plot.

To highlight the impact of these discrepancies, we scaled the dynamic mesh force plot obtained for a unit of transmission error by the amplitudes of the first three harmonics of the transmission error. The resulting responses are summarized in Figure 3.12 effectively illustrating the dynamic variations resulting from different estimations of STE.

For instance, the GENOM FE model registered the highest responses due to its excitation magnitude surpassing that of the other models. Furthermore, comparing the responses of ROMAX and GENOM Weber, we observed a difference in the emphasis placed on specific harmonics. ROMAX assigned higher importance to the response due to the first harmonic and to a lesser extent to the second and third harmonics. On the other hand, GENOM Weber showed a higher amplification in response to the second and third harmonics. In practical terms, if the objective is to optimize the reduction of the maximum dynamic response, different strategies should be considered. For ROMAX, the focus should be on the lower RPM range associated with the first harmonic (around $2,400$ RPM). In contrast, for GENOM Weber, attention should be directed toward the higher RPM ranges associated with the second and third harmonics (around 3500 and 7000 RPM).

Overall, this analysis further underscores the linear relationship between the ex-

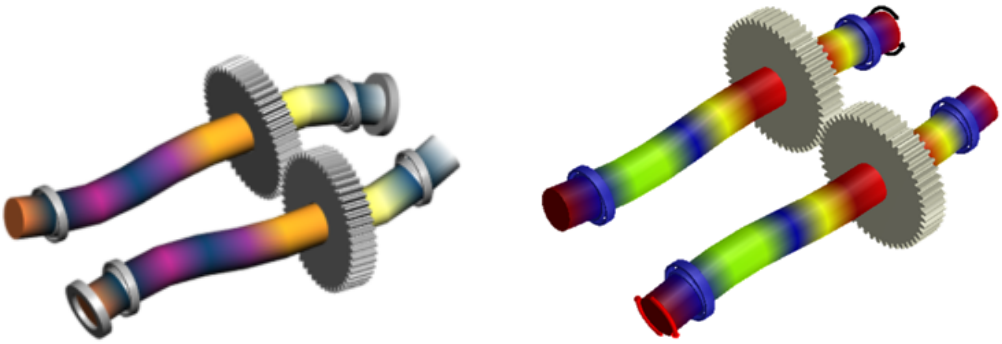

(a) MASTA Components ODS

(b) ROMAX Components ODS

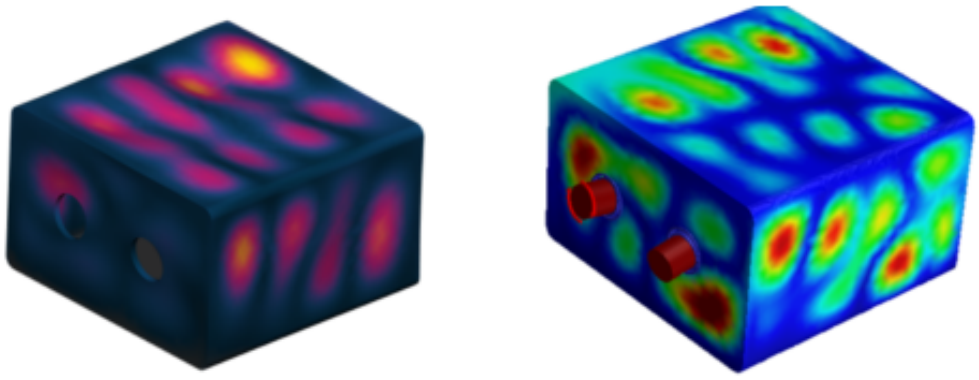

(c) MASTA Housing ODS

(d) ROMAX Housing ODS

Figure 3.10: Graphical representation of the operating deflected shapes at the main peak frequencies

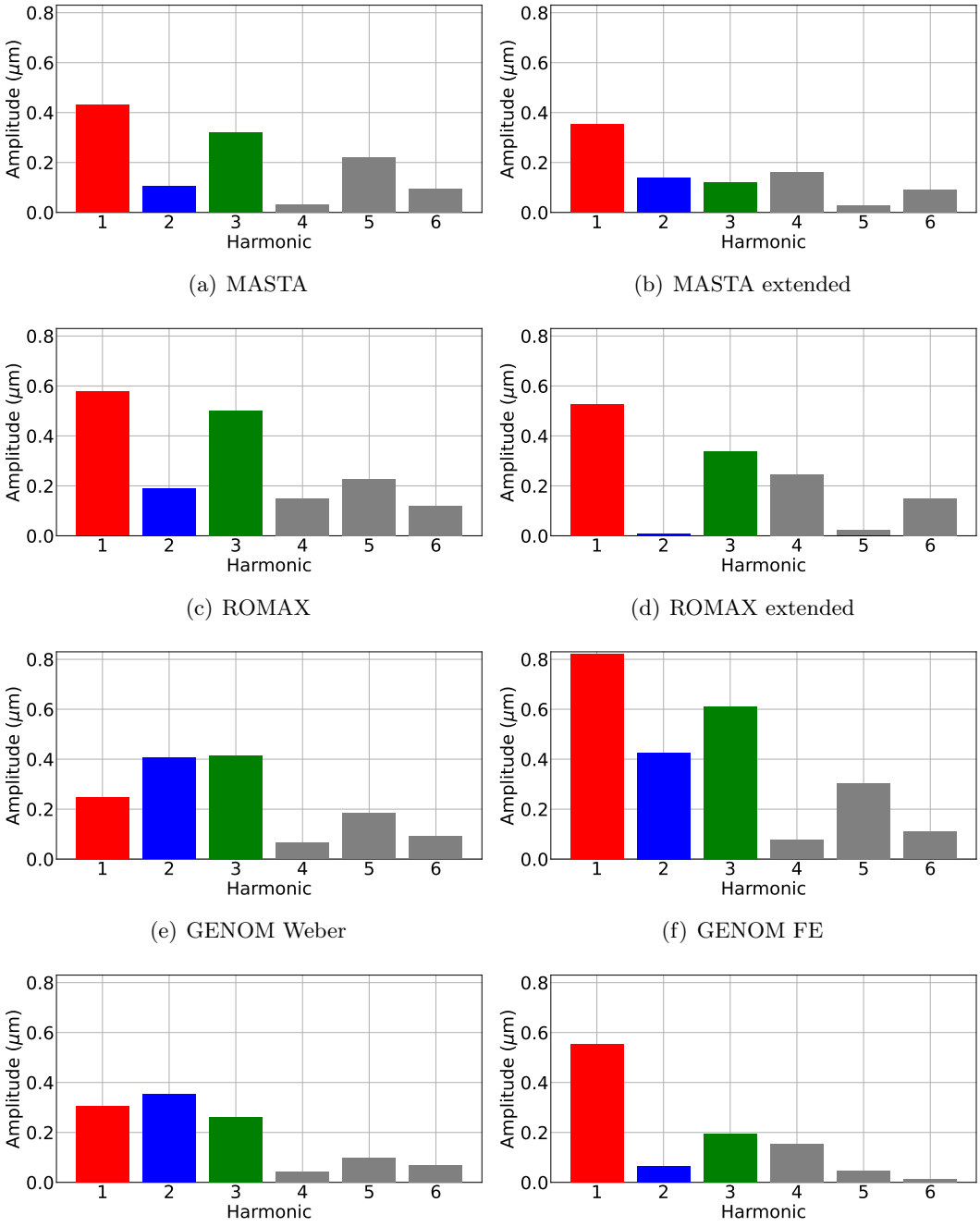

(a) MASTA

(b) MASTA extended

(c) ROMAX

(d) ROMAX extended

(e) GENOM Weber

(f) GENOM FE

(g) VIBRAGEAR

(h) ANSYS

Figure 3.11: Harmonics of the calculated static transmission error using the different software.

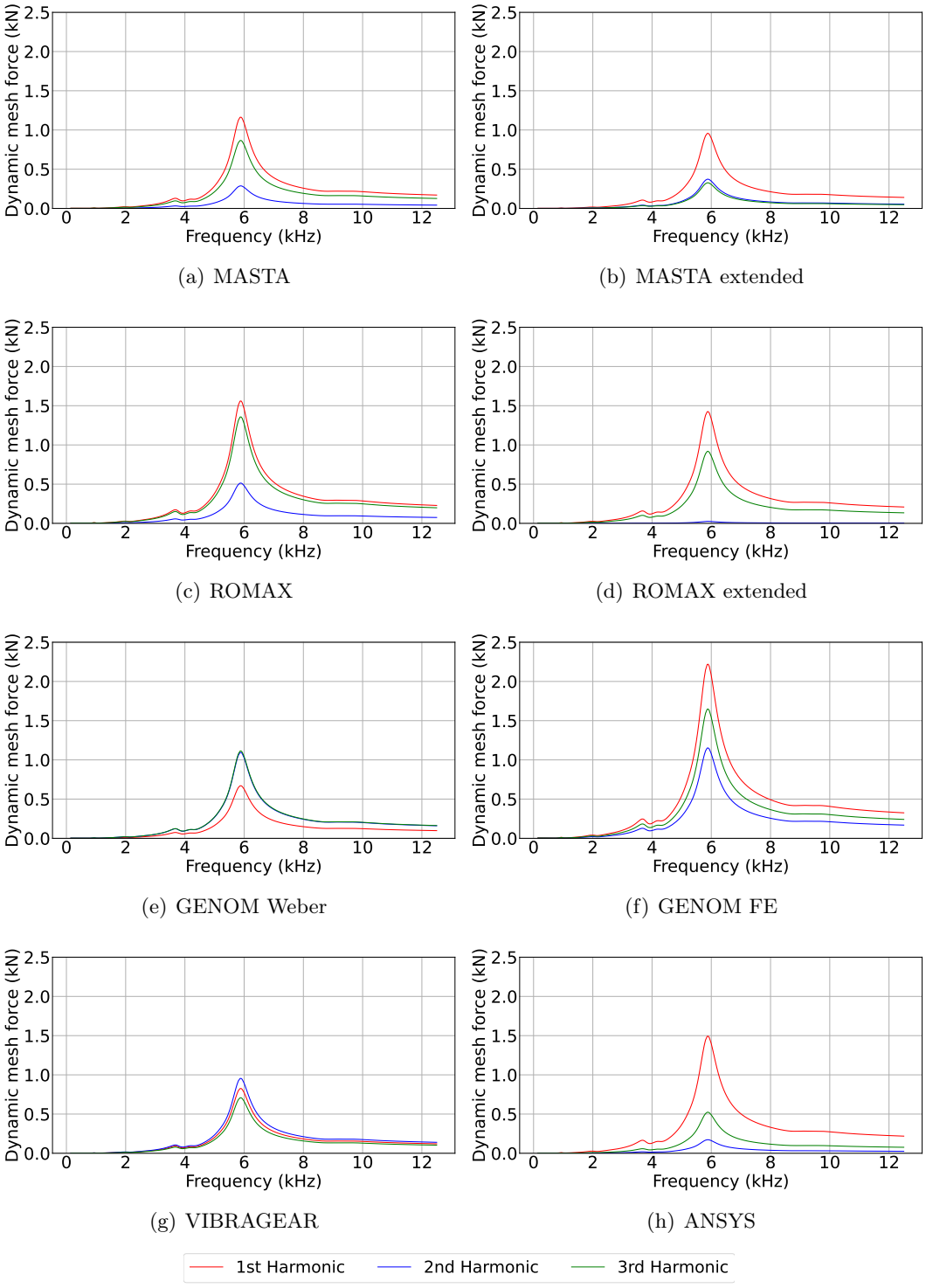

(a) MASTA (b) MASTA extended

(c) ROMAX (d) ROMAX extended

(e) GENOM Weber (f) GENOM FE

(g) VIBRAGEAR (h) ANSYS

Figure 3.12: Visualization of the dynamic mesh forces resulting from the first three harmonics of STE as obtained by the different LTCA tools.

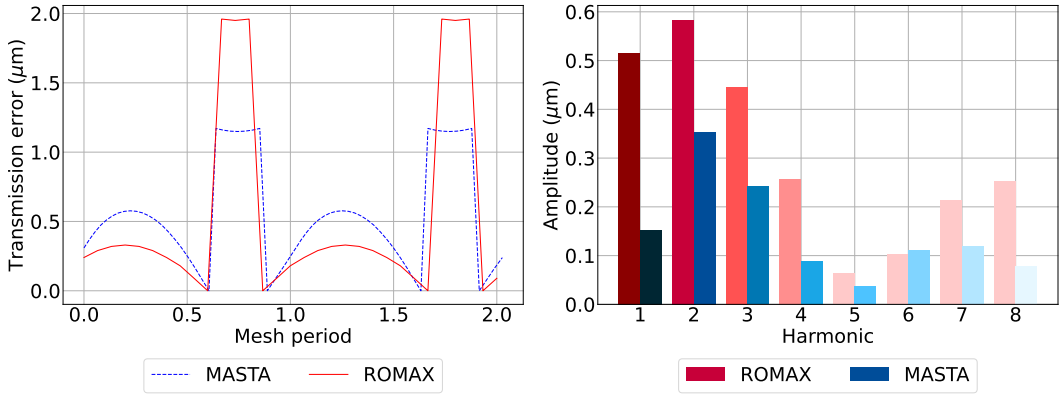

(a) Static transmission error

(b) Harmonic content

Figure 3.13: Trace and harmonics of the calculated static transmission error.

citation and the resulting dynamic response of a gearbox and therefore its sensitivity to variations in the TCA input data that could potentially influence the outcome of the design and optimization process.

3.3.3 Effect of the calculated transmission error on the dynamic response of a single Stage gearbox considering a calculated Meshing Stiffness

After evaluating the isolated effects of stiffness and excitation variations, we decided to conduct an analysis combining the effects of the mesh stiffness and STE variations which would normally represent the realistic outcome of each software treating the same transmission design case. For this purpose, the excitation not considering a tip relief was used as represented in Figure 3.13.

The results depicted in Figure 3.14 encapsulate the combined influence of varying mesh stiffnesses and excitations, manifesting in observable shifts in peak frequencies, response amplitudes, and the relative significance of different harmonics.

3.3.4 Influence of microgeometry modifications on the dynamic response

The linear scaling of the dynamic response by the harmonic amplitudes of the transmission error suggests that improving the response can be limited to the reduction of the excitation's amplitude which is one reason why microgeometry optimizations are sought in geared systems. These types of modifications relocate contact regions closer to the center of tooth flanks and farther from edges, reducing stress distribution on the tooth flanks and increasing gear lifespan while minimizing transmission error. An optimized microgeometry produces spectral content with lower-amplitude harmonics than the reference case, which automatically implies a reduction of meshing forces.

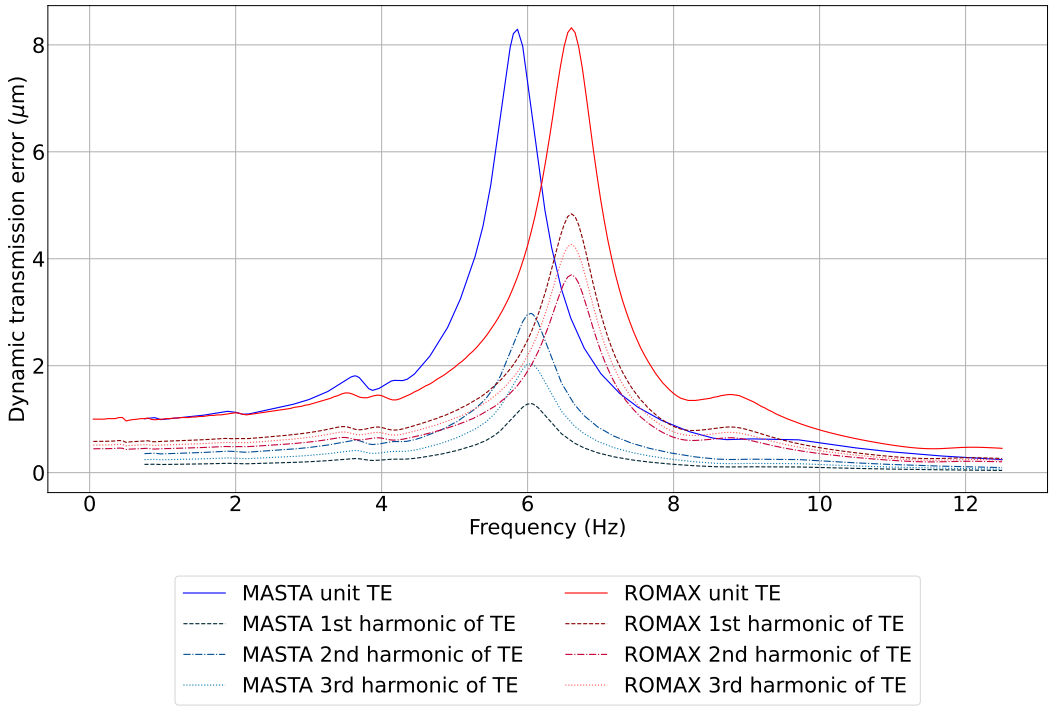

Figure 3.14: Dynamic transmission error for the first three harmonics of TE using ROMAX and MASTA

To validate the causal relationship described, the dynamic outcomes of the two-stage gearbox presented in Section 2.4.3 were examined using the corresponding LTCA data. The results, as shown in Figure 3.15, demonstrate a clear proportionality between the excitation's first harmonic and the resulting response, affirming the linear scaling effect.

Although the software programs generate different orders of magnitude for the responses, the relative improvement percentage between the non-optimized and optimized cases remains consistent. In this particular study, we observed a relative improvement of 70% in MASTA and 58% in ROMAX which corresponds to the same improvement percentage of the excitation. This further emphasizes the dependency of the dynamic analysis results on the type of software that is used. In other words, a different response can be obtained for different software. Additionally, if the objective is to change the response by a certain percentage, it is likely that the implemented tools would result in variations in the suggested microgeometry modifications.

Upon analyzing the deflected shapes of the system at the frequencies of the main peaks, namely $7.1KHz$ and $8.4KHz$, as shown in Figure 3.16, we observe a good degree of similarity in the deflection behavior, with the shaft modes appearing to contribute most significantly. Despite this similarity, there are some variations between the results obtained from MASTA and ROMAX. Specifically, MASTA exhibits a higher amplitude for the first peak, while ROMAX shows a con-

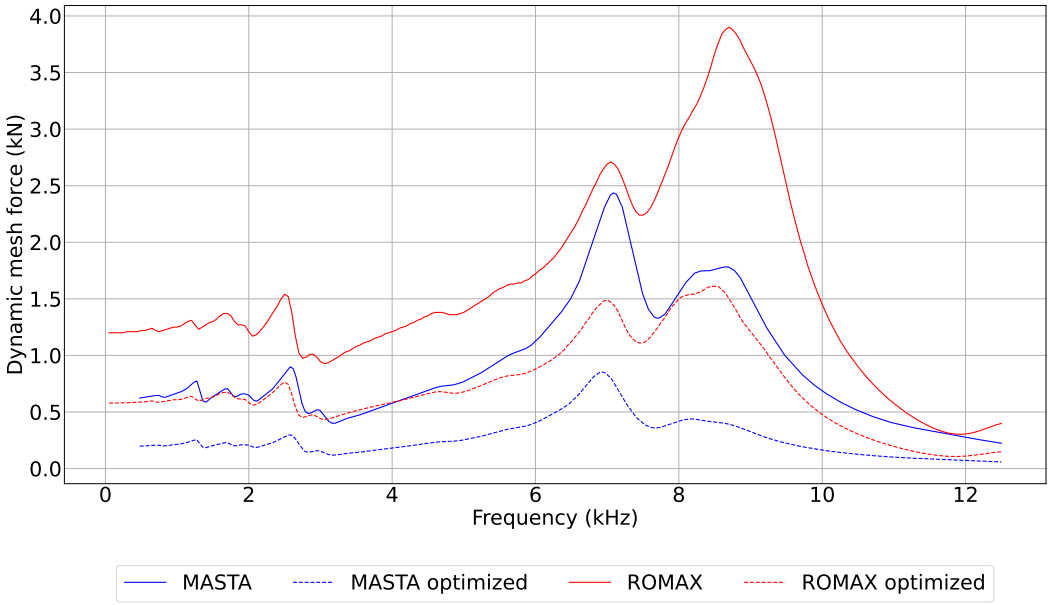

Figure 3.15: Dynamic transmission error in the case of an optimized microgeometry excited by the first harmonic of transmission error

siderably higher amplitude for the second peak. This discrepancy further highlights the hypersensitivity of the dynamic model to the variations in the determination of component stiffnesses, such as those of the gears and bearings. As the model grows in complexity, the stacking of these discrepancies becomes increasingly important and could potentially influence the modal distribution of the system.

3.3.5 Effect of introducing finite element components

So far, all the analyses performed have employed gearbox models in which the shafts and gear blanks were modeled using Timoshenko beam elements. This approach treats the gear blank as an extension of the shaft diameter up to the base diameter of the gear, treating them as a single entity. While the Timoshenko method is known for its efficiency and accuracy in most cases, it has certain limitations, especially when dealing with lightweight gears. When the mass of gears is reduced by decreasing the web width or removing material, it results in increased flexibility and a greater risk of out-of-plane motion, which cannot be adequately captured by Timoshenko elements.

To address this issue, we tested different gear blank modeling scenarios by combining standard and FE configurations.

It is worth noting that the tooth contact analysis does not consider the FE blank as represented in the dynamic model (i.e. what is perceived in the graphical user interface), but rather a stiffness that is established separately from the dynamic analysis. This distinction can be made by referring to Figure 3.17.

To address the issue of transmission error variations resulting from different

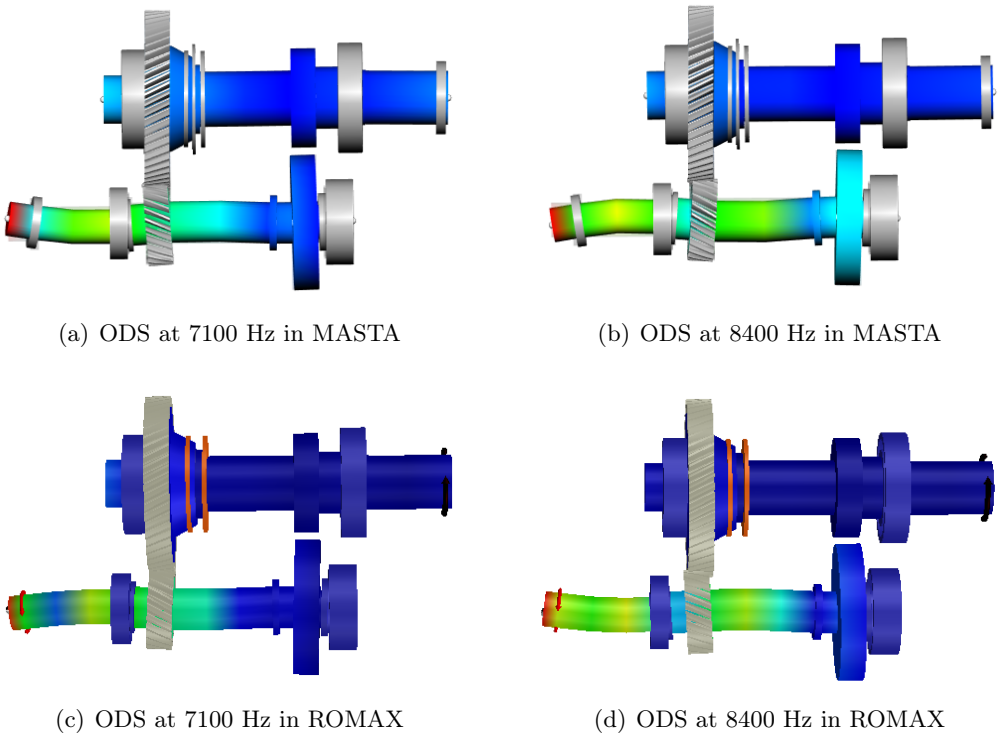

(a) ODS at 7100 Hz in MASTA

(b) ODS at 8400 Hz in MASTA

(c) ODS at 7100 Hz in ROMAX

(d) ODS at 8400 Hz in ROMAX

Figure 3.16: Visualisation of the operating deflecting shapes for the two main resonance peaks

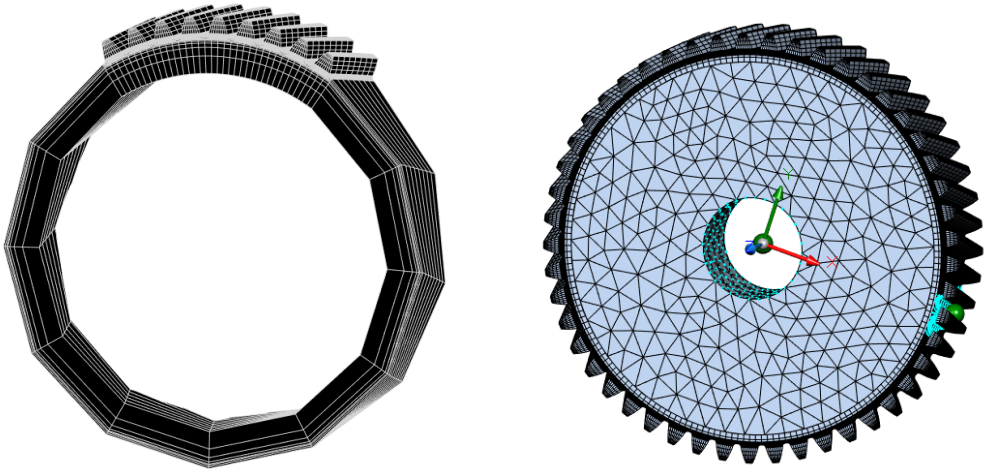

(a) Gear blank used in LTCA to estimate the STE

(b) Gear blank used in the dynamic model to estimate the dynamic response

Figure 3.17: Comparison between the blank representations used in the LTCA and the dynamic models.

blank representations in the contact analysis of ROMAX and MASTA, we conducted a dynamic analysis using a unit of transmission error. Specifically, we performed this analysis on the pinion and wheel of the two-stage gearbox previously discussed, considering various combinations of FE and Timoshenko blank models. By adopting this approach, we could focus on evaluating the impact of different blank representations on the mesh stiffness and the overall dynamic response of the system, as illustrated in Figure 3.18.

The plots demonstrate substantial variations across different combinations of blank types within the same software, as well as across the same combinations of different software packages. When replacing a Timoshenko blank with its FE equivalent, which possesses a higher number of degrees of freedom, the strain energy distribution of the system undergoes changes. These alterations provide a rationale for the observed variations in peak amplitudes and resonating frequencies.

By including an FE version of the pinion to the gearbox, The results in MASTA do not appear to be strongly affected. Conversely, ROMAX shows a significant reduction in the amplitude of the main peak accompanied by the appearance of a second peak at a higher frequency.

Replacing only the wheel with its FE analog results in a considerable amplitude reduction of the second peak in both software. Other peaks appear at the higher end of the spectrum which represent the deflection of the wheel body and teeth where the natural frequencies of such modes tend to be high relative to the rest of the system. The significant influence of the FE wheel compared to the FE pinion can be attributed to the aspect ratio of the part which reflects on the stiffness. In fact, the wheel has a high diameter-to-width ratio which generally results in a decrease in the stiffness in the axial direction making the part more susceptible to bending out-of-plane. Therefore, while the FE representation always provides a more accurate representation of the blank behavior, it is recommended to use it, especially in cases where the diameter-to-width ratio is believed to be significant. Moreover, considering that the gear blank natural frequencies are most of the time located above the rest of the components, the use of FE blanks becomes more justified as the operating frequency range increases and the modal contributions of the gears become more significant.

By using an FE pinion and wheel at once, a further reduction in the amplitude can be noticed but with the frequency of the second peak in ROMAX being lower than MASTA.

The investigation of the operating deflected shapes at the main peaks, as depicted in Figure 3.19, provides valuable insights into the underlying physics of the system. Examining the graphs reveals a clear distinction between the motion of the solid gears and their FE counterparts. The solid gears exhibit a wobbling motion while remaining perpendicular to the section they are mounted on, whereas the FE blanks exhibit a degree of out-of-plane bending.

This disparity in motion has several effects on the system. Firstly, it leads to misalignment, which represents the LOA gap created between the gears due to separating forces and the twisting of the gears. Misalignment can alter the con-

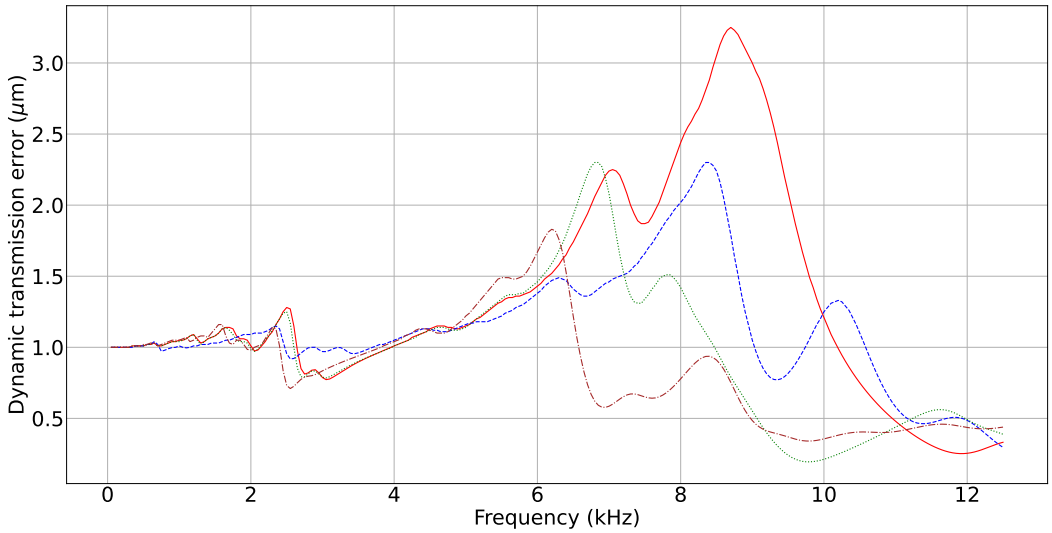

(a) ROMAX

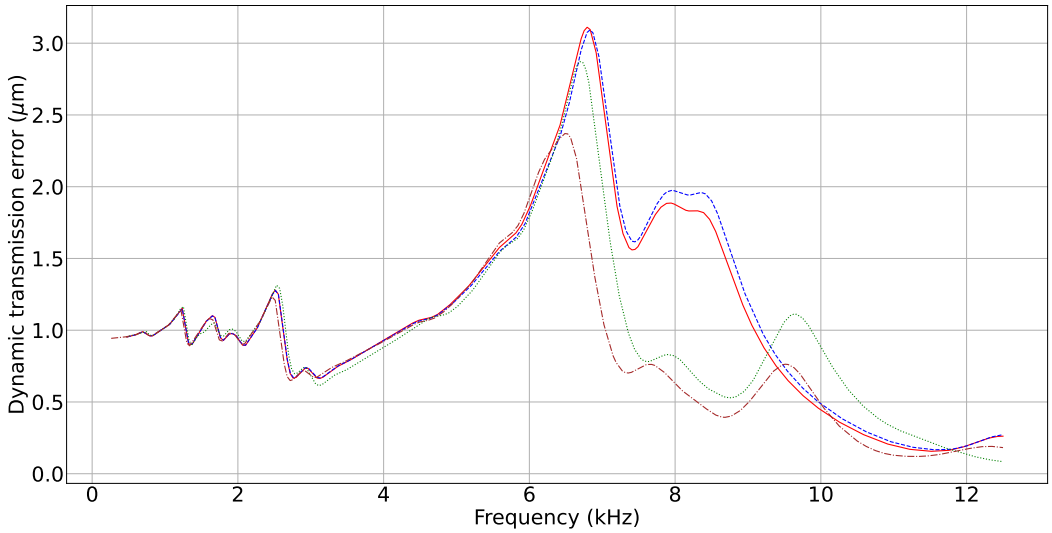

(b) MASTA

Figure 3.18: Evolution of the DTE with the different gear blank modeling methods using ROMAX and MASTA

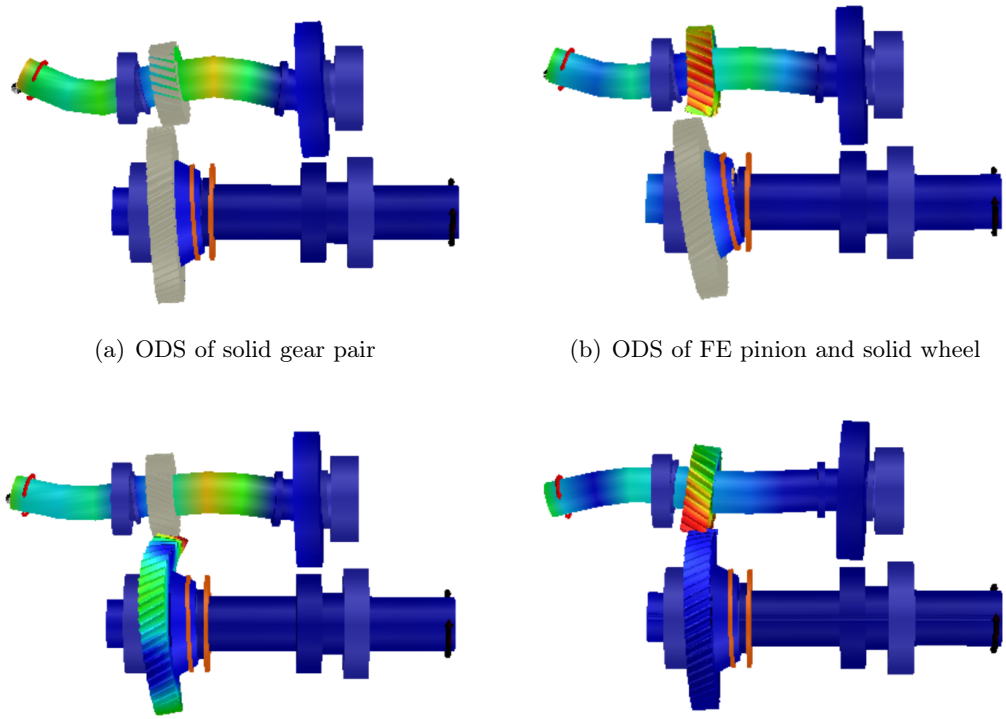

(a) ODS of solid gear pair

(b) ODS of FE pinion and solid wheel

(c) ODS of solid pinion and FE wheel

(d) ODS of FE gear pair

Figure 3.19: Visualisation of the operating deflecting shapes at the first main peak for different combinations of the gear blanks.

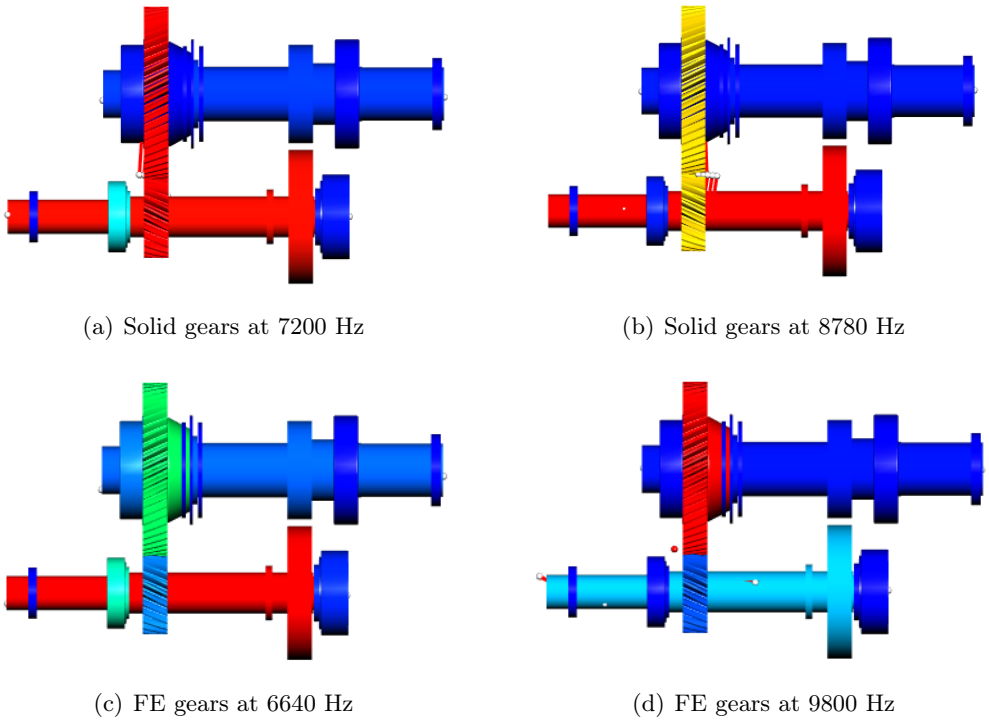

(a) Solid gears at 7200 Hz

(b) Solid gears at 8780 Hz

(c) FE gears at 6640 Hz

(d) FE gears at 9800 Hz

Figure 3.20: Graphical representation of the strain energy contribution per component for a solid and FE gear blank configurations in MASTA. The colors are represented as a rainbow spectrum with blue representing the lowest contributing parts and red being the highest contributing parts to the deflection of the system at the frequency of the highest DTE peak.

tact patches between the gears, resulting in higher stresses and an increase in the amplitude of the transmission error.

Furthermore, the presence of FE gear blanks has an impact on the overall energy distribution of the model. Since the FE component has more degrees of freedom, it is susceptible to locally deform and develops more bending strain energy which shifts the balance of energies in the system. Additionally, it appears that the blank local modes have lower modal flexibility and therefore contribute less to the LOA displacement which is manifested by the reduction in the DTE peak.

Figure 3.20 provides a good visualization of the transfer of strain energy contribution in MASTA from the input shaft and left bearing to the gears, the wheel in particular, as we go from a solid to an FE configuration. The blue color indicates a low contribution of the component whereas the red color indicates that the associated component contributes the most to the deflection behavior at the selected frequency.

In conclusion, the use of FE blanks is essential for accurately modeling the dynamic response of gearboxes, especially when dealing with higher frequencies and more flexible gears. The inclusion of FE elements enables capturing detailed deflec-

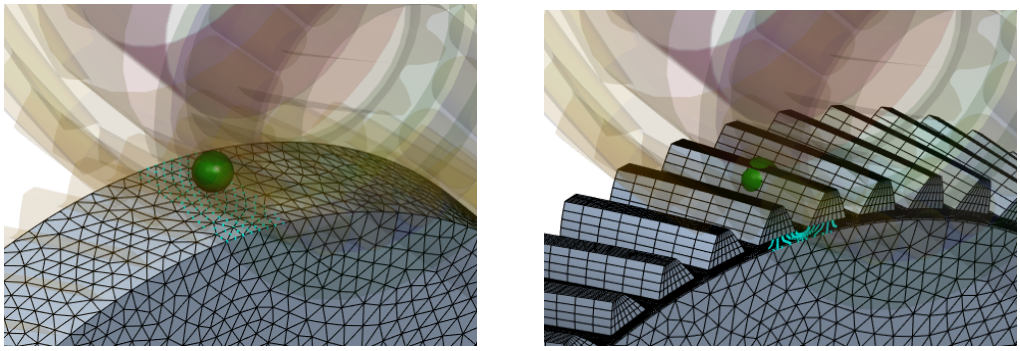

(a) Toothless FE blank (b) Toothed FE blank

Figure 3.21: Graphical representation of the non-toothed and toothed gear blanks

tion behaviors and can significantly impact the modal distribution and resonance peaks. However, careful consideration of computational resources and appropriate mesh refinement is necessary to achieve an optimal balance between accuracy and computational efficiency.

Moreover, this example exemplifies how the incorporation of additional modeling complexities can significantly impact the convergence of models when compared across different software packages, resulting in a broader range of variations in the dynamic response compared to the simplified gearbox mock-up. This underscores the challenges of constructing a high-fidelity, commercially viable transmission system.

3.3.6 Effect of including the teeth in the FE model of the gear blank

The significance of implementing FE gear blanks prompts the question of whether adding teeth to the model has a considerable impact on its accuracy. In fact, the gear teeth proved to drastically increase the mesh density of the part as they require very fine meshing which further hinders the dynamic condensation process and hence the computation speed. To explore this further, we examined four configurations of toothed and non-toothed FE gear blanks for the same gearbox. Figure 3.21 depicts the difference between a toothless and toothed configuration.

The results, as depicted in Figure 3.22, exhibit variations among the different study cases. Both toothless and toothed-wheel configurations display a similar trend, with minor discrepancies in the amplitudes of secondary peaks. However, the addition of teeth to the pinion introduces a slight leftward shift in the resonance peaks. Furthermore, incorporating teeth in both the pinion and wheel amplifies the magnitude of STE and gives rise to additional secondary resonances at high frequencies (over $7000Hz$).

In a toothless configuration, the condensation node is positioned within the pitch circle and connected to nearby nodes near the outer diameter of the blank through

the distribution of rigid body elements. The same principle applies to a toothed configuration, except that the condensation node connects to nodes belonging to the teeth, thereby accounting for their deflection. The inclusion of extra degrees of freedom not only impacts the overall modal response of the system, resulting in frequency shifts but also explains the emergence of auxiliary peaks associated with modes in which the teeth contribute significantly.

It is worth noting that, in this specific case, the toothed pinion exerts a more pronounced effect on the system's response compared to the toothed wheel. This is primarily because most resonances are associated with the deflection of the input shaft, on which the pinion is mounted, rather than the wheel. Alterations in modal behavior can consequently influence other system factors such as mesh misalignment and the distribution of contact forces, ultimately affecting the amplitude of dynamic responses.

To summarize, the impact of gear teeth on system behavior is highly influenced by the operating frequency range. Notable deviations start to emerge when the frequency reaches approximately $3000Hz$ and become more pronounced at higher frequencies. It is important to note that these discrepancies are specific to the design of the particular gear model and may not apply universally. Thus, it is essential to conduct a thorough assessment for each gearbox model to determine the practical relevance of including tooth modeling within the operating frequency range.

3.3.7 Convergence analysis and effect of modal reduction parameters

When experimenting with modal reduction control parameters, including mesh size, the number of master nodes in the ring, and axial nodes per angular position, we observed significant variations in excitation and dynamic response. It became clear that opting for an excessively fine mesh with numerous condensation points resulted in larger matrices, significantly increasing computation time and memory demands. Thus, a convergence analysis became essential for finding the right balance between resource efficiency and accuracy.

The convergence analysis for the excitation was investigated through a calculation of the Normalized Cross-Correlation factor Normalized Cross-Correlation (NCC) assuming that the calculated transmission error with the finest mesh and highest number of master nodes has the highest precision and therefore is taken as the reference value. The NCC measures the similarity between two signals based on the correlation between their harmonic components which are extracted from their calculated TE.

For each iteration i of condensation parameters, the vectors containing the amplitudes $\mathbf{a}_i$ and phases ϕ_i can be extracted from the trace of the STE using FFT. The complex representation of the j^{th} harmonic of a signal can be expressed as:

$$A_{i,j} = a_{i,j} \exp\left(\Im(\phi_{i,j})\right) \tag{3.27}$$

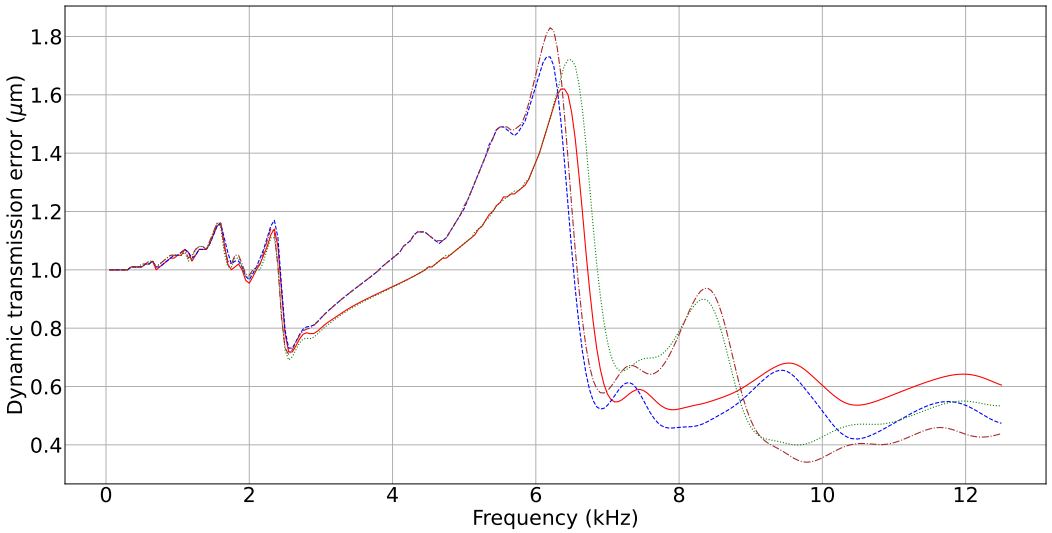

(a) ROMAX

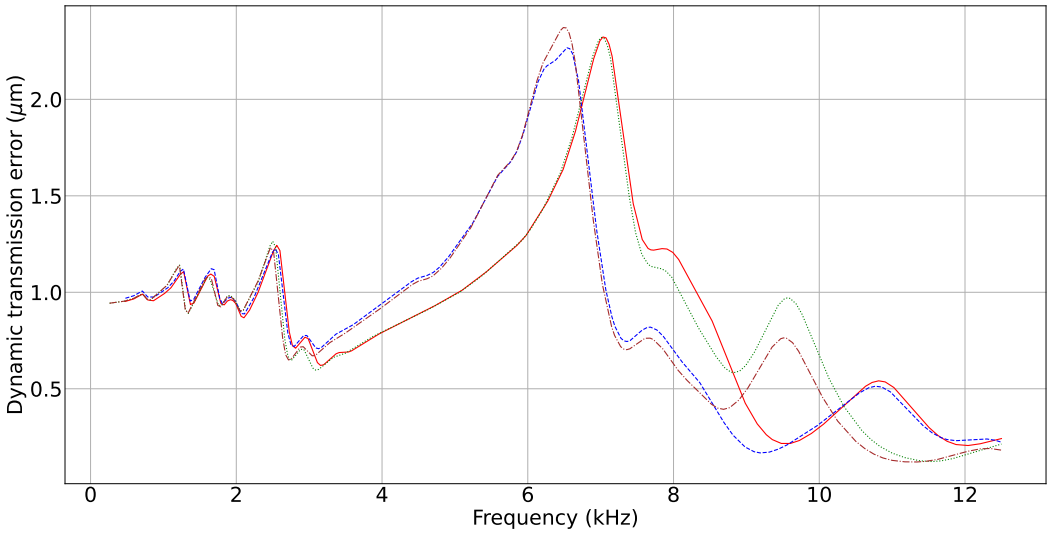

(b) MASTA

Figure 3.22: Influence of blank teeth on the evolution of the DTE in ROMAX and MASTA.

The NCC between the i^{th} iteration and the reference n^{th} iteration can be written as:

$$NCC = \frac{1}{N}\sum_{j=1}^{N}\frac{A_{i,j}\overline{A_{n,j}}}{\sqrt{\sum_{j=1}^{N}|A_{i,j}|^2\sum_{j=1}^{N}|A_{n,j}|^2}} \tag{3.28}$$

The dynamic convergence was assessed by conducting a thorough analysis of both local and global dynamics associated with the gear blank, as depicted in Figure 3.23. This analysis involved varying the parameter of interest while keeping the other two parameters fixed. The evaluation of local dynamics primarily centered on tracking the changes in natural frequency in response to the control parameters. On the other hand, the examination of global dynamics entailed monitoring frequency and amplitude shifts of the peak dynamic mesh force.

The influence of the modal reduction control parameters on the mesh TE is found to be negligible, as indicated by the perfect Cross-Correlation factor of 1. This suggests that all systems experience the same level of excitation. However, when comparing the system transmission, the impact becomes more evident. The NCC improves with finer mesh sizes and a higher number of angular master nodes but remains unaffected by the number of axial nodes.

The mesh TE primarily focuses on individual gear pairs and the line of action, accounting for gear profile modifications and local deflection behavior. In contrast, the system TE is better suited for capturing vibration transfer paths, which can be influenced by geometric discontinuities. The presence of master nodes at the interface can affect interactions and load distributions between different components, thus impacting the system's behavior.

Conversely, the mesh size has a more noticeable influence on the frequencies of reduced models, particularly at very high-frequency modes associated with local teeth behavior. However, these variations are insignificant as they occur well beyond the operating frequencies of the system.

Most discrepancies are observed when analyzing the system behavior, which encompasses local dynamics and excitations. The variations in the dynamic mesh force peak and its corresponding frequency for different configurations can be summarized as follows:

- Mesh variation: $200Hz$ frequency and $150N$ amplitude.
- Varying the number of angular condensation nodes: $200Hz$ frequency and $350N$ amplitude.
- Varying the number of axial condensation nodes: $40Hz$ frequency and $300N$ amplitude.

It can be concluded that the variation of these parameters has a more pronounced effect on the amplitude of the force rather than the frequency of the peak, especially when altering the number of master nodes. This effect is once more attributed to

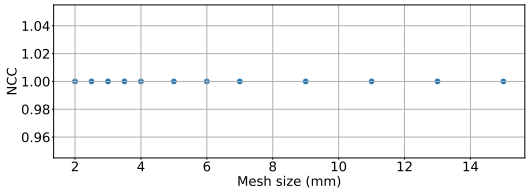

(a) Mesh TE: Effect of mesh size

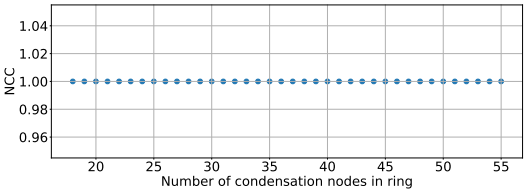

(b) Mesh TE: Effect of number of angular CDs

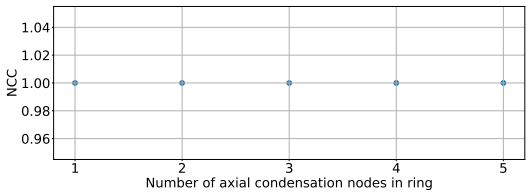

(c) Mesh TE: Effect of number of axial CDs

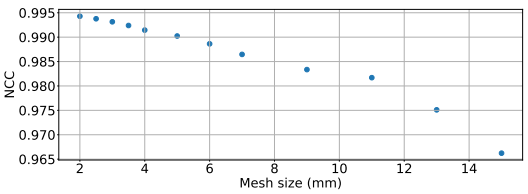

(d) System TE: Effect of mesh size

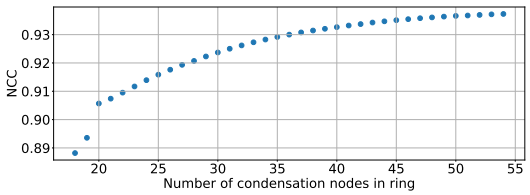

(e) System TE: Effect of number of angular CDs

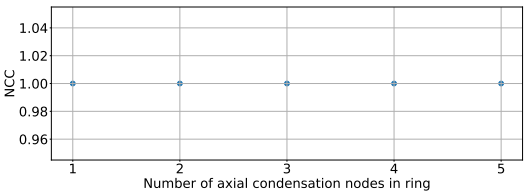

(f) System TE: Effect of number of axial CDs

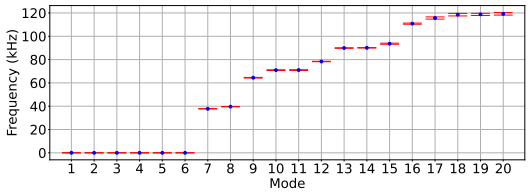

(g) Blank frequencies: Effect of mesh size

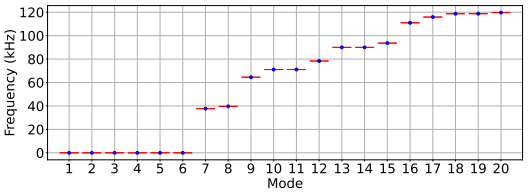

(h) Blank frequencies: Effect of number of angular CDs

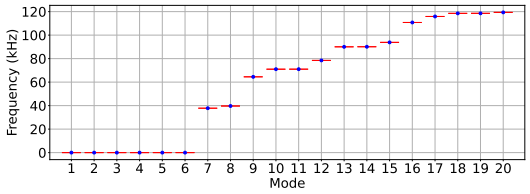

(i) Blank frequencies: Effect of number of axial CDs

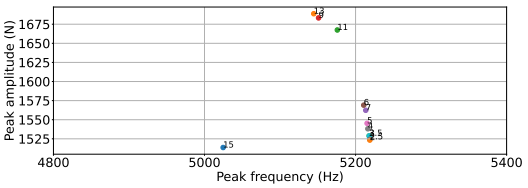

(j) DMF: Effect of mesh size

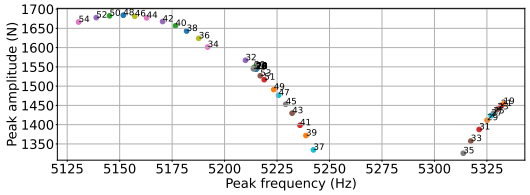

(k) DMF: Effect of number of angular CDs

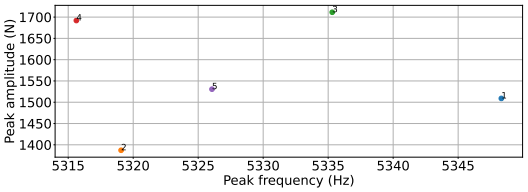

(l) DMF: Effect of number of axial CDs

Figure 3.23: Influence of the modal reduction parameters on the mesh-level and system-level responses

changes at the interface, impacting the load transfer properties between different sub-structures.

Based on the outcome of these analyses, the following studies will be conducted using a $5mm$ mesh, 55 angular condensation nodes (corresponding to one node per tooth), and a single axial node considering that this adds much more computation to the process (For 2 axial nodes the number of condensation nodes becomes 55×2) which substantially increases the computation time without much accuracy gain.

3.4 Conclusion

This chapter serves as a continuation of the previous chapter, delving into the effects of variations in contact analysis on the dynamic response of a system. It aims to shed light on potential pitfalls that one may encounter when conducting a fully numerical assessment.

Several factors have been identified that can significantly influence the dynamic outcome of a simulation, both across different software packages and within the same software. These factors can be summarized as follows:

- Difference in excitation: The choice of a different LTCA approach or different parameters within the same approach can result in variations in the dynamic response scaling. This discrepancy in results between software packages such as ROMAX and MASTA can be attributed to the different approaches used to calculate the excitation.

- Difference in the established dynamic model: Variations in the LTCA calculation can lead to different mesh stiffness, which in turn affects the overall dynamics of the system. Additionally, variations in auxiliary part stiffness, particularly for the bearing, can arise due to the inherent assumptions and numerical estimation, as well as potentially minor variations in formulations.

- Blank modeling method: While the Timoshenko element offers a reasonably accurate dynamic representation of the gear blank, its effectiveness diminishes as we consider lighter and more flexible gears that are prone to out-of-plane motion. In such cases, the FE model performs better in capturing the behavior. However, it is important to note that despite the additional DOFs introduced by the teeth, they play a crucial role in accurately representing the system's dynamics, particularly at higher frequencies.

- Meshing parameters: While the influence of meshing parameters is generally minor, they can have a slightly more noticeable impact at higher frequencies where the dynamics are primarily influenced by the teeth.

- Meshing master nodes: The selection of meshing master nodes has a significant influence on the transmission error and overall response, as it affects the dynamic coupling at the interfaces between various parts.

These findings highlight the hypersensitivity of the gearbox model to minor changes in modeling parameters that grow as a function of the complexity of the gearbox, suggesting the importance of establishing a proper benchmark. Despite not being perfectly compliant, the models demonstrated similar evolution when subjected to changes in designs, ensuring the overall stability of the results. This aspect becomes particularly useful when exploring lightweight designs.

Chapter 4

Assessment of the Lightweight Gear Design Impacts on the Static and Dynamic Conditions of a Gearbox

Contents

4.1 Introduction

When designing the geometry of gearbox parts, the potential configurations may seem limitless. However, attaining optimal performance requires careful consideration. The interplay between static and dynamic design criteria poses a significant challenge in determining the ideal structure. This challenge stems from the fact that reducing weight often results in heightened dynamic response but compromised static resistance, necessitating a delicate balance.

To address this challenge, this chapter thoroughly examines the implications associated with different gear geometries. At each design phase, the complexity level is heightened. This comprehensive exploration is facilitated through the use of multiple simulations. Our objective is to provide valuable insights into the performance characteristics of various configurations.

4.2 Analyzing the Impact of Rim and Web Thicknesses on Gear Performance

4.2.1 Design constraints, response metrics, and simulation scheme

To gain insights into various approaches for reducing the weight of a gear from a geometrical perspective, it is crucial to have a solid understanding of the gear's general geometry and identify areas where mass reduction can be achieved without compromising the static design constraints. Specifically, the minimum rim thickness must be carefully determined to ensure that the gear rim can withstand the bending stresses resulting from applied loads without failure.

In this study, we have chosen to adopt the guidelines outlined in the AGMA 2001-D04 standard [5]. According to this standard, the minimum rim thickness, denoted as t_R, is calculated as the product of the tooth height, h_t, and a backup ratio, m_B, using the following formula:

$$t_R = m_B h_t \tag{4.1}$$

In our case, we consider m_B to be equal to 1.2 which corresponds to the minimum allowable value, although it can increase based on the loading conditions.

Calculating the web thickness, on the other hand, presents a more intricate challenge, as it depends on various factors such as gear type, module, applied loads, and more. Chapter 2 of our study sheds light on the impact of a thin web, which can lead to pronounced out-of-plane motion, potentially amplifying the amplitude of transmission error.

To initiate our preliminary investigation, we have set a minimum blank thickness of $2mm$. This value serves as a starting point for our analysis, providing a baseline for further examination of the web thickness requirements. However, it is important to note that the actual determination of the optimal web thickness will involve comprehensive evaluations considering factors like gear type, material properties, load conditions, and industry standards.

To investigate the impact of the rim and web effects on various static ratings, a comprehensive parametric study was conducted on the gearbox in Figure 4.1. The static ratings were normalized relative to those of standard solid gears for comparative analysis. This study involved evaluating a series of 20 thickness samples, equidistantly spaced between the minimum allowable values and the maximum thickness required to form a complete solid gear. The samples were meticulously assessed for the following metrics:

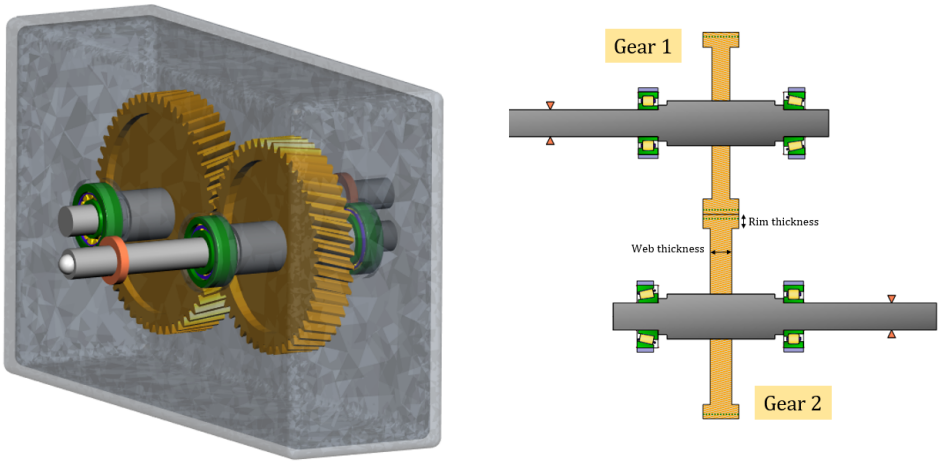

Figure 4.1: Graphical representation of the non-symmetric gearbox model.

- The mean TE represents the mean value of transmission error as obtained from the LTCA.
- The PPTE measures the peak-to-peak value of the transmission error which is considered as the primary excitation that serves to scale the dynamic response.
- The mean mesh stiffness K_m also derived from the contact analysis as shown in equation 1.9 provides valuable insights regarding the bulk and contact stiffnesses.
- The effective equivalent misalignment $f_{\beta y}$ calculated according to ISO 6336-1:2006, section 7.5.1 refers to the cumulative radial, axial, and angular misalignments occurring between the gears after running the static deflection simulation. It accounts for the initial gaps present due to the mounting and micro geometry conditions and is expressed as:

$$F_{\beta y} = F_{\beta x} - y_\beta = F_{\beta x}\chi_\beta \tag{4.2}$$

$F_{\beta x}$: The initial equivalent misalignment is defined as the absolute value of the cumulative sum of deformations, displacements, and manufacturing deviations in both the pinion and wheel, all measured within the plane of action.
y_β: The running-in allowance factor quantifying the reduction in initial misalignment through the running-in process.
χ_β: The running-in factor that characterizes the equivalent misalignment following the running-in procedure.

The running-in factors are influenced by factors such as the material, surface state, lubrication, and rotational speed.

- The contact and bending safety factors are obtained by dividing the allowable contact/bending stresses by the maximum nominal contact/bending Von Mises stresses estimated from the contact analysis. Therefore, the safety factor for contact can be expressed as:

$$S_H = \frac{\sigma_{HG}}{\sigma_H} \tag{4.3}$$

Similarly, the safety factor for bending can be written as:

$$S_F = \frac{\sigma_{FG}}{\sigma_F} \tag{4.4}$$

The safety factors for contact and bending were calculated based on ISO 6336 [103]. The contact stress is obtained from Hertz contact theory applied to two contacting cylinders as follows:

$$\sigma_H = Z_B \sigma_{H0} \sqrt{K_A K_V K_{H\beta} K_{H\alpha}} \tag{4.5}$$

$$\sigma_{H0} = Z_H Z_E Z_\varepsilon Z_\beta \sqrt{\frac{F_t}{d_1 b} \frac{u+1}{u}} \tag{4.6}$$

where:

σ_{H0}: The nominal stress at pitch point in perfect gears subjected to static nominal torque.
Z_B: A factor that converts pitch point contact stress to inner point tooth contact stress in the pinion.
Z_A: Accounts for load changes due to external variations in input or output torque.
Z_V: Considers load changes due to internal dynamic effects.
$K_{H\beta}$: Incorporates uneven load distribution across the facewidth due to various factors.
$K_{H\alpha}$: Addresses uneven load distribution in the transverse direction, often caused by pitch deviations.
σ_{HP}: The allowable contact stress.
Z_H: Considers flank curvatures at the pitch point and transforms tangential load at the reference cylinder to tangential load at the pitch cylinder.
Z_E: Accounts for material properties, including elasticity.
Z_ε: Takes into account the influence of the effective length of the lines of contact.
Z_β: Addresses the effects of the helix angle, such as load variation along the lines of contact.
F_t: The nominal tangential load, transverse to the reference cylinder.
b: The facewidth (for double helix gears, $b = 2b_B$).
d1: The reference diameter of the pinion.

u: The gear ratio, calculated as $u = z_2/z1$, where z_2 is the number of teeth on the gear, and z_1 is the number of teeth on the pinion.

Similarly, the bending stress approximates the gear tooth deflection to the bending of a loaded cantilever beam and can be expressed as:

$$\sigma_F = \sigma_{F0} K_A K_V K_{F\beta} K_{F\alpha} \tag{4.7}$$

with the nominal stress σ_{FO} being:

$$\sigma_{F0} = \frac{F_t}{b m_n} Y_F Y_S Y_\beta Y_B Y_{DT} \tag{4.8}$$

Y_F is a form factor accounting for the tooth form and the nominal root stress.
Y_S is a stress concentration factor.
Y_β is a helix angle factor that considers the influence of the helix angle on the bending stress.
Y_B is a rim thickness factor that adjusts the stresses on the rimmed gears.
Y_{DT} is a deep tooth factor only considered for high-precision applications where there is a high contact ratio.
The K factors represent the same entities as the contact safety factor but are calculated differently. The details will not be covered here.

The determination of permissible stress σ_{HG} and σ_{FG} can involve two key methods. One approach utilizes S-N or damage curves derived from tests conducted on actual gear pairs under real service conditions. Alternatively, it relies on damage curves tailored to common gear materials, factoring in considerations such as lubrication, velocity, surface roughness, work hardening, and size. The software in question employs the latter method, leveraging its existing material library for these calculations.

In our upcoming investigations, we've intentionally created a gear pair with different parts. This choice allows us to study how changing either the pinion, the wheel, or both components together affects the gear pair. You can find a detailed overview of the gear pair's properties in Table 4.1.

Table 4.1: Characteristics of the non-symmetric gear pair

Name	Designation	Gear 1	Gear 2	Unit
Module	m	2		mm
Number of teeth	Z	49	55	-
Pressure angle	α	20		deg
Helix angle	β	15		deg
Base diameter	d_b	94.941	105.566	mm
Profile shift coefficient	x	0	0	-
Addendum coefficient	h_α	1	1	-
Dedundum coefficient	h_f	1.25	1.25	-
Facewidth	b	20	20	mm
Center to center distance	a_f	107.669		mm

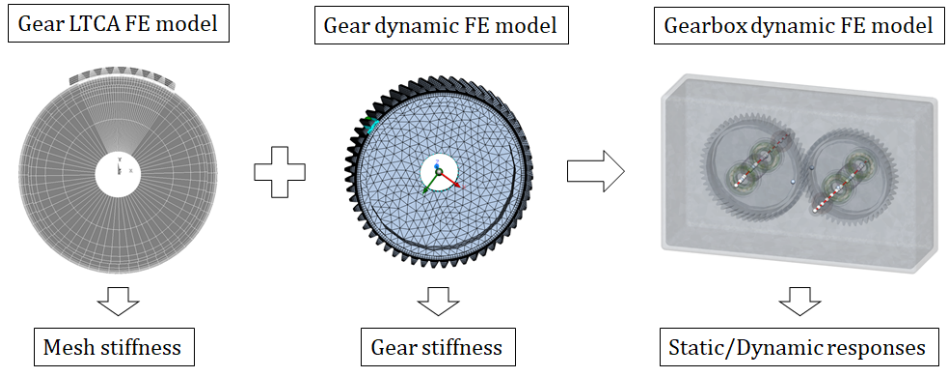

Figure 4.2: Gear replacement simulation scheme.

The simulation process is outlined in Figure 4.2. It begins with the creation of a finite element (FE) model for the gear LTCA, primarily used to estimate the overall stiffness of the gears. This stiffness value is then combined with Hertzian contact theory to estimate both the transmission error and meshing stiffness. The meshing process in this step is adjusted based on gear dimensions and desired precision. While certain dimensions like web and rim thicknesses can be specified, the model cannot accommodate complex geometries involving cavities. Ultimately, the average of the meshing stiffness derived from the contact analysis is applied to couple the gear pair.

In contrast, the dynamic gear model offers distinct advantages in accommodating complex geometries, rendering it particularly well-suited for accurately characterizing the dynamic behavior and vibration propagation within the rotating gear blank. Employing a finite element representation enhances precision, especially when addressing the behavior of thin-rimmed gears susceptible to out-of-plane bending. The integration of CMS approach dynamically adjusts the gear blank's stiffness. This blank is subsequently rigidly connected to the shaft and other gears using the time-averaged meshing stiffness, culminating in a comprehensive model that is equally proficient in assessing static system deflections and conducting dynamic computations.

The assessment of dynamic responses involved an in-depth examination of various factors constituting the primary transmission path of vibrations. This examination encompassed the local mesh dynamic forces, the gear body vibrations, and the vibrations of the housing.

To gauge the overall vibrational magnitude of the FE components, namely, the gear blank and the housing, we have adopted the Root Mean Squared Velocity (Root Mean Squared Velocity (RMSV)) as our metric. The excitation for the gear blank and housing is derived from the radial and axial forces and moments of the meshing and bearing forces, respectively, at their connection nodes. The spatial average of the velocity within the FE housing can be accurately computed by leveraging knowledge of the individual nodal velocities $v(i, \omega)$, as follows:

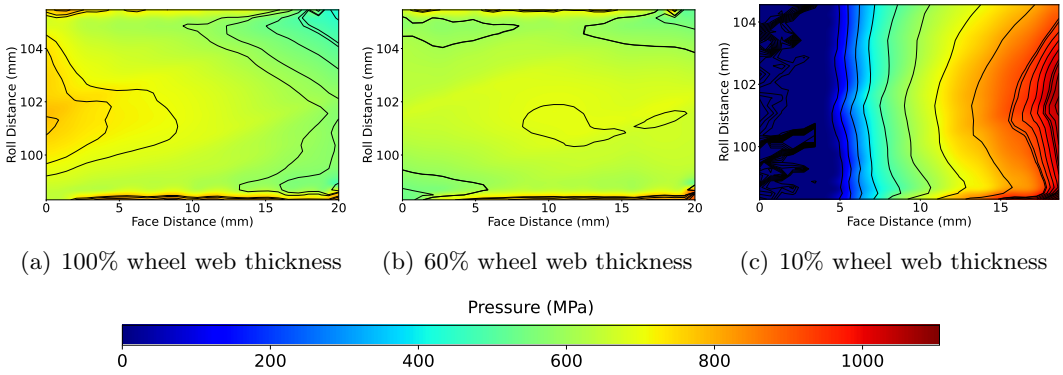

(a) 100% wheel web thickness (b) 60% wheel web thickness (c) 10% wheel web thickness

Figure 4.3: Evolution of the contact patterns with different web thicknesses

$$RMSV = \sqrt{\frac{1}{N}\sum_{i=1}^{N} v_i^2(\omega)} \tag{4.9}$$

4.2.2 Local sensitivity analysis: Individual gear replacement

4.2.2.1 Impact of web thickness on the static metrics

By varying the web thickness, we obtained the results shown in Figure C.1, which reveal clear non-linear trends for each of the analyzed outputs. These trends can be explained by delving into the contact physics of the gears.

When the web thickness of a gear is reduced, it significantly diminishes the supporting ground beneath the gear teeth, resulting in a notable decrease in gear stiffness. This reduction in stiffness facilitates motion along the line of action, leading to an increase in both the average amplitude of transmission error and the magnitude of its fluctuations. Consequently, the increased displacement results in a greater separation between the gear teeth, which explains the significant rise in relative misalignment, particularly for gears with thin webs.

Interestingly, around 60% of the wheel's web thickness, we observe a 20% improvement in PPTE before it starts to decline again as the thickness decreases. Figure 4.3 depicts the evolution of pressure contour patterns for different wheel web thicknesses. At 60% thickness, a slight enhancement in the pressure distribution, compared to the reference case, can be observed, which corresponds to a slight improvement in safety factors. In the case of more flexible designs, the substantial misalignment causes high edge loading, leading to a significant increase in PPTE as well as a deterioration in the safety factors.

4.2.2.2 Impact of rim thickness on the static metrics

Although the reduction in web thickness led to a decrease in the contact and bending safety factors, the analyses have indicated that these factors still remain comfortably

above the required values. Therefore, the primary focus should be on the peak-to-peak transmission error since it directly affects the dynamic response. With this in mind, we have determined the minimum web thickness that keeps the PPTE value below a 20% variation.

For this particular model, the retained web thickness values correspond to $11.5mm$ for the pinion and $9.6mm$ for the wheel. These values were then used for conducting a local sensitivity analysis targeting the variation of the rim thickness which extends from the tooth root up to the bore diameter. The results of this analysis are presented in Figure C.2.

Unlike the previous case, the simulations reveal a clear and sudden transition occurring at specific points along the rim thickness. Notably, the analyses demonstrate significant shifts occurring approximately at 68% and 60% of the rim thickness for the pinion and wheel, respectively. In simpler terms, these findings emphasize the presence of a critical minimum rim thickness below which both the moment of inertia distribution and the gear's stiffness experience severe compromises.

4.2.2.3 Impact of web thickness on the dynamic metrics

From a dynamic perspective, the reduction of the blank mass either by modifying the rim or web thicknesses results in a noticeable decrease of the dynamic mesh force considering that the structure is more flexible and the pressure energy is transferred into the displacement of the gear rather than the development of localized stresses. The overall trend is less smooth than in the case of the static metrics which is due to the presence of dynamic effects and resonances at specific blank configurations. For instance, it is possible to tune the mass and stiffness of the gear blank so that the energy distribution within the system is enhanced.

The frequency of the dynamic mesh force remains consistent across most of the mass range and varies slightly due to the shifting of the component-level natural frequencies. However, there is a significant change observed at very low mass values which indicates a complete change in the modal behavior in which lower frequency modes become more prominent and surpass the amplitude of the original resonance peak.

By examining the evolution of the maximum RMSV for the gears and the housing, a distinct inverse pattern emerges. Put simply, the valleys in the RMSV of the gears correspond to peaks in the RMSV of the housing, and vice versa. This observation underscores the interplay of energy among the various components within the system. For instance, the vibration could originate from localized vibrations in the gear blank, which have a minimal impact on the housing, or it could be the opposite case. This effect may be more pronounced for certain peaks compared to others. Hence, it is crucial to consider not only the energy level of the vibration but also the characteristics of the mode shape and its overall contribution to the displacement along the LOA. Higher modal flexibility modes are more susceptible to amplifying the excitation and subsequently affecting the housing response, even though the majority of vibrations primarily occur at the gear level.

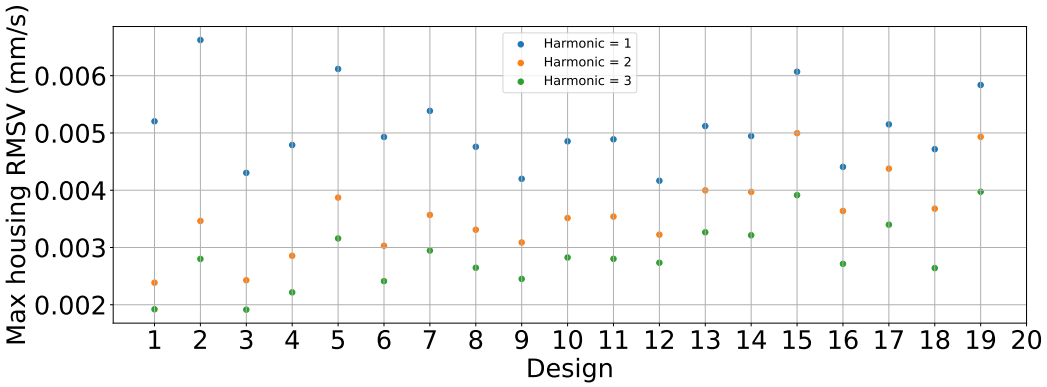

Figure 4.4: Root mean squared velocity of the housing for the first 3 harmonics of TE.

Moreover, upon a thorough analysis of the static and dynamic curves, one can notice that the high PPTE particularly associated with heavier gears does not necessarily correspond to an amplification of the housing RMSV. This implies that the dynamic effects resulting from modifications in design and macrogeometry hold greater significance compared to the static excitation effect, which is generally more influenced by alterations in microgeometry. Hence, it is crucial to acknowledge the utmost importance of the housing RMSV as the primary metric to consider when aiming to achieve lightweight gears.

It is essential to acknowledge that although reducing the overall blank stiffness impacts the amplitude of the transmission error, its influence on the TE trace is relatively minor. As the shape of the TE trace remains consistent across various designs, the relative importance of different harmonics remains unchanged. Consequently, tracking the evolution of the first order, which exhibits the highest magnitude, is sufficient to describe the dynamic behavior of the housing effectively.

4.2.3 Random forest-based global sensitivity analysis: Double gear replacement.

The previous local sensitivity analysis focused on individually substituting one variable of a gear blank at a time. The results revealed the potential for optimizing the gear blank by achieving an improvement in dynamic response without significantly compromising its static properties. This approach involved varying the web thickness to determine the optimal thickness that provides acceptable responses, followed by modifying the rim accordingly.

While this sequential process offers computational efficiency, it does not cover different combinations of design variables. This limitation becomes more pronounced when modifying both gears simultaneously. Considering that there are N discretized possible design values for each rim and web in a gear pair, the total number of combinations amounts to N^4. Collecting data for all these combinations may not be practically feasible.

To address this challenge, a simple random sampling method was adopted. Out of the numerous possible combinations, 100 combinations of the 4 design variables were selected. This approach not only reduces the computational burden for the assessment but also aims to establish meaningful inferences about the overall population.

To determine the appropriate method for conducting the sensitivity analysis, several factors need to be considered. The review by [26] provides valuable insights into various sensitivity analysis methods specifically applicable to vibroacoustic problems. These methods include variance-based approaches and surrogate model techniques. In order to make an informed choice, it is crucial to fully understand the problem context, as well as the characteristics of the input variables and output responses.

Regarding our specific application, the problem at hand can be characterized by the following aspects:

- Low number of inputs.
- A sampling approach based on random combinations of the design variables.
- Complex relationship between inputs and outputs resulting from the system's contact and dynamic non-linearities.

Given these circumstances, it becomes clear that sensitivity analysis methods like Sobol, which depend on a specific sampling pattern, may not be suitable. Instead, a data-driven approach that leverages the power of Machine Learning Machine Learning (ML) becomes more appropriate, as it does not necessitate assumptions about variable distributions. Although various methods could be considered, we have chosen to implement a Mean Decrease in Impurity Mean Decrease in Impurity (MDI) based Random Forest Surrogate Random Forest Surrogate (RFS). This method offers a robust and effective means of conducting the sensitivity analysis for our specific case.

In general, surrogate models act as stand-ins for computationally expensive functions. They are created using data that provides insights into the relationship between inputs and outputs. ML models, with their flexible structures, are trained to learn and mimic this relationship by adjusting their internal parameters. The training process aims to minimize the difference between the ML's predicted outputs and the true outputs from the original function.

In the case of an RFS, decision trees are employed as the fundamental framework for establishing the data relationships. These decision trees utilize straightforward rules to partition the input feature space at each branch. At a specific node n, the split is determined by a threshold t_n applied to an input feature q_{in}, resulting in the division of the current branch $\mathcal{C}$ into two distinct branches:

$$\mathcal{C}^{-}(q_{in}, t_n) = \{(\mathbf{q}, \mathbf{y}) \in \mathcal{C} : q_{in} \leq t_n\},$$
$$\mathcal{C}^{+}(q_{in}, t_n) = \{(\mathbf{q}, \mathbf{y}) \in \mathcal{C} : q_{in} > t_n\}.$$

with ($\mathbf{q}$, $\mathbf{y}$) representing the previously-defined sets of input-output pairs.

In a Random Forest algorithm, the goal of each node split is to group together samples that have similar outputs. This aggregation process is crucial during training. At each node, the algorithm aims to find the optimal pair of values (q_{in}, t_n) that minimizes the splitting error, also known as the impurity criterion $G_n(q_{in}, t_n)$.

In regression problems, a commonly used impurity criterion is based on the Mean Squared Error Mean Squared Error (MSE) of each subspace. The algorithm evaluates different potential splits based on their ability to minimize the MSE which is expressed as:

$$G_n(q_{in}, t_n) = \frac{L^-}{L}\left(\frac{1}{L^-}\sum_{y\in\mathcal{C}^-}(y-\mu^-)^2\right) + \frac{L^+}{L}\left(\frac{1}{L^+}\sum_{y\in\mathcal{C}^+}(y-\mu^+)^2\right) \tag{4.10}$$

With μ^- and μ^+ representing the mean output values of subspaces $\mathcal{C}^-$ and $\mathbf{C}^+$ respectively. L^-, L^- and L^+ denote the number of samples belonging to subspaces C^-, C^- and C^+.

The Random Forest algorithm constructs decision trees by selecting splits that minimize the Mean Squared Error MSE. This approach ensures that samples within each resulting subspace are more homogeneous and exhibit lower variance. By effectively minimizing splitting errors and employing MSE-based splits, Random Forest accurately predicts target variables in regression problems. Moreover, the ensemble of multiple decision trees enhances the model's predictive power and robustness, enabling it to handle diverse datasets and yield accurate outcomes.

The algorithm operates by iteratively dividing the decision tree into binary splits until a specified criterion is met, such as reaching the maximum depth. At the terminal nodes, each final subspace is assigned a scalar as the output prediction. To create a Random Forest predictor, individual decision trees are combined through bagging. This technique involves randomly selecting distinct sub-datasets to train each tree, ensuring that they are trained on different subsets of the data. The final prediction of the Random Forest is obtained by averaging the predictions of the decision trees in the ensemble. This ensemble approach mitigates variance and facilitates better generalization compared to individual predictors.

Random Forests offer interpretability, providing various methods to assess feature importance and gain insights into sensitivity indices. One such measure is the Mean Decrease in Impurity MDI, which derives from the training process of the Random Forest. The MDI approach gauges the significance of each input feature by analyzing its contribution to diminishing impurity error during the ensemble construction process. To calculate MDI, the following equation is employed:

$$\mathbf{MDI}(q_i) = \frac{1}{T}\sum_{\kappa=1}^{T}\sum_{n\in\Phi_\kappa} 1(q_{in}=q_i)\frac{L}{L_{tot}}\Delta G_n(q_{in}=t_n) \tag{4.11}$$

MDI quantifies the importance of a specific feature value q_i in a Random Forest. It calculates the average impurity decrease over all the decision trees in the ensemble.

For each sample, the indicator function checks if the value of the input feature matches the value being evaluated. If there is a match, the impurity reduction, represented by ΔG_n, is considered. The relative sample size, $\frac{L}{L_{tot}}$, also influences the importance calculation.

By summing up the contributions across all decision trees and training samples, the MDI score quantifies the significance of each input feature. A higher MDI score indicates that the feature plays a more crucial role in reducing impurity error during the construction of the random forest ensemble. Thus, the MDI principle allows for identifying essential input features and provides insights into their impact on the overall predictive power of the random forest model.

Figure 4.5 provides a comprehensive overview of the sensitivity indexes derived from a double gear replacement, based on a set of 100 randomly generated combinations of web and rim thickness. The sensitivity analysis takes into account two distinct housing configurations: one featuring a thinner and simpler geometry, and another characterized by a thicker, more complex, and consequently stiffer design (Figure 4.6).

The replacement of the housing shows no great influence on the different metrics. The most perceivable variation appears to be associated with the wheel and housing RMSVs where the pinion gains more importance in the case of the flexible housing. This is also reflected in the analysis of the individual gear masses as depicted in Figure 4.7. The change of the housing geometry in this case appears to affect the exchange of kinetic and strain energies between the pinion and the housing in particular.

In order to enhance our understanding of the input-output relationships, Figure C.6 provides a comprehensive visualization that captures the influence of individual decision variables in the case of flexible housing. Consistent with the sensitivity indexes, parameters with higher sensitivity exhibit more discernible and recognizable trends, while those with lower sensitivity indexes appear more chaotic in nature. The graph is also useful to understand different interactions between the inputs and their influence on the outputs. Overall, the total mass of the gears appears to present the highest influence on the static and dynamic metrics.

In light of the diverse outputs stemming from various input combinations, identifying the most optimal solution may not always be straightforward. Additionally, the presence of conflicting objectives necessitates well-defined rules to determine the compromises that must be made.

In this case, the housing RMSV was considered as the primary objective to be minimized since it is the most representative of the system behavior and the overall radiation efficiency of the gearbox. Furthermore, the housing vibration also encompasses information about the amplitude of the excitation making it the most adequate choice for the objective.

On the other hand, we want to minimize the weight of the components although this might result in a deterioration of the structural integrity of the gear blanks. Therefore, constraints regarding the static bending and contact safety factors were made to control the trade-off.

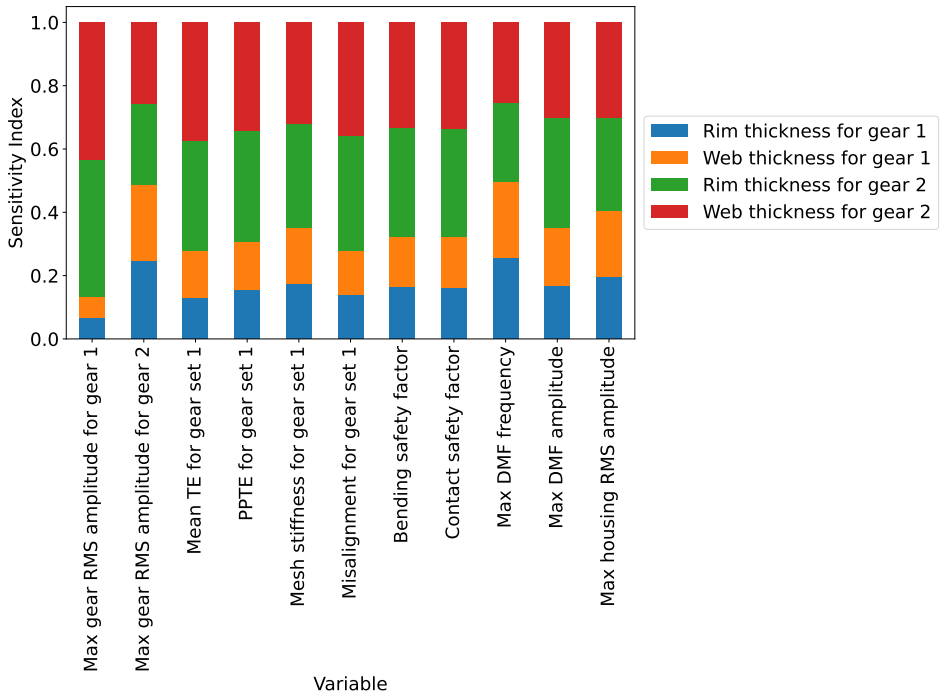

(a) Flexible housing

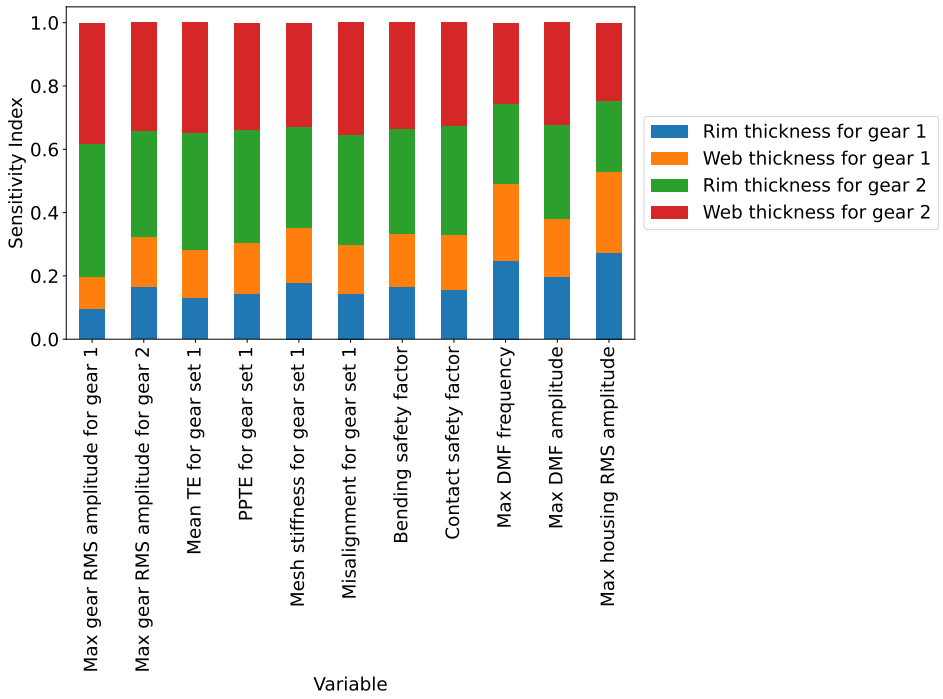

(b) Rigid housing

Figure 4.5: Sensitivity indexes of the web and rim thicknesses in the case of a double gear replacement.

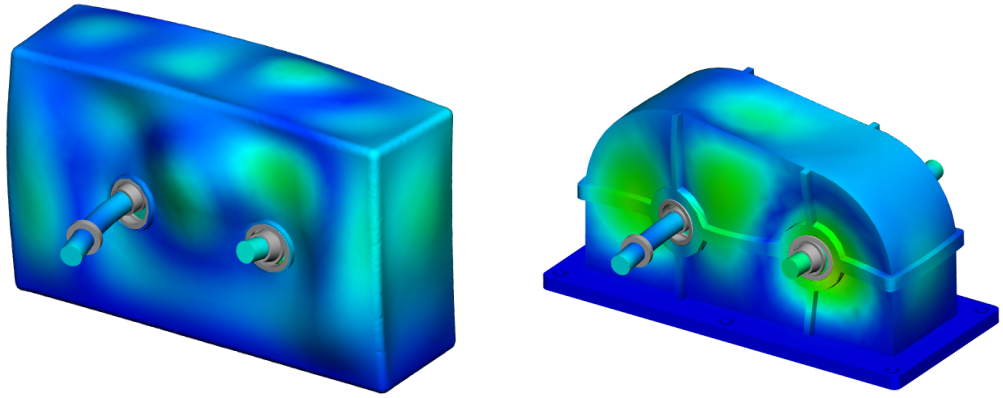

(a) Flexible housing (b) Rigid housing

Figure 4.6: Graphical representation of the flexible and rigid housing designs.

The aim of this investigation is to select the best set of solutions from the initial population that satisfy the chosen objectives. Although this might not guarantee an optimal configuration since the samples are discretized and random, we hope that the broad distribution of variables of the initial sample carries enough information to make inferences about the entire population and approximate the optimal solution.

For each evaluation, we assign a variable vector $\mathbf{x} \in \mathcal{R}^n$ containing the n number of decision variables, i.g, the rim and web thicknesses of both gears. The result is then plotted versus the chosen objectives. To ensure that the designs respect the static requirements, the safety factors were constrained so that they remain above a threshold value defined by the operator. The objective and constraints of the problem can therefore be formulated as follows:

$$\begin{aligned} Minimize: \quad & RMSV(\mathbf{x}) \\ Minimize: \quad & Mass(\mathbf{x}) \\ Subject\ to: \quad & SF_{bending}(\mathbf{x}) > minSF_{bending} \\ & SF_{contact}(\mathbf{x}) > minSF_{contact} \end{aligned}$$

In this particular scenario, the static constraints have undergone meticulous selection to guarantee that the static safety factors are not reduced by more than 10% when compared to the reference design. The feasible domain of the problem encompasses all solutions that adhere to these constraints. From this set of feasible solutions, the Pareto front, which consists of non-dominated solutions, is derived based on the optimization objectives. Each solution found on the Pareto front signifies an optimal trade-off between the objectives, ensuring that no further enhancement can be achieved in any objective without sacrificing at least one other objective.

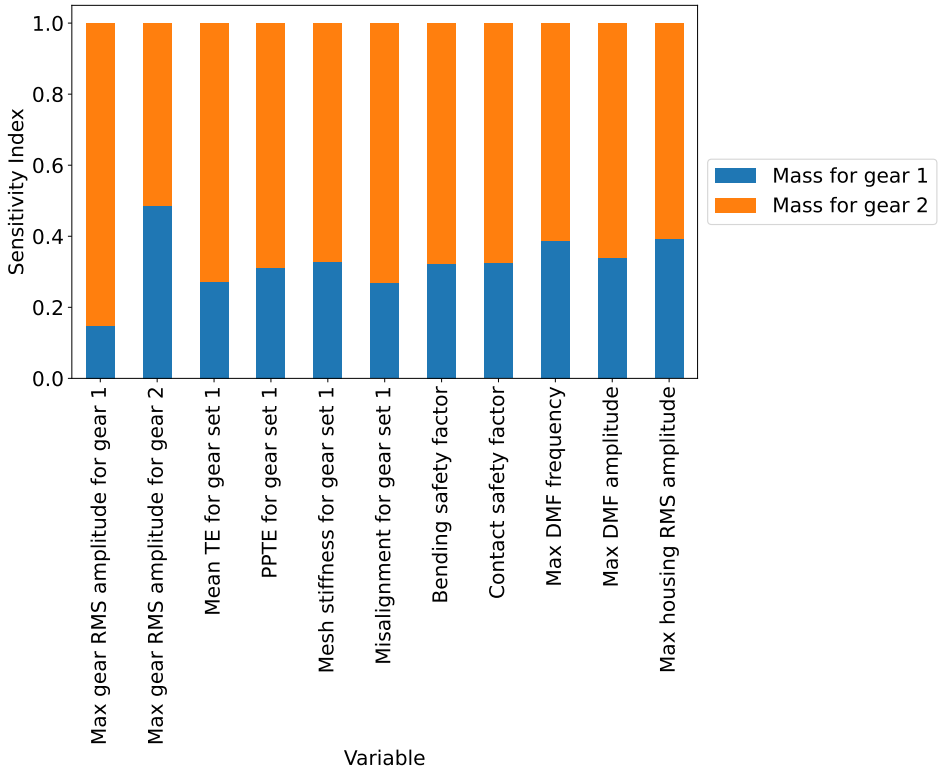

(a) Flexible housing

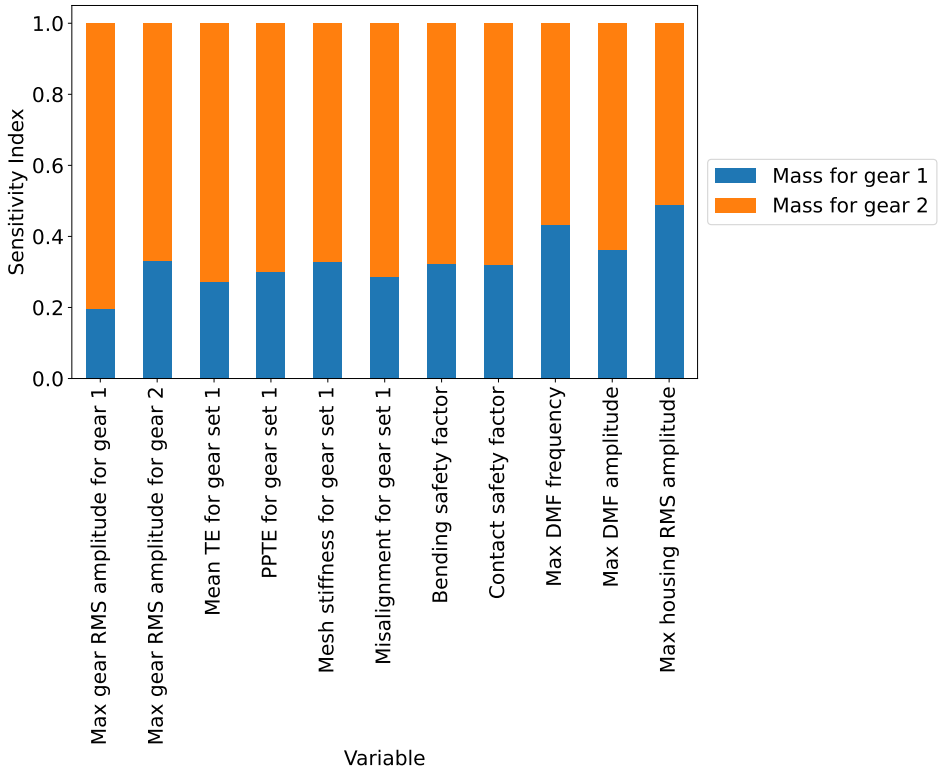

(b) Rigid housing

Figure 4.7: Sensitivity indexes of the individual gear masses.

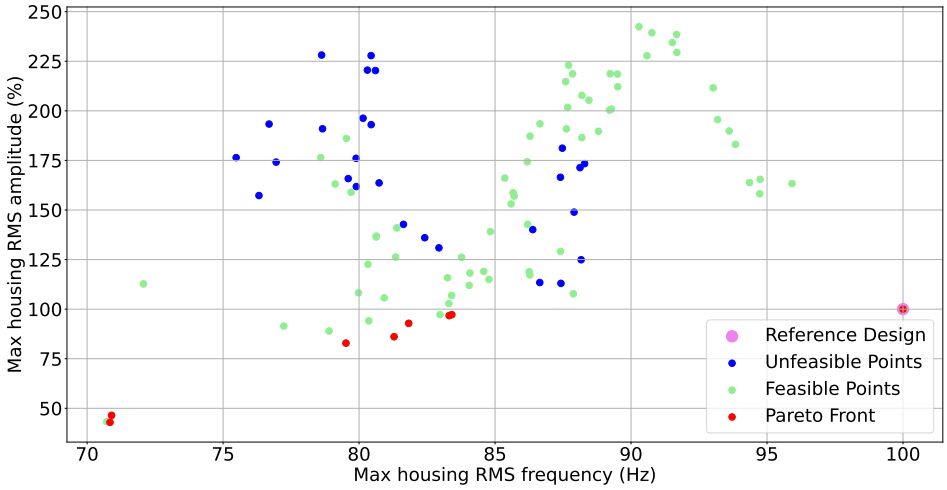

(a) Flexible housing

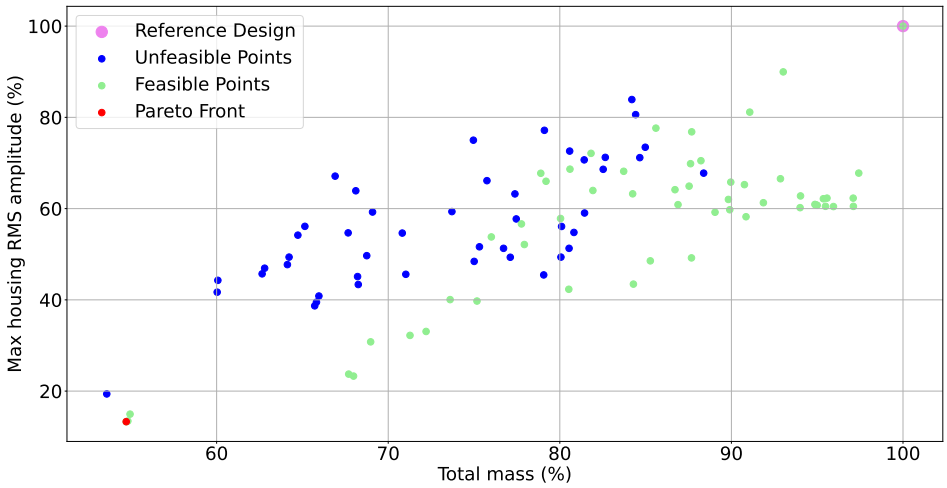

(b) Rigid housing

Figure 4.8: Pareto front for different housing designs.

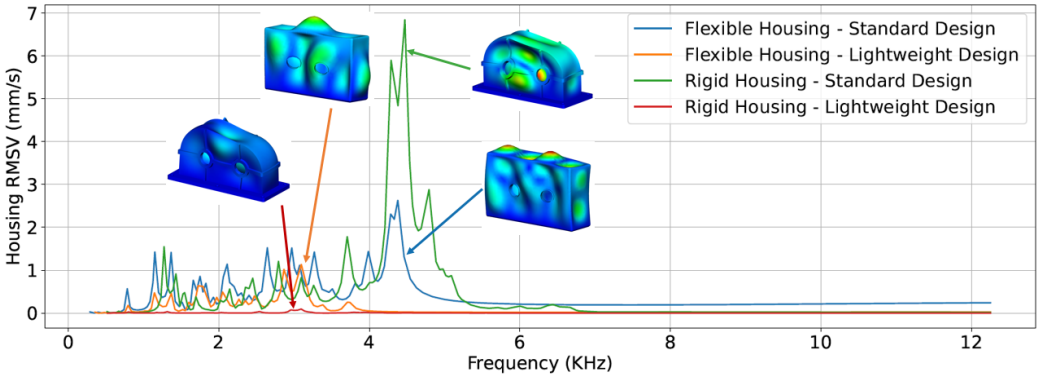

Figure 4.9: Root mean squared velocity for different combinations of housing and designs.

Figure 4.8 illustrates the objective outcomes for each design iteration. Remarkably, the plot showcases a distinct linear-like trend, revealing that the lightest gears exhibit the lowest amplitude of vibration while still effectively meeting the static constraints. This observation highlights the fact that standard gears may tend to be over-designed.

The graph demonstrates that the optimal solutions for both housing designs fall within the same mass range (approximately 55%). However, the improvement percentages differ significantly, with the rigid configuration showing a 30% improvement, while the flexible configuration boasts a remarkable 90% improvement.

To gain a deeper understanding of these results, an investigation of the housing's ODS for both the reference and lightweight gears was conducted (Figure 4.9). The analysis reveals interesting insights. When considering the reference gear design, the rigid housing exhibits a much higher response compared to the flexible housing. However, the situation changes with the lightweight gear, where the flexible design displays a higher response instead.

These findings suggest that the reference gear's inertia is sufficient to induce vibrations in both the rigid and flexible housings. On the other hand, the lightweight gear's reduced inertia has a minimal impact on the motion of the rigid housing, but it does have a noticeable effect on the flexible housing.

Additionally, it is crucial to note that the alteration in gear design not only leads to a variation in the maximum amplitude of vibrations but also causes a leftward shift of the resonance peak. This shift indicates a distinct deflection behavior, as evidenced by the observed operating deflected shapes. Furthermore, regardless of the housing design, the resonance peaks consistently occur at the same frequency for each specific gear design.

In practical scenarios, when lightweight components are introduced into a system, the overall flexibility of the system is reduced. This reduction in flexibility leads to a decrease in the system's natural frequencies. Consequently, there is a possibility that the system may encounter resonances at lower operating conditions

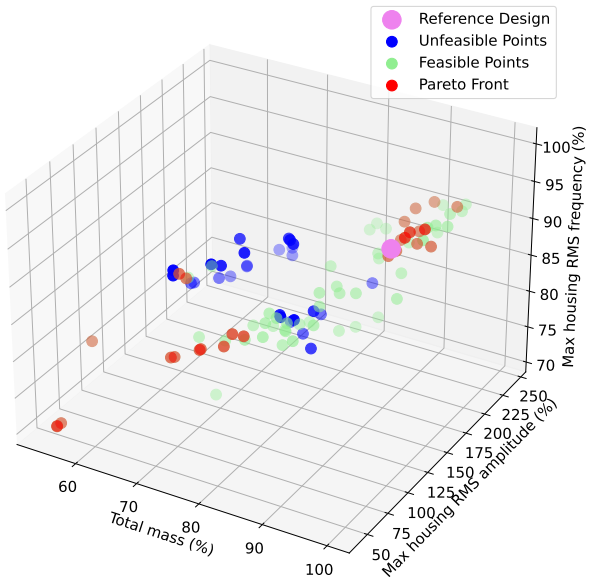

Figure 4.10: 3D Multi-Objective Visualization

than before. Additionally, this change in flexibility might bring forth new resonances that were previously outside the frequency range of interest.

The shift in the gearbox's resonating frequencies highlights the limitation of solely focusing on minimizing the amplitude of the response as the primary optimization objective. Recognizing this, we made the decision to incorporate an additional dimension to the optimization process, whereby the frequency of the peak amplitude is to be maximized.

By introducing this new dimension, the optimization aims to strike a balance between reducing the amplitude of vibrations and simultaneously ensuring that the resonant frequency remains within an acceptable range. This approach prevents the results from favoring the lightest design without taking into account the vibration mode and frequency characteristics of the system. The additional objective also favors the acquisition of a Pareto front with a larger number of non-dominated solutions to select from as showcased in Figure 4.10.

The RMS peak frequency was also plotted versus the remaining two objectives for a better visualization as shown in Figure 4.11.

In the first plot, a discernible trend emerges, displaying a slight non-linear relationship between frequency and mass reduction. This reduction in mass corresponds to a decrease in the system's natural frequencies. Conversely, the second plot exhibits a more evident non-linearity, revealing the appearance of system resonances when the gear blanks are finely tuned to specific relative masses. This phenomenon elucidates the sudden surge in amplitude seen in Figure 4.8 (a) immediately following the application of minimum mass reduction.

The 3D Pareto front leaves us with the question of how much frequency decrease

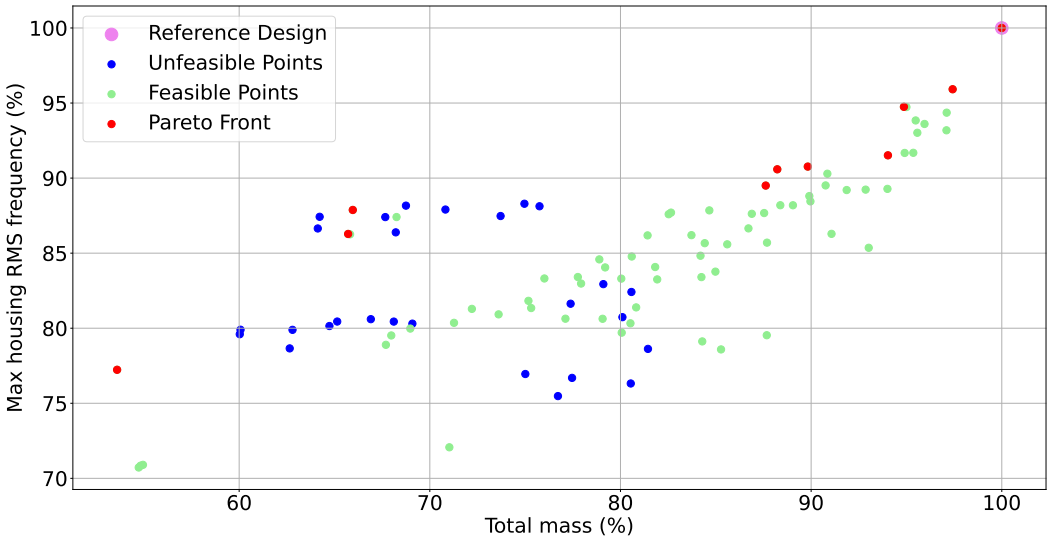

(a) Frequency Versus Mass

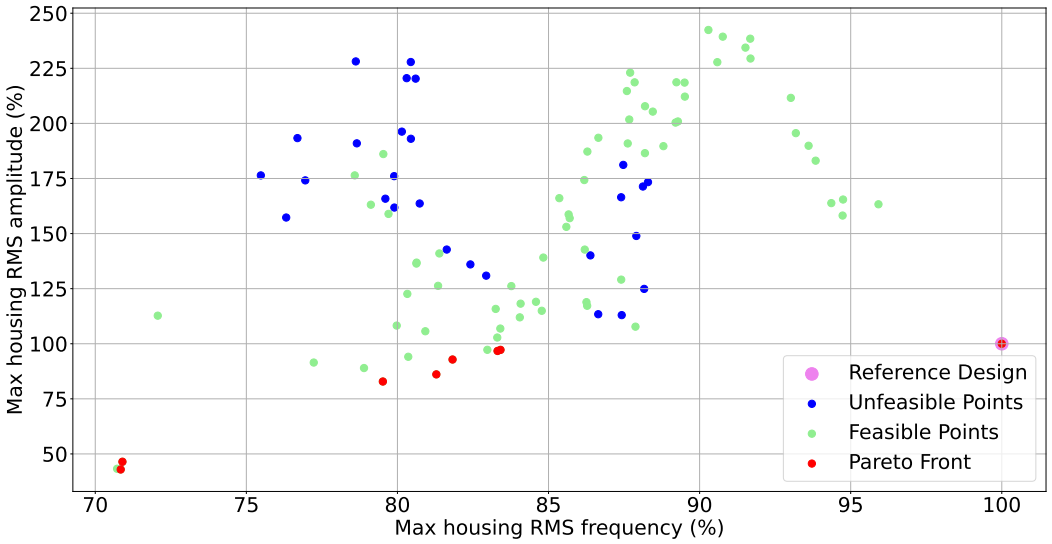

(b) Amplitude Versus Frequency

Figure 4.11: 2D representation of the objectives considering the inclusion of the housing's RMS peak frequency.

can be tolerated in order to reduce the amplitude of vibration. This results in consideration of different total mass percentages, namely 55%, 65%, or 90%. The design choice is strictly reliant on the application and loading conditions of the gearbox.

In general, it is recommended to displace the resonance peaks away from the critical operating frequencies of the gearbox. This approach enables the system to pass through resonating frequencies instead of operating continuously within their range. As a result, this helps in reducing vibrations and significantly extends the lifespan of the system.

In conclusion, the optimal decision regarding the trade-off between frequency decrease and vibration reduction is contingent upon the application's priorities and the consideration of critical operating frequencies. The decision-making can be based on assigning weights to the different objectives according to the preferences of the user as well as the requirements of the problem.

4.3 Analyzing the Impact of Randomized Hole Patterns on the Gear Performance.

The previous analyses have emphasized the potential benefits of employing lightweight gears to improve the dynamic response of the system. The observed quasi-linear trend in the housing's RMSV indicates the potential for further reduction in the response. However, the conventional approach of incorporating holes into the gear web to achieve this has not received extensive research attention in terms of optimizing the distribution of these holes, including factors such as size, number, and position. The lack of comprehensive research in this area can be attributed to the complex and nonlinear behavior exhibited by a loaded transmission system, making it challenging to intuitively determine the optimal hole distribution that guarantees the best response.

4.3.1 Automatic Gear Blank Pattern Randomizer (AGBPR)

To facilitate the generation of diverse random patterns, we developed a CAD-integrated routine called the Automatic Gear Blank Pattern Randomizer (AGBPR). This innovative algorithm incorporates various factors, including the gear's macro-geometry parameters, rim dimensions, and web dimensions obtained from the preceding optimization process. By randomly changing the design parameters, the AGBPR algorithm effectively produces different gear designs.

The process of pattern generation is visually depicted in Figure 4.3.1. Initially, the algorithm creates a standard gear blank, incorporating its macro-geometry details, rim dimensions, and blank thicknesses. To meet axisymmetry requirements, the pattern is constructed on a "slice" of the gear, which is then replicated by revolving it around the axial direction. Consequently, the initial set of holes is strategically positioned within the angular interval $[\theta_{inner}, \theta_{outer}]$, delineated by the shaded region

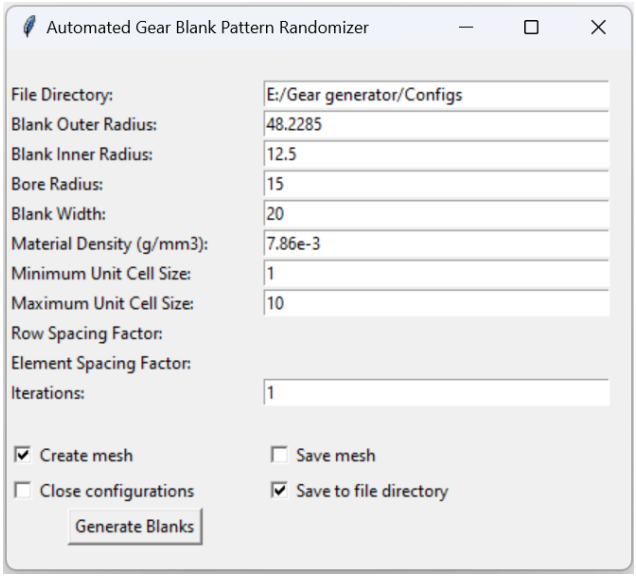

(a) Graphical user interface of the AGBPR

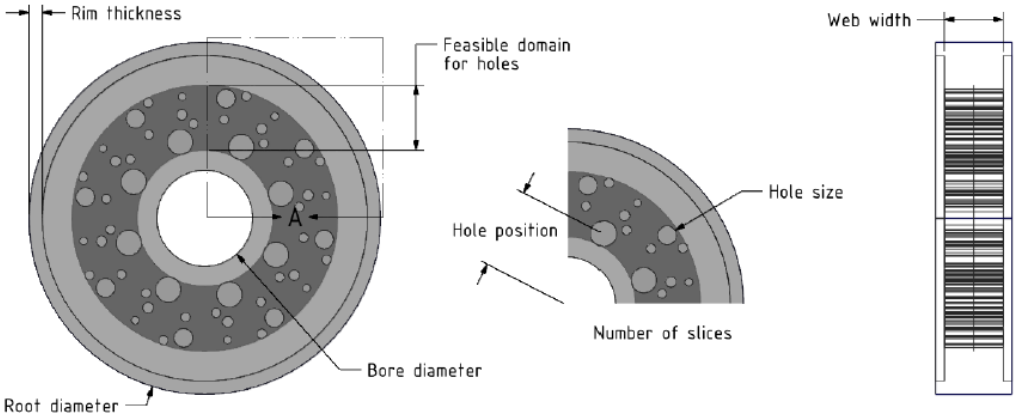

(b) Graphical representation of the pattern parameters.

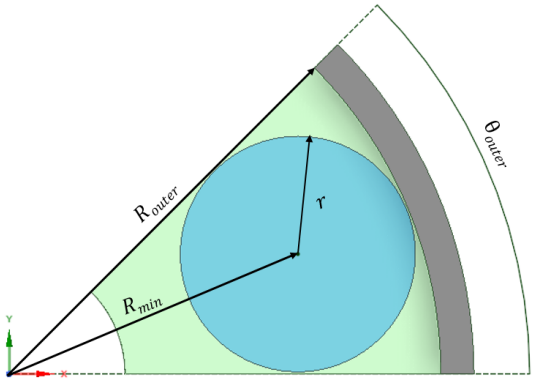

Figure 4.12: Determination of the maximum allowable hole radius

in Figure 4.3.1 (b). Furthermore, to prevent overlap with the bore and rim regions, the holes are constrained to exist within the virtual radial boundary $[R_{inner}, R_{outer}]$.

Figure 4.12 illustrates the determination of the maximum allowable hole radius. The triangular shape of the gear blank slice dictates that the maximum circle radius that can fit within the feasible geometrical domain relies on the slice's dimensions, as depicted in Figure 4.12. This radius can be calculated through a straightforward geometric transformation:

$$r_{max} = R_{outer} \frac{sin(\frac{\theta_{outer}}{2})}{1 + sin(\frac{\theta_{outer}}{2})} (1 - k\,\theta_{outer}) \tag{4.12}$$

Here, k is a randomly generated factor introduced to shrink the size of the largest possible circle so it does not interfere with the boundaries of the feasible domain.

The generation process for the holes commences by randomly generating a circle i, characterized by its radial position R_i, angular position θ_i, and radius r_i, adhering to the positional and size conditions:

$$\begin{aligned} R_i &\in [R_{\text{inner}}, R_{\text{outer}}] \\ \theta_i &\in [0, \theta_{\text{outer}}] \\ r_i &\in [1, r_{max}] \end{aligned}$$

In this context, we have taken into account a minimum circle radius of $1mm$.

Alternatively, we can express the circle's position in Cartesian coordinates through the following transformations:

$$X_i = R_i cos(\frac{2\pi\theta_i}{360}) \tag{4.13}$$

$$Y_i = R_i cos(\frac{2\pi\theta_i}{360}) \tag{4.14}$$

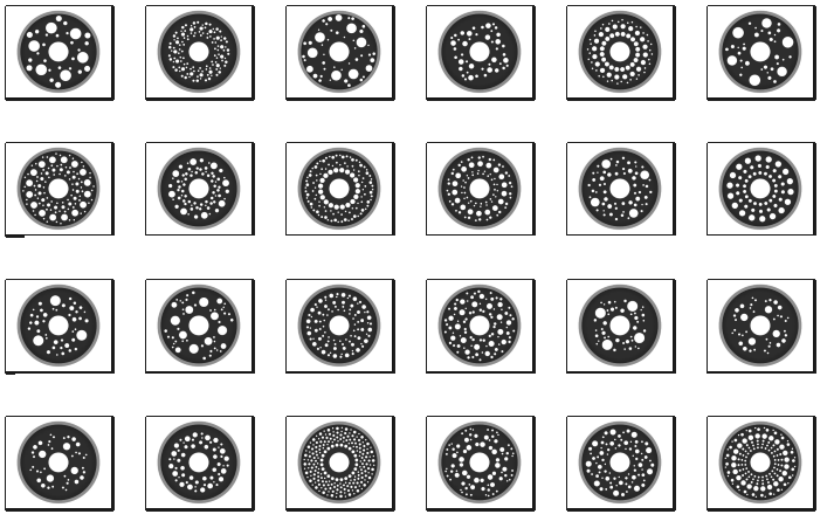

Figure 4.13: Graphical representation of a sample of randomly generated patterns.

Considering that the initial geometrical boundaries were set with reference to the hole center, the application of the circle requires the validation of the following criteria accounting for its edge:

$$R_{inner} + r_i < r_i < R_{outer} - r_i$$
$$\theta_{inner} + (\frac{180}{\pi})arcsin(\frac{r_i}{R_i}) < \theta_i < \theta_{outer} - (\frac{180}{\pi})arcsin(\frac{r_i}{R_i})$$

The process proceeds by generating a second circle, denoted as j, with the additional condition that it does not overlap with the previous circle, while also ensuring that there is enough distance between them to avoid excessively thin blank material in that region. The distance between circles i and j can be determined as follows:

$$d_{ij} = \sqrt{(x_i - x_j)^2 + (y_i - y_j)^2} \tag{4.15}$$

Hence, the non-overlapping condition suggests:

$$d_{ij} < (r_i + r_j) + D(r_i, r_j)$$

Here, $D(r_i)$ represents the spacing factor, which adapts according to the radii of the circles.

The process continues iteratively until the maximum number of circles per slice is reached or until the required number of iterations for generating an additional feasible circle is achieved. Subsequently, the slice is revolved to form the complete blank. This process can be applied to a total of n gear blanks. Figure 4.13 provides an exemplary representation of the randomly generated patterns.

4.3.2 Defining problem parameters using a statistical approach

The AGBPR algorithm stores data related to each pattern in a $N \times M$ Matrix. In this matrix, N represents the number of holes, while M corresponds to the number of variables involved in generating the pattern. These variables include the position of each hole within the 2D local cylindrical coordinate system of the blank, denoted as (R, θ), as well as the hole radius, the number of holes, the number of slices, the rim and web thicknesses, and the mass of the blank.

However, the present variable definition proves inadequate for conducting a sensitivity analysis, given that the number of holes (denoted as N) is generated randomly in each instance. Consequently, this approach leads to varying dimensions for the storage matrix across different iterations. To address this challenge, we have adopted a statistical methodology that entails characterizing the pattern through its distribution, rather than relying on specific details of individual holes defined by their radial position within the blank R_i and radius r_i.

Hence, the following variables were adopted:

$$Centroid\_radius = \frac{\sum_{i=1}^{N}(\pi r_i^2 \cdot R_i)}{\sum_{i=1}^{N} \pi r_i^2} \tag{4.16}$$

$$Mean\_radius = \frac{\sum_{i=1}^{N} r_i}{N} \tag{4.17}$$

$$MAD = \frac{\sum_{i=1}^{N} |r_i - Mean\_radius|}{N} \tag{4.18}$$

$$Skewness = \frac{1}{N} \frac{\sum_{i=1}^{N}(r_i - Mean\_radius)^3}{STD^3} \tag{4.19}$$

$$with, \qquad STD = \sqrt{\frac{1}{n}\sum_{i=1}^{n}(r_i - Mean\_radius)^2} \tag{4.20}$$

where:

- Centroid radius: Define the holes' centroid position within the geometrical domain of the gear blank.
- Mean radius: The mean radius of the holes
- Skewness: Captures the degree and direction of the asymmetry in the distribution. A positive skewness implies a greater number of larger holes while negative skewness indicates more smaller holes. However, due to the limitations of the geometrical feasible domain in the blank, most of the iterations are characterized by positive skewness as it is easier to fit smaller holes. It is important to note that the Standard Deviation (STD) measuring the average distance between the data points and the mean, is embedded in the skewness calculation but not considered as part of the essential decision variables that will serve for the upcoming sensitivity analysis.

Table 4.2: Comparison of the computation steps.

	Single Tooth Evaluation	**Full Rotation Evaluation**
Number of Condensation Nodes	1 at a specific meshing position	18+
Meshing Stiffness	Calculated Once	Updated for each meshing position
Harmonic Orders to consider	Fundamental and Multiples	Fundamental, Multiples and Sidebands

It is noteworthy that the selection of these variables occurred subsequent to an exhaustive correlation analysis conducted across a broader range of distribution variables, as depicted in Figure C.4. To ensure the robustness of the sensitivity analysis, only variables exhibiting minimal correlation were retained for further consideration.

4.3.3 Evaluation process

Prior to delving into the results, it is crucial to elucidate the computational approach employed for the patterned gears and the key distinctions they exhibit when compared to the standard solid configurations.

These differences are concisely depicted in Figure 4.14. In the case of solid gears, the absence of stiffness fluctuations in the blank allows for evaluating a single tooth, which suffices to identify the higher amplitude harmonics, typically comprising the fundamental harmonic and its integer multiples. The resulting waterfall diagram exhibits order lines associated with each of these harmonics $(1, 2, 3, etc.)$.

Conversely, patterned gears manifest varying stiffness characteristics at each meshing position, rendering the evaluation of a single tooth inadequate in providing a complete representation of the excitation. As shown in the figure, the TE trace for patterned gears is characterized by fluctuating average and peak-to-peak values. The harmonic content of such signals is notably richer, encompassing not only the fundamental frequencies and their harmonics but also frequency sidebands that represent additional sources of excitation. Notably, the primary meshing frequency in this scenario corresponds to an order of 49, reflecting the number of teeth on the input reference gear. Subsequently, the multiples of the fundamental frequency are of order 98, 147, and so forth.

The computation of a full rotation poses a significantly greater computational burden compared to evaluating a single tooth, as evident from the comparisons presented in Table 4.2. This discrepancy arises due to various factors, as discussed in the previous chapter.

To achieve an accurate representation of the static and dynamic behavior at multiple circumferential positions, the evaluation of transmission error for a full rotation necessitates the establishment of several condensation nodes located at the rim level, leading to an increase in the size of the reduced matrix. Additionally, for each time step, the mesh stiffness must be updated to account for the presence of cavities.

While the process of substituting gears and conducting system deflection and harmonics analyses remains feasible with the current computational capabilities (8-core i7-7700 CPU @ 3.60GHz and 16Gb RAM), the most demanding task lies in

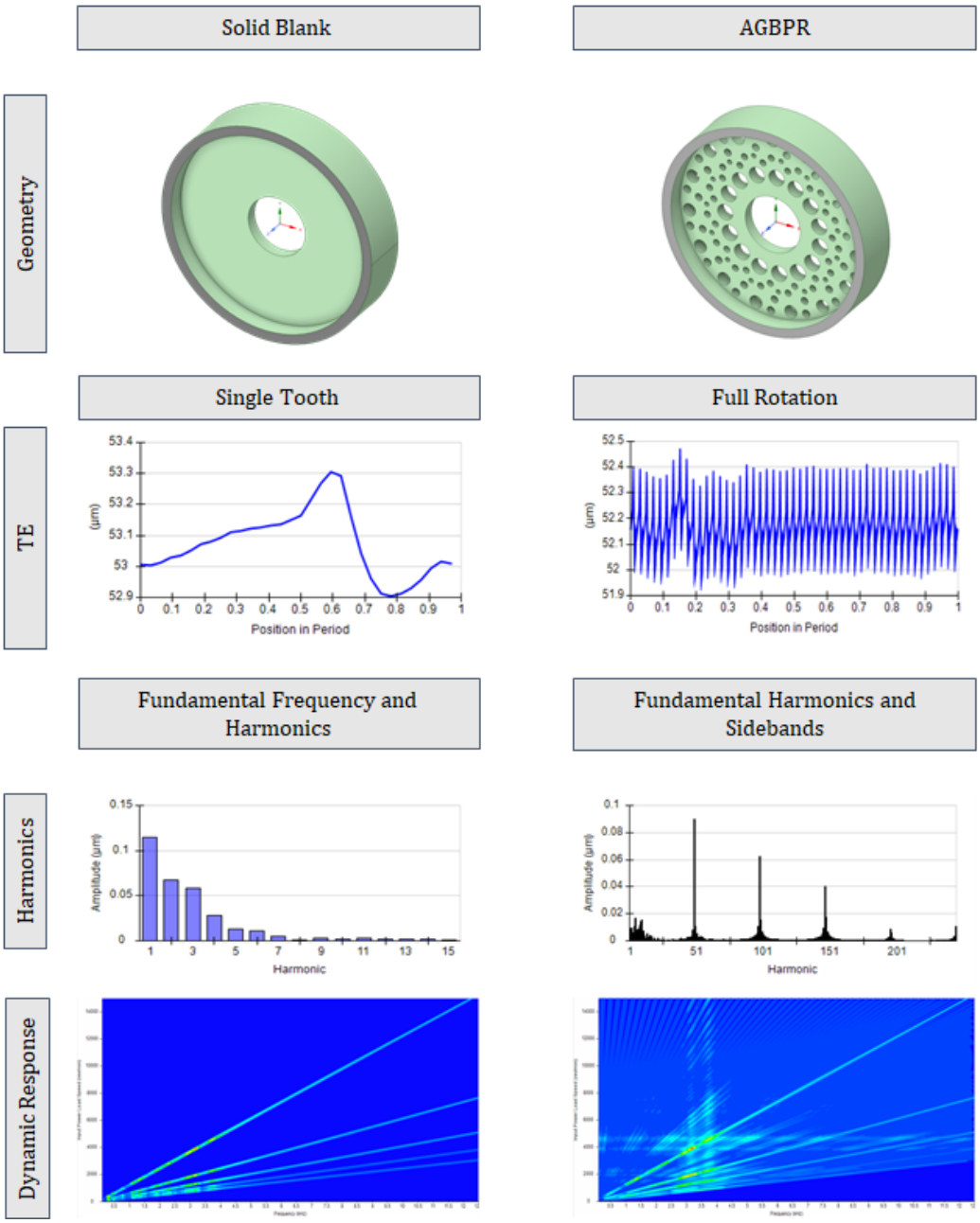

Figure 4.14: Comparison between the single tooth and full revolution evaluation processes.

evaluating the dynamic response, namely the RMSV, for each individual harmonic order. For comparison, when limited to the first fundamental frequency of transmission error, a single tooth evaluation merely requires calculating the dynamic response for the 1^{st} order. In contrast, a full rotation necessitates evaluating the entire spectrum up to the 49^{th} order, and even further if higher-order sidebands are to be considered.

Unfortunately, the current machine proved incapable of performing such extensive computations, leading to the need for several compromises that can be summarized as follows:

- Streamlining the measurement process: In light of the challenges posed by calculating the housing RMSV, we adopted an alternative approach by measuring the housing's velocity at specific locations, which are depicted in Figure [insert figure number for accelerometer placements]. The selection of these measurement locations was based on a thorough analysis of the mode shapes and operating deflected shapes within the relevant frequency range.

  To ensure accurate measurements, virtual accelerometers (shown in red) were strategically placed at desired locations represented by condensation nodes, describing the motion of nearby nodes (depicted in blue). While this technique proved effective in capturing the required data, it led to an increased size of the condensation matrix and longer extraction times for displacement data. To optimize the computational feasibility and the locations of the sensors, several iterations were conducted, resulting in the final decision to employ 5 sensors on one of the faces, as indicated by the white circles.

- Frequency Range Truncation: The investigation of the mode shapes at higher frequencies has revealed that the deformation patterns are much more complex and may not be properly captured by the currently adopted sensor positions. This is particularly true for modes that excite the upper and side surfaces of the housing.

  Furthermore, the frequency truncation results in a reduction in the number of data points that need to be calculated and stored, thereby facilitating the process.

4.3.4 Sensitivity analysis: Effect of the pattern distribution.

The sensitivity analysis considering the pattern distribution variables was conducted in a similar manner to the previous process. The static outputs, specifically the contact and bending factors, were taken into account, alongside several dynamic outputs.

The dynamic outputs considered in the sensitivity analysis were as follows:

- The maximum value of the velocities averaged across the 5 sensors for the fundamental harmonic, denoted as $A_{avg}(\omega)$, is determined as follows for each frequency:

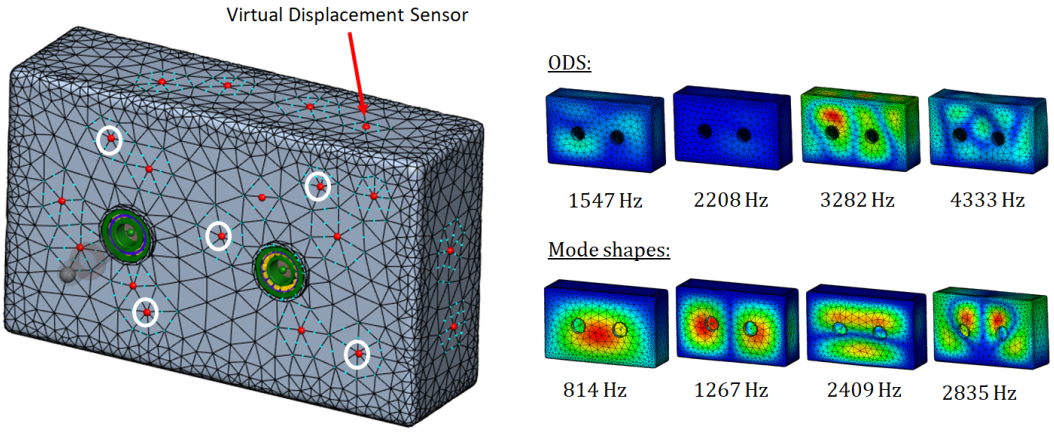

Figure 4.15: Graphical representation of the virtual sensors locations.

$$A_{avg}(\omega) = \frac{1}{N}\sum_{i=1}^{5} A_i(\omega) \tag{4.21}$$

- The frequency Associated with Maximum Peak expressed as:

$$\omega_{\max} = \arg\max_{\omega} A_{\text{avg}}\,(\omega) \tag{4.22}$$

- Calculation of the total area under the averaged velocity order lines: Considering the likelihood of geometrical cavities to induce a fluctuation in the response throughout the blank rotation which makes the excitation side-bands more energetic in nature, the cumulative area under the different harmonics was compared to get a glimpse about the energy distribution between the fundamental harmonic and sidebands.

  The response energy of each harmonic k is estimated by calculating the area under its corresponding order line using the trapezoidal rule. Given a set of data points (x_i, y_i) for $i = 0, 1, 2..., n$, where x_i represents the frequency and x_i represents the amplitude, the definite integral of the function can be approximated using the trapezoidal rule as:

$$E_k = \int_{x_0}^{x_n} y dx \approx \frac{h}{2}\left[y_0 + 2\sum_{i=1}^{n-1} y_i + y_n\right] \tag{4.23}$$

  In this equation:

  h is the step size, which is the difference between adjacent x values.
  n is the total number of frequency data points.

y_0 and y_n are the y-values at the endpoints.
y_i represents the y-values at the data points between the endpoints.

Therefore, the total cumulative area $E_{sidebands}$ for all the individual secondary order lines E_k is expressed as:

$$E_{sidebands} = \sum_{k=1}^{N_h} E_k \tag{4.24}$$

where N_h denotes the total number of harmonics and m refers to the index of the fundamental meshing order (in this case is 49).

The outcomes illustrated in Figure 4.16 highlight the varying degrees of sensitivity exhibited by different harmonics in response to changes in the pattern distribution variables. This outcome aligns with expectations, given the strong correlation between the dynamic response and the intensity of transmission error harmonics. These harmonics fluctuate in accordance with the distribution of holes within the blank.

Regarding the maximum averaged velocity, as well as the area beneath the main harmonic and sideband order lines, the parameter with the most pronounced importance is the mean radius. Following this, the centroid position holds secondary significance, succeeded by the skewness.

In contrast, the scenario shifts when considering the frequency linked to the peak response. Here, all parameters exhibit a similar level of significance. The absence of a distinct dominant parameter's effect could stem from multiple factors. One possibility is the intricate interplay among the features, which might obscure the individual feature importance. This complexity is likely compounded by the influence of geometrical boundary conditions. Alternatively, this outcome raises the question of whether the chosen inputs comprehensively capture the essence of the system's response.

The input-output relationships accounting for the pinion web and rim thicknesses are plotted in Figure C.7 and highlight the weak correlation between the inputs and outputs. It is worth noting that the pattern does not result in a significant mass variation compared to what could be obtained by varying the rim and web thicknesses. For this purpose, the mass was represented in Kilograms and shows in this case that the maximum mass variation with respect to the patternless thin-rimmed gear is around 0.04 Kg.

The dynamic behavior of this model differs significantly from the rim and web effects, which exhibited a non-linear trend in the evolution of peak frequencies with mass. For this model, however, the frequencies exhibit sudden jumps regardless of the holes' mass contribution and distribution. Moreover, the analysis of maximum amplitudes reveals that using these patterns can both enhance and deteriorate the dynamic response. As a result, a more comprehensive investigation is necessary to fully understand the implications of utilizing these patterns on the model's behavior.

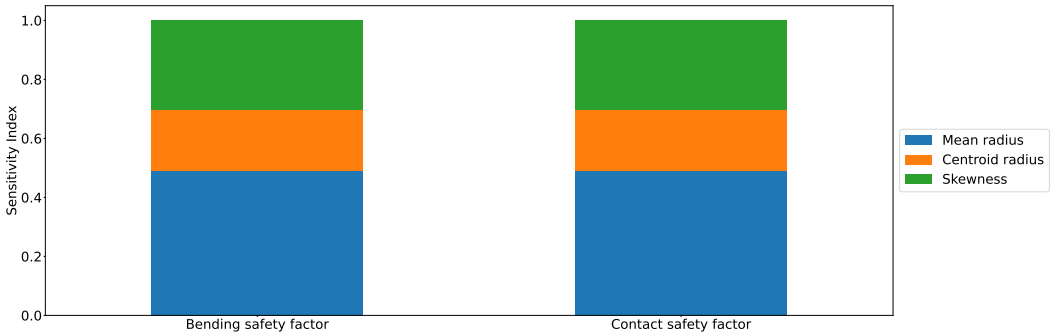

(a) Static safety factors

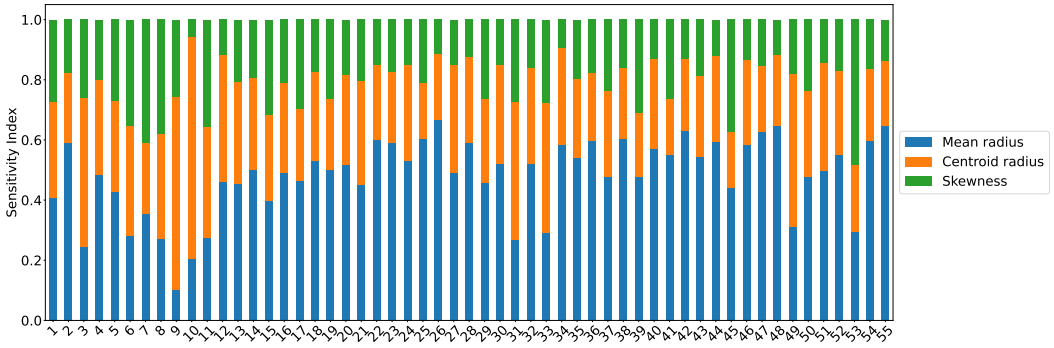

(b) Maximum averaged velocity

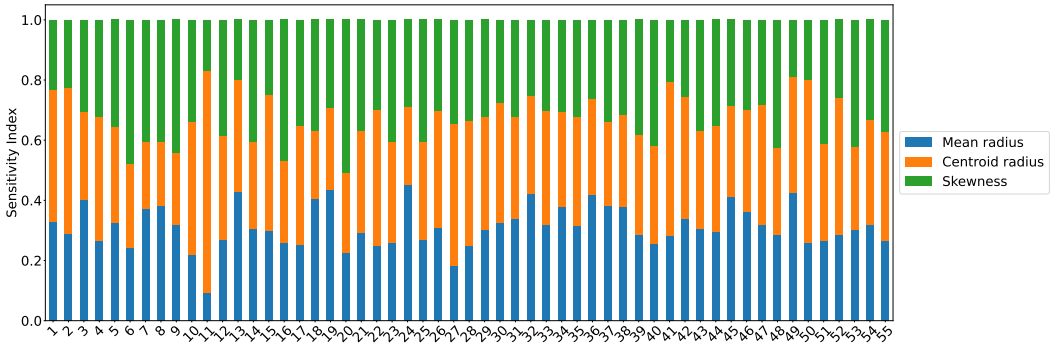

(c) Frequency of maximum averaged velocity

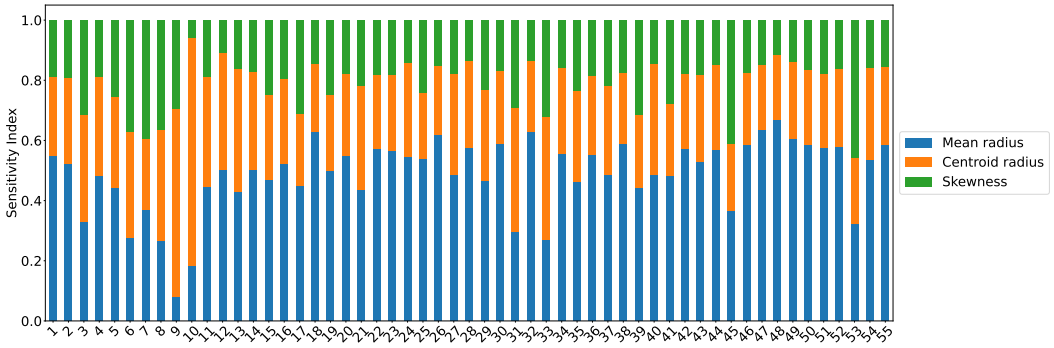

(d) Area under averaged velocity order lines

Figure 4.16: Sensitivity analysis of the static and dynamic metrics to the change of the pattern distribution variables.

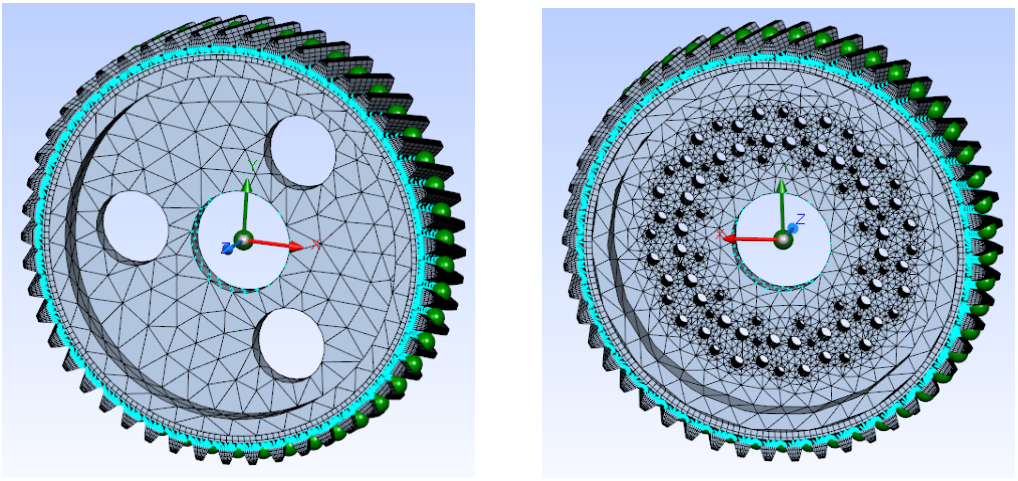

(a) Gear 1: 3 large holes. (b) Gear 2: Patterned gear.

Figure 4.17: Graphical representation of the compared gears with equivalent mass.

4.3.5 Comparative study of two gears with equivalent mass and different holes distribution

To gain deeper insights into the impact of the geometrical pattern, we conducted a dynamic response comparison between two gears with equivalent masses but different patterns. Specifically, we examined two gear designs: the first featuring three large holes, and the second displaying multiple smaller holes that, when combined, occupied the same volume as the cavities in the initial design. The highlighted designs can be observed in Figure 4.17.

4.3.5.1 Comparison of the excitation

Initially, the gears were evaluated based on the system-level static transmission error response measured between the input and output power loads. The results of this comparison are presented in Figure 4.18.

The initial aspect that immediately draws attention from the visualized data is the stark disparity in the static transmission error response between the two gear configurations. Notably, the configuration with larger holes displays a significantly more pronounced fluctuation in the average TE. This can be attributed to the presence of these larger holes, which introduces a marked stiffness gradient. The material absence within the holes, coupled with its concentration in the surrounding regions, gives rise to the observed fluctuation in the average TE that depends on the angular position of the meshing.

In contrast, the gear with smaller holes showcases a more uniform mass distribution across its structure. The even distribution of mass ensures that there are no localized regions of significantly higher stiffness. Consequently, this uniformity in stiffness leads to lower fluctuations in the TE for this gear.

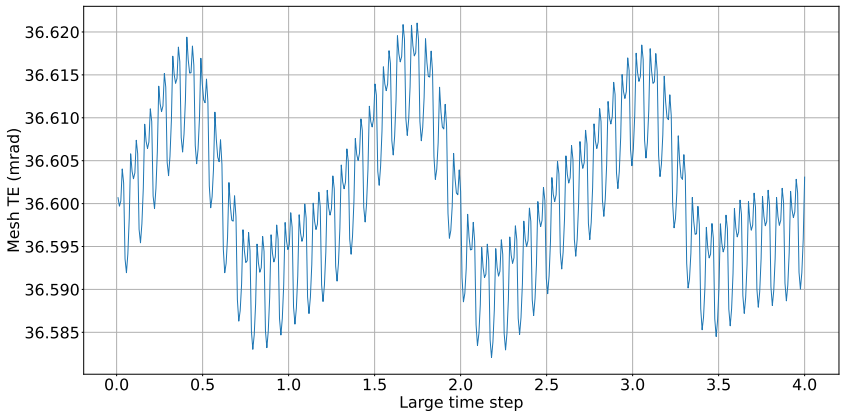

(a) Gear 1

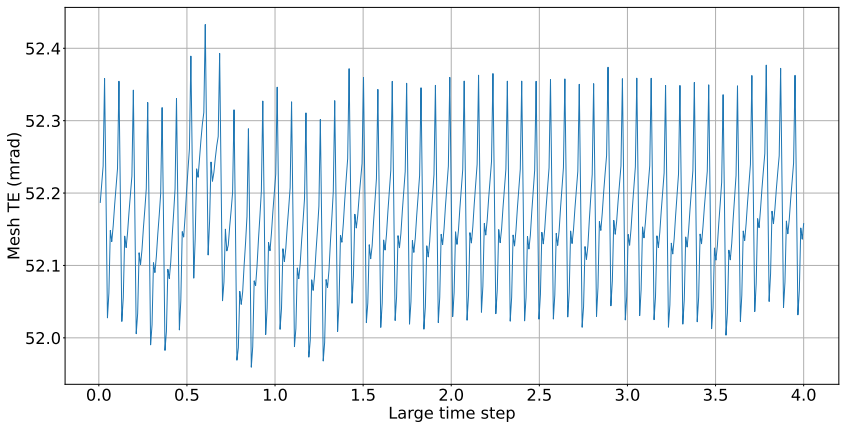

(b) Gear 2

Figure 4.18: System TE of the two gears.

However, this uniform mass distribution also implies a higher level of flexibility. As a result, the average as well as the peak-to-peak static transmission error increase for the gear with smaller holes.

It should be noted that the irregularities observed in the shape of the static transmission error curve, particularly in the second gear, can be attributed to several factors, including system-level deflections influencing the local meshing behavior during specific large time-steps, as well as the simulation parameters employed. In fact, The gear configurations with smaller stiffness gradients pose challenges in accurately capturing these fluctuations which often requires further model refinement.

However, one could argue that due to the minor fluctuations observed in the patterned case, the variation in energy distribution among different harmonics should also be relatively insignificant. Consequently, the primary focus should be on accurately capturing the overall order of magnitude of the signal rather than the variations in the individual harmonics.

Taking this into consideration, we proceeded to analyze the spectral content of

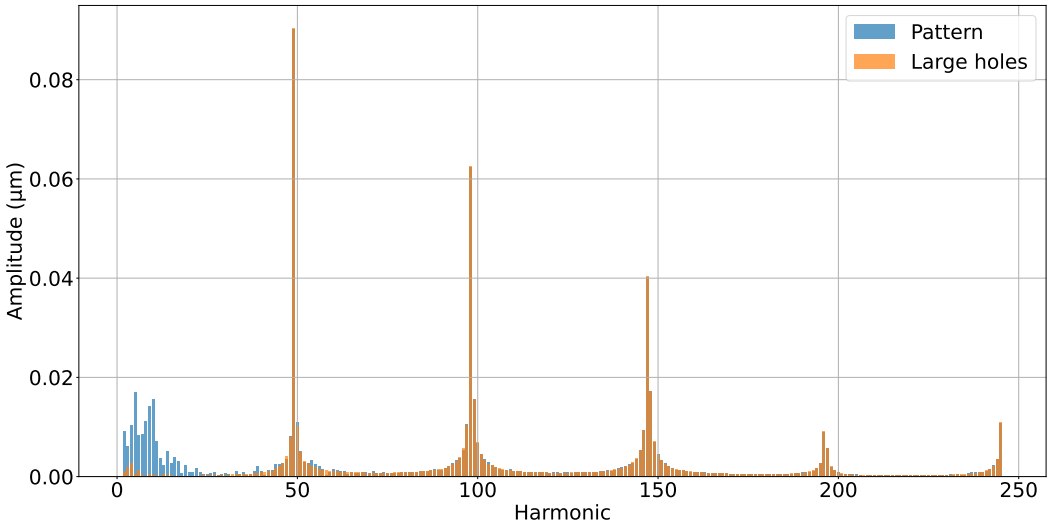

Figure 4.19: Mesh TE harmonics for Gear 1 and Gear 2

the mesh TE for both signals, as depicted in Figure 4.19. Overall, the harmonics demonstrate a high level of agreement across the spectrum, with the exception of the first few harmonics owing to the reduced bulk stiffness of the patterned gear.

4.3.5.2 Comparison of the dynamic response

As a consequence of the richer spectral content observed in the patterned gears, which suggests a possible higher contribution of the dynamic response from the lower-order harmonics, an analysis of the displacements at one of the bearings was undertaken. The outcomes of this analysis are illustrated in Figure 4.20.

As expected, Gear 1 exhibits a concentrated energy distribution primarily in the fundamental meshing order, with a slight presence of adjacent harmonics of order 49 ± 3. In contrast, Gear 2 displays a broader energy distribution and shows a more significant amplitude response at lower frequencies and across extended speed ranges. This behavior arises from the combined effects of higher torsional excitation and lower component stiffness in Gear 2.

To understand the effect on the maximum amplitude, the housing RMSV for the fundamental harmonic was also analyzed. The results, presented in Figure 4.21, show that the large hole configuration of Gear 1 is characterized by one prominent resonance peak at a frequency of $3307Hz$, followed by a smaller peak at $3764Hz$. In contrast, the patterned gear exhibits a substantial amplification of the second peak and a decrease in the first peak. In other words, the change in gear design modifies the inertia and stiffness characteristics of the system, thereby affecting the modal distribution. Gear 1 prominently resonates at the 33^{rd} mode, while Gear 2 is more sensitive to the 39^{th} mode.

While Gear 1 exhibits elevated peak vibration levels, Gear 2 demonstrates a greater accumulation of overall energy, as indicated by the area beneath the RMSV

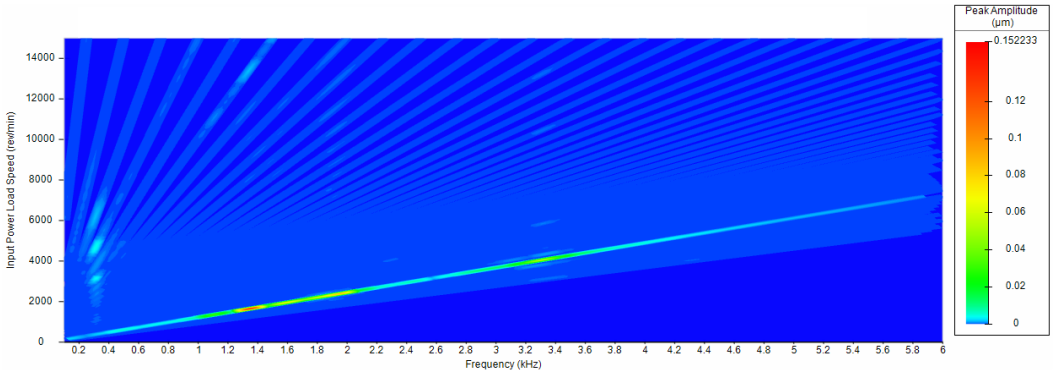

(a) Gear 1

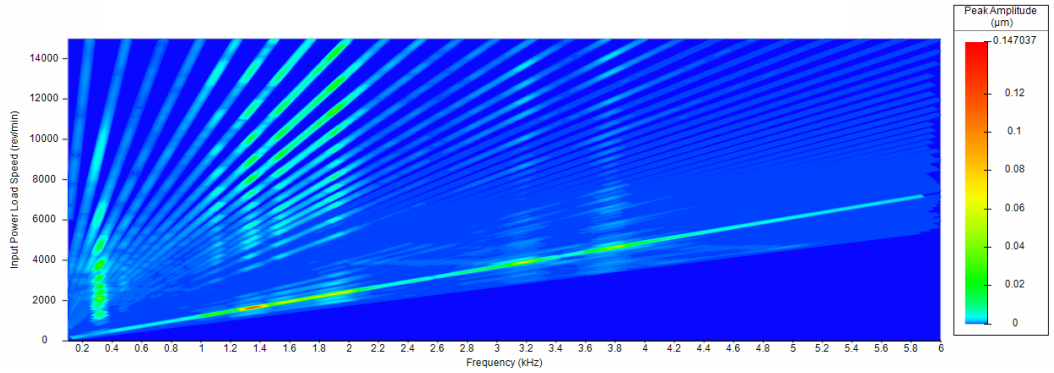

(b) Gear 2

Figure 4.20: Waterfall diagram of the displacements at the inner right bearing.

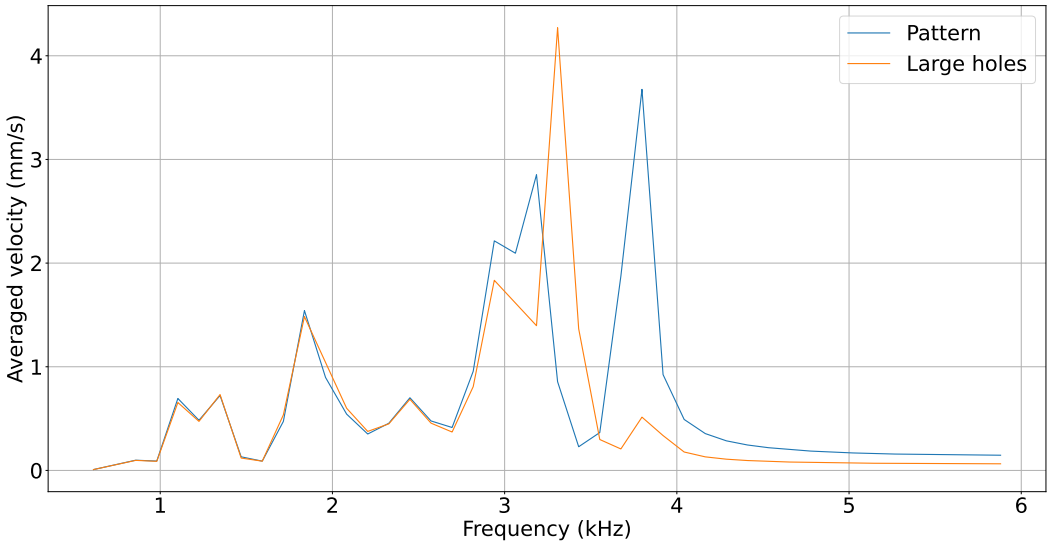

Figure 4.21: Comaparison of the housing RMSV for the 49^{th} order

plot. This effect extends to the energy levels of the sidebands that require a further investigation.

To elaborate, if the aim is to diminish the amplitude of the RMSV peak while shifting it to a higher frequency, the patterned hole configuration is the more suitable choice. Conversely, should the goal be to prevent the emergence of additional resonance peaks and to curtail the amplification of sidebands, the gear with larger holes emerges as a preferable option.

The modal distribution can be better comprehended through an analysis of the strain energy contribution per component associated with the highest response peak of each configuration, as depicted in Figure 4.22. It becomes evident that the more flexible patterned gear is prone to experiencing greater deformation, resulting in a higher strain energy contribution within the system. The increased strain experienced by the patterned gear blank alleviates the vibration of the housing, leading to a reduction in the maximum amplitude when compared to the stiffer blank.

It is intriguing to investigate the dynamic behavior of the system during rotation and its impact on the overall system dynamics. Specifically, as the gears rotate, their contact and bulk stiffness undergo periodic changes. This cyclic variation in stiffness results in slight fluctuations in the resonating frequency of the system, potentially leading to parametric excitation.

Figure 4.23 displays the system's natural modes associated with the resonance peak, corresponding to the 33^{rd} mode for the first gear and the 39^{th} mode for the second gear. These natural modes signify the characteristic frequencies at which the gears tend to resonate and experience heightened vibrations during operation.

For Gear 1, the natural frequency exhibits clear fluctuations occurring at intervals corresponding to the number of holes present in the gear blank. These fluctuations indicate the transitions between positions of higher stiffness and those

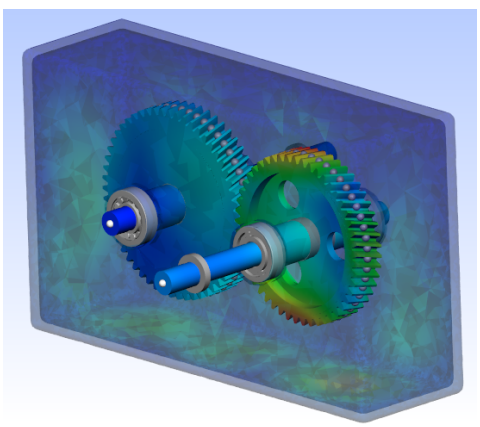

(a) Gear 1: Displacement

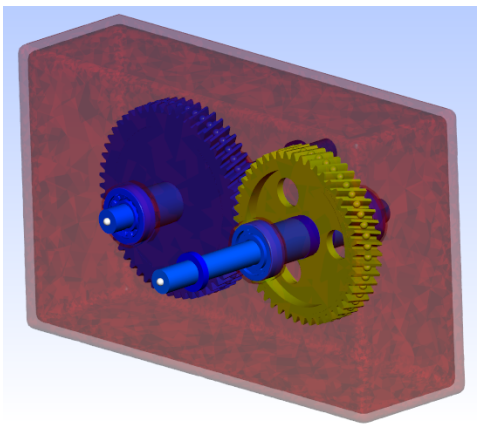

(b) Gear 1: Strain energy

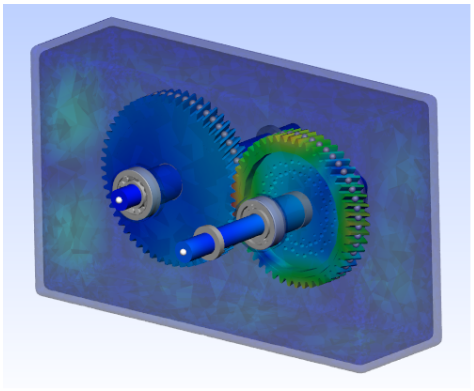

(c) Gear 2: Displacement

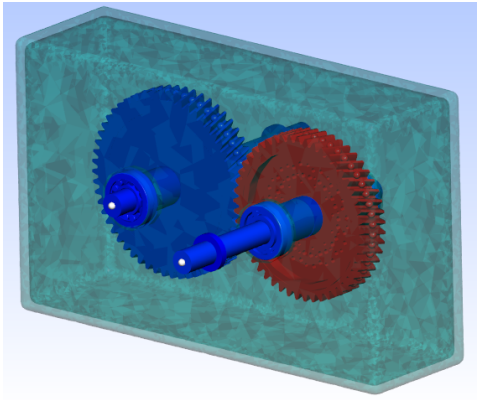

(d) Gear 2: Strain energy

Figure 4.22: Graphical representation of the ODSs and strain energy per component for Gear 1 and Gear 2.

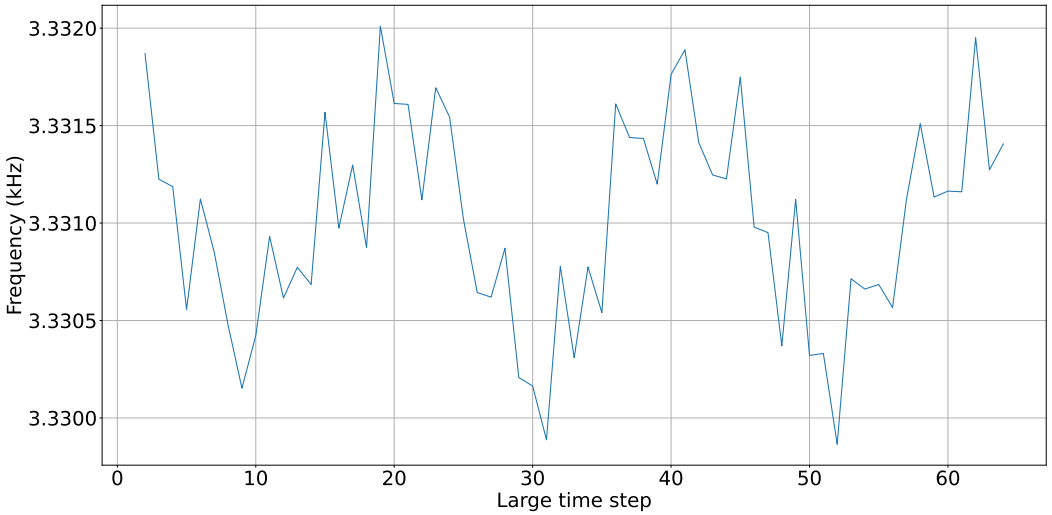

(a) Gear 1: Mode 33

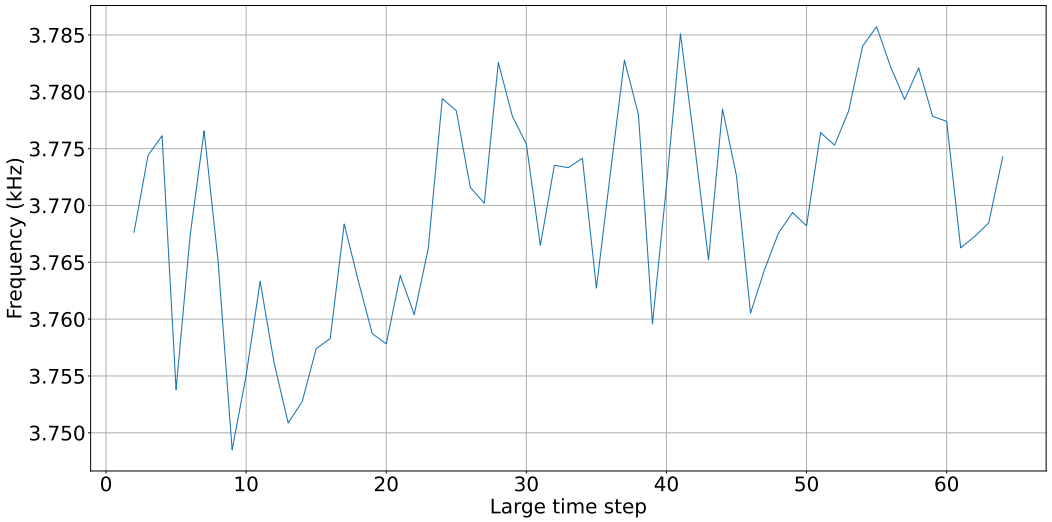

(b) Gear 2: Mode 39

Figure 4.23: Evolution of the resonance frequency modes throughout the rotation of the gear.

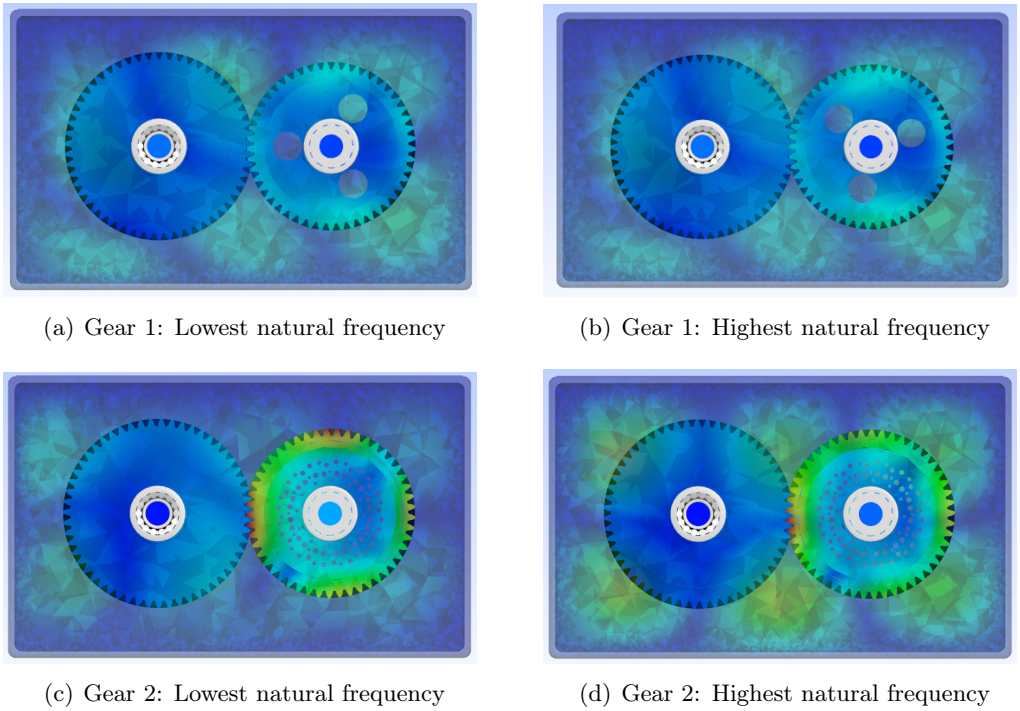

(a) Gear 1: Lowest natural frequency

(b) Gear 1: Highest natural frequency

(c) Gear 2: Lowest natural frequency

(d) Gear 2: Highest natural frequency

Figure 4.24: Comparison of the ODS between the lowest and highest stiffness positions.

of lower stiffness within the gear. On the other hand, in Gear 2 with a patterned configuration, fluctuations are also observed, but they do not seem to follow a specific order related to the pattern creation parameters. These trends strictly depend on the model refinement and the analysis settings.

Although both gears demonstrate a marginal range of variation in natural frequency, Gear 1 displays even less significant variation compared to Gear 2 ($20Hz$ versus $35Hz$), primarily due to its overall higher stiffness.

To gain better insights into the stiffness variation, Figure 4.24 offers a more illustrative visualization of the gear's lowest and highest stiffness positions, as identified through modal analysis. Notably, the patterned gears exhibit a more pronounced influence of stiffness variation, especially when comparing the lowest and highest stiffness positions. In the lowest stiffness position, the gear undergoes more deformation, while the housing experiences less deformation, leading to a reduction in its maximum RMSV.

From these in-depth investigations, we were able to identify the major impacts of conventional and more complicated hole patterns on the dynamic response of the system. For instance, considering that both gears have the same mass, it is more likely that the different distribution of inertia and stiffness makes the patterned gears less flexible and more susceptible to amplifying the response, especially at the lower frequencies. This manifests through a more scattered waterfall diagram in which the energy appears to be smeared over several harmonics, unlike the concentrated

holes where the main order lines usually relate to the number of large holes present in the blank.

After analyzing the results of this investigation, the design optimization can be directed toward two distinct dimensions:

- Spreading the energy over several harmonics: By distributing energy across multiple frequencies, this approach helps achieve a more uniform stress distribution throughout the component. Consequently, stress concentration at specific frequencies is minimized, reducing the risk of resonances and excessive vibrations associated with certain modes. However, it is essential to consider that this approach may result in a more complex design, as the structure must be capable of accommodating a broader range of frequencies. Additionally, the modulation of the signal can become sort of unpleasant noises that are not possible to assess numerically and need to be further studied from a psycho-acoustical perspective.

- Optimizing energy concentration by emphasizing highly energetic orders: This approach aims to focus the energy on specific order lines, resulting in increased energy amplitudes at those particular frequencies. While adopting this approach may lead to heightened energy levels at targeted frequencies, it offers the advantage of reducing the number of frequency bins that need to be considered and therefore offers an easier tuning of the component.

Regardless, of the adopted strategy, the random exploration of different patterns highlights the possibility of improving the dynamic response of the system with respect to the thinly-rimmed solid gear.

4.3.5.3 Establishment of the Pareto front for the series of randomized patterns

To identify the most promising AGBPR-generated designs, we adopted a comprehensive evaluation approach based on three primary objectives. Firstly, we analyzed the maximum amplitude of the fundamental meshing order and its corresponding frequency to understand the maximum vibrational level that the system is likely to achieve. Secondly, we examined the cumulative area under the curves of each order line up to the 55^{th} order, which provided valuable insights into the energy distribution within the system, particularly in the secondary orders.

Figure 4.25 illustrates the progression of response metrics across various designs. Notably, when taking into account the contact and bending static safety factors that were previously adopted, it becomes evident that all data points fall within the feasible set of solutions. This observation highlights the limited impact of the pattern on the static metrics, as the variations do not exceed 2% in comparison to the reference thin-rimmed design.

The graph also highlights the presence of 5 non-dominated solutions referenced as [8, 27, 36, 43, 44] which are highlighted in Figure 4.26.

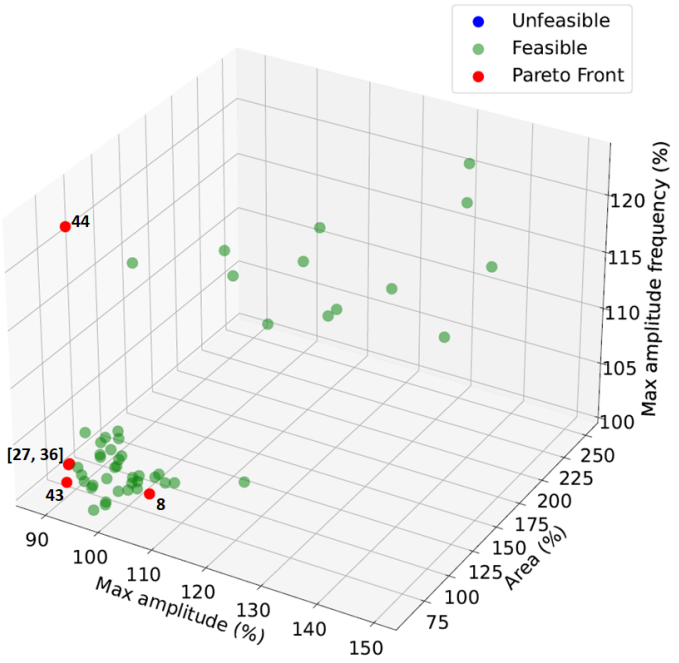

Figure 4.25: Evolution of the dynamic response metrics across the designs.

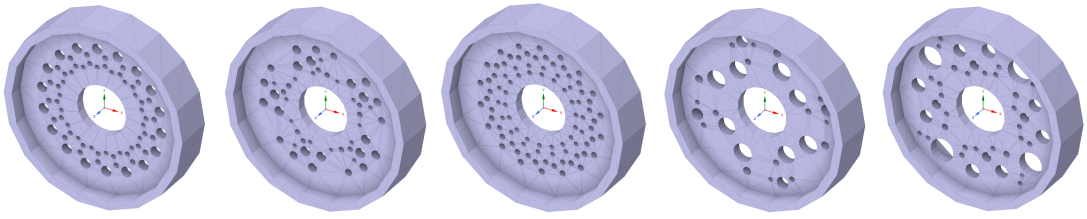

(a) Design 8 (b) Design 27 (c) Design 36 (d) Design 43 (e) Design 44

Figure 4.26: Graphical representation of the non-dominated designs

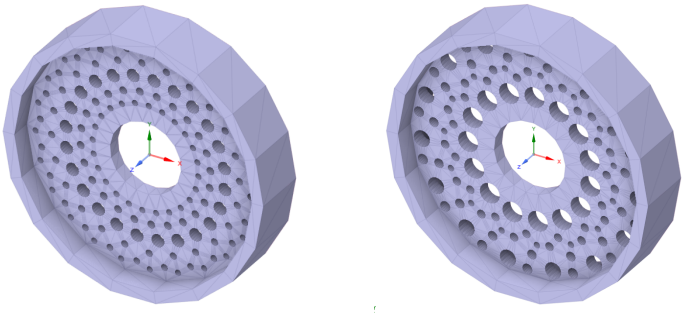

(a) Design 15: Highest maximum averaged velocity

(b) Design 32: Highest energy in the sidebands

Figure 4.27: Graphical representation of the gear blanks with the worst responses.

Visually, establishing clear relationships between gear patterns and their dynamic responses proves challenging. However, upon conducting a manual investigation of several gear blanks, interesting observations emerged. Gears with larger holes positioned near the rim, which influence tooth bending stiffness more significantly, exhibited higher TE modulation and excitations with orders corresponding to the number of teeth.

Conversely, gears with denser patterns of comparable-sized holes, uniformly scattered in the web, showcased a more diverse energy distribution across lower-order lines. This distinction became more pronounced when the holes approached the bore, substantially increasing the torsional flexibility.

Figure 4.27 displays the randomized pattern associated with the highest amplitude and area under the velocity order lines, supporting the previous findings. It highlights that denser hole patterns are more likely to cause a deterioration in the dynamic properties of the gear blank.

Interestingly, while some degradation was noticed for the amplitude responses, the patterns do not appear to significantly affect the frequencies at which the peaks appear. In fact, some of these, notably, the 44^{th} experience an increase in the frequency associated with the peak amplitude. This justifies the equal importances of the pattern parameters in Figure 4.16 (c).

Despite comparing the dynamic response based on average velocity measurements obtained from various sensor positions, the adequacy of these positions in capturing the complete deflection shapes of the gear housing is a valid concern. Particularly, in scenarios where the modal behavior undergoes changes, the chosen sensor positions may not fully encompass the range of deflection modes exhibited by the gear housing during dynamic motion.

This limitation warrants consideration for a more comprehensive assessment of the gear housing's dynamic behavior. Therefore, a thorough investigation was undertaken, focusing on the housing's RMSV for the fundamental meshing order. The results for the non-dominated solutions have been depicted in Figure 4.28. Unlike the scenarios involving thin and rim modifications, the graph illustrates that no

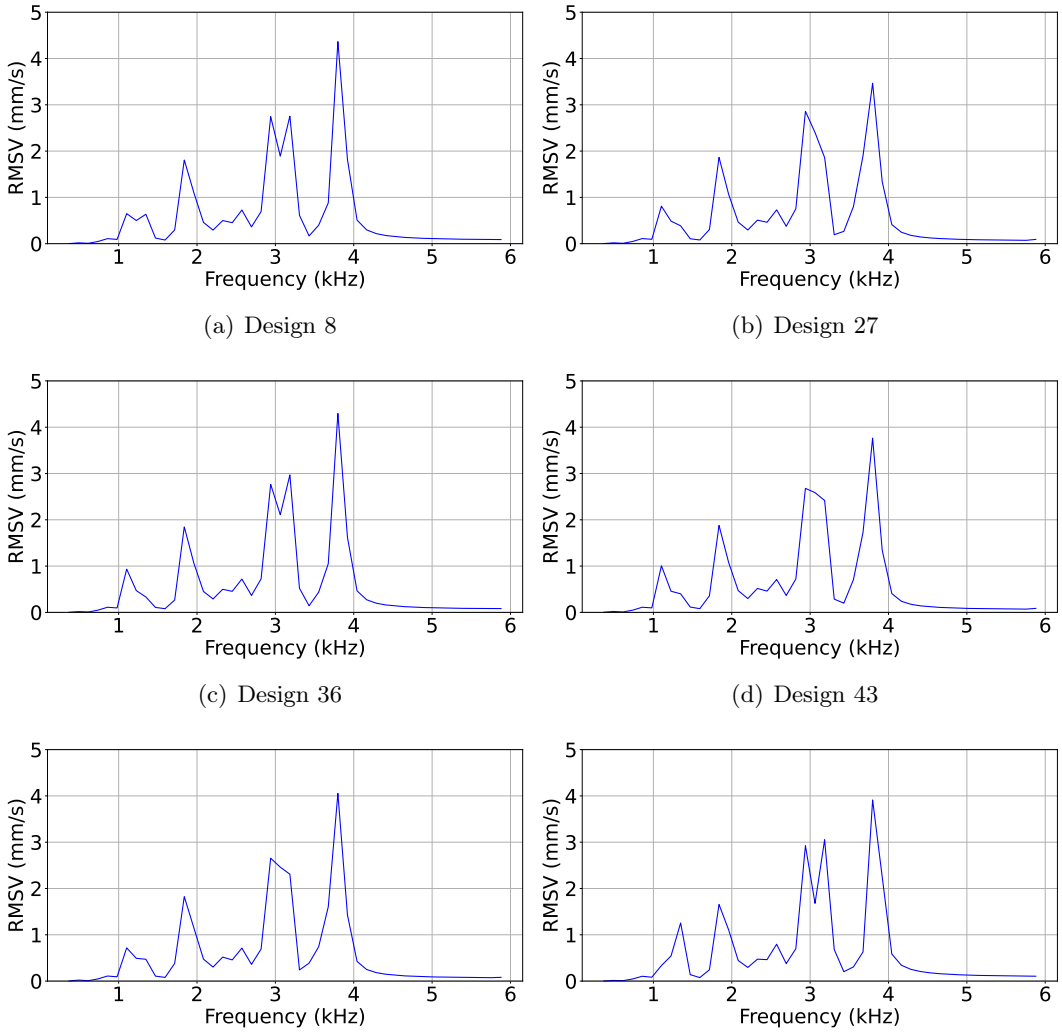

(a) Design 8

(b) Design 27

(c) Design 36

(d) Design 43

(e) Design 44

(f) Default (No Pattern)

Figure 4.28: Fundamental order housing RMSV across the different designs.

significant changes in the modal behavior occur, as there are no observable shifts in the resonance peaks. This can be attributed to the relatively low stiffness and inertia contributions of the holes. As a consequence, the sensor measurement can be considered fairly reliable in this case allowing for a significant decrease in the computation time.

Nonetheless, the investigation reveals noticeable impacts on the amplitude, indicating the transfer of energy between the modes. It is noteworthy that the pattern of changes in peak amplitudes varies, with some modes being amplified while others are reduced. This observation highlights the potential of holes in further optimizing the gear blank.

However, it is essential to acknowledge that these conclusions may not be universally applicable to all designs. In this specific example, the web width is initially

thin, resulting in a relatively small volume occupied by the holes compared to the overall volume of the blank. Consequently, the induced mass reduction by the holes is less significant. It is conceivable that in a thicker blank, the mass reduction from the holes could be more substantial, leading to more drastic changes in the peak amplitudes and the frequencies at which they occur.

4.4 Conclusion

In this section, we were interested in investigating the effect of lightweight gears on the static and dynamic behavior of the housing targeting the change of the web and rim dimensions, followed by applying a pattern of holes in the web. The analyses have shown that the geometry of the gear influences the static metrics, namely, the transmission error. However, the influence of the excitation remains minor compared to the change induced by the dynamic tuning of the gear blank.

The different combinations of the rim and web dimensions have resulted in the presence of several local minima in the housing RMSV response which indicates that standard gears are over-designed and that it is possible to achieve mass and dynamic response reduction simultaneously.

In the second stage, an AGBPR algorithm was used to generate random patterns of holes and study the dynamic implications of their different distributions. Considering the small relative value volume of the holes compared to the optimized gear blank thicknesses, they are likely to displace the blank from its tuned mass and inertia. However, since the holes come with stiffness fluctuations, the transmission was analyzed for a full rotation of the input gear to consider the excitation sidebands.

The results were compared in terms of the averaged velocity from 5 sensors positioned in the front rectangular face of the gearbox, the frequency at which the main peak occurs, and the area under the individual velocity order lines.

A sensitivity analysis considering parameters that represent the statistical distribution of the holes within the web has shown that the overall size of the holes contributes the most to the response amplitude-wise. However, the level of correlation remains weak considering the complex nature of interactions between the parameters.

Subsequently, the outcomes were plotted against the three objectives, leading to the establishment of a Pareto front comprising solutions that were non-dominated. This front revealed additional enhancements over the thin-rimmed configuration. The validation was conducted by comparing the RMSV linked to the fundamental orders. While the sidebands might necessitate further investigation, certain insights can be gleaned from an analysis of the energy distribution across the accelerometers. In simpler terms, designs characterized by elevated amplitude velocity in secondary orders should logically correspond to augmented amplitudes in secondary orders of the RMSV as well.

Chapter 5

Enhancing Weight and Dynamic Response Optimization with a Dual-Level Particle Swarm Optimization Scheme

Contents

5.1 Introduction

The examination of how the weight reduction strategies impact on the static and dynamic responses of a gearbox has underscored the crucial significance of perforated thin-rimmed lightweight gears. These gears play a pivotal role in not only trimming down overall weight but also enhancing the dynamic performance of the system.

Our investigation delves into the realm of optimizing gear designs by generating a multitude of random combinations of design variables. Through this process, we establish a Pareto front consisting of non-dominated solutions that effectively meet our design criteria: minimizing weight while optimizing dynamic response. However, the success of this endeavor is linked to the initial population of randomly generated

solutions. In essence, the crux lies in whether these designs align with the local or global optima of the problem.

This challenge is further magnified when dealing with intricate designs demanding the fine-tuning of multiple components. As the complexity increases, so does the multitude of potential designs, and it becomes imperative to encompass as many of these design possibilities as feasible.

Hence, the central objective of this chapter takes shape: to devise an optimization framework that capitalizes on the insights gleaned from prior results and sensitivity analyses. This framework serves as a guide, streamlining the pursuit of optimal solutions within a reduced number of iterations. In doing so, we navigate the landscape of design possibilities with the aim of uncovering superior solutions efficiently and effectively.

5.2 Development of a dual-level PSO-based lightweight gear optimization scheme.

In the face of intricate engineering problems characterized by complex interactions and non-linear behaviors, metaheuristic-type algorithms emerge as strong contenders. These algorithms possess a unique adaptability that enables them to effectively navigate the wide landscape of potential solutions. They offer a distinct advantage in their ability to foster diversity within the solution pool. This diversity, which is established through the population of potential solutions, facilitates a thorough exploration of the problem's nuances. Consequently, this approach aids in identifying unconventional yet impactful solutions that might remain hidden when using traditional methods.

Furthermore, metaheuristics are particularly well-suited for scenarios where explicit problem formulations and precise mathematical descriptions are challenging to establish. By treating the problem as a "black box", they provide a versatile platform for optimizing systems that are influenced by real-world complexities, uncertain parameters, and intricate relationships.

The utility of metaheuristics has been widely embraced across an extensive spectrum of problems, spanning from singular objectives to multifaceted. In the context of transmission system applications, several metaheuristic-based optimization studies can be found treating all sorts of objectives such as power loss [10], gearbox weight [13], and mesh excitation [16].

Several studies have also focused on the single objective of reducing the weight [15], or the volume of the gearbox [19] using population-based or trajectory-based metaheuristics such as genetic algorithms and simulated annealing. While other studies addressed the trade-offs that can be made by further considering the load carrying capacity [132], power losses [173], power and efficiency [111], or contact stresses and transmission error [85].

These approaches can be scaled to tackle all sorts of gearboxes at different levels of complexity spanning from single-stage transmissions, two-stage [117], up to multi-

stage gearboxes [16]. They were also adopted to optimize the macro and micro geometries for various kinds of gears including cylindrical [73, 28, 179], bevel [136, 17], and planetary [116, 25, 27].

While various metaheuristics exist, Genetic Algorithm (GA), particularly, the Non-dominated Sorting Genetic Algorithm II (Non-dominated Sorting Genetic Algorithm II (NSGA-II)) remain the most common. The NSGA-II algorithm's prominence lies in its capacity to effectively establish the Pareto front comprising non-dominated solutions. Subsequently, during the decision-making phase, a singular solution can be meticulously selected based on the discerned objective preferences.

However, in the context of our problem, we chose to utilize a population-based algorithm known as Particle Swarm Optimization Particle Swarm Optimization (PSO) as it seemed to perfectly fit the characteristics of our problem. For instance, the PSO has been selected considering the following factors:

- The continuity and smoothness of the search space, i.g, the variables can be selected between the upper and lower bounds instead of discretized values.
- The speed of convergence for a smaller initial population compared to GAs.
- The ease of implementation given the lower number of convergence parameters to be tuned.

The PSO algorithm is a nature-inspired optimization technique that models the behavior of a swarm of particles to search for optimal solutions in a multi-dimensional search space. Given a fitness function $f(x)$ to be minimized, where x represents a multi-dimensional vector of parameters, the PSO algorithm initializes a swarm of particles with random positions and velocities in the search space. Each particle i is characterized by its position $\mathbf{x}_i = (x_{i1}, x_{i2}, ..., x_{id})$, where d is the dimensionality of the problem, and its velocity $\mathbf{v}_i = (v_{i1}, v_{i2}, ..., v_{id})$.

The position update equation for each particle i is given by:

$$\mathbf{v}_i(t+1) = w\mathbf{v}_i(t) + c_1 r_1(\mathbf{p}_i - \mathbf{x}_i(t)) + c_2 r_2(\mathbf{p}_{global} - \mathbf{x}_i(t)) \tag{5.1}$$

where:

- w is the inertia weight that controls the impact of the particle's previous velocity.
- c_1 and c_2 are the cognitive and social acceleration coefficients that control the impact of the particle's personal best ($\mathbf{p}_i$) and the global best positions ($\mathbf{p}_{global}$), respectively.
- $\mathbf{r}_1$ and $\mathbf{r}_2$ are random vectors.
- t represents the current iteration.

In the following iteration the velcity vector $\mathbf{v}_i(t+1)$ is used to update the current position vector to $(\mathbf{x}(t+1))$ as follows:

$$\mathbf{x}_i(t+1) = \mathbf{x}_i(t) + \mathbf{v}_i(t+1) \tag{5.2}$$

The personal best position of each particle $\mathbf{p}_i$ is updated based on its current fitness value and previous personal best:

$$\mathbf{p}_i = \begin{cases} \mathbf{x}_i & \text{if } f(\mathbf{x}_i) < f(\mathbf{p}_i) \\ \mathbf{p}_i & \text{otherwise} \end{cases} \tag{5.3}$$

The global best position $\mathbf{p}_{global}$ is updated by selecting the best position from the entire swarm. The PSO algorithm iterates through these steps until a termination criterion is met, in this case, a maximum number of iterations was implemented as shown in Figure 5.1.

To create patterned thin-rimmed gears, the PSO process is conducted in two distinct stages. The initial level is focused on refining the gear masses through adjustments to the rim and web thicknesses. Subsequently, the second stage is employed to optimize the distribution of patterns. These stages differ not only in their analysis approaches but also in terms of the outputs used for evaluating the fitness and the overall PSO convergence process overall. The specifics of the formulation will be comprehensively elaborated upon in the subsequent discussion.

5.2.1 Web and rim thickness optimization: Level 1 PSO formulation

In the first stage of PSO a position vector $\mathbf{x}_i$ is created with its dimensions equal to $2 \times N_g$ which represents the web and rim thicknesses for all the N_g gears that are present in the gearbox.

In the case of a single-stage gearbox, the particles' positions vector can be written as $\mathbf{x}_i = (W_{i1}, R_{i1}, W_{i2}, R_{i2})$ with W_i and R_i representing respectively the thicknesses of the web and rim of the i^{th} of each gear for the i^{th} particle. The values for the initial generation are generated at random according to the following conditions:

$$W_{min} < W_i < W_{max}$$
$$R_{min} < R_i < R_{max}$$

The minimum and maximum thickness values play a pivotal role in defining the extent of material removal from the blank. The selection of these values can be informed by a preliminary analysis of the gear, identifying critical thickness thresholds that could trigger intense amplification of dynamic response.

The position vector serves as the initiator of two simultaneous processes. Firstly, it triggers the generation of the LTCA mesh within the MASTA software, facilitating tooth contact analysis and the subsequent determination of meshing stiffness. Secondly, the data is relayed through an external sub-routine to Spacelcaim. In

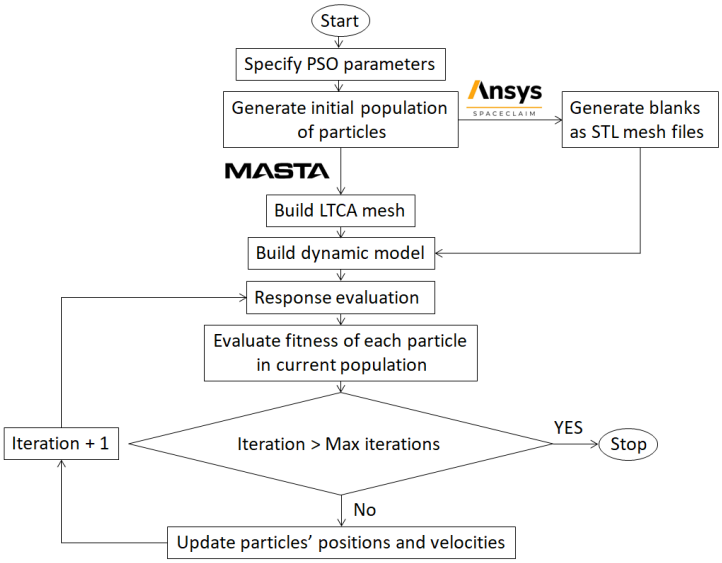

(a) PSO scheme

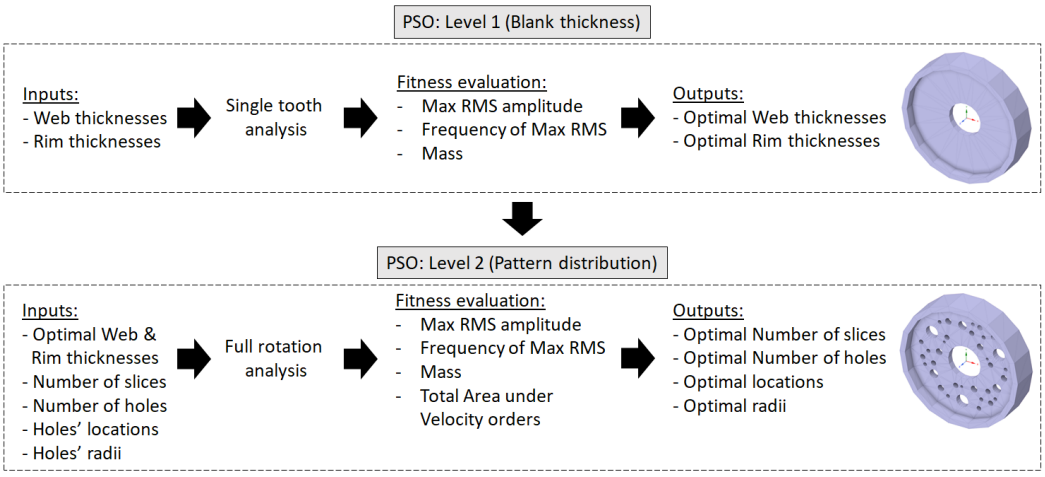

(b) Evaluation process per optimization level

Figure 5.1: Optimization scheme

this stage, the gear is formulated and meshed according to desired specifications, subsequently integrating it back into the dynamic model.

During each iteration, we compute and normalize several key parameters with respect to their initial design values. These parameters include the total mass of the system, denoted as M_{total}, static safety factors, the maximum amplitude of housing RMSV $A_{RMSV_{max}}$, and its corresponding frequency $F_{RMSV_{max}}$:

$$Output_{Norm} = \frac{Output}{Output_{Ref}} \tag{5.4}$$

The fitness function F for a single-tooth analysis is therefore defined as:

$$F_{single-tooth} = w_1 A_{RMSV_{max}} + w_2 F_{RMSV_{max}} + w_3 M_{total} \quad \text{with} \begin{cases} w_1, w_3, w_4 > 0, \\ w_2 < 0. \end{cases} \tag{5.5}$$

The values of $w1$, $w2$, and $w3$ correspond to the user-defined output weights, allowing the user to discern the preferred objectives based on the requirements of the problem. In the current context, the highest weight has been assigned to the maximum RMSV amplitude.

To address the considerations of static contact and bending constraints, an auxiliary penalty function has been incorporated into the fitness function. This penalty function plays a pivotal role in discouraging the algorithm from converging towards infeasible solutions by imposing higher fitness values on solutions that breach the defined constraints. Essentially, this mechanism establishes a strong deterrent against solutions that deviate from the defined constraints (when safety factors are below the minimum allowable values), thereby guaranteeing that the optimization process stays in harmony with the desired feasibility criteria. This enhancement of fitness values is accomplished by introducing a penalty factor into the fitness calculation.

$$F_{single-tooth} = \begin{cases} F_{single-tooth} + P, & \text{if } S_F < S_{F_{min}} \text{ or } S_H < S_{H_{min}} \\ F_{single-tooth}, & \text{otherwise} \end{cases} \tag{5.6}$$

5.2.2 Level 1: Results

In our pursuit of developing an optimization algorithm that not only delivers superior results but also converges rapidly, we conducted a series of experiments, focusing on fine-tuning the control parameters of the PSO algorithm. These parameters include the cognitive coefficient (c_1 and c_2), and the associated weights related to the maximum RMSV amplitude and its corresponding frequency.

Figure 5.2 presents a selection of simulations conducted during our parameter experimentation. Due to computational constraints, our analysis was based on 10 iterations, employing 5 particles. The aim was to assess the trade-off between the speed of convergence and the quality of results achieved.

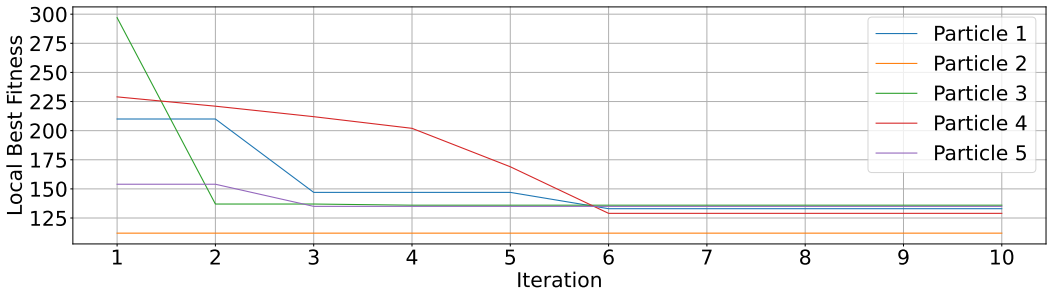

(a) Increased c_2 and $w1$: Generation 1

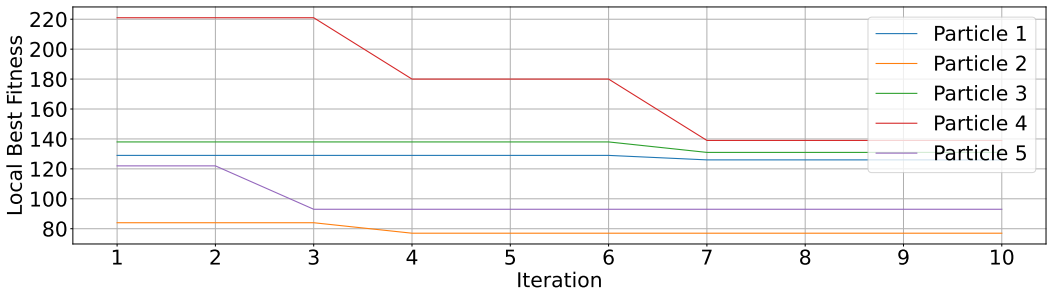

(b) Increased c_1 and $w1$

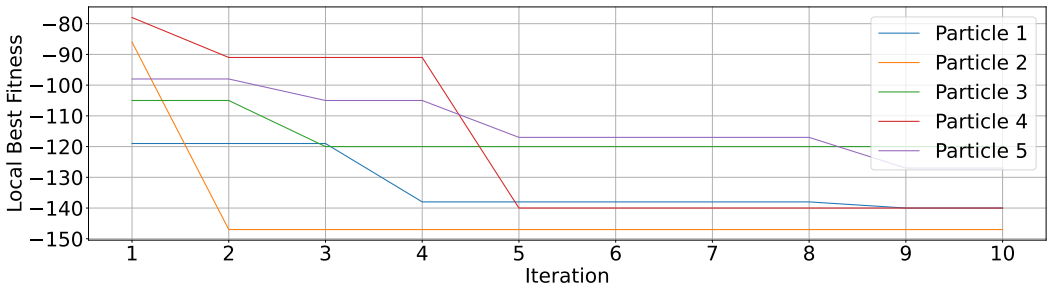

(c) Increased c_2 and $w2$

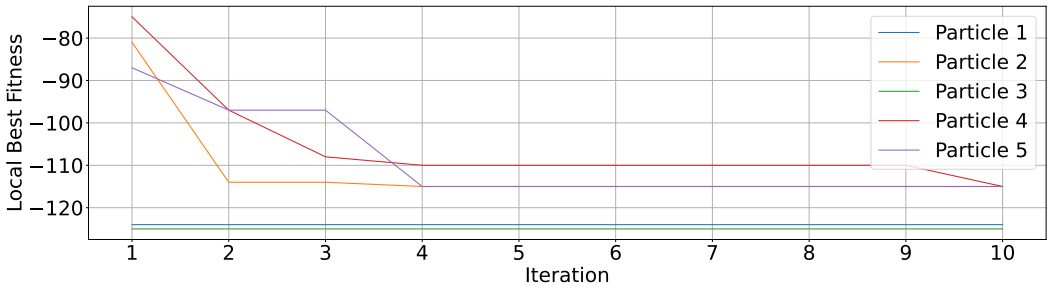

(d) Increased c_1 and $w2$

Figure 5.2: Effect of the cognitive and social coefficients (c_1 and w_2) on the convergence of the PSO in the case of higher Amplitude weight (w_1) and Frequency weight (w_2).

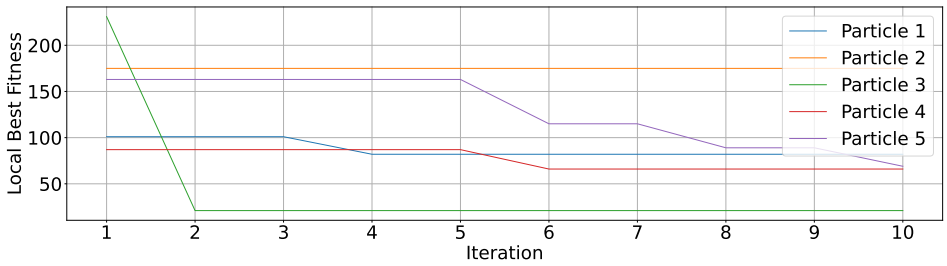

Figure 5.3: Increased c_2 and w_1: Generation 2

Notably, experiments where the social coefficient c_2 was increased in comparison to the cognitive coefficient c_1 demonstrated a significantly accelerated overall convergence, often converging in approximately half the number of the input iterations.

We further scrutinized the results by summarizing the inputs corresponding to the lowest fitness values in Table 5.1. It became evident that experiments with higher c_2 values tended to produce a relatively thicker rim as the solution that minimizes the fitness function. This can be attributed to the inherent non-linearities encountered when examining the evolution of the maximum RMSV response concerning the mass of the blanks.

In essence, a higher social coefficient c_2 encourages the swarm to embark on a more extensive exploration in the vicinity of the best-known global position, even if it doesn't necessarily align with the global optimum. This increased emphasis on exploring globally can, at times, constrain the search for optimal solutions individual particles might possess, potentially hindering the discovery of superior solutions elsewhere.

Conversely, the cognitive coefficient c_1 exerts significant control over how the swarm's best-known position affects the velocity update of an individual particle. This control mechanism fosters a more intensive exploration of the search space, enabling the particle to explore various local minima in greater detail. This heightened exploration often results in more refined solutions, which clarifies why this approach consistently yielded gears with lower mass compared to analyses conducted with higher social coefficients.

It's worth emphasizing that both analyses can be improved significantly by increasing the number of iterations and particles. In fact, a subsequent iteration, as demonstrated in Figure 5.3, which places a stronger emphasis on global exploration and reduces amplitude, has produced markedly superior results. These results approach the solution obtained when using a higher cognitive coefficient, underscoring the significant influence of the initial conditions. Furthermore, the observation that convergence is achieved with fewer iterations compared to the initial setup suggests that it may be more effective to boost the number of particles to facilitate early exploration and consequently reduce the number of required iterations.

Nevertheless, these results underscore the algorithm's capability to achieve substantial reductions in gear mass, even when operating with relatively conservative

Table 5.1: Optimized dimensions and mass results.

	Increased c2 and w1 GEN1	Increased c2 and w1 GEN2	Increased c1 and w1	Increased c2 and w2	Increases c1 and w2
Web thickness 1 (mm)	7.8	8.9	4.9	4.8	12.7
Rim thickness 1 (mm)	28.6	16.5	7.7	28.6	9.7
Mass 1 (Kg)	1.1	0.95	0.63	1.08	0.93
Web thickness 1 (mm)	9.5	4.9	4.8	13.6	10
Rim thickness 2 (mm)	22.7	6.5	6.5	7.7	6.5
Mass 2 (Kg)	1.32	0.79	0.78	1.21	1.03
Total mass (%)	50.41	30.24	30	46.53	39.46

Table 5.2: Housing RMSV amplitude and frequency results.

	Reference	Design 1	Design 2	Design 3	Design 4
Amplitude (mm/s)	5.28	4.77	0.72	3.37	2.95
Improvement (%)	0	10.69	633	56.67	79
Frequency (kHz)	4.27	3.4	2.86	3.56	3.71
Improvement (%)	0	-25.58	-49.3	-19.94	-15

parameter settings. In fact, the algorithm was able to achieve a noteworthy mass reduction of up to 70% with reference to the standard design under these conditions.

Furthermore, the control over the optimization process can be fine-tuned by adjusting the Frequency weight w_2 within the fitness function. This adjustment can lead to the production of stiffer gears with peak frequency characteristics shifted to the right, offering more control over the gear's performance.

An alternative approach to expedite convergence and refine the optimization is to introduce additional geometric constraints. These constraints may involve limiting the rim's thickness to a narrower interval or incorporating greater variability in the velocity vector related to the web thickness. Such adjustments can further enhance the algorithm's ability to optimize gear designs effectively

To effectively illustrate the impact of optimized gear designs on the dynamic response of the housing, we examined the RMSV responses in Figure 5.2 and compared them to the reference design, as depicted in Figure 5.4. As anticipated, all simulations exhibited a noteworthy reduction in peak amplitude, accompanied by a slight leftward shift in frequency. Of particular interest is the second optimized design, which stands out not only for its lightweight characteristics but also for delivering a substantial 633% reduction in RMSV amplitude, as detailed in Table 5.2.

The designs that yielded the lowest RMSV values, namely, designs (2) and (4), were selected to initiate the second phase of pattern optimization.

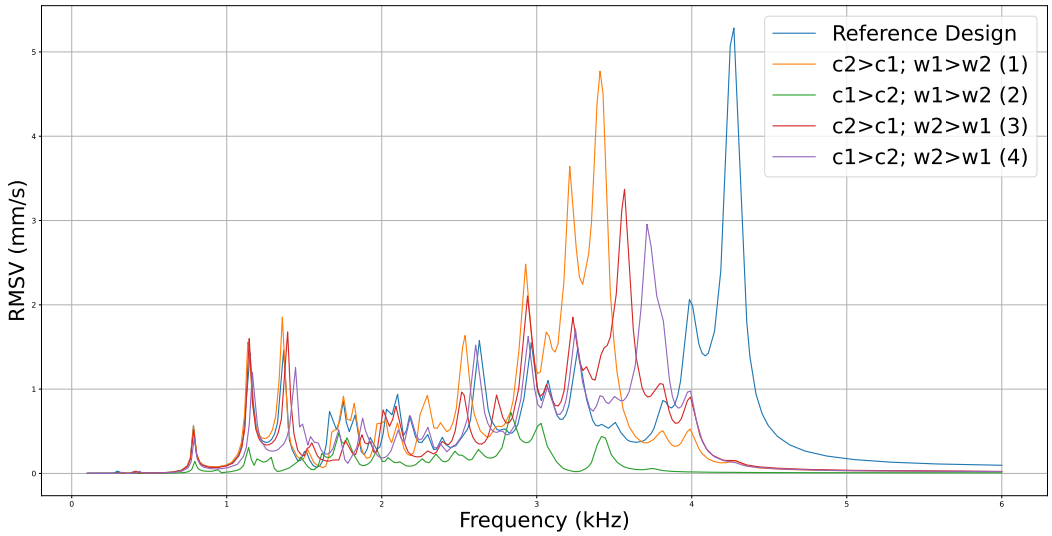

Figure 5.4: Housing RMSV outputs for the web and rim thickness optimization.

5.2.3 Pattern distribution optimization: Level 2 PSO formulation

In the context of pattern optimization, the application of PSO becomes notably intuitive, as it transforms the problem into a swarm of holes tasked with exploring the gear blank. These holes dynamically adjust in size and position until they collectively discover the optimal distribution that minimizes the fitness function.

The initial implementation of PSO in the first optimization stage is relatively straightforward. However, integrating it into the second stage poses a higher level of complexity, primarily stemming from several factors. One significant challenge emerging from the pattern-generation process is the dynamic generation of holes, which leads to a non-constant number of holes. This introduces complexity to the problem as the number of parameters defining the pattern will vary from one iteration to the next.

To address this challenge, a dynamic approach is typically employed to handle these parameters. This dynamic approach necessitates ongoing adjustments to the number of variables as the algorithm advances. However, implementing this process is exceptionally complex due to the complex relationships between the parameters governing the creation of the holes and the constraints that define the geometric boundaries of the gear blank.

To address this issue, we employed an alternative approach that incorporates pattern distribution parameters introduced in the previous chapter. These parameters were utilized as indirect variables, allowing us to regulate particle positions. Specifically, for each particle's primary position vector p_i^d, which outlines the circle parameters, we introduced an additional positions vector denoted as p_i^{ind}. This supplementary vector encompasses the pattern distribution parameters, including the centroid position, mean hole radius, and skewness.

The procedure initiates by creating an initial population of particles, comprising

a set of N patterns generated using the AGBPR. These patterns are defined by their direct and indirect position vectors. The fitness function is based on the weighted sum of the metrics established in equations 4.23, 4.22, 4.24 as well as the total mass of the gears M_{total}. The only adjustment is made to the cumulative area function to only account for the energy level in the sidebands by excluding the fundamental harmonic (order 49 in this case):

$$E_{sidebands} = \sum_{k=1,k\neq m}^{N_o} E_k \tag{5.7}$$

The Fitness function is therefore expressed as:

$$F = w_1 \max_{\omega} A_{avg} + w_2\omega_{max} + w_3 M_{total} + w_4 E_{sidebands} \quad \text{with} \begin{cases} w_1, w_3, w_4 > 0, \\ w_2 < 0. \end{cases} \tag{5.8}$$

In each iteration, the personal and best indirect position vectors are maintained and then updated along with the velocity vectors for the next iteration. However, a challenge arises when generating the subsequent pattern: translating the indirect position vector into a direct position vector. This complication is due to the absence of a clear, explicit formula for converting distribution parameters back into individual hole parameters as there are infinite possibilities to generate holes that have the same distribution characteristics. Consequently, achieving a direct position vector that perfectly aligns with the desired indirect parameters proves to be unattainable.

Furthermore, even if attainable, this translation gives rise to another obstacle. The challenge lies in ensuring that the newly generated holes, intended to meet the indirect parameters, adhere to the geometric constraints and contribute to a feasible gear blank. This necessitates the assurance that the holes neither interfere with one another nor transgress the boundaries of the permissible area.

To address these challenges, an iterative approach was employed. Instead of generating entirely new sets of holes to precisely match the newly updated indirect position vectors, a series of iterations involving randomly generated patterns was conducted. The iteration that exhibits the closest convergence to the updated target indirect position vector is selected. This selection process is safeguarded through introducing a pattern error function, designed to quantify the alignment between the distribution parameters of the randomly generated pattern and the desired updated indirect positions. This error function is individually defined for each particle as follows:

$$\varepsilon = \sum_{i=1}^{n}\sum_{j=1}^{m} e_{ij} W_j \tag{5.9}$$

where:

- n represents the number of gears.

- e_{ij} represent the absolute error for gear i and metric j.
- W_j represents the weight assigned to metric j.

In our scenario, the total number of generations was set to 100. Among these generations, the one that minimizes the error ε between the computed and target pattern distribution parameters within the updated indirect position vectors is selected. The associated hole parameters extracted from this chosen generation are subsequently utilized as the new direct positions vector to update the design and the iterative process proceeds.

It is noteworthy that the weights W_j draw inspiration from the sensitivity analysis conducted in the preceding chapter. Greater emphasis is assigned to the most influential pattern distribution parameters by allocating them higher weights.

This method ensures a controlled random generation process, wherein only designs converging toward the most optimal solutions are generated. This stands in contrast to the previous approach characterized by a fully randomized process. For a better understanding, the process is visualized in Figure 5.5.

5.2.4 Level 2: Results

The analyses were conducted for 5 iterations and 7 particles. For the second thin design, the weights of the fitness function were adjusted so that more importance is attributed to minimizing the amplitudes within the fundamental order and sidebands whereas the focus was on minimizing the frequency shift for the fourth design.

The pattern optimization convergence plot is shown in Figure 5.7 tracking the evolution of the local best fitness for each particle. While the convergence quality can be further optimized through a parametric study, even a few iterations are enough in order to considerably decrease the fitness function leaving a selection of designs associated with the local best fitness of each particle that can be studied separately.

In order to focus on the validation process, the designs associated with the global best fitness were taken as shown in Figure **??**. The normalized responses are summarized in table **??**.

5.3 Acoustic validation

An extensive acoustic analysis was undertaken to gain a deeper understanding of the acoustic implications resulting from the utilization of the optimized lightweight gears. This analysis draws upon the excitation generated within the mesh structure and leverages the RMSV data obtained from the housing. This approach facilitates a comprehensive assessment of acoustic performance.

To accurately simulate the acoustic response of the housing under the influence of a vibrational excitation, a comprehensive acoustic model is constructed. This modeling process begins with the creation of a specialized surface mesh, often referred

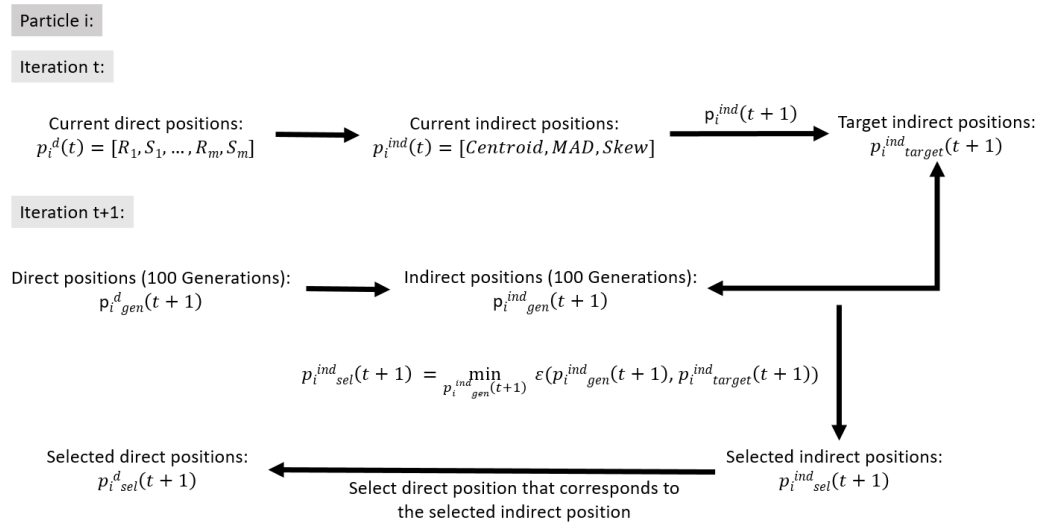

(a) Process

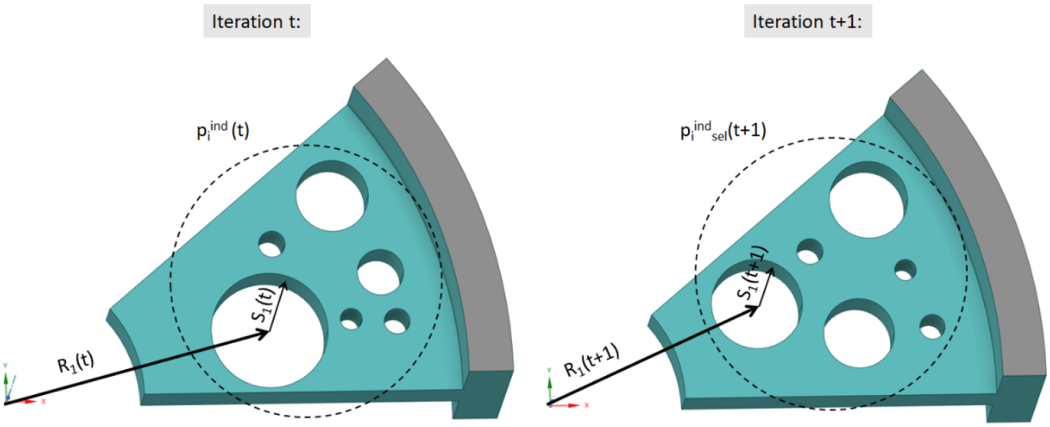

(b) Results

Figure 5.5: Design pattern update convergence scheme based on the indirect position vectors.

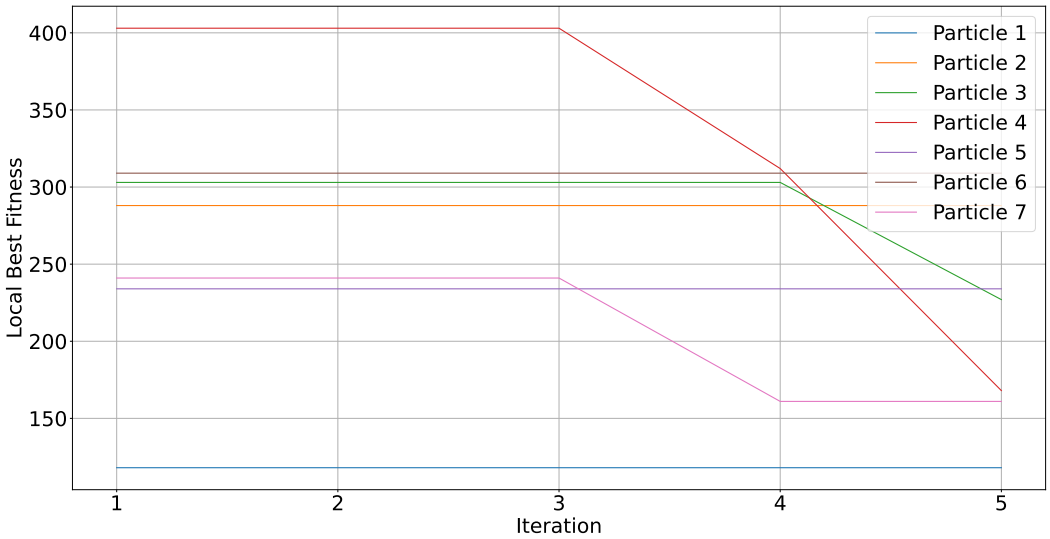

(a) Design (2)

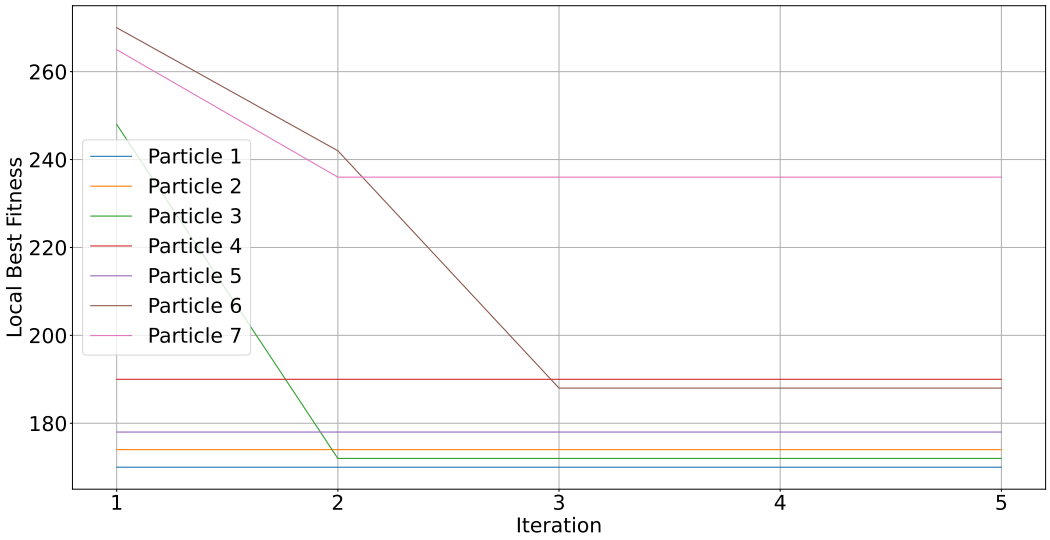

(b) Design (4)

Figure 5.6: Progression of local best fitness among particles across iterations

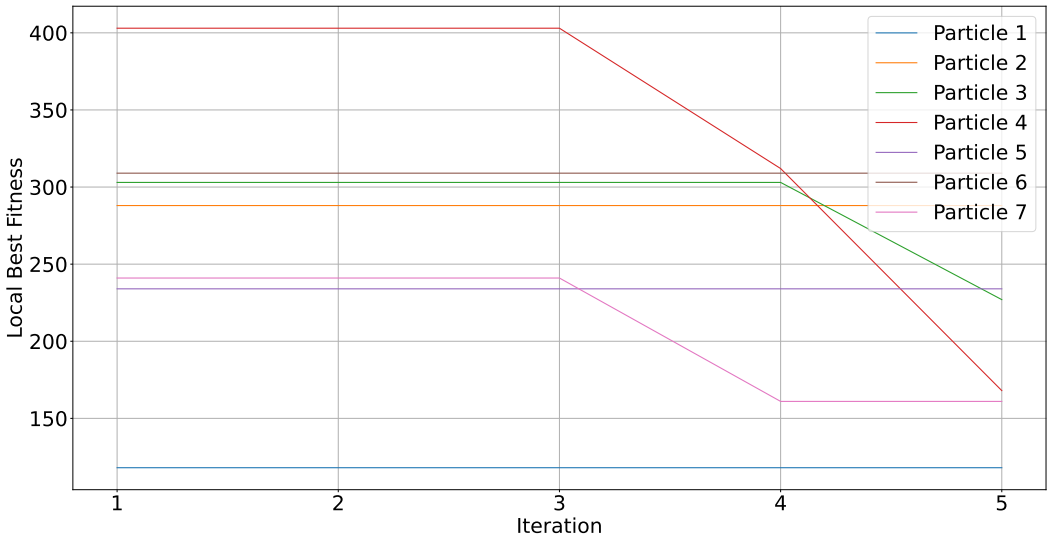

(a) Design (2)

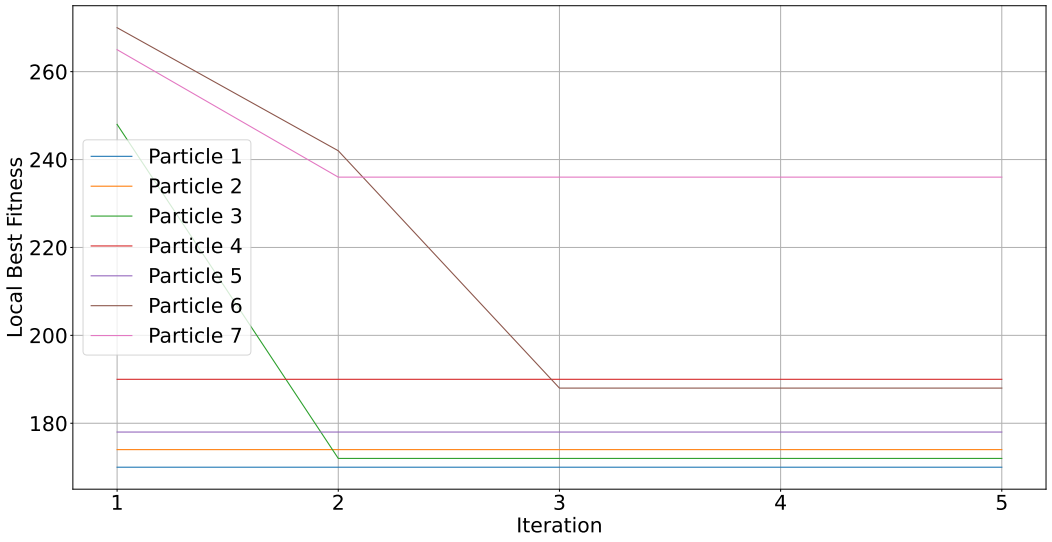

(b) Design (4)

Figure 5.7: Progression of local best fitness among particles across iterations

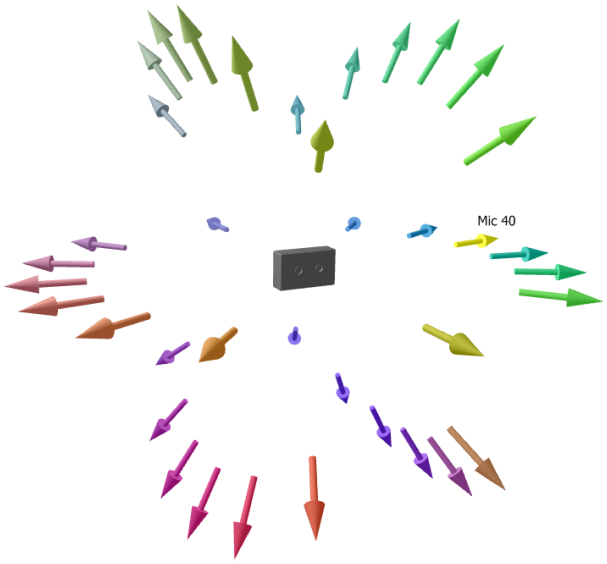

Figure 5.8: Graphical representation of the positioning of measurement microphones around the housing.

to as a "Shrinkwrap" mesh. This mesh closely approximates the outer boundaries of the solid housing while also defining the inner surface of the acoustic mesh.

Subsequently, a three-dimensional volume mesh is generated to establish the acoustic near-field. This volume mesh is typically created using an efficient cubic meshing technique. To enhance the accuracy of the simulation and minimize the impact of unwanted reflections, a Perfectly Matched Layer Perfectly Matched Layer (PML) technique is employed. The PML acts as an absorptive boundary layer, effectively dampening the reflection of acoustic waves at the computational boundaries. This allows for a more precise assessment of pressure and sound behavior beyond the acoustic finite element mesh.

In order to pick up the pressure waves emitted from the radiating housing. A total of 40 microphones were positioned spherically according to ISO 3744 standards with a distance of $1m$ with respect to the center of the housing. The microphone positions on the imaginary spherical surface surrounding the source and ending on the reflecting plane are shown in Figure 5.8.

The A-weighted airborne sound pressure level L_{pA} is calculated by taking the logarithmic average of the weighted sound pressures measured at multiple microphones. Each individual sound pressure level L_{pj} is first adjusted to account for the sensitivity of the human ear at different frequencies using the corresponding A-weighting factor A_j. The adjusted sound pressures are then summed across all microphones, and the result is expressed in decibels (dB) as follows:

$$L_W = 10\log\left[\sum_j 10^{0.1(L_{p_j}+A_j)}\right] + 10log\left(\frac{S}{S_0}\right)\text{dB} \tag{5.10}$$

where:
L_{pA} is the A-weighted airborne sound power level in decibels.
L_{p_j} is the measured sound pressure level in decibels (dB) at the j^{th} microphone.
A_j is the A-weighting correction factor for the j^{th} microphone's frequency band.
S is the surface area of the housing's radiating surface.
S_0 is a reference surface taken as $1m^2$.

Through the utilization of optimized gears across all excitation orders, we generated the graphs presented in Figure 5.9. In cases where the fitness function was fine-tuned to prioritize the frequency range over amplitude reduction, it is noteworthy that design (4) succeeded in reducing the mass of the gears with minimal impact on the noise produced by the housing. An intriguing observation is that while the slender version exhibits higher excitation levels in lower-order harmonics, reaching up to $60dB$, the textured version avoids this issue, with only the primary fundamental order displaying significantly high amplitude.

In the broader context, the pattern choice seems to have a negligible effect on acoustics, especially concerning the fundamental order, as highlighted in the preceding chapter. However, the primary distinction lies in the shapes of the plots and the emergence of resonance peaks, particularly noticeable in the secondary orders.

It's crucial to acknowledge that due to computational constraints, the inclusion of system modes was limited, and thus, the influence of higher-frequency modes on those within the specified range remains incompletely assessed and a more comprehensive analysis may be necessary to address this. Nevertheless, it's worth noting that this data-driven optimization method's accuracy is contingent on the fidelity of the simulation scheme, and therefore, the output should account for any refinements of the model.

5.4 Finite element analysis for validating the static resistance of an optimized gear Blank design.

In the optimization process, the static constraints were exclusive to the safety factors related to bending and pitting. However, these factors exhibited minimal variation, which was even more pronounced when considering pattern application. This underscores the limited influence of the gear body on contact behavior, particularly when the rim adheres to established gear design standards, as was the case in this instance.

This section encompasses a static validation focused on Von Mises stresses within the gear body. This validation is conducted through a numerical finite element analysis using the final results obtained from the optimized designs (2) and (4).

To streamline the problem and enhance computational efficiency, we adopted

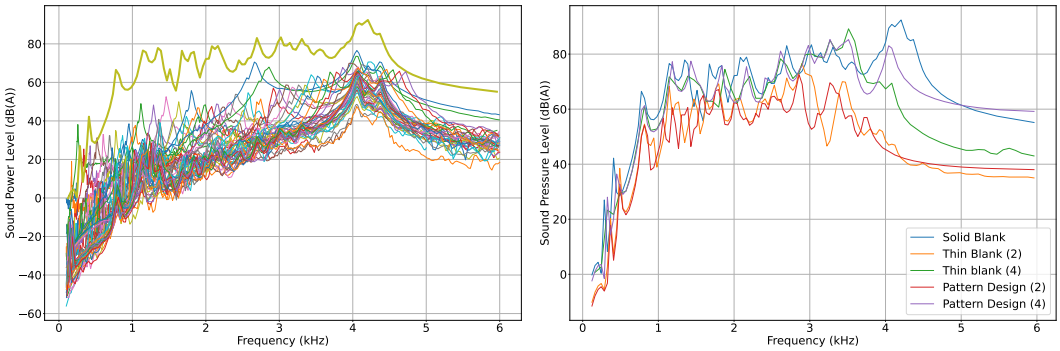

(a) Reference design - All orders

(b) All designs - Fundamental order

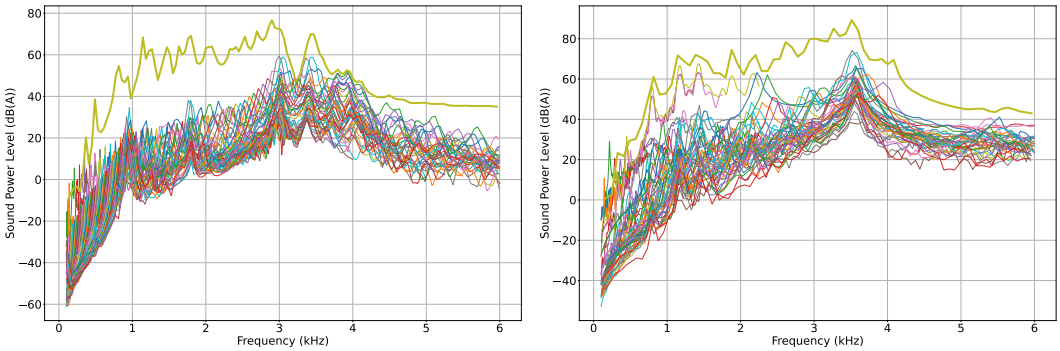

(c) Thin design (2) - All orders

(d) Thin design (4) - All orders

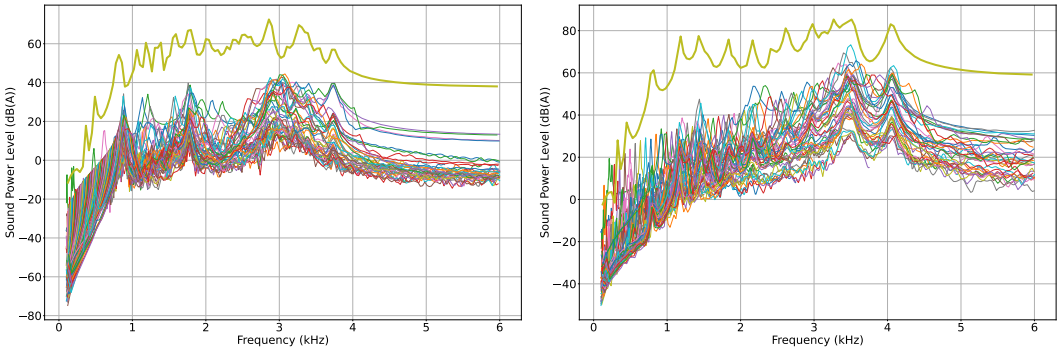

(e) Thin + Pattern (2) - All orders

(f) Thin + Pattern (4) - All orders

Figure 5.9: Progression of local best fitness among particles across iterations

a numerical simulation where the rim was considered as a rigid entity linked to the optimized blank via bonded contact. The mesh configuration for the gears was directly imported from the contact analysis, comprising approximately $330,000$ linear tetrahedral elements. The mesh contact type was set to frictionless. To facilitate load transmission, we identified a central remote point within each gear, connected with the inner bore surface through the use of kinematic rigid body elements.

The analysis entailed a single-tooth engagement, encompassing a gradual rotation spanning ten steps, which was applied to the pinion-side remote point along the axial direction. Simultaneously, we introduced an opposing torque of $115Nm$ to the remote point on the wheel side.

The analysis results are presented in Figure 5.10, illustrating the notable influence of the holes in redistributing stresses within the structure. This redistribution has the potential to alleviate stress concentrations in other critical regions.

In particular, when we examine the lightest design (design (2)), a higher stress concentration can be noticed particularly around the inner row of holes considering that the torsional stresses are more accentuated near the center. However, it's crucial to emphasize that even in this scenario, the highest stress observed reaches approximately $90MPa$. Importantly, this value remains significantly below the yield stress limit for structural steel. As such, under static conditions, it can be confidently asserted that the structure maintains its safety and structural integrity.

5.5 Conclusion

"In conclusion, this section introduced a dual-level optimization strategy aimed at achieving a reduction in gear weight while maintaining an optimized computational efficiency. The utilization of a Particle Swarm Optimization (PSO) algorithm enabled this weight reduction by initially decreasing the blank's thickness and subsequently introducing cavities with controlled statistical distribution parameters. The outcomes of this approach revealed significant enhancements in dynamic response characteristics, with the ability to fine-tune the trade-off between vibration amplitude and frequency through precise control of the fitness function.

Furthermore, the validity of these results was established by assessing the acoustic sound power level and the maximum Von Mises stresses within the blank. Ultimately, this optimization process led to the proposal of two distinct designs: one prioritizing a reduction in airborne noise levels by approximately $25dB$, characterized by an overall larger mean radius for the cavities, and another emphasizing the minimization of mass without compromising the gear's dynamic performance. These findings underscore the effectiveness of the dual-level optimization scheme in achieving a balance between weight reduction and performance enhancement in gear design.

The improvement percentages of the different fitness metrics are summarized in table 5.3.

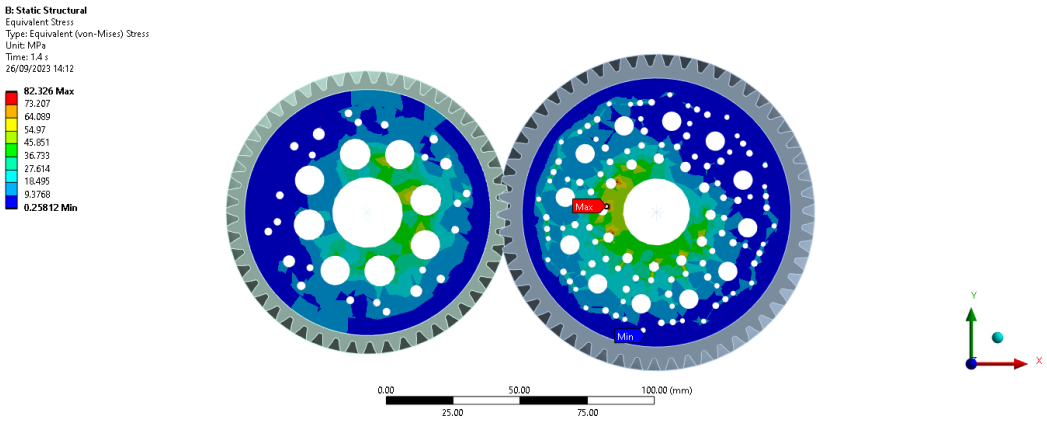

(a) Design (2)

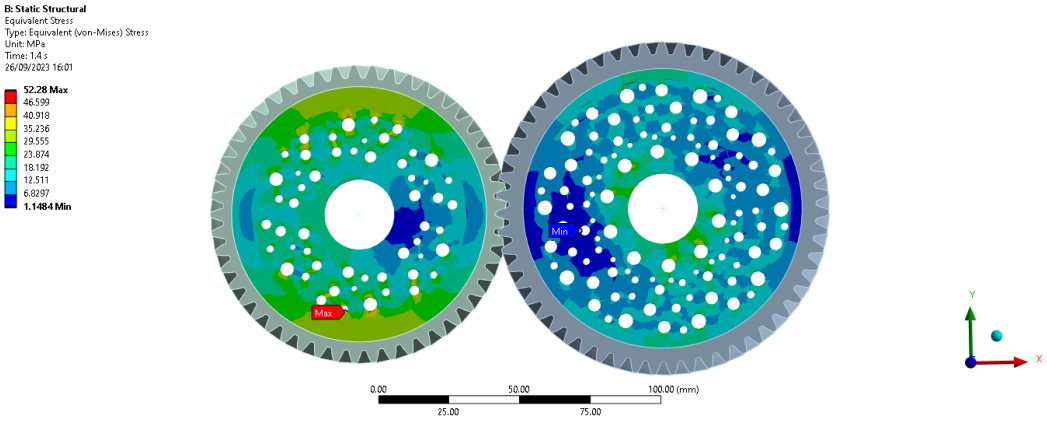

(b) Design (4)

Figure 5.10: Visualization of the Von Mises stress distributions.

Table 5.3: Housing RMSV amplitude and frequency results.

	Reference	**Design 2 "Thin rim"**	**Design 4 "Thin rim"**	**Design 2 "TR+Pattern"**	**Design 4 "TR+Pattern"**
Amplitude (mm/s)	0.001956	0.000623	0.003107	0.000223	0.014799
Amplitude (%)	100	31.85	97.5	11.4	75.7
Frequency (Hz)	3920	2695	3552.5	3307.5	3552.5
Frequency (%)	100	68.75	90.625	84.3	90.6
Area (mm/s)	0.067484	0.016903	0.047286	0.001707	0.014799
Area (%)	100	25	70	2.5	22
Mass (Kg)	1.973	1.437	1.973	1.348	1.824
Mass (%)	100	72.83	100	68.3	95.5

Conclusions and perspectives

5.6 General conclusions

In this thesis, an optimization scheme that serves to optimize the weight and dynamic response of a transmission system by changing the geometrical shape of the gears was developed. The main contributions of the thesis are listed below:

- **Conducting a benchmarking study of different gear contact analysis tools and methods on the static and dynamic response of transmission systems**. Before commencing the optimization process, we identified a substantial gap in the availability of a robust benchmark for assessing the reliability of both industrial and academic-level software when it comes to addressing the dynamic behaviors of gearboxes. To bridge this gap, we leveraged our expertise in various numerical tools, allowing us to conduct a comprehensive comparative analysis of responses across a range of case studies that included varying complexity levels and mounting conditions. This rigorous evaluation not only facilitated the identification of the most suitable tools for optimizing lightweight gears but also provided valuable insights into their performance from a scientific standpoint.

- **The study of the gearbox's dynamic model parameters on the variability of the response**. Having chosen the appropriate software, we delved into the intricacies of configuring settings associated with finite element part meshing and modal reduction. Our objective was to discern which parameters carried the greatest influence on the results. Following an exhaustive convergence analysis, we successfully constructed a more resilient and streamlined single-stage model, primed for in-depth dynamic analysis.

- **Conducting a sensitivity analysis of a few lightweight gear design parameters on different static and dynamic response metrics**. To explore the impact of lightweight gears on the vibrations emanating from a housing, we focused on discerning the influence of specific geometric parameters. In the initial phase, we conducted a sensitivity analysis on the thicknesses of the gear's web and rim. This analysis underscored the role of gear mass in fine-tuning response peaks. In the subsequent phase, we developed a gear blank generator capable of introducing a random hole pattern into the blank. Here, we probed the influence of various pattern distribution parameters, shedding light on the potential for additional weight reduction by incorporating perforations in the structure.

- **Establishing a dual-leveled PSO-based optimization scheme for the dynamic response optimization**. Building upon the insights acquired from

the investigation presented in Chapter 4, we introduced a PSO approach aimed at reducing the weight of the gears through two sequential processes. The initial step involved thinning the gear blank, followed by optimizing hole locations through the management of their statistical distribution parameters. This methodology not only enhanced the system's overall performance but also achieved a reduction in gear weights. Subsequently, we conducted a comprehensive numerical analysis to validate the structural integrity of the optimized component, specifically in terms of stress considerations.

5.7 Future work

- **Experimental validation**. Given that the majority of our work was conducted through numerical methods and the discerned variances during software benchmarking, the reliability and accuracy of our results are intrinsically tied to the precision of our numerical methods and models. Consequently, when pursuing numerical validation, careful attention should be given to the choice of the output gear for evaluation.

- **Application to a higher complexity commercial level gearbox**. Harnessing enhanced computational capabilities, there arises an intriguing opportunity to implement the optimization process within a real-world context. This endeavor enables us to evaluate the applicability of our approach to practical systems, thereby unveiling both the dynamic and economic advantages that can be gleaned from its implementation.

- **More Fine tuning of the optimization parameters**. Although we tested several combinations of PSO parameters, opportunities for enhancement persist to ensure swifter convergence and precise results. These observations suggest the necessity of formulating a comprehensive parameter tuning framework aligned with practical objectives for the gearbox.

- **Investigating the effect of damping and lightweight materials**. An essential aspect not addressed in this study pertains to the influence of structural damping, which could conceivably be impacted by the formation of cavities in the gear blank. It becomes increasingly intriguing to explore the potential benefits of employing both geometrically designed patterns and innovative lightweight materials, such as composites, in enhancing response characteristics through the improvement of structural damping.

Appendices

Appendix A

Chapter 2 Appendix

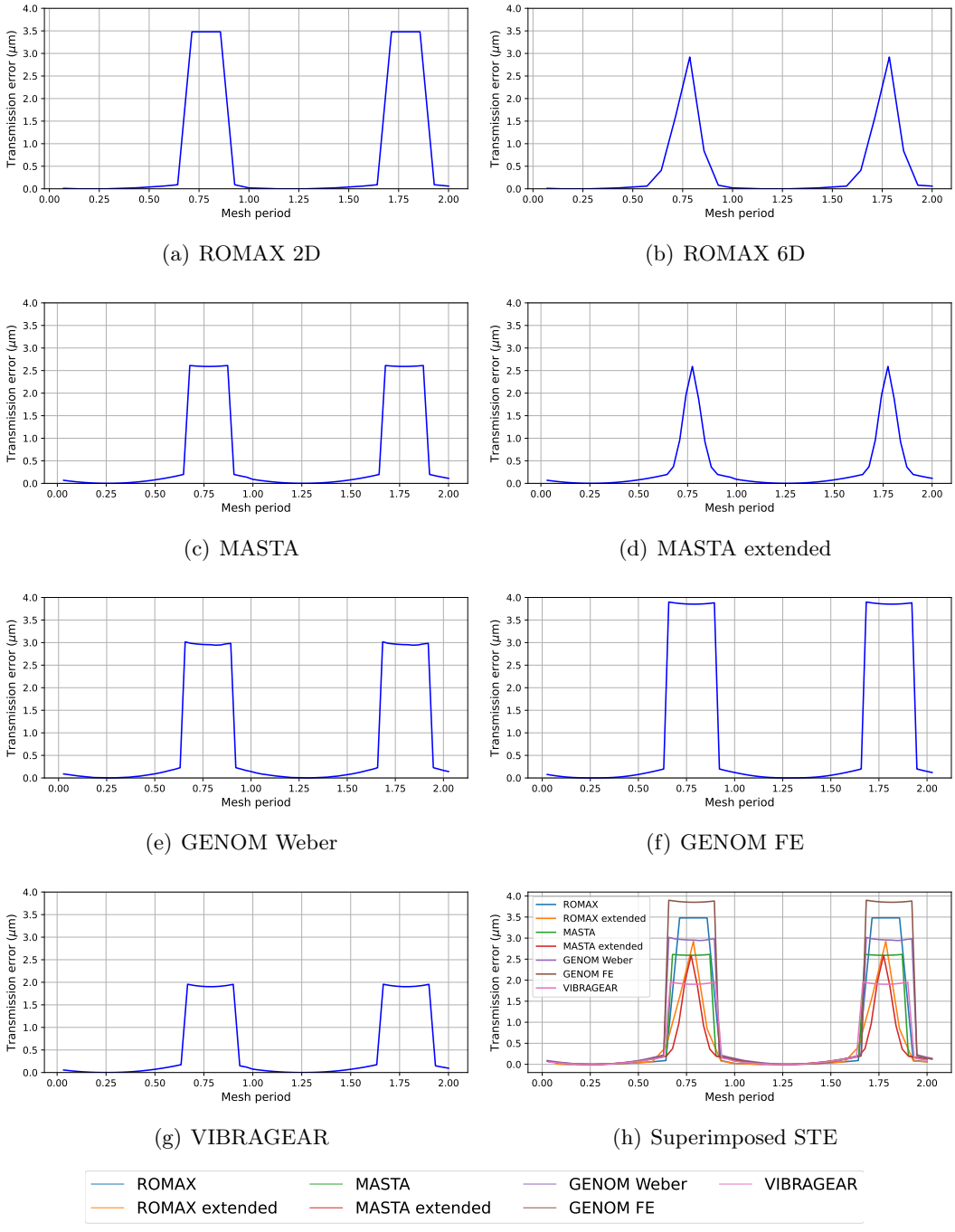

(a) ROMAX 2D

(b) ROMAX 6D

(c) MASTA

(d) MASTA extended

(e) GENOM Weber

(f) GENOM FE

(g) VIBRAGEAR

(h) Superimposed STE

Figure A.1: Static transmission error, after shifting the plots such that the minimum value corresponds to zero, for the case of 115Nm loaded perfectly involute spur gears.

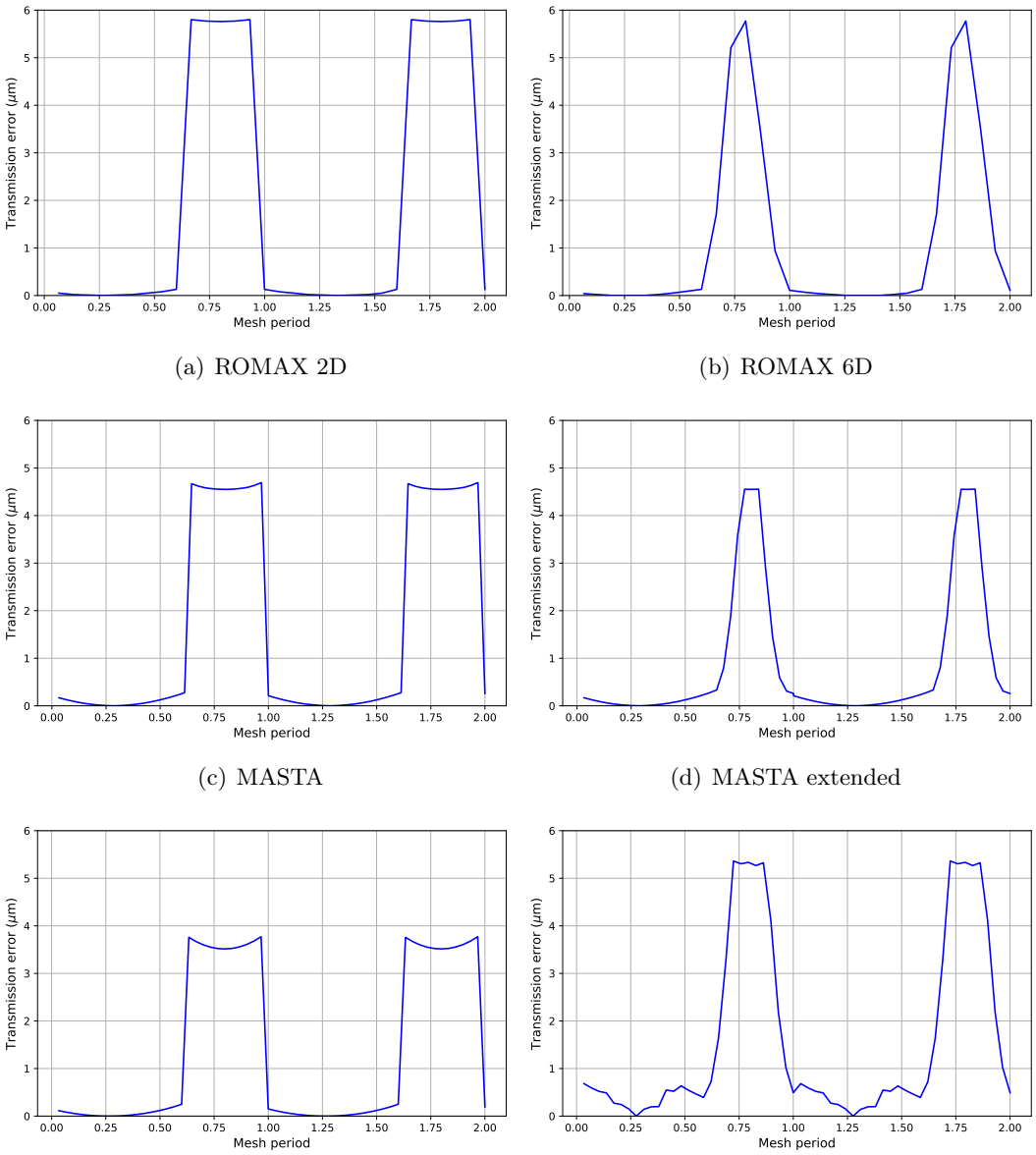

(a) ROMAX 2D

(b) ROMAX 6D

(c) MASTA

(d) MASTA extended

(e) VIBRAGEAR

(f) MARC

Figure A.2: Comparison of the static transmission error, after shifting the plots such that the minimum value corresponds to zero, for the case of 50Nm loaded perfectly involute spur gears.

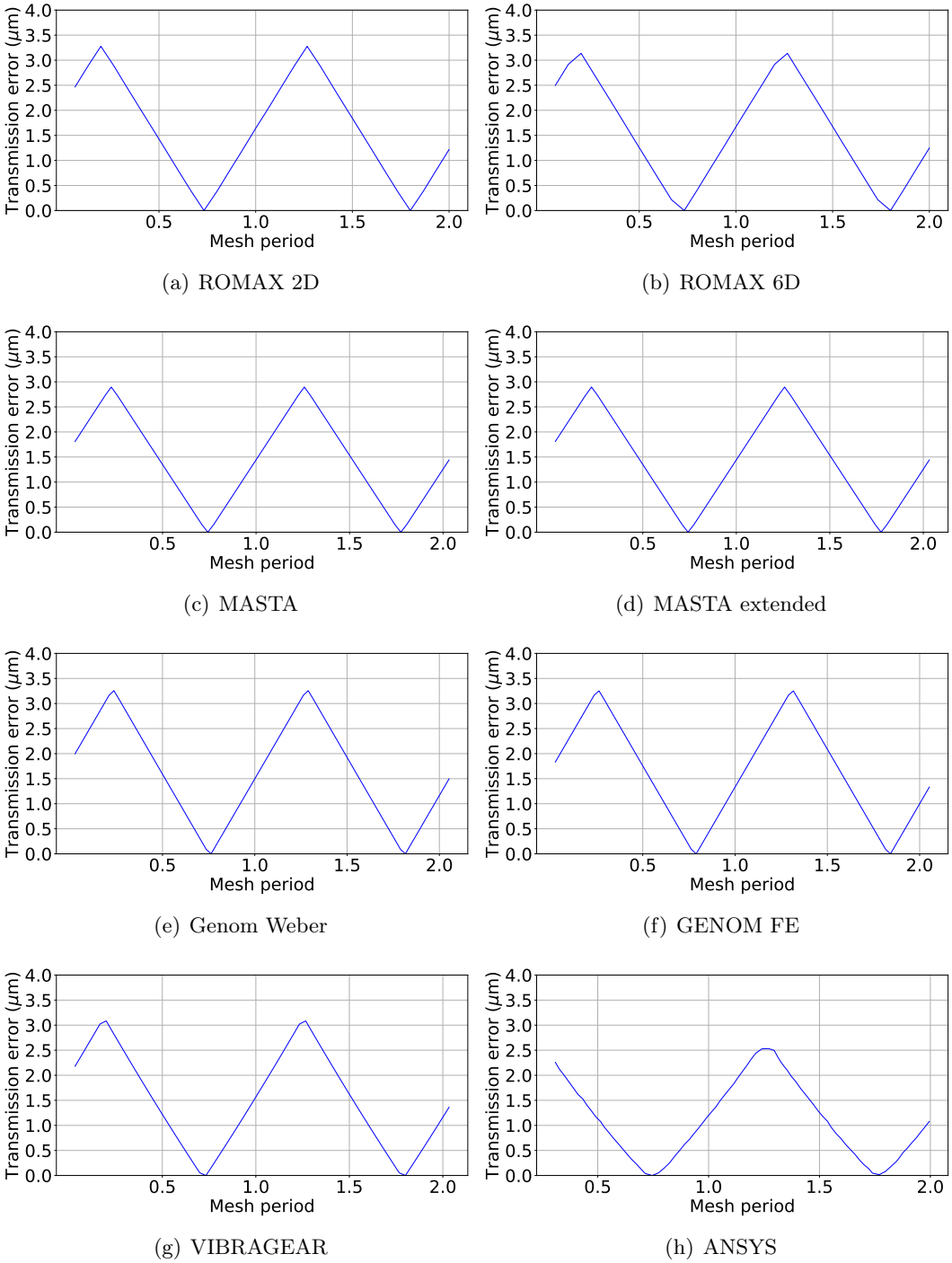

(a) ROMAX 2D

(b) ROMAX 6D

(c) MASTA

(d) MASTA extended

(e) Genom Weber

(f) GENOM FE

(g) VIBRAGEAR

(h) ANSYS

Figure A.3: Comparison of the static transmission error for the case of unloaded spur gears with tip relief.

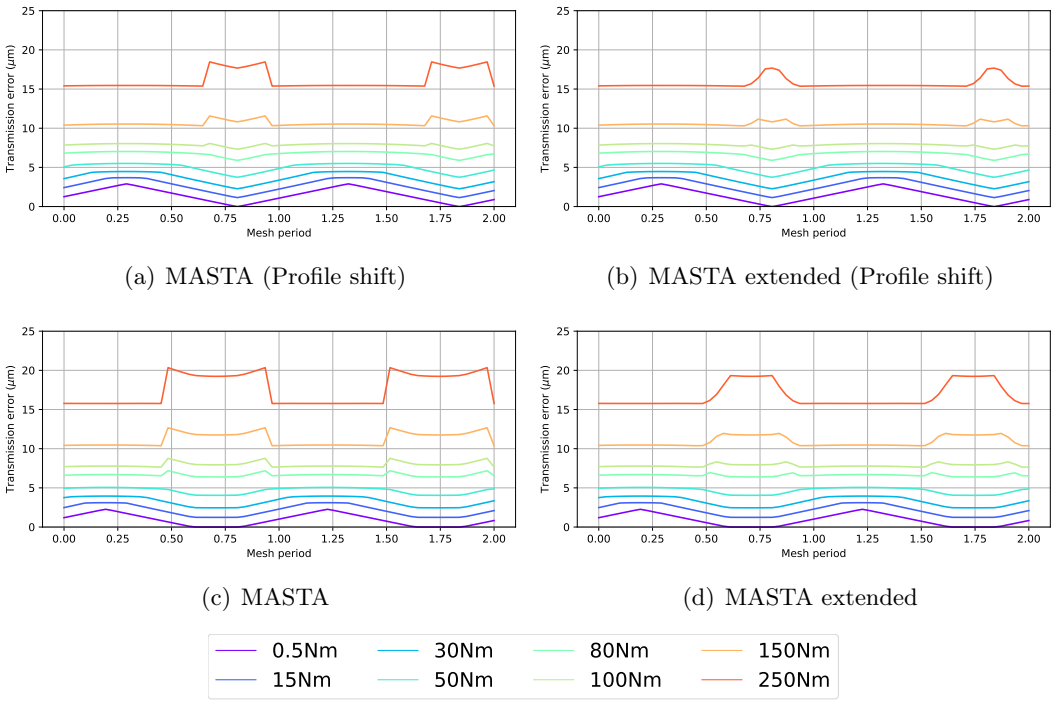

(a) MASTA (Profile shift)

(b) MASTA extended (Profile shift)

(c) MASTA

(d) MASTA extended

Figure A.4: Evolution of STE values within a torque range T = [0.5, 15, 30, 50, 80, 100, 150, 250] in MASTA considering the tooth thickness effect. Note that the case of MASTA with profile shift should not be compared directly to other tools due to its unique microgeometry.

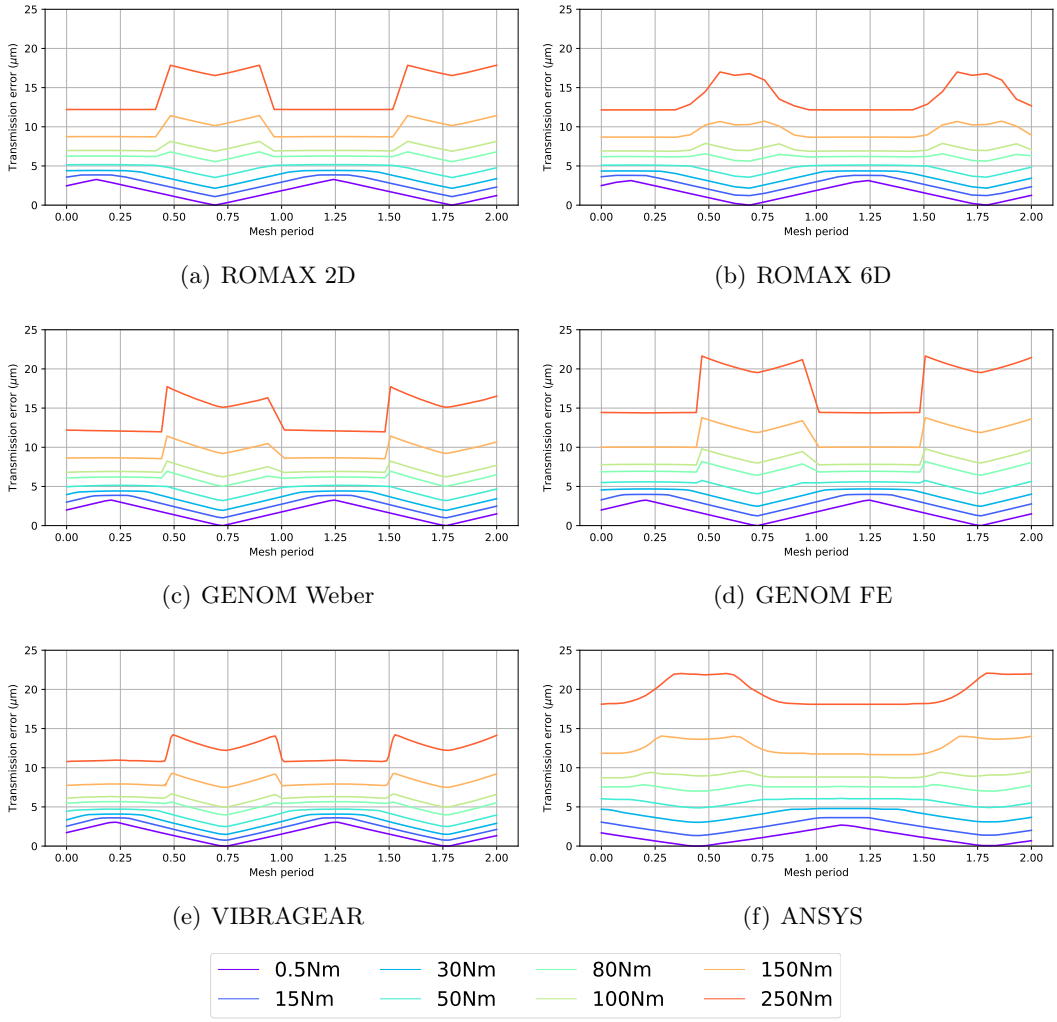

(a) ROMAX 2D

(b) ROMAX 6D

(c) GENOM Weber

(d) GENOM FE

(e) VIBRAGEAR

(f) ANSYS

Figure A.5: Evolution of STE values within a torque range T = [0.5, 15, 30, 50, 80, 100, 150, 250] using different software solutions for the case of spur gear with tip relief.

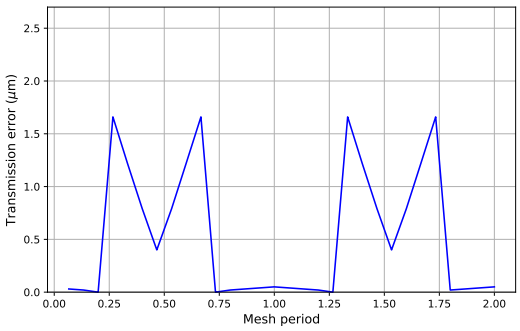

(a) ROMAX 2D

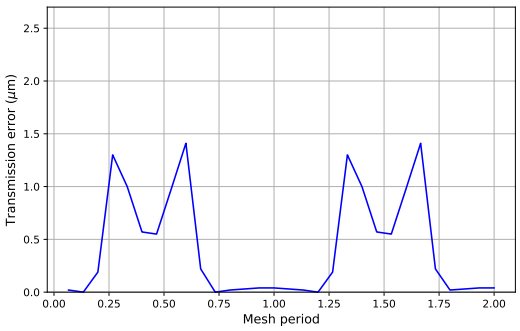

(b) ROMAX 6D

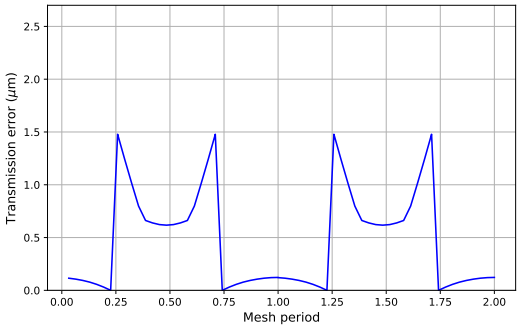

(c) MASTA

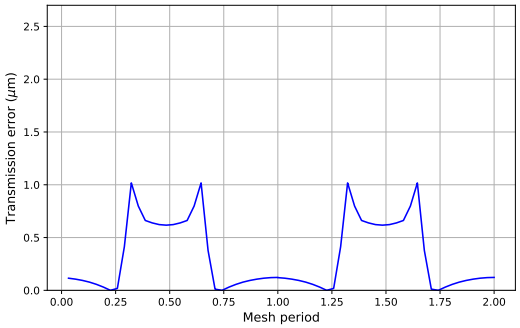

(d) MASTA extended

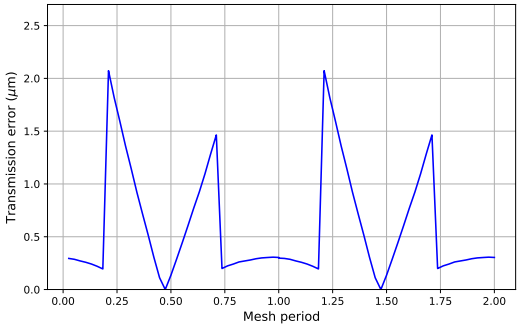

(e) GENOM Weber

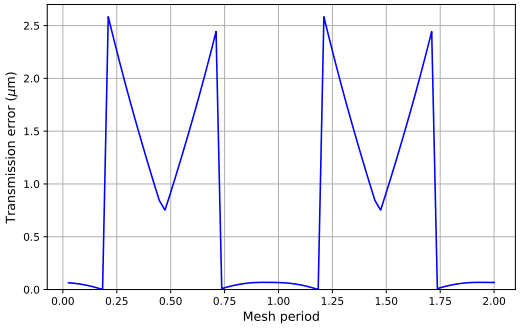

(f) GENOM FE

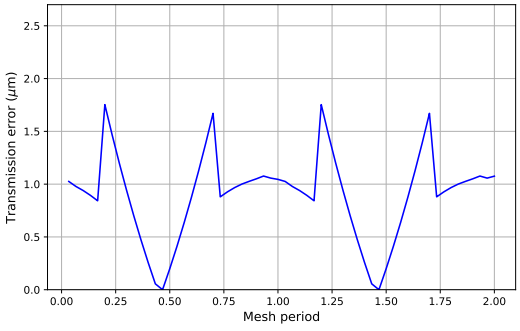

(g) VIBRAGEAR

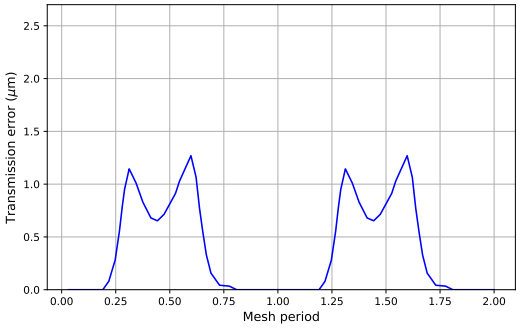

(h) ANSYS

Figure A.6: Comparison of the static transmission error, after shifting the plots such that the minimum value corresponds to zero, for the case of 115Nm loaded spur gears with tip relief.

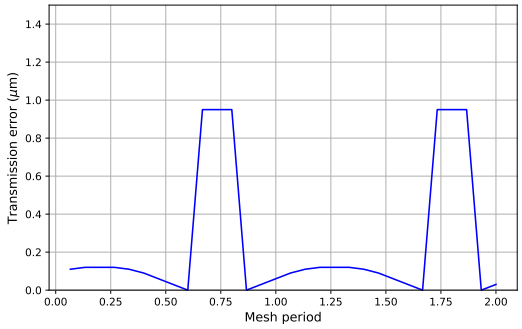

(a) ROMAX 2D

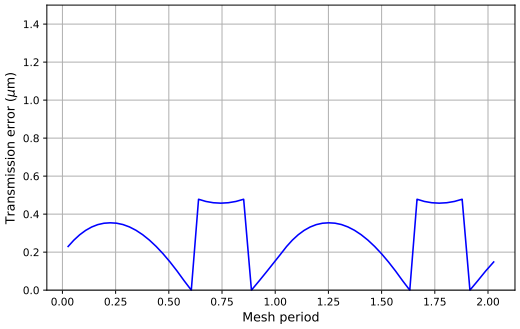

(b) MASTA

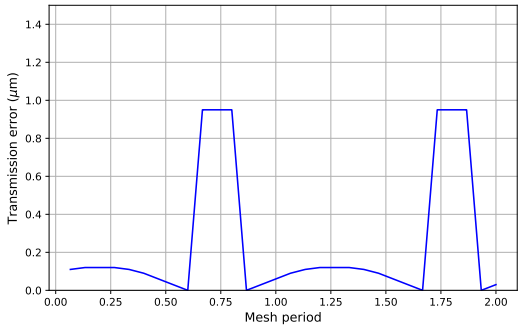

(c) ROMAX 6D

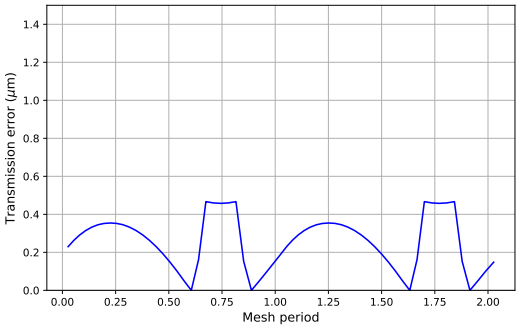

(d) MASTA extended

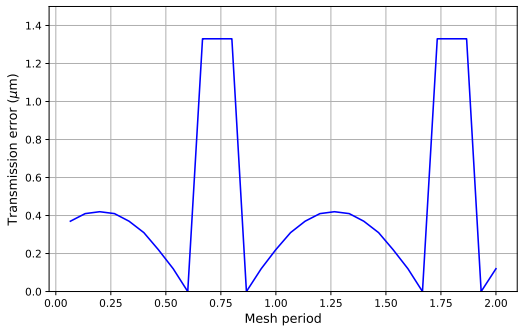

(e) ROMAX 2D with parallelism defect

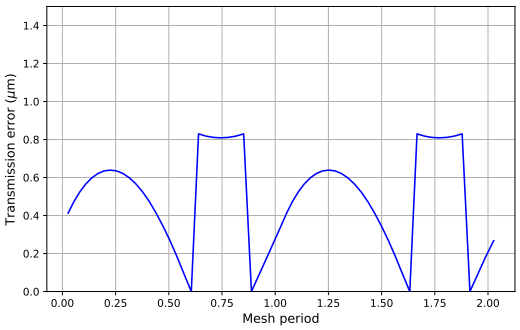

(f) MASTA with parallelism defect

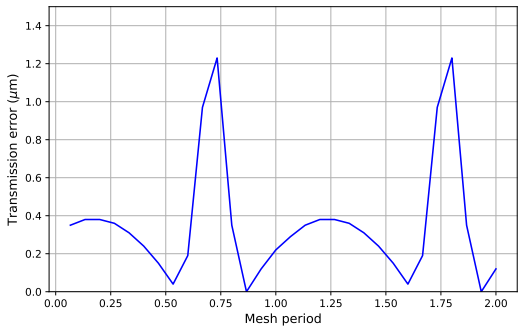

(g) ROMAX 6D with parallelism defect

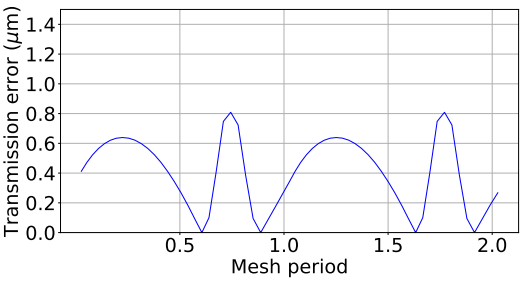

(h) MASTA extended with parallelism defect

Figure A.7: Parallelism defect influence on the static transmission error, after shifting the plots such that the minimum value corresponds to zero, for a $115Nm$ loaded perfectly involute spur gear.

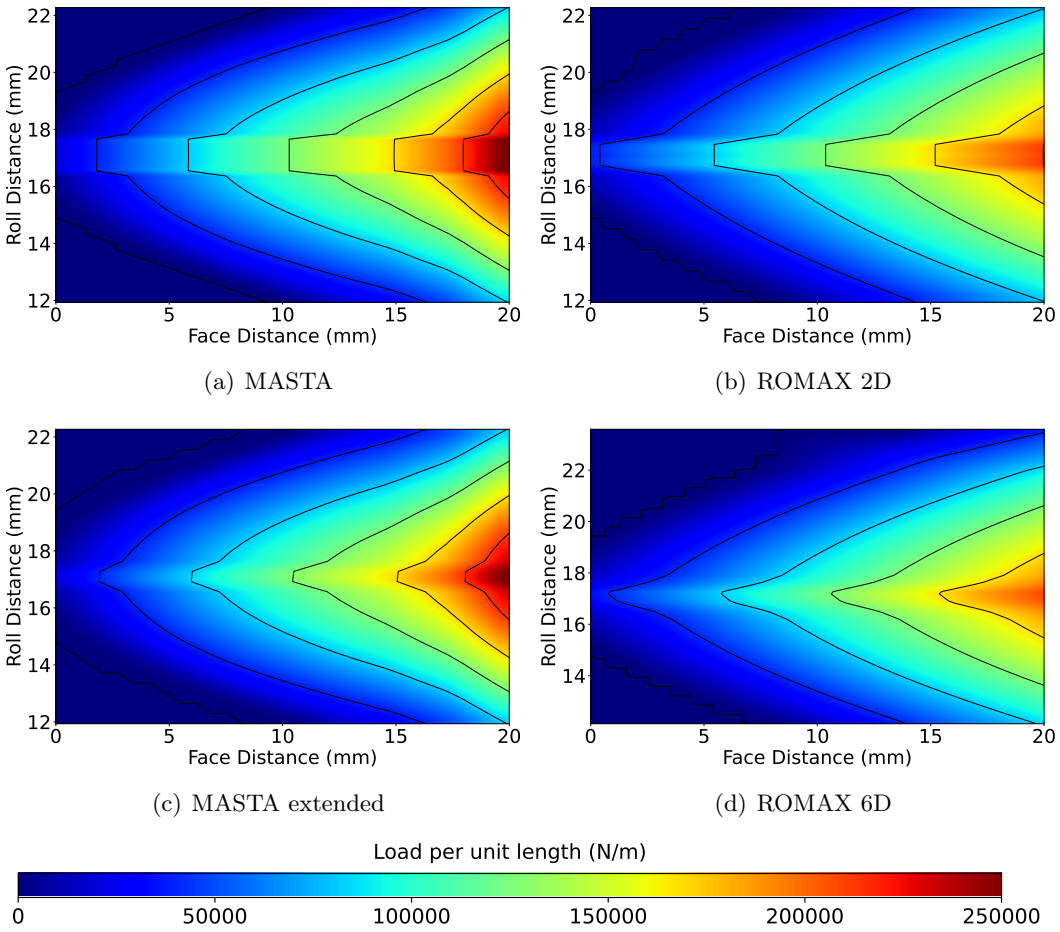

(a) MASTA (b) ROMAX 2D

(c) MASTA extended (d) ROMAX 6D

Figure A.8: Comparison of the contact patterns for the case of perfectly involute spur gears in the presence of a misalignment error using ROMAX and MASTA

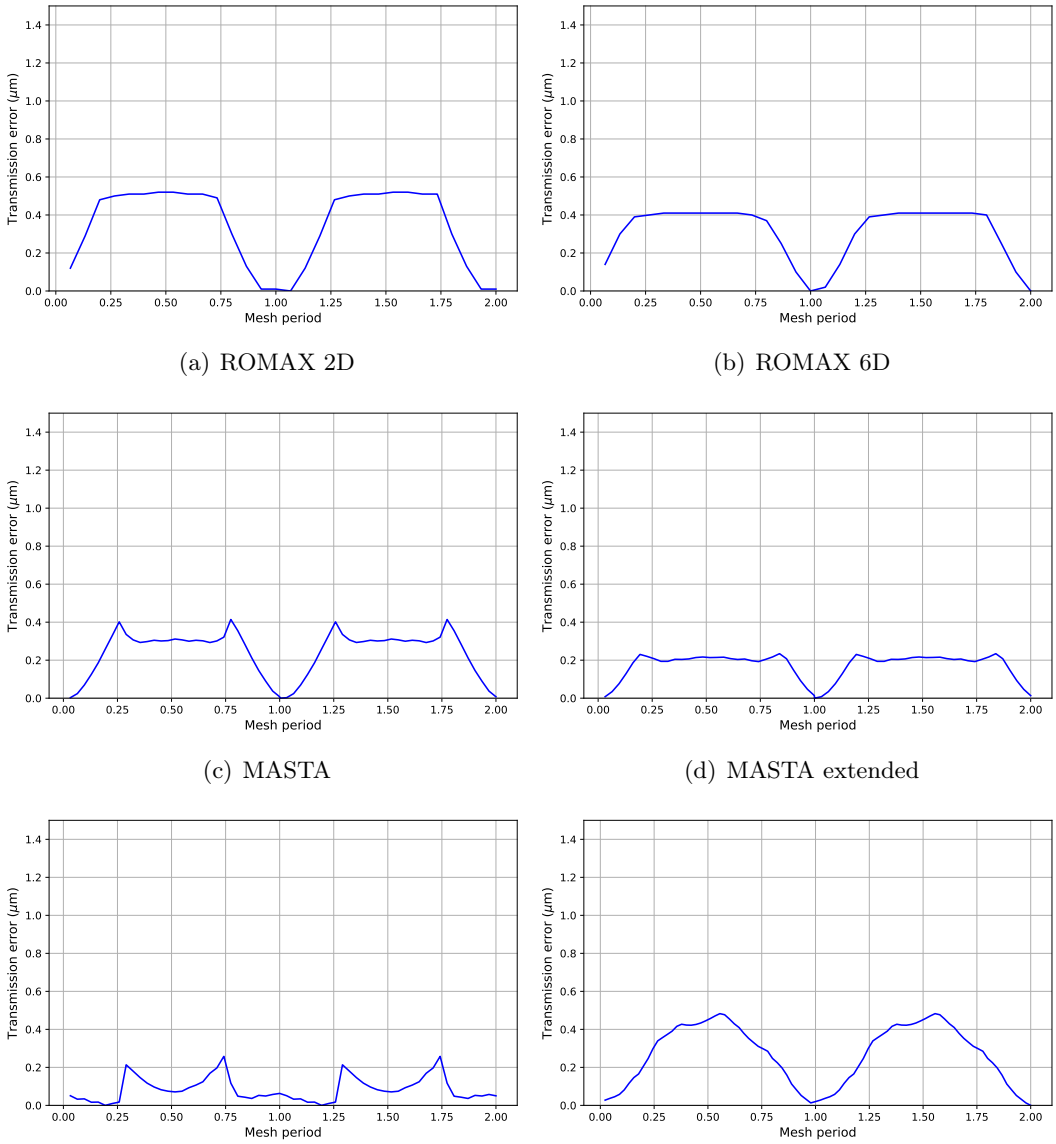

(a) ROMAX 2D

(b) ROMAX 6D

(c) MASTA

(d) MASTA extended

(e) VIBRAGEAR

(f) MARC

Figure A.9: Comparison of the static transmission error, after shifting the plots such that the minimum value corresponds to zero, for the case of 115Nm loaded perfectly involute helical gears.

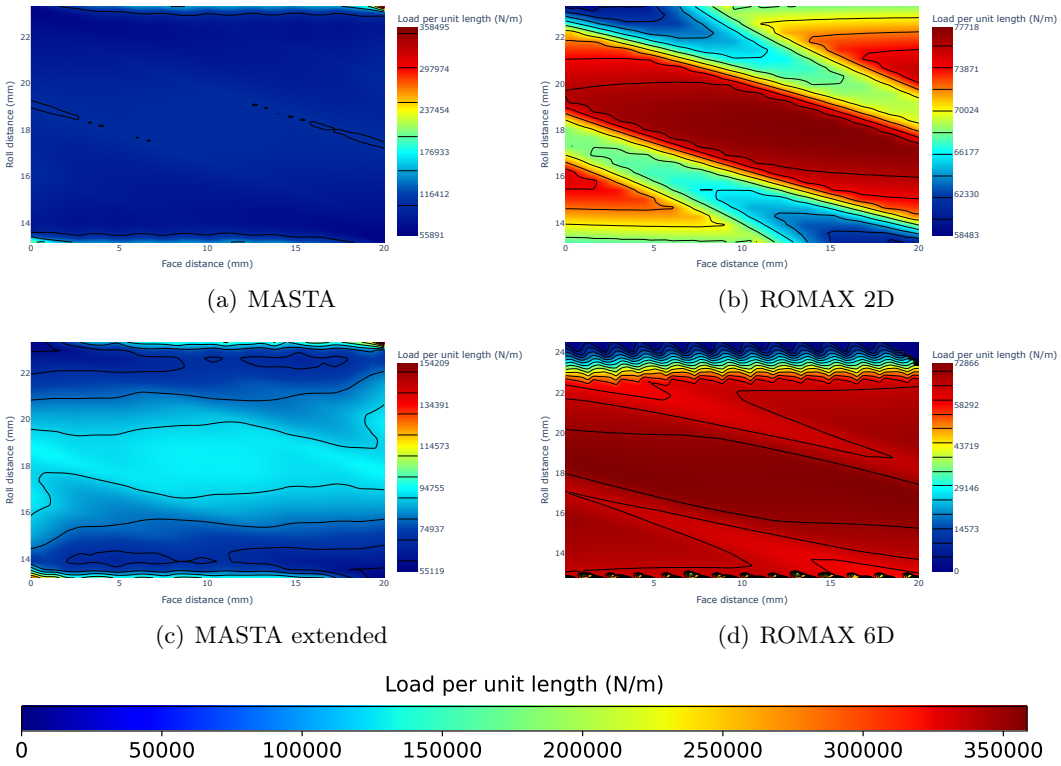

(a) MASTA

(b) ROMAX 2D

(c) MASTA extended

(d) ROMAX 6D

Figure A.10: Comparison of the contact patterns for the case of perfectly involute helical gears.

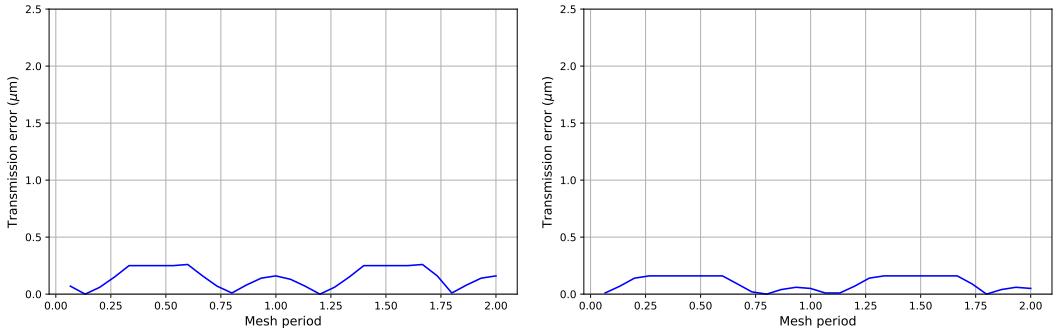

(a) ROMAX 2D

(b) ROMAX 6D

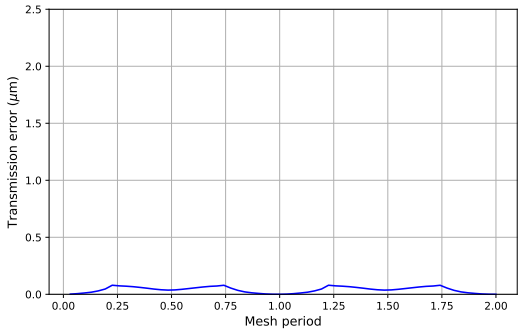

(c) MASTA

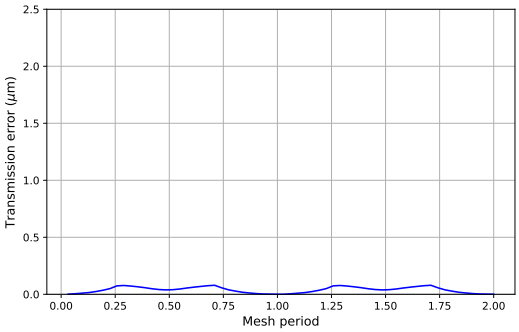

(d) MASTA extended

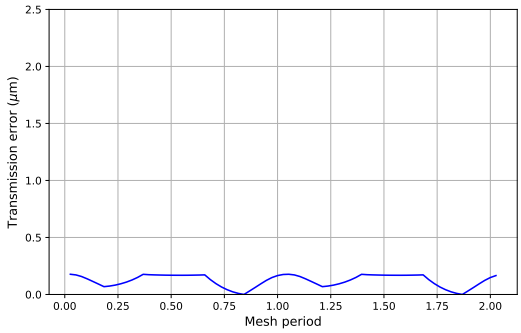

(e) GENOM Weber

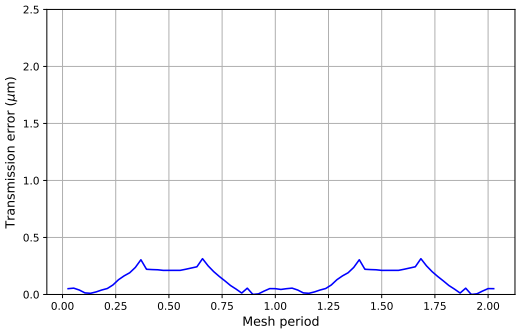

(f) GENOM FE

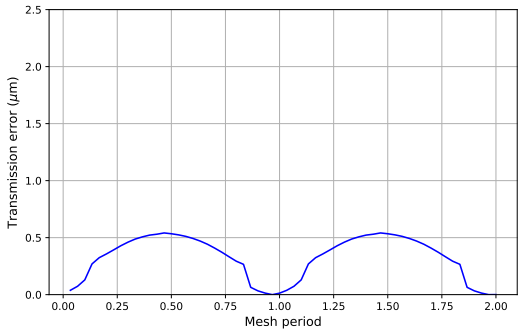

(g) VIBRAGEAR

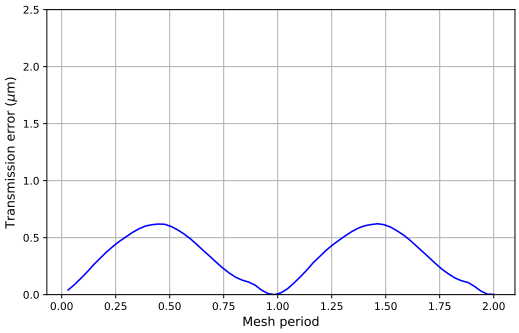

(h) ANSYS

Figure A.11: Static transmission error, after shifting the plots such that the minimum value corresponds to zero, for the case of a 115Nm loaded helical gear pair with tip relief.

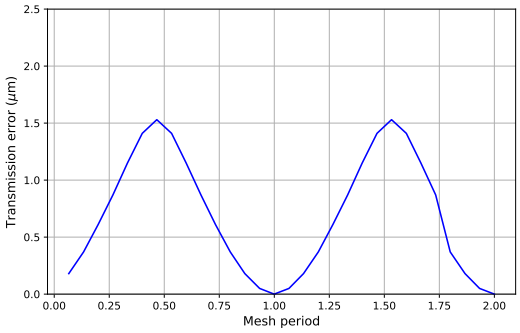

(a) ROMAX 2D

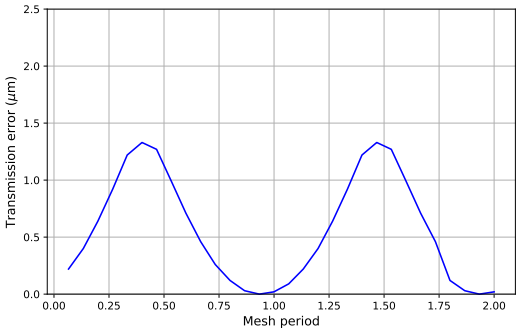

(b) ROMAX 6D

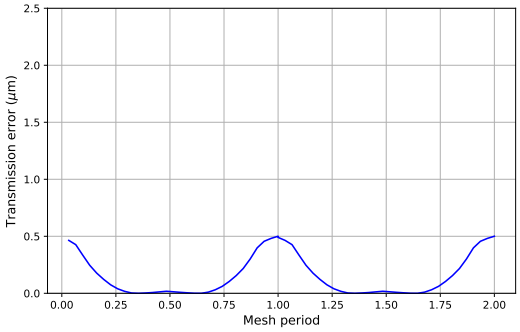

(c) MASTA

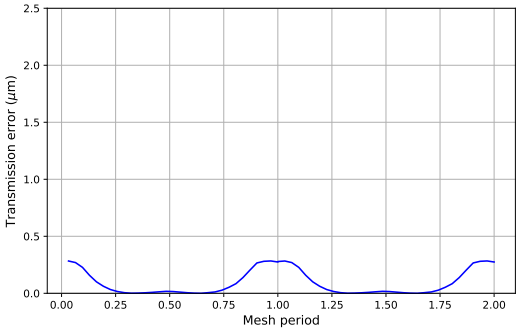

(d) MASTA extended

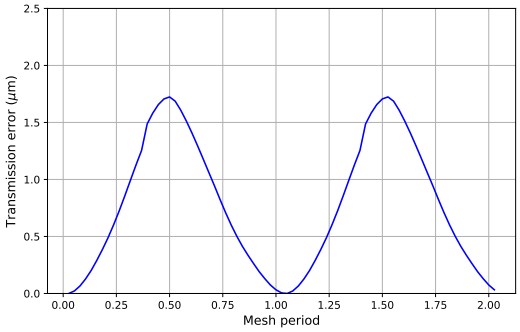

(e) GENOM Weber

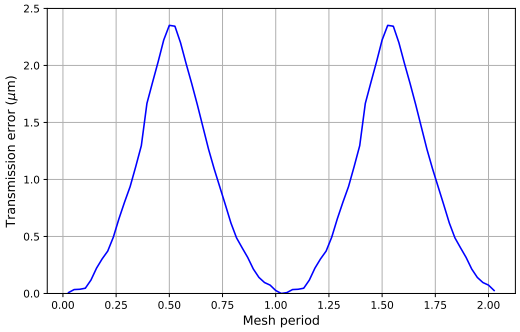

(f) GENOM FE

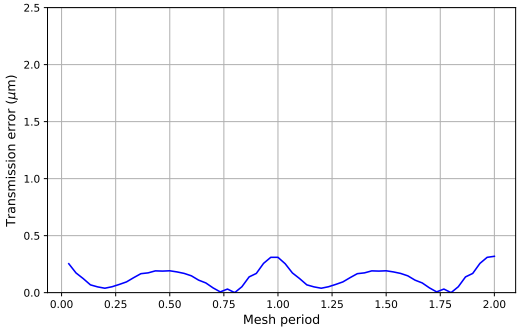

(g) VIBRAGEAR

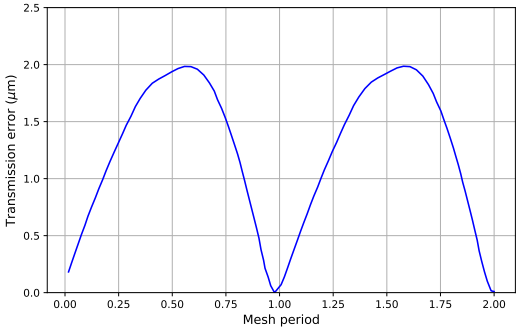

(h) ANSYS

Figure A.12: Static transmission error, after shifting the plots such that the minimum value corresponds to zero, for the case of a 115Nm loaded helical gear pair with tip relief and lead crowning.

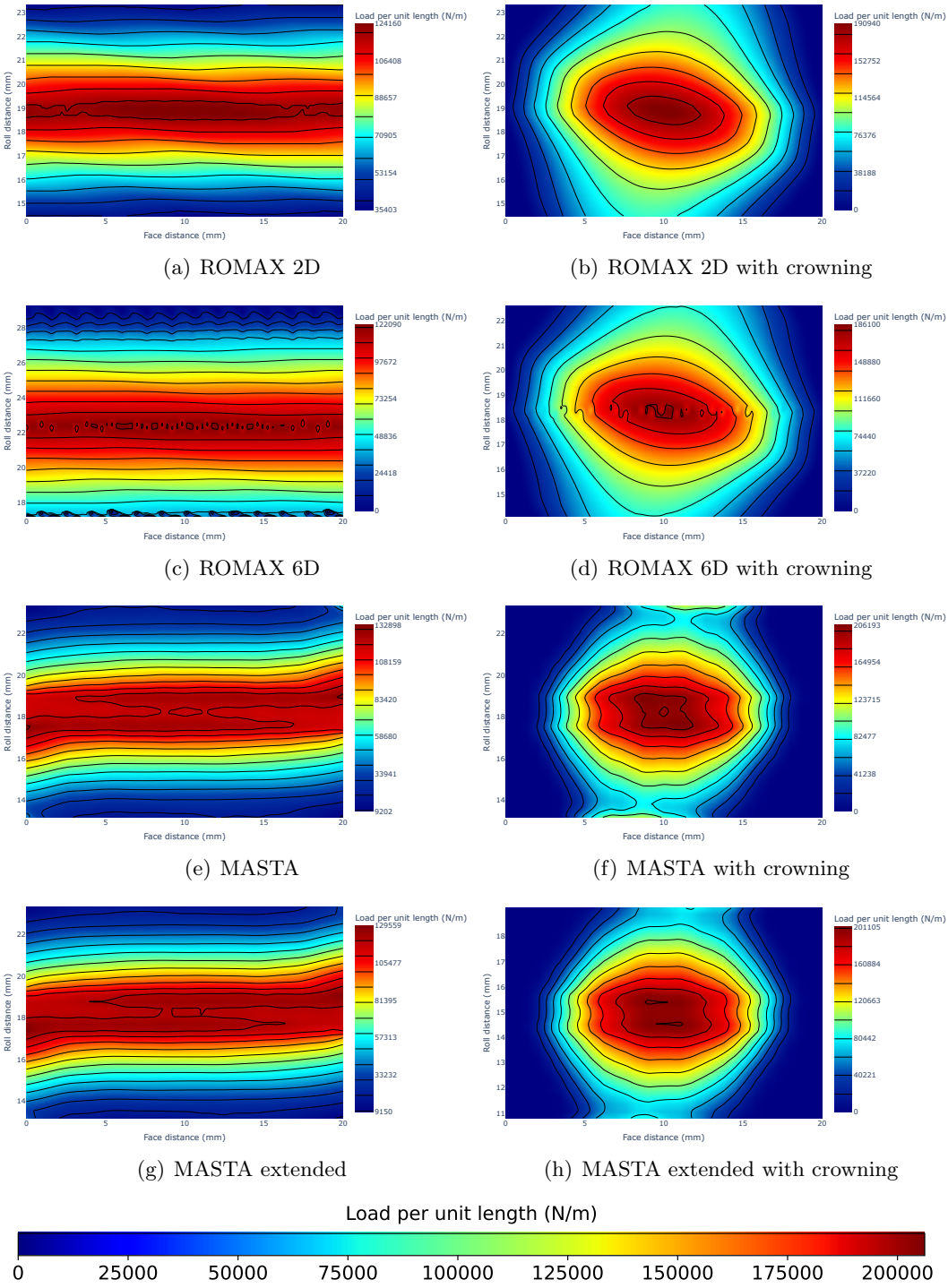

(a) ROMAX 2D

(b) ROMAX 2D with crowning

(c) ROMAX 6D

(d) ROMAX 6D with crowning

(e) MASTA

(f) MASTA with crowning

(g) MASTA extended

(h) MASTA extended with crowning

Figure A.13: Comparison of the contact patterns in the presence of a longitudinal crowning.

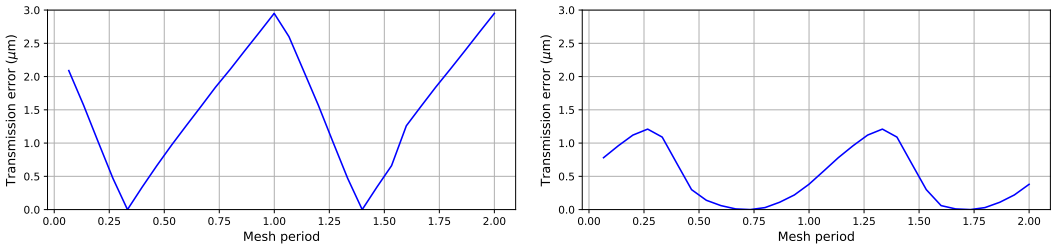

(a) ROMAX 2D

(b) ROMAX 2D optimized

(c) ROMAX 6D

(d) ROMAX 6D optimized

Figure A.14: Evolution of the static transmission error in ROMAX, after shifting the plots such that the minimum value corresponds to zero, with the change in the geometry of the flank for an 80Nm loaded helical gearbox.

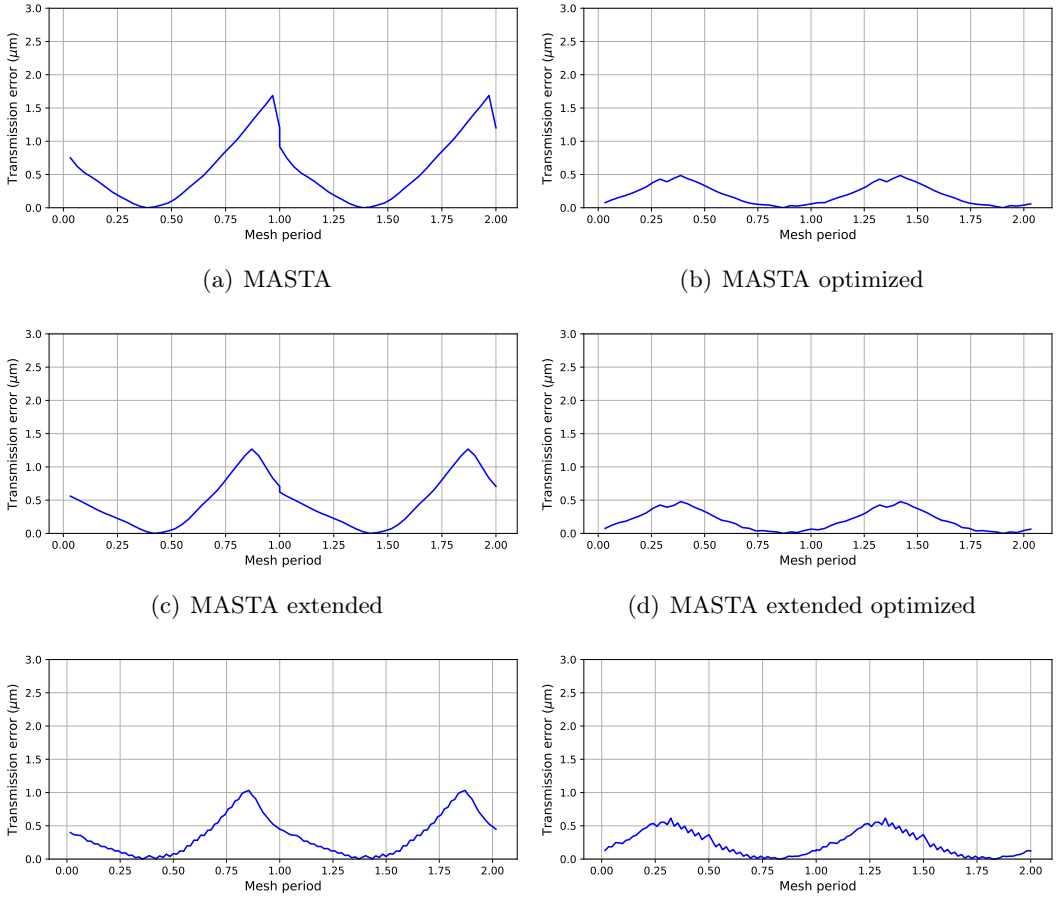

(a) MASTA

(b) MASTA optimized

(c) MASTA extended

(d) MASTA extended optimized

(e) MASTA extended (asd)

(f) MASTA extended (asd) optimized

Figure A.15: Evolution of the static transmission error in MASTA, after shifting the plots such that the minimum value corresponds to zero, with the change in the geometry of the flank for an 80Nm loaded helical gearbox.

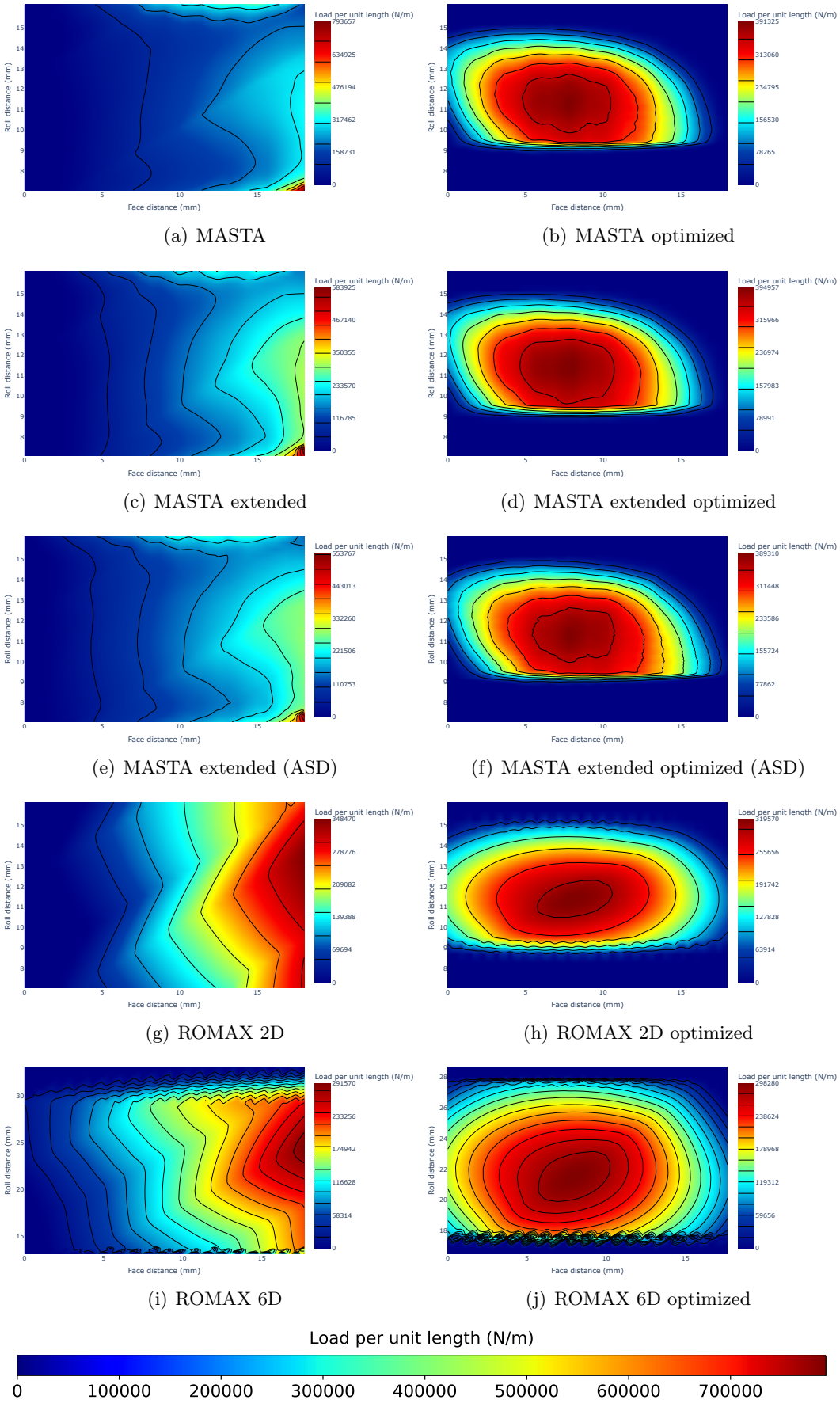

(a) MASTA

(b) MASTA optimized

(c) MASTA extended

(d) MASTA extended optimized

(e) MASTA extended (ASD)

(f) MASTA extended optimized (ASD)

(g) ROMAX 2D

(h) ROMAX 2D optimized

(i) ROMAX 6D

(j) ROMAX 6D optimized

Figure A.16: Visualization of the evolution of the contact path resulting from a microgeometry optimization.

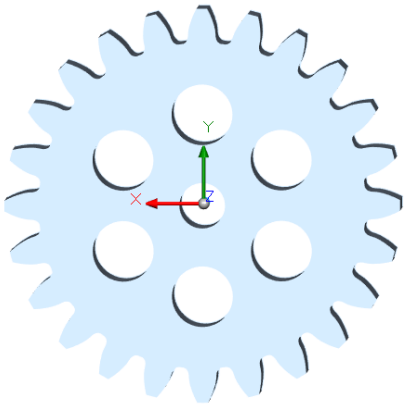

(a) Gear blank of gear pair 1

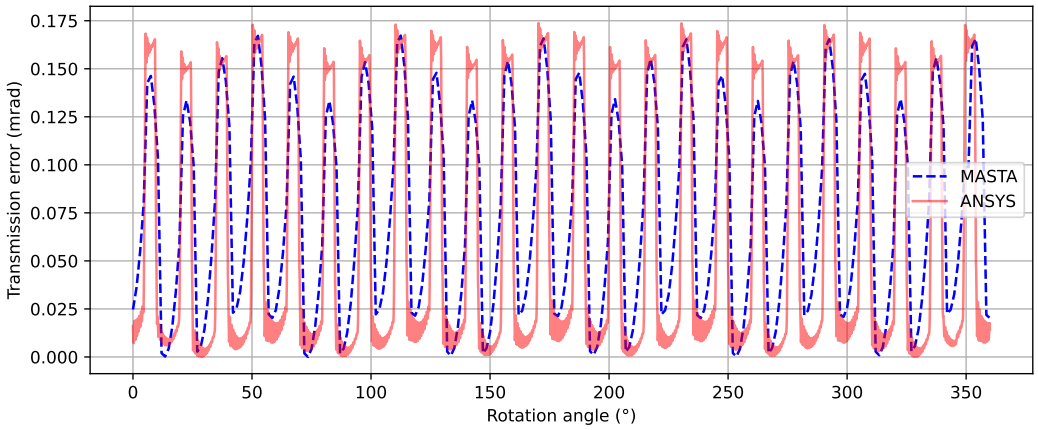

(b) Transmission error

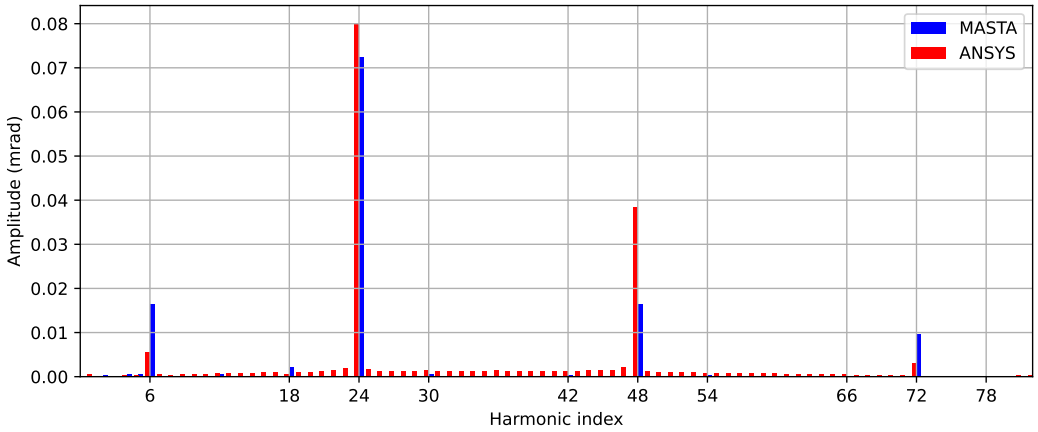

(c) Harmonics

Figure A.17: STE fluctuation and harmonic content for the case of a 6-hole spur gear pair using MASTA and ANSYS

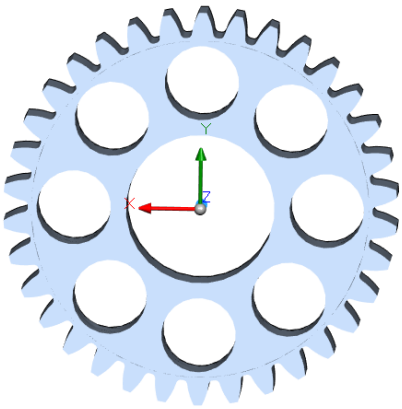

(a) Gear blank of gear pair 2

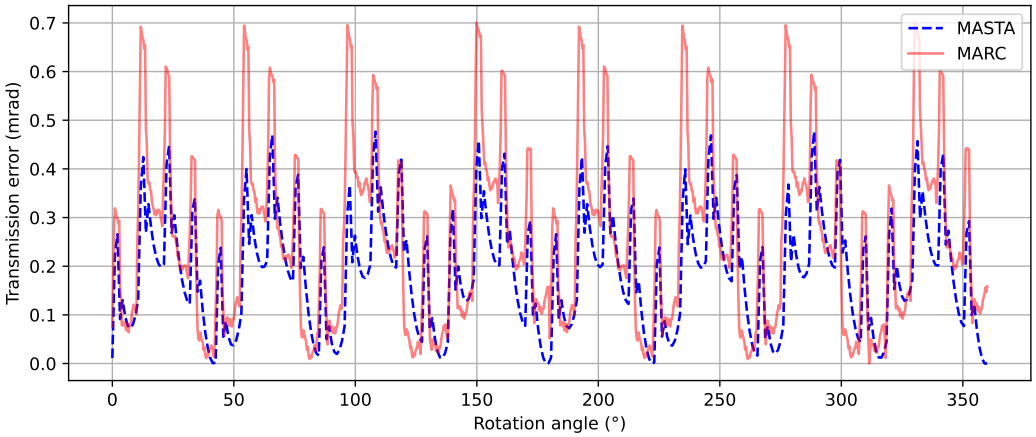

(b) Transmission error

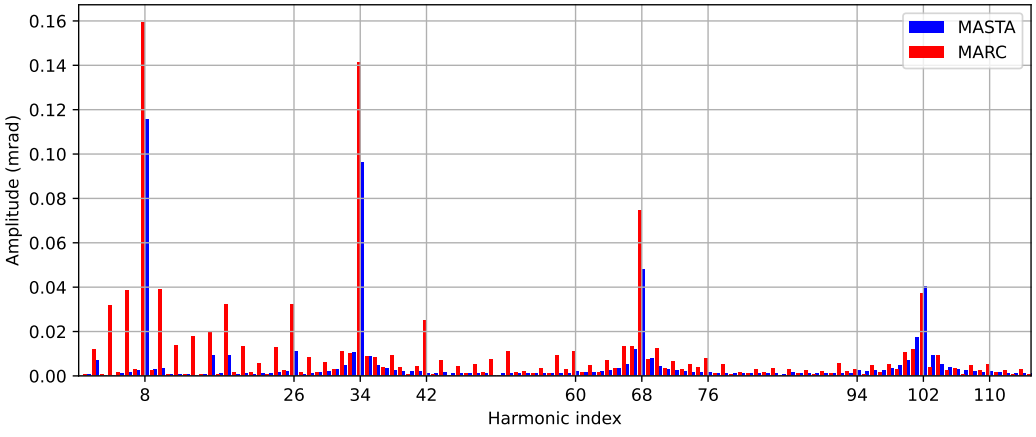

(c) Harmonics

Figure A.18: STE modulation and harmonic content for the case of an 8-hole spur gear pair using MASTA and MARC.

Appendix B

Chapter 3 Appendix

B.1 Timoshenko beam element formulation

$$\mathbf{K_s^e} = \begin{bmatrix}
\frac{EA}{l} & 0 & 0 & 0 & 0 & 0 & \frac{-EA}{l} & 0 & 0 & 0 & 0 & 0 \\
0 & \frac{12EI_z}{l^3(1+\Phi_y)} & 0 & 0 & 0 & \frac{6EI_z}{l^2(1+\Phi_y)} & 0 & \frac{-12EI_z}{l^3(1+\Phi_y)} & 0 & 0 & 0 & \frac{6EI_z}{l^2(1+\Phi_y)} \\
0 & 0 & \frac{12EI_y}{l^3(1+\Phi_z)} & 0 & \frac{-6EI_y}{l^2(1+\Phi_z)} & 0 & 0 & 0 & \frac{-12EI_y}{l^3(1+\Phi_z)} & 0 & \frac{-6EI_y}{l^2(1+\Phi_z)} & 0 \\
0 & 0 & 0 & \frac{GJ}{l} & 0 & 0 & 0 & 0 & 0 & \frac{-GJ}{l} & 0 & 0 \\
0 & 0 & \frac{-6EI_y}{l^2(1+\Phi_z)} & 0 & \frac{(4+\Phi_z)EI_y}{l(1+\Phi_z)} & 0 & 0 & 0 & \frac{6EI_y}{l^2(1+\Phi_z)} & 0 & \frac{(2-\Phi_z)EI_y}{l(1+\Phi_z)} & 0 \\
0 & \frac{6EI_z}{l^2(1+\Phi_y)} & 0 & 0 & 0 & \frac{(4+\Phi_y)EI_z}{l(1+\Phi_y)} & 0 & \frac{-6EI_z}{l^2(1+\Phi_y)} & 0 & 0 & 0 & \frac{(2-\Phi_y)EI_z}{l(1+\Phi_y)} \\
\frac{-EA}{l} & 0 & 0 & 0 & 0 & 0 & \frac{EA}{l} & 0 & 0 & 0 & 0 & 0 \\
0 & \frac{-12EI_z}{l^3(1+\Phi_y)} & 0 & 0 & 0 & \frac{-6EI_z}{l^2(1+\Phi_y)} & 0 & \frac{12EI_z}{l^3(1+\Phi_y)} & 0 & 0 & 0 & \frac{-6EI_z}{l^2(1+\Phi_y)} \\
0 & 0 & \frac{-12EI_y}{l^3(1+\Phi_z)} & 0 & \frac{6EI_y}{l^2(1+\Phi_z)} & 0 & 0 & 0 & \frac{12EI_y}{l^3(1+\Phi_z)} & 0 & \frac{6EI_y}{l^2(1+\Phi_z)} & 0 \\
0 & 0 & 0 & \frac{-GJ}{l} & 0 & 0 & 0 & 0 & 0 & \frac{GJ}{l} & 0 & 0 \\
0 & 0 & \frac{-6EI_y}{l^2(1+\Phi_z)} & 0 & \frac{(2-\Phi_z)EI_y}{l(1+\Phi_z)} & 0 & 0 & 0 & \frac{6EI_y}{l^2(1+\Phi_z)} & 0 & \frac{(4+\Phi_z)EI_y}{l(1+\Phi_z)} & 0 \\
0 & \frac{6EI_z}{l^2(1+\Phi_y)} & 0 & 0 & 0 & \frac{(2-\Phi_y)EI_z}{l(1+\Phi_y)} & 0 & \frac{-6EI_z}{l^2(1+\Phi_y)} & 0 & 0 & 0 & \frac{(4+\Phi_y)EI_z}{l(1+\Phi_y)}
\end{bmatrix} \tag{B.1}$$

$$\Phi_i = \frac{12EI_i}{GA_{si}l^2}, \quad i = y, z \tag{B.2}$$

$$\frac{\mathbf{M_s^e}}{m_e} = \begin{bmatrix}
\frac{1}{3} & 0 & 0 & 0 & 0 & 0 & \frac{1}{6} & 0 & 0 & 0 & 0 & 0 \\
0 & \frac{13}{35}+\frac{6I_z}{5Al^2} & 0 & 0 & 0 & \frac{11l}{210}+\frac{I_z}{10Al} & 0 & \frac{9}{70}-\frac{6I_z}{5Al^2} & 0 & 0 & 0 & -\frac{13l}{420}+\frac{I_z}{10Al} \\
0 & 0 & \frac{13}{35}+\frac{6I_y}{5Al^2} & 0 & -\frac{11l}{210}-\frac{I_y}{10Al} & 0 & 0 & 0 & \frac{9}{70}-\frac{6I_y}{5Al^2} & 0 & \frac{13l}{420}-\frac{I_y}{10Al} & 0 \\
0 & 0 & 0 & \frac{J_p}{3A} & 0 & 0 & 0 & 0 & 0 & \frac{J_p}{6A} & 0 & 0 \\
0 & 0 & -\frac{11l}{210}-\frac{I_y}{10Al} & 0 & \frac{l^2}{105}+\frac{2I_y}{15A} & 0 & 0 & 0 & -\frac{13l}{420}+\frac{I_y}{10Al} & 0 & -\frac{l^2}{140}-\frac{I_y}{30A} & 0 \\
0 & \frac{11l}{210}+\frac{I_z}{10Al} & 0 & 0 & 0 & \frac{l^2}{105}+\frac{2I_z}{15A} & 0 & \frac{13l}{420}-\frac{I_z}{10Al} & 0 & 0 & 0 & -\frac{l^2}{140}-\frac{I_z}{30A} \\
\frac{1}{6} & 0 & 0 & 0 & 0 & 0 & \frac{1}{3} & 0 & 0 & 0 & 0 & 0 \\
0 & \frac{9}{70}-\frac{6I_z}{5Al^2} & 0 & 0 & 0 & \frac{13l}{420}-\frac{I_z}{10Al} & 0 & \frac{13}{35}-\frac{6I_z}{5Al^2} & 0 & 0 & 0 & -\frac{11l}{210}-\frac{I_z}{10Al} \\
0 & 0 & \frac{9}{70}-\frac{6I_y}{5Al^2} & 0 & -\frac{13l}{420}+\frac{I_y}{10Al} & 0 & 0 & 0 & \frac{13}{35}+\frac{6I_y}{5Al^2} & 0 & \frac{11l}{210}+\frac{I_y}{10Al} & 0 \\
0 & 0 & 0 & \frac{J_p}{6A} & 0 & 0 & 0 & 0 & 0 & \frac{J_p}{3A} & 0 & 0 \\
0 & 0 & \frac{13l}{420}-\frac{I_y}{10Al} & 0 & -\frac{l^2}{140}-\frac{I_y}{30A} & 0 & 0 & 0 & \frac{11l}{210}+\frac{I_y}{10Al} & 0 & \frac{l^2}{105}+\frac{2I_y}{15A} & 0 \\
0 & -\frac{13l}{420}+\frac{I_z}{10Al} & 0 & 0 & 0 & -\frac{l^2}{140}-\frac{I_z}{30A} & 0 & -\frac{11l}{210}-\frac{I_z}{10Al} & 0 & 0 & 0 & \frac{l^2}{105}+\frac{2I_z}{15A}
\end{bmatrix} \tag{B.3}$$

where:
E: Young's modulus
G: Shear modulus
l: Element's length
$m_e = \rho Al$: Element's mass
ρ: Material's density
A: Element's cross-sectional area
ϕ: Shear deformation importance factor ($\phi = 0$ indicates neglected shear effects which converges the Timoshenko beam to an Euler-Bernoulli beam)
For a cylindrical shaft, the second moment of area (I_y, I_z), polar second moment of inertia J, and cross-sectional shear area (A_{sy}, A_{sz}) are expressed as:

$$I_y = I_z = \frac{\pi r_s^4}{4} \tag{B.4}$$

$$J = \frac{\pi r_s^4}{2} \tag{B.5}$$

$$A = \pi r_s^2 \tag{B.6}$$

$$A_{sy} = I_{sz} = \frac{9A}{10} \tag{B.7}$$

B.2 Static and Dynamic condensation theories

Considering a simple static problem of the form $\mathbf{Ku} = \mathbf{F}$, it is possible to decompose the global stiffness matrix into retained DOFs ($\mathbf{u}_m$) and eliminated DOFs ($\mathbf{u}_s$).

$$\begin{bmatrix} \mathbf{K_{mm}} & \mathbf{K_{ms}} \\ \mathbf{K_{sm}} & \mathbf{K_{ss}} \end{bmatrix} \begin{Bmatrix} \mathbf{u_m} \\ \mathbf{u_s} \end{Bmatrix} = \begin{Bmatrix} \mathbf{F_m} \\ \mathbf{F_s} \end{Bmatrix} \tag{B.8}$$

The retained DOFs correspond to the master nodes, while the eliminated DOFs correspond to the slave nodes as shown in figure B.1.

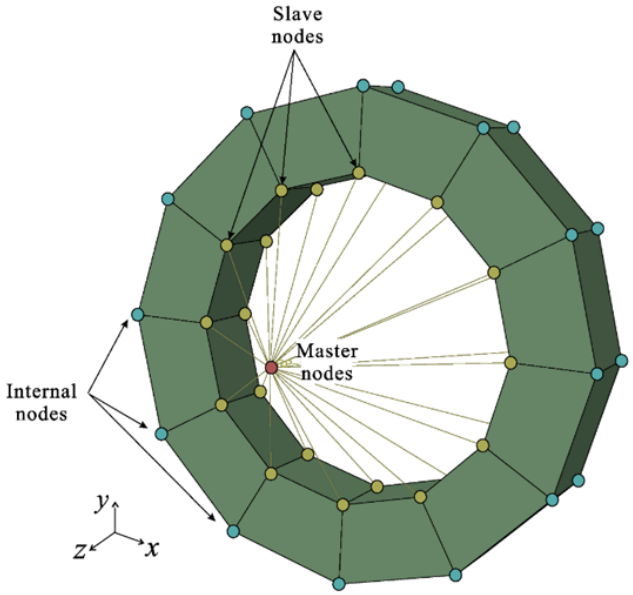

Figure B.1: Visual representation of the node partitioning in a reduced model

Expanding Equation B.8 we obtain:

$$\mathbf{K_{mm}u_m} + \mathbf{K_{ms}u_s} = \mathbf{F_m} \tag{B.9}$$

$$\mathbf{K_{sm}u_m} + \mathbf{K_{ss}u_s} = \mathbf{F_m} \tag{B.10}$$

Rearranging Equation B.10 in terms of the slave DOFs results in:

$$\mathbf{u_s} = \mathbf{K_{ss}^{-1}F_s} - \mathbf{K_{ss}^{-1}K_{sm}u_m} \tag{B.11}$$

Substituting Equation B.12 into Equation B.9 enables the determination of the substructure DOFs from the motions of the master DOFs as follows:

$$[\mathbf{K_{mm}} - \mathbf{K_{ms}K_{ss}^{-1}K_{sm}}]\mathbf{K_{ms}} = \mathbf{F_m} - \mathbf{K_{ms}K_{ss}^{-1}F_s} \tag{B.12}$$

The reduced stiffness matrix $\mathbf{K_r}$ is expressed as:

$$\mathbf{K_r} = \mathbf{K_{mm}} - \mathbf{K_{ms}K_{ss}^{-1}K_{sm}} \tag{B.13}$$

The reduced matrix can therefore be obtained by applying the transformation matrix ($\mathbf{J}$) to the global stiffness matrix ($\mathbf{K}$) as follows:

$$\mathbf{J} = \begin{bmatrix} \mathbf{I} \\ -\mathbf{K_{ss}^{-1}K_{sm}} \end{bmatrix} \tag{B.14}$$

$$\mathbf{K_r} = \mathbf{J}^T\mathbf{K}\mathbf{J} \tag{B.15}$$

($\mathbf{I}$) stands for the identity matrix.

The following technique which interprets the dynamics of slave nodes in a quasi-static sense is known as the static condensation or the Guyan condensation.

When the response of a system becomes significantly influenced by the inertial forces and their contribution becomes as important as the elastic forces, a dynamic condensation technique becomes more appropriate. In such cases, the Craig-Bampton Component Mode Synthesis (CMS) method can be effectively employed. CMS allows for an accurate representation of the dynamic behavior by reducing the number of degrees of freedom while capturing the system's dynamic response efficiently. Besides the master DOFs, the Craig-Bampton method further considers the generalized DOFs $\mathbf{q}$ associated with the natural modes of the substructure. The transformation matrix $\mathbf{J}$, in this case, comprises the previously static transfer matrix in addition to the matrix of eigenvectors (ϕ_E):

$$\mathbf{J} = \begin{bmatrix} \mathbf{I} & 0 \\ -\mathbf{K_{ss}^{-1}K_{sm}} & (\phi_E) \end{bmatrix} \tag{B.16}$$

Applying the transfer matrix to the equation of motion yields the reduced equation which accounts for the dynamic properties in a truncated frequency range depending on the number of modes in (ϕ_E):

$$\mathbf{J}^T\mathbf{M}\mathbf{J}\begin{Bmatrix} \ddot{\mathbf{u}} \\ \ddot{\mathbf{q}} \end{Bmatrix} + \mathbf{J}^T\mathbf{C}\mathbf{J}\begin{Bmatrix} \dot{\mathbf{u}} \\ \dot{\mathbf{q}} \end{Bmatrix} + \mathbf{J}^T\mathbf{K}\mathbf{J}\begin{Bmatrix} \mathbf{u} \\ \mathbf{q} \end{Bmatrix} = \mathbf{J}^T\mathbf{P} \tag{B.17}$$

Appendix C

Chapter 4 Appendix

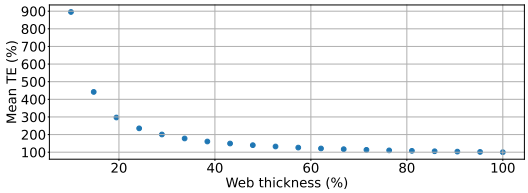

(a) Pinion mean TE

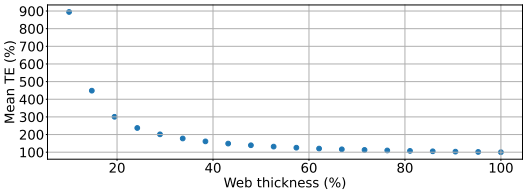

(b) Wheel mean TE

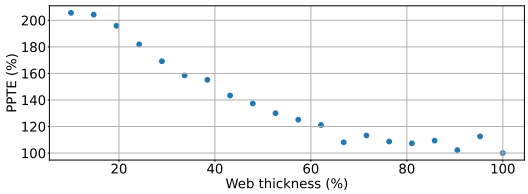

(c) Pinion PPTE

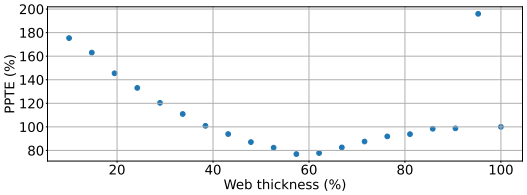

(d) Wheel PPTE

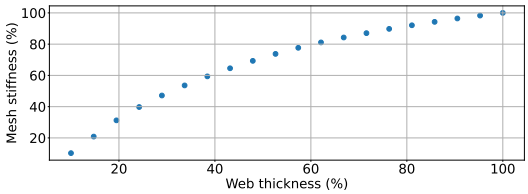

(e) Pinion mesh stiffness

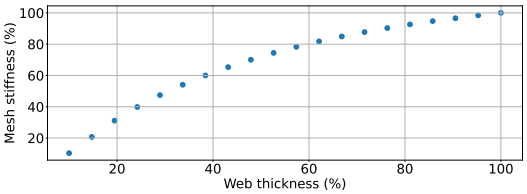

(f) Wheel mesh stiffness

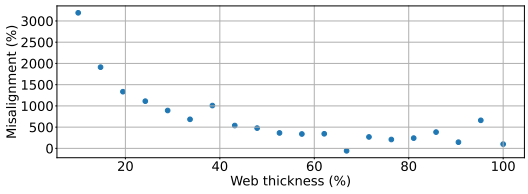

(g) Pinion misalignment

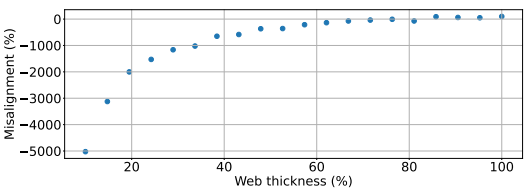

(h) Wheel misalignment

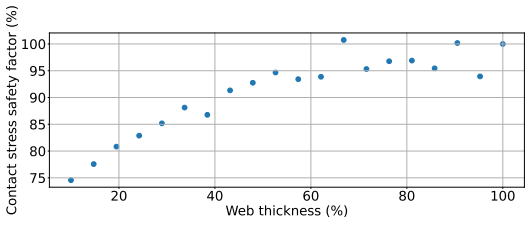

(i) Pinion contact safety factor

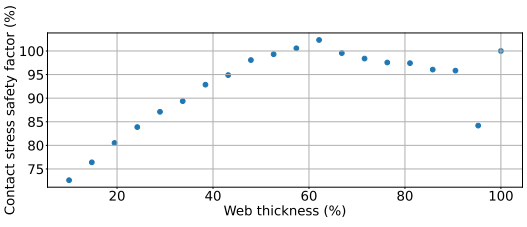

(j) Wheel contact safety factor

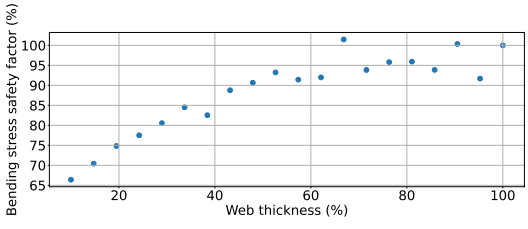

(k) Pinion bending safety factor

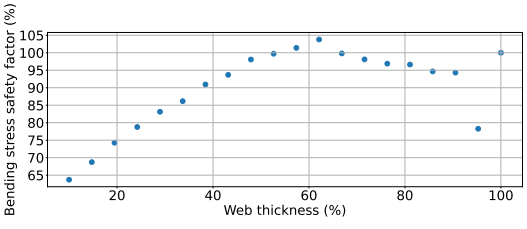

(l) Wheel bending safety factor

Figure C.1: Evolution of the static metrics with the change of the web thickness.

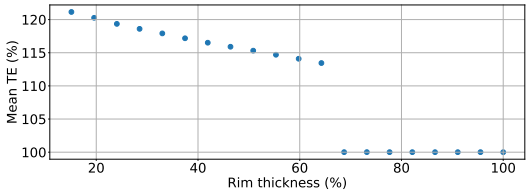

(a) Pinion mean TE

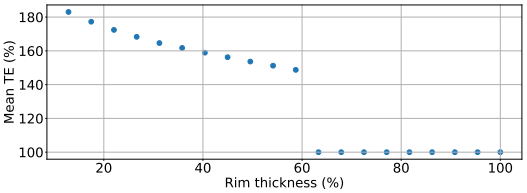

(b) Wheel mean TE

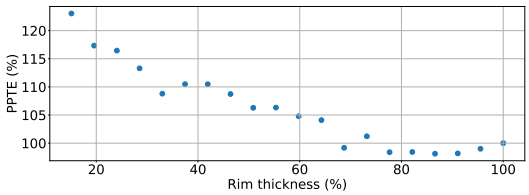

(c) Pinion PPTE

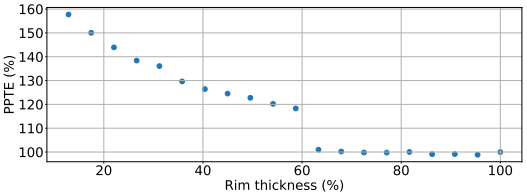

(d) Wheel PPTE

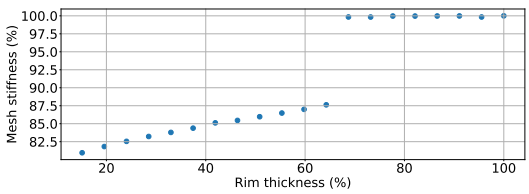

(e) Pinion mesh stiffness

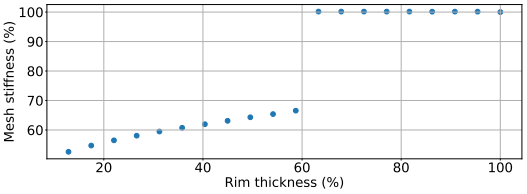

(f) Wheel mesh stiffness

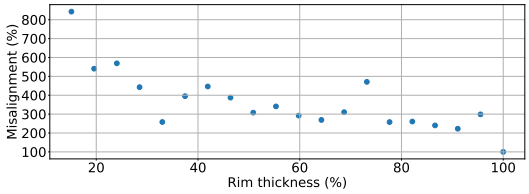

(g) Pinion misalignment

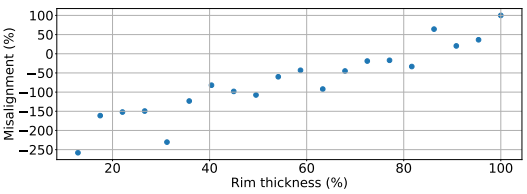

(h) Wheel misalignment

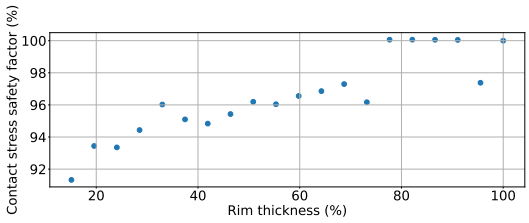

(i) Pinion contact safety factor

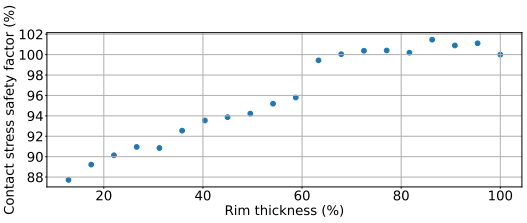

(j) Wheel contact safety factor

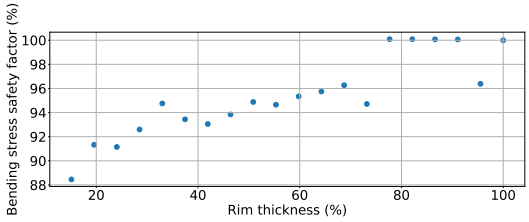

(k) Pinion bending safety factor

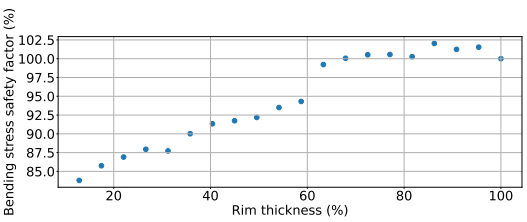

(l) Wheel bending safety factor

Figure C.2: Evolution of the static metrics with the change of the rim thickness.

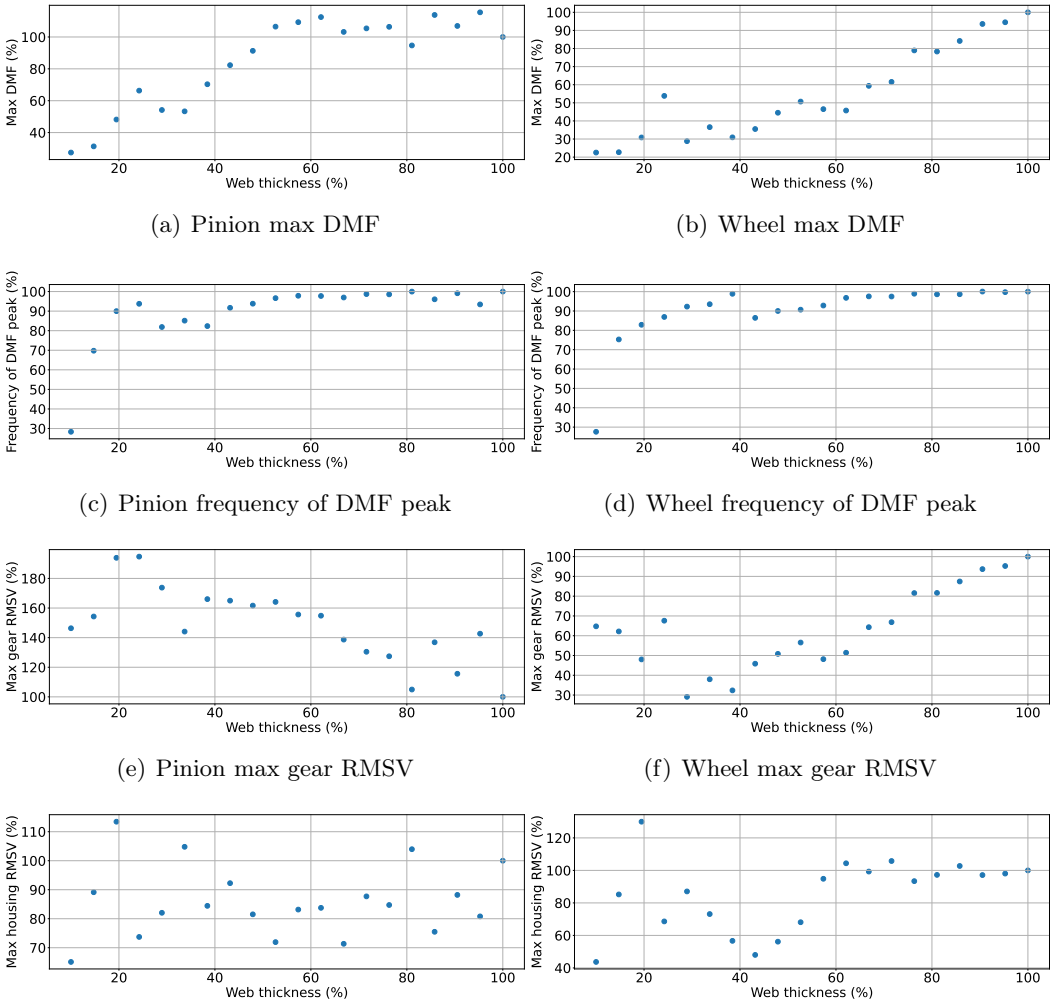

(a) Pinion max DMF

(b) Wheel max DMF

(c) Pinion frequency of DMF peak

(d) Wheel frequency of DMF peak

(e) Pinion max gear RMSV

(f) Wheel max gear RMSV

(g) Pinion max housing RMSV

(h) Wheel max housing RMSV

Figure C.3: Evolution of the dynamic metrics with the change of the web thickness.

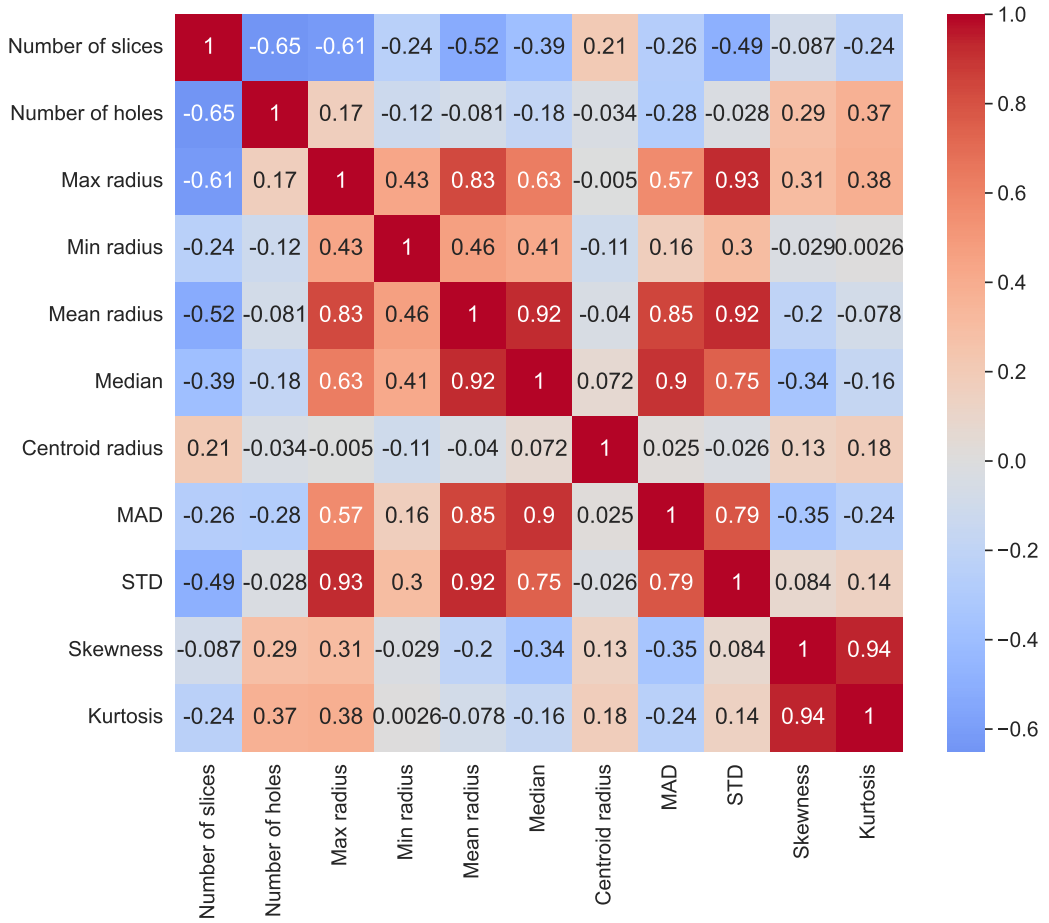

(a) Full correlation matrix.

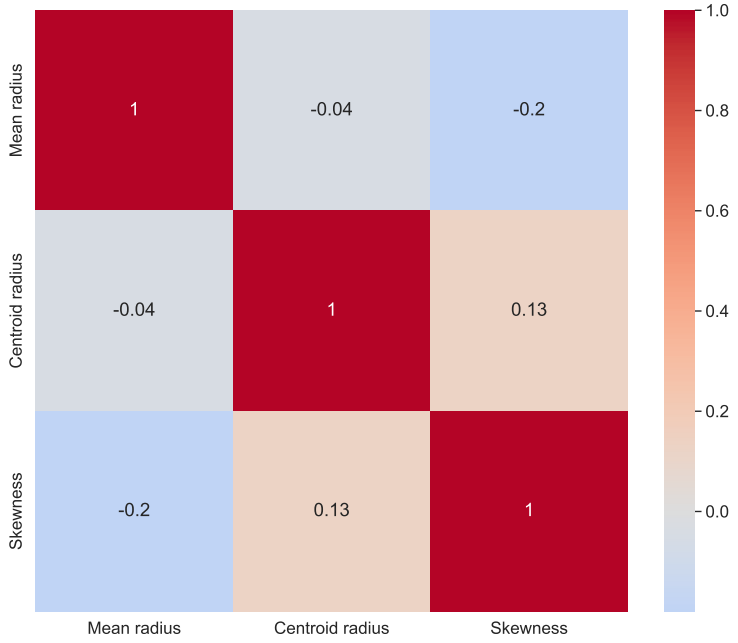

(b) Reduced correlation matrix.

Figure C.4: Pattern variable selection.

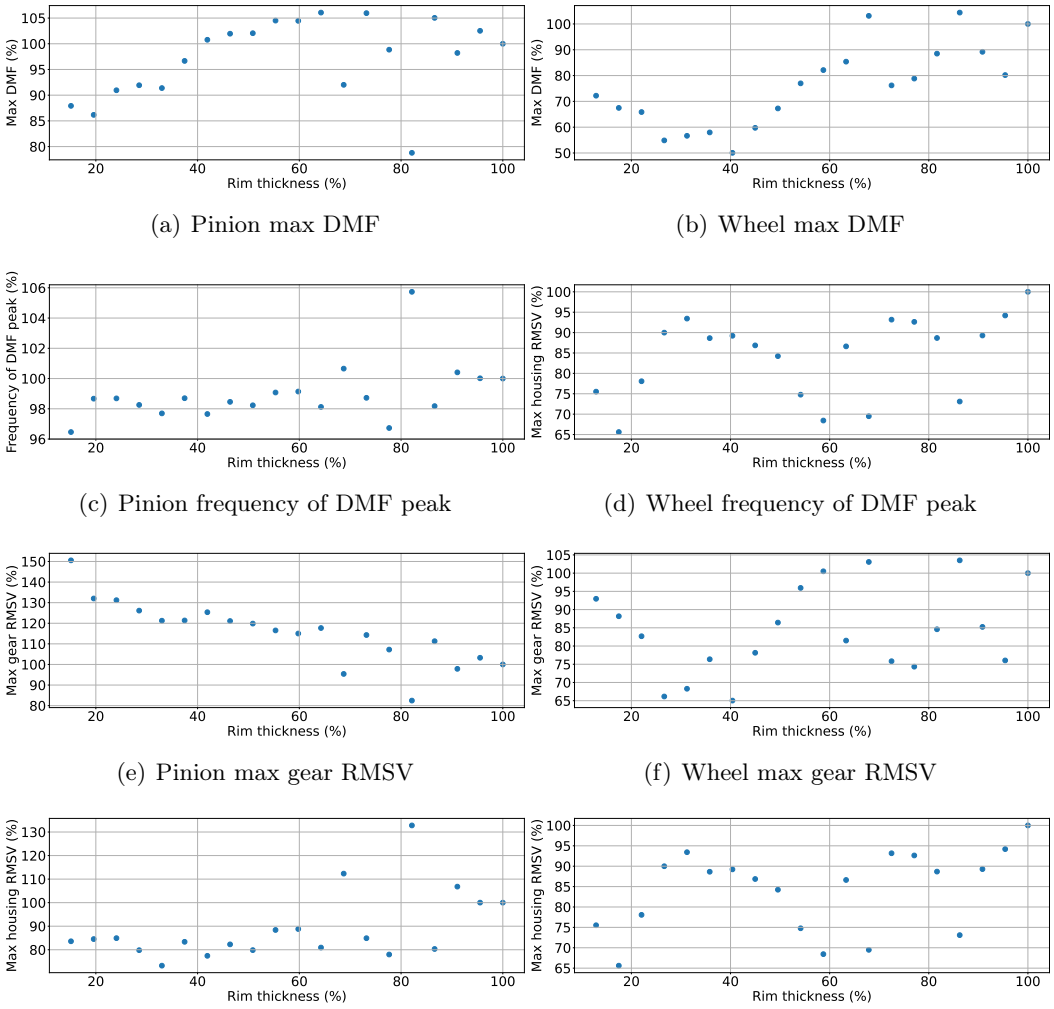

(a) Pinion max DMF

(b) Wheel max DMF

(c) Pinion frequency of DMF peak

(d) Wheel frequency of DMF peak

(e) Pinion max gear RMSV

(f) Wheel max gear RMSV

(g) Pinion max housing RMSV

(h) Wheel max housing RMSV

Figure C.5: Evolution of the dynamic metrics with the change of the rim thickness.

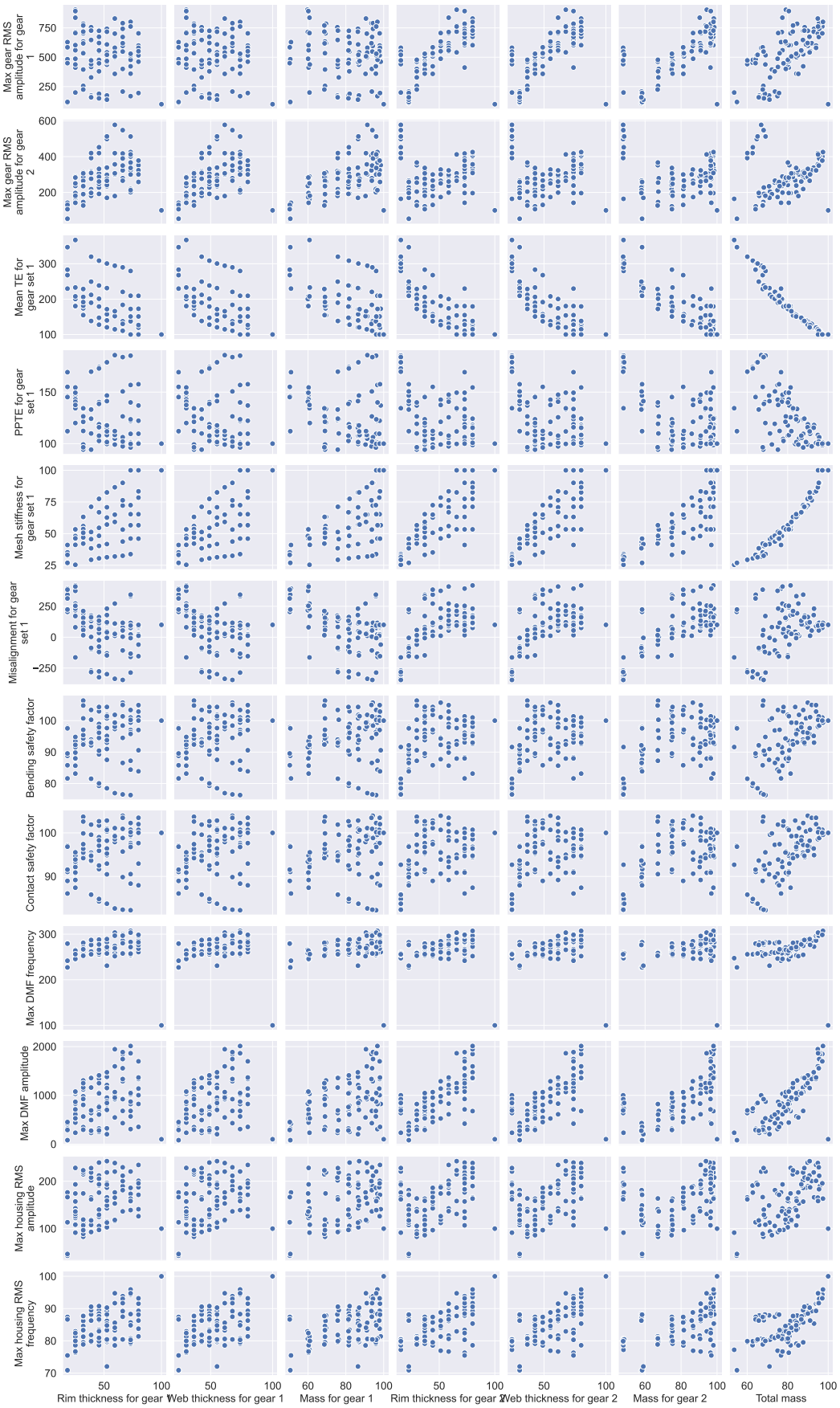

Figure C.6: Input-Output relationship pair-plot for web and rim modification with double gear replacement

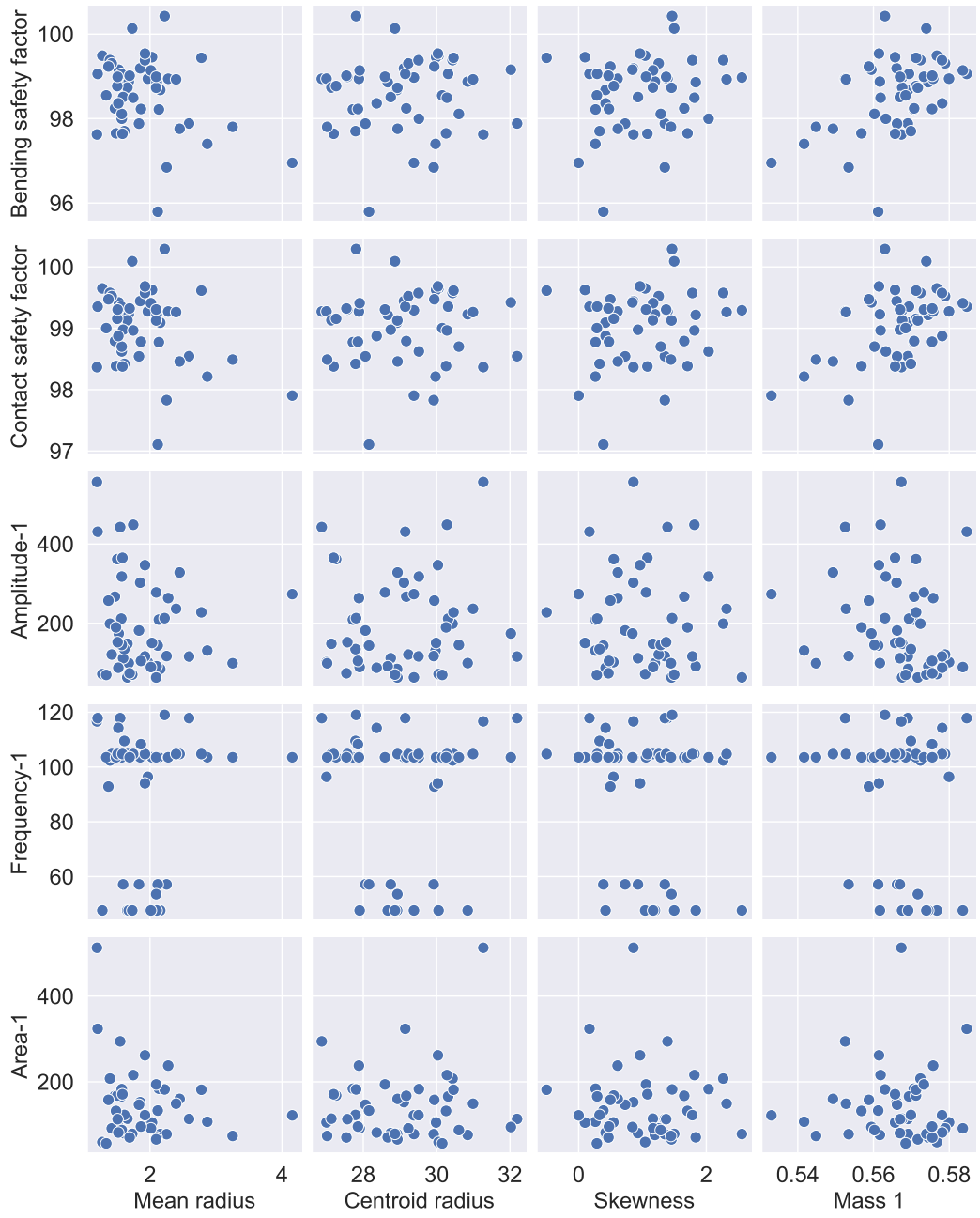

Figure C.7: Input-Output relationship pair-plot for pattern modification in the case of a single gear replacement.

Appendix D

Publications during the thesis

D.1 Journal Papers

- BEJAR, F., PERRET-LIAUDET, J., BAREILLE, O., ICHCHOU, M., FONTANA, M. Benchmarking study of different gear contact analysis software in terms of the static transmission error response. Under review: Journal of Applied Acoustics.
- BEJAR, F., PERRET-LIAUDET, J., BAREILLE, O., ICHCHOU, M., FONTANA, M. Enhancing weight and dynamic response optimization with a dual-level particle swarm optimization scheme. In progress.

D.2 Refereed conference papers

- BEJAR, F., PERRET-LIAUDET, J., BAREILLE, O., ICHCHOU, M., FONTANA, M. Numerical assessment of the static and dynamic behaviors resulting from gear blanks with holes. In the 7^{th} European Conference on Structural Control (EACS), Warsaw, Poland, July 10-13, 2022.
- BEJAR, F., PERRET-LIAUDET, J., BAREILLE, O., ICHCHOU, M., FONTANA, M. Influence of various gear blank geometry patterns on the dynamic response of a transmission system. In the Proceedings of ISMA 2022-International Conference on Noise and Vibration Engineering and USD 2022-International Conference on Uncertainty in Structural Dynamics (ISMA), Leuven, Belgium, September 12-14, 2022.
- BEJAR, F., PERRET-LIAUDET, J., BAREILLE, O., ICHCHOU, M., FONTANA, M. Local sensitivity analysis of the dynamic response of a transmission system to material and geometrical parameters of lightweight gears. In the 4^{th} International Conference on Acoustics and Vibration (ICAV), Sousse, Tunisia, December 19-21, 2022.

Bibliography

[1] Nasa's revolutionary hybrid gear lightens your load. (Cited on page 24.)

[2] Åkerblom, M. Gear noise and vibration: a literature survey. (Cited on page 9.)

[3] Anichowski Jr, B., Kahraman, A., and Talbot, D. Dynamic transmission error measurements from spur gear pairs having tooth indexing errors. In *International Design Engineering Technical Conferences and Computers and Information in Engineering Conference* (2017), vol. 58240, American Society of Mechanical Engineers, p. V010T11A017. (Cited on page 9.)

[4] Asai, Y., Nagae, T., and Hirabayashi, Y. Time domain nv simulation with a/t assy model by modal synthesis method. Tech. rep., SAE Technical Paper, 2018. (Cited on pages 55 and 56.)

[5] Association, A. G. M., et al. Ansi/agma 2001-d04, fundamental rating factors and calculation methods for involute spur and helical gear teeth. *Alexandria, VA: American Gear Manufacturers Association* (2004). (Cited on page 100.)

[6] Bae, J.-H., Jung, K.-C., Yoo, S.-H., Chang, S.-H., Kim, M., and Lim, T. Design and fabrication of a metal-composite hybrid wheel with a friction damping layer for enhancement of ride comfort. *Composite Structures 133* (2015), 576–584. (Cited on page 27.)

[7] Bai, W., Qin, D., Wang, Y., and Lim, T. C. Dynamic characteristics of motor-gear system under load saltations and voltage transients. *Mechanical Systems and Signal Processing 100* (2018), 1–16. (Cited on page 23.)

[8] Benaicha, Y., Mélot, A., Rigaud, E., Beley, J.-D., Thouverez, F., and Perret-Liaudet, J. A decomposition method for the fast computation of the transmission error of gears with holes. *Journal of Sound and Vibration 532* (2022), 116927. (Cited on page 55.)

[9] Benaïcha, Y., Perret-Liaudet, J., Beley, J.-D., Rigaud, E., and Thouverez, F. On a flexible multibody modelling approach using fe-based contact formulation for describing gear transmission error. *Mechanism and Machine Theory 167* (2022), 104505. (Cited on pages 39 and 44.)

[10] Bonori, G., Barbieri, M., and Pellicano, F. Optimum profile modifications of spur gears by means of genetic algorithms. *Journal of sound and vibration 313*, 3-5 (2008), 603–616. (Cited on page 144.)

[11] Borner, J., and Houser, D. R. Friction and bending moments as gear noise excitations. *SAE transactions 105* (1996), 1669–1676. (Cited on pages 14 and 15.)

[12] Brecher, C., Gorgels, C., Hesse, J., and Hellmann, M. Dynamic transmission error measurements of a drive train. *Production Engineering 5* (2011), 321–327. (Cited on page 9.)

[13] Bruyère, J., Gu, X., and Velex, P. On the analytical definition of profile modifications minimising transmission error variations in narrow-faced spur helical gears. *Mechanism and Machine theory 92* (2015), 257–272. (Cited on pages 11 and 144.)

[14] Bruyère, J., and Velex, P. Derivation of optimum profile modifications in narrow-faced spur and helical gears using a perturbation method. *Journal of Mechanical Design 135*, 7 (2013), 071009. (Cited on page 11.)

[15] Buiga, O., and Popa, C.-O. Optimal mass design of a single-stage helical gear unit with genetic algorithms. *Proceedings of the Romanian academy, series a 13*, 3 (2012), 243–250. (Cited on page 144.)

[16] Carbonelli, A., Perret-Liaudet, J., Rigaud, E., and Le Bot, A. Particle swarm optimization as an efficient computational method in order to minimize vibrations of multimesh gears transmission. *Advances in Acoustics and Vibration 2011* (2011). (Cited on pages 144 and 145.)

[17] Chandrasekaran, G., Sreebalaji, V., Saravanan, R., and Maniraj, J. Multiobjective optimisation of bevel gear pair design using nsga-ii. *Materials Today: Proceedings 16* (2019), 351–360. (Cited on page 145.)

[18] Cho, D. H., Choi, J. H., et al. Manufacture of one-piece automotive drive shafts with aluminum and composite materials. *Composite structures 38*, 1-4 (1997), 309–319. (Cited on page 27.)

[19] Chong, T. H., Bae, I., and Park, G.-J. A new and generalized methodology to design multi-stage gear drives by integrating the dimensional and the configuration design process. *Mechanism and machine theory 37*, 3 (2002), 295–310. (Cited on page 144.)

[20] Choy, F. K., Ruan, Y., Tu, R., Zakrajsek, J., and Townsend, D. Modal analysis of multistage gear systems coupled with gearbox vibrations. (Cited on page 22.)

[21] Choy, F. K., Ruan, Y. F., Zakrajsek, J., and Oswald, F. B. Modal simulation of gear box vibration with experimental correlation. *Journal of Propulsion and Power 9*, 2 (1993), 301–306. (Cited on page 23.)

[22] Choy, F. K., Tu, Y. K., Zakrajsek, J. J., and Townsend, D. P. Effects of gear box vibration and mass imbalance on the dynamics of multistage gear transmission. (Cited on page 22.)

[23] Chung, C.-H., Steyer, G., Abe, T., Clapper, M., and Shah, C. Gear noise reduction through transmission error control and gear blank dynamic tuning. *SAE transactions* (1999), 2829–2837. (Cited on page 74.)

[24] Craig Jr, R. R., and Bampton, M. C. Coupling of substructures for dynamic analyses. *AIAA journal 6*, 7 (1968), 1313–1319. (Cited on page 55.)

[25] Cui, D., Wang, G., Lu, Y., and Sun, K. Reliability design and optimization of the planetary gear by a ga based on the dem and kriging model. *Reliability Engineering & System Safety 203* (2020), 107074. (Cited on page 145.)

[26] Cunha, B. Z., Ichchou, M., Droz, C., Zine, A.-M., and Foulard, S. Interpretable and physics-supported machine learning model for sound transmission loss analysis. In *International Conference on Noise and Vibration Engineering, ISMA2022* (2022). (Cited on page 108.)

[27] Daoudi, K., Boudi, E. M., and Abdellah, M. Genetic approach for multiobjective optimization of epicyclical gear train. *Mathematical Problems in Engineering 2019* (2019), 1–10. (Cited on page 145.)

[28] Dhafer, G., Jérôme, B., Philippe, V., Michel, O., and Mohamed, H. Multi-objective optimization of gear tooth profile modifications. In *Design and Modeling of Mechanical Systems: Proceedings of the Fifth International Conference Design and Modeling of Mechanical Systems, CMSM´ 2013, Djerba, Tunisia, March 25-27, 2013* (2013), Springer, pp. 189–197. (Cited on page 145.)

[29] Dobrzański, L. A., Tański, T., Čížek, L., and Brytan, Z. Structure and properties of magnesium cast alloys. *Journal of Materials Processing Technology 192* (2007), 567–574. (Cited on page 24.)

[30] Du, S. Dynamic modelling and simulation of gear transmission error for gearbox vibration analysis. (Cited on page 18.)

[31] El-Saeidy, F. M. Effect of tooth backlash and ball bearing deadband clearance on vibration spectrum in spur gear boxes. *The Journal of the Acoustical Society of America 89*, 6 (1991), 2766–2773. (Cited on page 22.)

[32] Fawcett, J. *1994 International Gearing Conference*. Mechanical Engineering Publications Limited, 1994. (Cited on page 23.)

[33] Fernández, A., Iglesias, M., De-Juan, A., García, P., Sancibrián, R., and Viadero, F. Gear transmission dynamic: Effects of tooth profile deviations and support flexibility. *Applied Acoustics 77* (2014), 138–149. (Cited on page 23.)

[34] Garambois, P., Perret-Liaudet, J., and Rigaud, E. Nvh robust optimization of gear macro and microgeometries using an efficient tooth contact model. *Mechanism and Machine Theory 117* (2017), 78–95. (Cited on pages 23 and 34.)

[35] Gargiulo, E. A simple way to estimate bearing stiffness. *Machine design 52*, 17 (1980), 107–110. (Cited on page 64.)

[36] Ghribi, D., Bruyère, J., Velex, P., Octrue, M., and Haddar, M. A contribution to the design of robust profile modifications in spur and helical gears by combining analytical results and numerical simulations. (Cited on page 10.)

[37] Gregory, R., Harris, S., and Munro, R. Dynamic behaviour of spur gears. *Proceedings of the institution of mechanical engineers 178*, 1 (1963), 207–218. (Cited on pages 10 and 20.)

[38] Gregory, R., Harris, S., and Munro, R. Paper 6: Torsional motions of a pair of spur gears. In *Proceedings of the Institution of Mechanical Engineers, Conference Proceedings* (1963), vol. 178, SAGE Publications Sage UK: London, England, pp. 166–173. (Cited on pages 6 and 20.)

[39] Guilbault, R., Gosselin, C., and Cloutier, L. Helical gears, effects of tooth deviations and tooth modifications on load sharing and fillet stresses. (Cited on page 10.)

[40] Guilbert, B., Velex, P., Dureisseix, D., and Cutuli, P. A mortar-based mesh interface for hybrid finite-element/lumped-parameter gear dynamic models—applications to thin-rimmed geared systems. *Journal of Mechanical Design 138*, 12 (2016). (Cited on page 25.)

[41] Guilbert, B., Velex, P., Dureisseix, D., and Cutuli, P. Modular hybrid models to simulate the static and dynamic behaviour of high-speed thin-rimmed gears. *Journal of Sound and Vibration 438* (2019), 353–380. (Cited on page 25.)

[42] Gunda, R., and Singh, R. Dynamic analysis of sliding friction in a gear pair. In *International Design Engineering Technical Conferences and Computers and Information in Engineering Conference* (2003), vol. 37025, pp. 441–448. (Cited on page 14.)

[43] Guo, H., Zhang, J., and Yu, H. Dynamic modelling and parametric optimization of a full hybrid transmission. *Proceedings of the Institution of Mechanical Engineers, Part K: Journal of Multi-body Dynamics 233*, 1 (2019), 17–29. (Cited on page 16.)

[44] Guo, Y., and Parker, R. G. Stiffness matrix calculation of rolling element bearings using a finite element/contact mechanics model. *Mechanism and machine theory 51* (2012), 32–45. (Cited on page 65.)

[45] Gupta, P. Dynamics of rolling-element bearings—part i: Cylindrical roller bearing analysis. (Cited on page 65.)

[46] Gupta, P. Dynamics of rolling-element bearings—part iii: Ball bearing analysis. (Cited on page 65.)

[47] Guyan, R. J. Reduction of stiffness and mass matrices. *AIAA journal 3*, 2 (1965), 380–380. (Cited on page 55.)

[48] Handschuh, R. F., LaBerge, K. E., DeLuca, S., and Pelagalli, R. Vibration and operational characteristics of a composite-steel (hybrid) gear. Tech. rep., 2014. (Cited on page 27.)

[49] Handschuh, R. F., Sinnamon, R., Stringer, D. B., Dykas, B. D., Kohlman, L. W., et al. Hybrid gear preliminary results-application of composites to dynamic mechanical components. In *68th American Helicopter Society (AHS) Annual forum and Technology Display* (2012), no. E-18121-1. (Cited on page 27.)

[50] Harris, S. L. Dynamic loads on the teeth of spur gears. *Proceedings of the Institution of Mechanical Engineers 172*, 1 (1958), 87–112. (Cited on pages 6, 8, 10, 18 and 46.)

[51] Harris, T. A. *Rolling bearing analysis*. John Wiley and sons, 2001. (Cited on page 64.)

[52] Harris, T. A., and Kotzalas, M. N. *Advanced concepts of bearing technology: rolling bearing analysis*. CRC press, 2006. (Cited on page 65.)

[53] He, S., Gunda, R., and Singh, R. Effect of sliding friction on the dynamics of spur gear pair with realistic time-varying stiffness. *Journal of Sound and Vibration 301*, 3-5 (2007), 927–949. (Cited on page 14.)

[54] Hernot, X., Sartor, M., and Guillot, J. Calculation of the stiffness matrix of angular contact ball bearings by using the analytical approach. *J. Mech. Des. 122*, 1 (2000), 83–90. (Cited on page 65.)

[55] Hou, L., Lei, Y., Fu, Y., and Hu, J. Effects of lightweight gear blank on noise, vibration and harshness for electric drive system in electric vehicles. *Proceedings of the Institution of Mechanical Engineers, Part K: Journal of Multi-Body Dynamics 234*, 3 (2020), 447–464. (Cited on page 25.)

[56] Houser, D. *Gear Noise Sources and Their Prediction Using Mathematical Models*. Gear Dynamics and Gear Noise Research Laboratory, Ohio State Univ., 1985. (Cited on page 12.)

[57] Houser, D. R., Vaishya, M., and Sorenson, J. D. Vibro-acoustic effects of friction in gears: an experimental investigation. Tech. rep., SAE Technical Paper, 2001. (Cited on page 15.)

[58] Howard, I., Jia, S., and Wang, J. The dynamic modelling of a spur gear in mesh including friction and a crack. *Mechanical systems and signal processing 15*, 5 (2001), 831–853. (Cited on pages 19 and 21.)

[59] Hurty, W. C. Dynamic analysis of structural systems using component modes. *AIAA journal 3*, 4 (1965), 678–685. (Cited on page 55.)

[60] Iida, H., Tamura, A., KIKUCHI, K., and Agata, H. Coupled torsional-flexural vibration of a shaft in a geared system of rotors: 1st report. *Bulletin of JSME 23*, 186 (1980), 2111–2117. (Cited on page 21.)

[61] Jia, C., Fang, Z., and Zhang, Y. Topography of modified surfaces based on compensated conjugation for the minimization of transmission errors of cylindrical gears. *Mechanism and Machine Theory 116* (2017), 145–161. (Cited on page 10.)

[62] Johnson, D. Modes and frequencies of shafts coupled by straight spur gears. *Journal of Mechanical Engineering Science 4*, 3 (1962), 241–250. (Cited on page 21.)

[63] Jones, A. B. *New departure engineering data: analysis of stresses and deflections*, vol. 2. New Departure Division, General Motors Corporation, 1946. (Cited on page 64.)

[64] Kahraman, A. Effect of axial vibrations on the dynamics of a helical gear pair. (Cited on page 22.)

[65] Kahraman, A., Bajpai, P., and Anderson, N. Influence of tooth profile deviations on helical gear wear. (Cited on page 10.)

[66] Kahraman, A., and Blankenship, G. Effect of involute tip relief on dynamic response of spur gear pairs. (Cited on page 8.)

[67] Kahraman, A., and Singh, R. Interactions between time-varying mesh stiffness and clearance non-linearities in a geared system. *Journal of Sound and Vibration 146*, 1 (1991), 135–156. (Cited on pages 12, 19 and 20.)

[68] Kahraman, A., and Singh, R. Non-linear dynamics of a geared rotor-bearing system with multiple clearances. *Journal of sound and vibration 144*, 3 (1991), 469–506. (Cited on pages 19 and 20.)

[69] Kang, M. R., and Kahraman, A. Measurement of vibratory motions of gears supported by compliant shafts. *Mechanical Systems and Signal Processing 29* (2012), 391–403. (Cited on page 9.)

[70] Kapelevich, A. L., and Kleiss, R. E. Direct gear design for spur and helical involute gears. *Gear Technology 19*, 5 (2002), 29–35. (Cited on page 10.)

[71] Karpat, F., Yilmaz, T. G., Doğan, O., and Kalay, O. C. Stress and mesh stiffness evaluation of bimaterial spur gears. In *ASME International Mechanical Engineering Congress and Exposition* (2019), vol. 59384, American Society of Mechanical Engineers, p. V02BT02A025. (Cited on page 27.)

[72] Kim, B. J., Kim, H. S., et al. Design of hybrid steel/composite circular plate cutting tool structures. *Composite structures 75*, 1-4 (2006), 250–260. (Cited on page 27.)

[73] Kim, S.-c., Moon, S.-g., Sohn, J.-h., Park, Y.-j., Choi, C.-h., and Lee, G.-h. Macro geometry optimization of a helical gear pair for mass, efficiency, and transmission error. *Mechanism and Machine Theory 144* (2020), 103634. (Cited on page 145.)

[74] Klema, V., and Laub, A. The singular value decomposition: Its computation and some applications. *IEEE Transactions on automatic control 25*, 2 (1980), 164–176. (Cited on page 73.)

[75] Knaapen, R., Kodde, L., and de Kraker (A.). *Experimental determination of rolling element bearing stiffness*. Technische Universiteit Eindhoven Eindhoven, 1997. (Cited on page 65.)

[76] Kohler, H., Pratt, A., and Thompson, A. Paper 14: dynamics and noise of parallel-axis gearing. In *Proceedings of the Institution of Mechanical Engineers, Conference Proceedings* (1969), vol. 184, SAGE Publications Sage UK: London, England, pp. 111–121. (Cited on pages 6 and 21.)

[77] Korka, Z. An overview of mathematical models used in gear dynamics. *Romanian Journal of Acoustics and Vibration 4*, 1 (2007), 43–50. (Cited on pages 18 and 32.)

[78] Korta, J. A., and Mundo, D. Multi-objective micro-geometry optimization of gear tooth supported by response surface methodology. *Mechanism and Machine Theory 109* (2017), 278–295. (Cited on page 10.)

[79] Kurokawa, S., Ariura, Y., and Ohtahara, M. Transmission errors of cylindrical gears under load-influence of tooth profile modification and tooth deflection. *American Society of Mechanical Engineers, Design Engineering Division (Publication) DE 88* (1996), 213–217. (Cited on pages 8 and 10.)

[80] LaBerge, K. E., Handschuh, R. F., Roberts, G., and Thorp, S. Performance investigation of a full-scale hybrid composite bull gear. In *AHS 2016 Forum* (2016), no. GRC-E-DAA-TN30632. (Cited on page 27.)

[81] LaBerge, K. E., Johnston, J. P., Handschuh, R. F., and Roberts, G. D. Evaluation of a variable thickness hybrid composite bull gear. In *Annual Forum of the American Helicopter Society* (2017), no. GRC-E-DAA-TN54603. (Cited on page 27.)

[82] Lanczos, C. An iteration method for the solution of the eigenvalue problem of linear differential and integral operators. (Cited on page 72.)

[83] Langlois, P., Al, B., and Harris, O. Hybrid hertzian and fe-based helical gear-loaded tooth contact analysis and comparison with fe. *Gear Technology 6* (2016), 54–57. (Cited on pages 33 and 38.)

[84] Laschet, A., and Troeder, C. Torsional and flexural vibrations in drive systems: A computer simulation. *Computers in Mechanical Engineering 3* (1984), 32–43. (Cited on page 21.)

[85] Li, R., Chang, T., Wang, J., and Wei, X. Multi-objective optimization design of gear reducer based on adaptive genetic algorithm. In *2008 12th International Conference on Computer Supported Cooperative Work in Design* (2008), IEEE, pp. 229–233. (Cited on page 144.)

[86] Li, S. Experimental investigation and fem analysis of resonance frequency behavior of three-dimensional, thin-walled spur gears with a power-circulating test rig. *Mechanism and Machine Theory 43*, 8 (2008), 934–963. (Cited on page 24.)

[87] Lim, T., and Singh, R. Vibration transmission through rolling element bearings, part v: effect of distributed contact load on roller bearing stiffness matrix, 1994. (Cited on page 65.)

[88] Lim, T. C., and Singh, R. Vibration transmission through rolling element bearings, part i: bearing stiffness formulation. *Journal of sound and vibration 139*, 2 (1990), 179–199. (Cited on page 64.)

[89] Lim, T. C., and Singh, R. Vibration transmission through rolling element bearings, part ii: system studies. *Journal of sound and vibration 139*, 2 (1990), 201–225. (Cited on page 64.)

[90] Lim, T. C., and Singh, R. Vibration transmission through rolling element bearings. part iii: Geared rotor system studies. *Journal of sound and vibration 151*, 1 (1991), 31–54. (Cited on page 22.)

[91] Lin, H. H., Townsend, D. P., and Oswald, F. B. Profile modification to minimize spur gear dynamic loading. Tech. rep., 1987. (Cited on page 10.)

[92] Lin, S., and Poster, S. Development of a braided-composite drive shaft with captured end fittings. In *60th annual forum of the American Helicopter Society International* (2004). (Cited on page 27.)

[93] Lisle, T. J., Shaw, B. A., and Frazer, R. C. External spur gear root bending stress: a comparison of iso 6336: 2006, agma 2101-d04, ansys finite element analysis and strain gauge techniques. *Mechanism and Machine Theory 111* (2017), 1–9. (Cited on page 33.)

[94] Liu, C., Qin, D., and Liao, Y. Dynamic modeling and analysis of high-speed planetary gear including centrifugal force. *Journal of the Brazilian Society of Mechanical Sciences and Engineering 39* (2017), 3769–3778. (Cited on page 23.)

[95] Liu, C., Qin, D., Lim, T. C., and Liao, Y. Dynamic characteristics of the herringbone planetary gear set during the variable speed process. *Journal of Sound and Vibration 333*, 24 (2014), 6498–6515. (Cited on page 23.)

[96] Lu, W., Zhang, Y., Cheng, H., Zhou, Y., and Lv, H. Research on dynamic behavior of multistage gears-bearings and box coupling system. *Measurement 150* (2020), 107096. (Cited on page 23.)

[97] Luo, Y., Baddour, N., and Liang, M. Dynamical modeling and experimental validation for tooth pitting and spalling in spur gears. *Mechanical Systems and Signal Processing 119* (2019), 155–181. (Cited on page 23.)

[98] Ma, H., Yang, J., Song, R., Zhang, S., and Wen, B. Effects of tip relief on vibration responses of a geared rotor system. *Proceedings of the Institution of Mechanical Engineers, Part C: Journal of Mechanical Engineering Science 228*, 7 (2014), 1132–1154. (Cited on page 10.)

[99] Mahr, B. E. B., KISSsoft, A., and Kissling, U. Vergleich der resultate verschiedener kommerzieller programme für die kontaktanalyse von stirnrädern. *technischer Bericht der KISSsoft AG* (2016). (Cited on page 40.)

[100] Mark, W. D. Analysis of the vibratory excitation of gear systems: basic theory. *The Journal of the Acoustical Society of America 63*, 5 (1978), 1409–1430. (Cited on page 6.)

[101] Mayeux, F., Rigaud, E., and Perret-Liaudet, J. Dispersion of critical rotational speeds of gearbox: effect of bearings stiffnesses. *arXiv preprint physics/0701048* (2007). (Cited on page 21.)

[102] Mbarek, M., Rhaiem, S., Kharrat, M., and Dammak, M. Experimental simulation of the friction, temperature, and wear distributions for polyamide–steel gear contact using twin-disc setup. *Proceedings of the Institution of Mechanical Engineers, Part J: Journal of Engineering Tribology 230*, 9 (2016), 1127–1138. (Cited on page 27.)

[103] McVittie, D. Calculating spur and helical gear capacity with iso 6336. *Gear Technology 15* (1998), 11–14. (Cited on page 102.)

[104] Mohammed, O. D., Bhat, A. D., and Falk, P. Robust multi-objective optimization of gear microgeometry design. *Simulation Modelling Practice and Theory 119* (2022), 102593. (Cited on page 10.)

[105] Munro, R. Gear transmission error. *AGMA paper 239*, 10 (1967). (Cited on page 6.)

[106] Mura, A., Curà, F., and Pasculli, L. Optimisation methodology for lightweight gears to be produced by additive manufacturing techniques. *Proceedings of the Institution of Mechanical Engineers, Part C: Journal of Mechanical Engineering Science 232*, 19 (2018), 3512–3523. (Cited on page 25.)

[107] Neriya, S., Bhat, R., Sankar, T., et al. Coupled torsional-flexural vibration of a geared shaft system using finite element analysis. *The Shock and Vibration Bulletin 55*, 3 (1985), 13. (Cited on page 21.)

[108] Oh, S., Oh, S., Kang, J., Lee, I., and Lyu, S. A study on modeling and optimization of tooth microgeometry for a helical gear pair. *International Journal of Precision Engineering and Manufacturing 14* (2013), 423–427. (Cited on page 10.)

[109] Ohrn, K. E. Aircraft energy use. *Encyclopedia of Energy Engineering and Technology (first ed.)* (Florida (2007)), 24–30. (Cited on page 24.)

[110] Opitz, H. A discussion on the origin and treatment of noise in industrial environments-noise of gears. *Philosophical Transactions of the Royal Society of London. Series A, Mathematical and Physical Sciences 263*, 1142 (1968), 369–380. (Cited on page 6.)

[111] Padmanabhan, S., Ganesan, S., Chandrasekaran, M., and Raman, V. S. Gear pair design optimization by genetic algorithm and fea. In *Frontiers in Automobile and Mechanical Engineering-2010* (2010), IEEE, pp. 301–307. (Cited on page 144.)

[112] Palermo, A., Britte, L., Janssens, K., Mundo, D., and Desmet, W. The measurement of gear transmission error as an nvh indicator: theoretical discussion and industrial application via low-cost digital encoders to an all-electric vehicle gearbox. *Mechanical Systems and Signal Processing 110* (2018), 368–389. (Cited on page 9.)

[113] Palmgren, A. Ball and roller bearing engineering. *Philadelphia: SKF Industries Inc* (1959). (Cited on page 64.)

[114] Park, C. I. Multi-objective optimization of the tooth surface in helical gears using design of experiment and the response surface method. *Journal of mechanical science and technology 24* (2010), 823–829. (Cited on page 10.)

[115] Parker, R., Vijayakar, S., and Imajo, T. Non-linear dynamic response of a spur gear pair: modelling and experimental comparisons. *Journal of Sound and vibration 237*, 3 (2000), 435–455. (Cited on page 12.)

[116] Parmar, A., Ramkumar, P., and Shankar, K. Macro geometry multi-objective optimization of planetary gearbox considering scuffing constraint. *Mechanism and Machine Theory 154* (2020), 104045. (Cited on page 145.)

[117] Patil, M., Ramkumar, P., and Shankar, K. Multi-objective optimization of the two-stage helical gearbox with tribological constraints. *Mechanism and Machine Theory 138* (2019), 38–57. (Cited on page 144.)

[118] Perret-Liaudet, J. An original method for computing the response of a parametrically excited forced system. *Journal of Sound and Vibration 196*, 2 (1996), 165–177. (Cited on page 12.)

[119] Pogačnik, A., and Kalin, M. Parameters influencing the running-in and long-term tribological behaviour of polyamide (pa) against polyacetal (pom) and steel. *Wear 290* (2012), 140–148. (Cited on page 27.)

[120] Prabhu, M. S. *Load distribution and transmission error in thin-rimmed gears through finite element analysis*. PhD thesis, Ohio State University, 1994. (Cited on page 37.)

[121] Przemieniecki, J. S. *Theory of matrix structural analysis*. Courier Corporation, 1985. (Cited on page 63.)

[122] Ramadani, R., Belsak, A., Kegl, M., Predan, J., and Pehan, S. Topology optimization based design of lightweight and low vibration gear bodies. *Int. J. Simul. Model 17*, 1 (2018), 92–104. (Cited on page 26.)

[123] Reissner, E. The effect of transverse shear deformation on the bending of elastic plates. (Cited on page 35.)

[124] Reissner, E. On a variational theorem in elasticity. *Journal of Mathematics and Physics 29*, 1-4 (1950), 90–95. (Cited on page 35.)

[125] Remmers, E. Gear mesh excitation spectra for arbitrary tooth spacing errors, load and design contact ratio. (Cited on pages 6 and 20.)

[126] Remond, D., and Mahfoudh, J. From transmission error measurements to angular sampling in rotating machines with discrete geometry. *Shock and vibration 12*, 2 (2005), 149–161. (Cited on page 9.)

[127] Ren, Y., Chang, S., Liu, G., Wu, L., and Lim, T. C. Impedance synthesis based vibration analysis of geared transmission system. *Shock and Vibration 2017* (2017). (Cited on page 23.)

[128] Rezayat, A., Catera, P. G., Capalbo, C., Cosco, F., and Mundo, D. Numerical and experimental analysis of the transmission error in hybrid metal-composite gears. *Composite Structures 298* (2022), 116012. (Cited on page 27.)

[129] Rigaud, E., and Barday, D. Modélisation et analyse de l'erreur statique de transmission d'un engrenage. influence des déformations des roues et interactions entre les couples de dents en prise. *Mec. Ind. Mater. 51*, physics/0701043 (2007), 58–60. (Cited on page 13.)

[130] Rigaud, E., and Sabot, J. Effect of elasticity of shafts, bearings, casing and couplings on the critical rotational speeds of a gearbox. *arXiv preprint physics/0701038* (2007). (Cited on page 21.)

[131] Sabot, J. Computation of noise radiated by a simplified gearbox. In *Proceedings of the Int. Gearing Conf., University of Newcastle upon Tyne* (1994), pp. 63–68. (Cited on page 23.)

[132] Sanghvi, R., Vashi, A., Patolia, H., Jivani, R., et al. Multi-objective optimization of two-stage helical gear train using nsga-ii. *Journal of optimization 2014* (2014). (Cited on page 144.)

[133] Shah, C., Thigale, S., and Shah, R. Optimizing weight of a gear using topology optimization. *International Journal of Science, Engineering and Technology Research 7*, 6 (2018), 403–406. (Cited on page 26.)

[134] Shweiki, S., Palermo, A., and Mundo, D. A study on the dynamic behaviour of lightweight gears. *Shock and Vibration 2017* (2017). (Cited on pages 24 and 33.)

[135] Shweiki, S., Rezayat, A., Tamarozzi, T., and Mundo, D. Transmission error and strain analysis of lightweight gears by using a hybrid fe-analytical gear contact model. *Mechanical Systems and Signal Processing 123* (2019), 573–590. (Cited on page 33.)

[136] Simon, V. V. Multi-objective optimization of hypoid gears to improve operating characteristics. *Mechanism and Machine Theory 146* (2020), 103727. (Cited on page 145.)

[137] Singh, R., Lake, A., Asnani, V., and He, S. Vibro-acoustic model of a geared system including friction excitation. In *INTER-NOISE and NOISE-CON Congress and Conference Proceedings* (2007), vol. 2007, Institute of Noise Control Engineering, pp. 2921–2930. (Cited on page 14.)

[138] Steward, J. H. *Elastic analysis of load distribution in wide-faced spur gears.* PhD thesis, Newcastle University, 1989. (Cited on page 37.)

[139] Tamminana, V. K., Kahraman, A., and Vijayakar, S. A study of the relationship between the dynamic factors and the dynamic transmission error of spur gear pairs. (Cited on page 9.)

[140] Tavakoli, M., and Houser, D. Optimum profile modifications for the minimization of static transmission errors of spur gears. (Cited on page 10.)

[141] Teja, R., Milind, T., Glover, R. C., and Sonawane, S. Dynamic analysis of helical gear pair due to te and shuttling moment excitations. Tech. rep., SAE Technical Paper, 2017. (Cited on page 15.)

[142] Terauchi, Y., Nadano, H., and NOHARA, M. On the effect of the tooth profile modification on the dynamic load and the sound level of the spur gear. *Bulletin of JSME 25*, 207 (1982), 1474–1481. (Cited on page 10.)

[143] Tesfahunegn, Y. A., Rosa, F., and Gorla, C. The effects of the shape of tooth profile modifications on the transmission error, bending, and contact stress of spur gears. *Proceedings of the Institution of Mechanical Engineers, Part C: Journal of Mechanical Engineering Science 224*, 8 (2010), 1749–1758. (Cited on page 10.)

[144] Tiwari, R., and Chakravarthy, V. Simultaneous identification of residual unbalances and bearing dynamic parameters from impulse responses of rotor–bearing systems. *Mechanical systems and signal processing 20*, 7 (2006), 1590–1614. (Cited on page 65.)

[145] Tordion, G., and Gerardin, H. Dynamic measurement of the transmission error in gears. In *Proc. JSME Semi-International Symposium September* (1967), pp. 279–287. (Cited on page 20.)

[146] Toso, A., van Wermeskerken, F., Cappellini, N., and Heirman, G. On the effect of lightweight gear blank topology on transmission dynamics. In *International Design Engineering Technical Conferences and Computers and Information in Engineering Conference* (2015), vol. 57205, American Society of Mechanical Engineers, p. V010T11A027. (Cited on page 24.)

[147] Tuma, J. *Vehicle gearbox noise and vibration: Measurement, signal analysis, signal processing and noise reduction measures.* John Wiley & Sons, 2014. (Cited on page 16.)

[148] Tuplin, W. Gear-tooth stresses at high speed. *Proceedings of the Institution of Mechanical Engineers 163*, 1 (1950), 162–175. (Cited on pages 18 and 19.)

[149] Umeyama, M. Effects of deviation of tooth surface errors of a helical gear pair on the transmission error. *Nippon Kikai Gakkai Ronbunshu, C Hen/Transactions of the Japan Society of Mechanical Engineers, Part C 61*, 587 (1995), 3101–3107. (Cited on page 10.)

[150] Vaishya, M., and Singh, R. Analysis of periodically varying gear mesh systems with coulomb friction using floquet theory. *Journal of sound and vibration 243*, 3 (2001), 525–545. (Cited on page 14.)

[151] Vaishya, M., and Singh, R. Sliding friction-induced non-linearity and parametric effects in gear dynamics. *Journal of sound and vibration 248*, 4 (2001), 671–694. (Cited on page 14.)

[152] Van Khang, N., Cau, T. M., and Dien, N. P. Modelling parametric vibration of gear-pair systems as a tool for aiding gear fault diagnosis. *Technische Mechanik-European Journal of Engineering Mechanics 24*, 3-4 (2004), 198–205. (Cited on page 22.)

[153] Vedmar, L. *On the design of external involute helical gears*. na, 1981. (Cited on page 37.)

[154] Velex, P., Bruyère, J., and Houser, D. Some analytical results on transmission errors in narrow-faced spur and helical gears: influence of profile modifications. (Cited on page 11.)

[155] Velex, P., and Maatar, M. A mathematical model for analyzing the influence of shape deviations and mounting errors on gear dynamic behaviour. *Journal of Sound and Vibration 191*, 5 (1996), 629–660. (Cited on page 21.)

[156] Vijayakar, S. Contact analysis of gears using a combined finite element and surface integral method. *Gear Technology 10* (1993), 26–26. (Cited on pages 20 and 33.)

[157] Vinayak, H., Singh, R., and Padmanabhan, C. Linear dynamic analysis of multi-mesh transmissions containing external, rigid gears. *Journal of Sound and Vibration 185*, 1 (1995), 1–32. (Cited on page 12.)

[158] Walker, H., et al. Gear tooth deflection and profile modification. *Engineer 166* (1938), 409–412. (Cited on page 10.)

[159] Walters, C. T. The dynamics of ball bearings. (Cited on page 65.)

[160] Wang, C. On analytical evaluation of gear dynamic factors based on rigid body dynamics. (Cited on page 20.)

[161] Wang, S., and Morse Jr, I. Torsional response of a gear train system. (Cited on page 21.)

[162] Weber, C. The deformation of loaded gears and the effect on their load-carrying capacity. *Sponsored Research (Germany), British Dept. of Scientific and Industrial Research, Report 3* (1949). (Cited on pages 33 and 35.)

[163] Weber, C., and Banaschek, K. The deformation of loaded gears and the effect on their load carrying capacity (part i). *DSIR, London* (1949). (Cited on page 35.)

[164] Welbourn, D. Fundamental knowledge of gear noise: a survey. Tech. rep., 1979. (Cited on pages 6 and 8.)

[165] White, R., and Palan, V. Measurement of transmission error using rotational laser vibrometers. In *International Design Engineering Technical Conferences and Computers and Information in Engineering Conference* (2007), vol. 48086, pp. 527–545. (Cited on page 9.)

[166] Wink, C., and Serpa, A. Investigation of tooth contact deviations from the plane of action and their effects on gear transmission error. *Proceedings of the Institution of Mechanical Engineers, Part C: Journal of Mechanical Engineering Science 219*, 5 (2005), 501–509. (Cited on page 10.)

[167] Wu, Y.-j., Wang, J.-j., and Han, Q.-k. Contact finite element method for dynamic meshing characteristics analysis of continuous engaged gear drives. *Journal of Mechanical Science and Technology 26*, 6 (2012), 1671. (Cited on page 20.)

[168] Wu, Y.-j., Wang, J.-j., and Han, Q.-k. Static/dynamic contact fea and experimental study for tooth profile modification of helical gears. *Journal of mechanical science and technology 26* (2012), 1409–1417. (Cited on page 10.)

[169] Xiang, L., and Gao, N. Coupled torsion–bending dynamic analysis of gear-rotor-bearing system with eccentricity fluctuation. *Applied Mathematical Modelling 50* (2017), 569–584. (Cited on page 8.)

[170] Xiao, W., Huang, Y., Jiang, H., and Jin, L. Effect of powder material on vibration reduction of gear system in centrifugal field. *Powder Technology 294* (2016), 146–158. (Cited on page 28.)

[171] Xiao, W., Li, J., Wang, S., and Fang, X. Study on vibration suppression based on particle damping in centrifugal field of gear transmission. *Journal of Sound and Vibration 366* (2016), 62–80. (Cited on page 28.)

[172] Yaldirim, N., and Munro, R. A new type of profile relief for high contact ratio spur gears. *Proceedings of the Institution of Mechanical Engineers, Part C: Journal of Mechanical Engineering Science 213*, 6 (1999), 563–568. (Cited on page 10.)

[173] Yao, Q. Multi-objective optimization design of spur gear based on nsga-ii and decision making. *Advances in Mechanical Engineering 11*, 3 (2019), 1687814018824936. (Cited on page 144.)

[174] Yi, Y., Qin, D., and Liu, C. Investigation of electromechanical coupling vibration characteristics of an electric drive multistage gear system. *Mechanism and machine theory 121* (2018), 446–459. (Cited on page 23.)

[175] Yildirim, N., and Munro, R. A systematic approach to profile relief design of low and high contact ratio spur gears. *Proceedings of the Institution of Mechanical Engineers, Part C: Journal of Mechanical Engineering Science 213*, 6 (1999), 551–562. (Cited on page 10.)

[176] Yilmaz, T. G., Doğan, O., and Karpat, F. A comparative numerical study of forged bi-metal gears: bending strength and dynamic response. *Mechanism and Machine Theory 141* (2019), 117–135. (Cited on pages 25 and 27.)

[177] Yilmaz, T. G., Tüfekçi, M., and Karpat, F. A study of lightweight door hinges of commercial vehicles using aluminum instead of steel for sustainable transportation. *Sustainability 9*, 10 (2017), 1661. (Cited on page 24.)

[178] Yoon, K., and Rao, S. Dynamic load analysis of spur gears using a new tooth profile. (Cited on page 10.)

[179] Younes, E. B., Changenet, C., Bruyère, J., Rigaud, E., and Perret-Liaudet, J. Multi-objective optimization of gear unit design to improve efficiency and transmission error. *Mechanism and Machine Theory 167* (2022), 104499. (Cited on page 145.)

[180] Yu, Y., Shi, J., Shen, C., Luo, Y., Wang, T., and Zhu, Z. Dynamic modelling of gearbox with multiple localized defects and its coupled vibration analysis. *Mechanical Systems and Signal Processing 180* (2022), 109469. (Cited on page 24.)

[181] Yuce, C., Karpat, F., Yavuz, N., and Sendeniz, G. A case study: Designing for sustainability and reliability in an automotive seat structure. *Sustainability 6*, 7 (2014), 4608–4631. (Cited on page 24.)

[182] Zhang, Q., Kang, J., Dong, W., and Lyu, S. A study on tooth modification and radiation noise of a manual transaxle. *International Journal of Precision Engineering and Manufacturing 13* (2012), 1013–1020. (Cited on page 10.)

[183] Zhang, Y., Sun, G., Lim, T. C., and Xie, L. A fast and reliable numerical method for analyzing loaded rolling element bearing displacements and stiffness. *Journal of Vibroengineering 17*, 2 (2015), 620–642. (Cited on page 65.)

[184] Zhao, X., Yan, X., Chen, Z., Li, L., Ren, R., et al. Dynamic and static multiobjective topology optimization for gears of directional drill transmission system. *Advances in Civil Engineering 2023* (2023). (Cited on page 26.)

[185] Zhu, C., Xu, X., Liu, H., Luo, T., and Zhai, H. Research on dynamical characteristics of wind turbine gearboxes with flexible pins. *Renewable Energy 68* (2014), 724–732. (Cited on page 23.)

[186] Zorko, D., Tavčar, J., Šturm, R., and Bergant, Z. Investigation of the durability and performance of autoclave-cured, woven carbon fiber-reinforced polymer composite gears in mesh with a steel pinion. *Composite Structures 273* (2021), 114250. (Cited on page 27.)